

Engineered Nanomaterial Interactions with Bacterial Cells

A DISSERTATION
SUBMITTED TO THE FACULTY OF THE GRADUATE SCHOOL
OF THE UNIVERSITY OF MINNESOTA
BY

Ian Lyle Gunsolus

IN PARTIAL FULFILLMENT OF THE REQUIREMENTS
FOR THE DEGREE OF
DOCTOR OF PHILOSOPHY

Christy L. Haynes, Advisor

May, 2016

© Ian Lyle Gunsolus 2016

Acknowledgements

This dissertation is the product of many collaborations, small and large, professional and personal. Here I would like to acknowledge the generous support of all my collaborators, including professors, colleagues, friends, and family; without their support, this dissertation would not exist.

First, I would like to thank my advisor, Prof. Christy Haynes, for building a research environment that helped me grow from a classroom student of chemistry to an independent researcher. By encouraging me to think beyond my independent work and actively engage with the broader scientific community, Christy has made me into a better scientist, and I thank her for it.

I would also like to thank Prof. Philippe Bühlmann for his insightful contributions to my research throughout my thesis work. Through his service on my preliminary exam and thesis committees and his role as co-principal investigator (along with Christy) on research assessing the environmental behavior of silver nanoparticles, Phil has sharpened the focus of my research and deepened my critical analysis of chemical phenomena.

My involvement in the Center for Sustainable Nanotechnology (CSN) has been a highlight of my graduate studies, and I am grateful to all past and present CSN members. I would particularly like to thank Prof. Robert Hamers, whose example of leadership through dedicated service amazes and inspires me; Prof. Joel Pedersen, who has improved my scientific reasoning and communication skills by emphasizing thorough, careful analysis and clarity of presentation; Prof. Vivian Feng, who has generously shared her perspective on research and professional development through numerous conversations; and Dr. Galya Orr and her coworkers at Pacific Northwest National Laboratory, including Drs. Dehong Hu, Craig Szymanski, and Cosmin Mihai and William Chrisler, who made my two-month research exchange both productive and enjoyable. I am grateful to the National Science Foundation's Centers for Chemical Innovation program, which has funded the CSN under grant CHE-1503408.

I have had the opportunity to work with many talented graduate students and postdocs both at the University of Minnesota and at other institutions throughout my thesis work. I would particularly like to thank Dr. Maral Mousavi, who has been a dedicated collaborator and who has modeled excellence in analytical research; Dr. Melissa Maurer-Jones, who introduced me to research in the Haynes lab and provided invaluable support in preparation for my preliminary exams; the CSN students I have most-closely collaborated with, including Mimi Hang, Drs. Kurt Jacobson and Samuel Lohse, Julianne Troiano, Marco Torelli, Dr. Thomas Kuech, Eric Melby, and Arielle Mensch; and all past and present Haynes group members. I have also been fortunate to mentor and work with many talented undergraduate students, including Kadir Hussein, Hilena Frew, and Lyle Nyberg.

I am grateful for the support of many staff members in the University of Minnesota Department of Chemistry, including Nancy Thao, who has answered numerous questions and provided advice to keep my graduate studies on track; Chris Lundby, who provided outstanding support during my industrial job-search; and Eric Schultz, who has helped me solve many computer and electronics issues.

I am also grateful to the University of Minnesota faculty that have generously shared their resources and knowledge with me, including Prof. Kent Mann, who kindly allowed me gain research experience by working in his laboratory after I completed my undergraduate studies; and Profs. Pete Carr, Michael Sadowsky, and Michael Bowser, who, along with Profs. Christy Haynes and Philippe Bühlmann, taught my graduate courses. I would like to thank my thesis committee members not already mentioned, specifically Profs. Santiago Romero-Vargas Castrillon and Edgar Arriaga. Moreover, I am grateful to all the Professors of Chemistry at St. Olaf College who sparked my interest in the subject and provided me with a solid foundation of chemical knowledge, especially Profs. Wesley Pearson, Gary Miessler, and Jeffrey Schweinfus.

I am indebted to the members of the Minneapolis Torske Klubben, who provided generous financial support during my second and third years of graduate study, and to the University of Minnesota Biotechnology Training Grant and Doctoral Dissertation Fellowship for partial funding of my research.

Finally, I would like to express my deep gratitude my family. To my parents, Jeffrey and Karla Gunsolus: thank you for your devoted support throughout my journey. You have been a wellspring of knowledge, guidance, and inspiration and have made this journey possible. To my fiancée, Kirsten Petersen: thank you for enriching my life with your kindness, humor, and intelligence. You have provided me with astute perspective and continual encouragement and have made this journey possible. To my grandparents, Elton and Luella Gunsolus: thank you for your foresight and commitment to my education. You were exceptionally generous to me and have made this journey possible.

Dedication

This thesis is dedicated to all my family, friends, and colleagues.

Abstract

Nanomaterials occur naturally in a variety of forms. They exist, for example, in the aerosols produced from sea spray and in the particulates produced from incomplete combustion of hydrocarbons. In the latter 20th century, development of instruments such as the scanning tunneling microscope and atomic force microscope have allowed us to directly see and to manipulate nanoscale matter. Armed with these instrumental capabilities and a desire to push the limits of our ability to create and manipulate matter, we have begun to engineer nanomaterials for our own use. Today, nanomaterials are used as additives in numerous commercial products to improve performance and/or reduce cost. Examples include silver nanomaterials in fabrics to inhibit microbial growth and titanium dioxide nanomaterials in outdoor paints to reduce weathering. Less often, nanomaterials serve a primary function in product performance; one important example of this is the use of nanoscale mixed metal oxides as cathode materials in lithium-ion batteries, used in some electric vehicles.

The increasing commercial use of engineered nanomaterials increases direct human contact with nanoscale matter beyond that which formerly occurred naturally. Taking a proactive view of these developments, a small group of researchers began, in the early 2000s, to assess the implications of nanomaterial exposure on human health, giving rise to the field of nanotoxicology. In recent years, the field has expanded its focus beyond human health to include environmental health, recognizing that the waste streams resulting from the production, use, and disposal of products containing nanomaterials serve as new sources in natural environments. The goal of environmental nanotoxicity

research, of which my dissertation research is a part, is to promote the sustainable use of engineered nanomaterials by assessing their environmental toxicity and informing their design in order to minimize environmental impact. As a project rooted in chemistry, my dissertation focuses in particular on identifying molecular structures, both nanomaterial and biological, that can be used to predict and control the environmental impact of nanomaterials.

My research focuses on characterizing the interactions of commercially relevant nanomaterials with microorganisms, which play fundamental roles in healthy ecosystems. The bacterium *Shewanella oneidensis* MR-1, grown in culture, was used throughout my research as a model, albeit greatly simplified, of microorganism communities in natural environments. This particular bacterium was chosen due to the worldwide distribution of its genus, *Shewanella*, and its ability to survive in many environments, including aerobic, anaerobic, low-temperature, and high-salinity environments. Using this drastically simplified model greatly facilitates isolation of experimental variables, which would be much more difficult to achieve in the extremely chemically complex environment of soil or water samples collected from nature. This, in turn, greatly facilitates hypothesis testing. However, experimentation using samples obtained directly from nature is also necessary to develop a complete understanding of nanomaterial behavior in the environment.

My research specifically addresses the following questions: What impact does natural organic matter (a ubiquitous component of natural sediments, soils, and water bodies) have on nanoparticle toxicity to bacteria in aquatic environments? How can we visually

observe nanomaterial interactions with bacteria, both of which are near or below the diffraction limit of light, under hydrated conditions? Which structures on the bacterial cell surface primarily interact with nanomaterials? By what mechanism(s) might nanoscale battery cathode materials be toxic to bacteria, and how can we design less-toxic materials? The five major outcomes of my research, briefly summarized below, are presented in detail in Chapters 2-6.

To address the first question (Chapters 2 and 3), I investigated the interactions between silver nanoparticles (also silver ions -- produced under aerobic conditions by the dissolution of silver nanoparticles) and natural organic matter. Natural organic matter is a complex mixture of polysaccharides, proteins, nucleic acids, and lipids and is produced through the decomposition of vegetative and microbial matter. Engineered nanoparticles entering natural environments, including soils, sediments, and water bodies, will inevitably encounter natural organic matter. Previous research has demonstrated that nanoparticle transport, persistence, and toxicity are influenced by interactions with natural organic matter. However, some reports conflict with these results and have demonstrated little or no impact of natural organic matter on nanoparticle behavior (e.g., colloidal stability). This conflict may result from a lack of attention paid to differences in the chemical composition of natural organic matter derived from various natural sources. The chemical heterogeneity of natural organic matter in various natural environments is significant, but researchers have often considered it to be a standard “class” of molecules that has common patterns of interaction with nanoparticles. My research, conducted in collaboration with Drs. Philippe Bühlmann and Maral Mousavi at the University of

Minnesota—Twin Cities, sought to more specifically define the characteristics of natural organic matter that influence the behavior of silver nanoparticles and ions in natural aquatic environments.

This research revealed that natural organic matter adsorption to silver nanoparticles and binding to silver ions depend greatly on the concentration of sites with high affinity for silver (e.g., sites rich in S and N). This result was affirmed by subsequent experiments with *Shewanella*, wherein silver nanoparticles and ions were less toxic only when first exposed to natural organic matter with this high binding affinity. This research also demonstrated a novel application of ion-selective electrodes in real-time monitoring of the dissolution kinetics of silver nanoparticles and the kinetics of natural organic matter binding to silver ions. This approach represents a significant improvement over the previous state-of-the-art (i.e., inductively-coupled plasma optical emission spectroscopy/mass spectrometry), which was limited to observing total silver concentration only (rather than distinguishing complexed and free forms of silver) and could be applied only at discrete time-points rather than being used for continuous measurements.

To address the problem of visually observing nanomaterial interactions with bacterial cells (Chapter 4), I developed a novel and facile method to fluorescently stain bacterial cell surfaces for super-resolution fluorescence microscopy (SRFM). SRFM is uniquely capable of visualizing biological samples with high (sub-diffraction-limited) resolution under hydrated conditions. Electron microscopy, the current gold standard for high-resolution imaging, achieves higher resolution than SRFM but requires that samples be

dehydrated and embedded in resin, procedures that can significantly alter the sample from its native state. Despite this advantage over electron microscopy, SRFM has been underutilized due to the complex fluorescent labeling strategies required. Current strategies based on genetic encoding of fluorescent proteins and fluorescent small-molecule labels require significant development time and are not generalizable across bacterial types (i.e., gram-positive and gram-negative bacteria).

The fluorescent labeling strategy I developed uses only commercially available reagents and can be used to label both gram-positive and gram-negative bacterial cells. Utilizing the imaging instrumentation and resources at the Pacific Northwest National Laboratory, Richland, WA and with the collaboration of Dr. Galya Orr's laboratory, super-resolution images of the gram-negative *Shewanella oneidensis* and the gram-positive *Bacillus subtilis* were acquired using two SRFM techniques (structured-illumination microscopy and stochastic optical reconstruction microscopy). In addition, structured-illumination microscopy was performed to visualize *Shewanella oneidensis* exposed to fluorescent cadmium selenide/zinc sulfide core-shell quantum dots under hydrated conditions. This method achieved sufficient resolution to determine that quantum dots were bound to the cell surface without translocating across the cell membrane.

Research to further characterize the site of bacterial cell-nanomaterial interactions was motivated in part by the aforementioned SRFM imaging of *Shewanella oneidensis* exposed to quantum dots. My goal was to determine which surface membrane species mediated the interaction of the quantum dots with the bacterial cells. I hypothesized that lipopolysaccharides, abundant molecules in the outer leaflet of gram-negative bacterial

cell membranes and extending from the membrane surface into the surrounding solution, was the critical species. Lipopolysaccharides form a highly cross-linked, hydrated barrier that helps protect the lipid membrane from damage caused by antimicrobial peptides, hydrophobic antibiotics, and surfactants. Using ethylenediaminetetraacetic acid to release divalent cation crosslinkers between adjacent molecules, I reduced the concentration of lipopolysaccharides in the outer membrane of live *Shewanella oneidensis* cells. After exposing cells with either intact or depleted lipopolysaccharides to gold nanoparticles, I quantified nanoparticle-to-cell association using a novel flow cytometry method developed in this work. This method exploited the high light-scattering cross section of gold nanoparticles as well as fluorescent labeling of cells to rapidly screen cells for gold nanoparticle association with high throughput. To more precisely assess lipopolysaccharide-nanoparticle interactions, parallel experiments using supported lipid bilayers were conducted by Dr. Kurt Jacobson in the laboratory of Dr. Joel Pedersen at the University of Wisconsin—Madison. The association between gold nanoparticles and supported lipid bilayers containing lipopolysaccharides was quantified using quartz crystal microbalance with dissipation. Use of supported lipid bilayers enabled greater control over lipopolysaccharide concentration and length than was possible using whole cells. Our combined results showed that lipopolysaccharide density and length determine the extent and distance of nanoparticle interaction with the gram-negative bacterial cell outer membrane. This work provides a basis for predicting the extent of interaction between nanoparticles and gram-negative bacteria, whose constituent lipopolysaccharides

vary in length and density, and for engineering nanoparticles with enhanced or reduced bactericidal activity.

The environmental implications of nanomaterial use in lithium-ion batteries is the subject of the final experimental chapter of my thesis, Chapter 6. This research, performed in collaboration with Mimi Hang from the laboratory of Dr. Robert Hamers at the University of Wisconsin—Madison, focused on nanoscale lithium nickel manganese cobalt oxide (NMC), currently used as a cathode material in the batteries of some commercially available electric vehicles. The goal of this research was to characterize the impact of NMC exposure on *Shewanella oneidensis* and to use this knowledge to propose a modified material design that reduces potential biological and environmental impacts. Our results show that exposure to NMC reduces bacterial growth and respiration and that this effect is attributable to leaching of metal ions (in particular Ni and Co species) from NMC in aqueous environments. Subsequently, we synthesized a series of Mn-enriched (and Ni- and Co-depleted) NMC species and characterized their impact on *Shewanella oneidensis*. Manganese enrichment significantly reduced but did not eliminate NMC's toxicity. Ongoing research is focused on developing new synthetic strategies to limit metal ion leaching, including capping NMC with an insoluble layer, such as lithium iron phosphate.

In summary, this research has identified several molecular-level phenomena that govern engineered nanomaterial interactions with bacterial cells, which are key members of natural ecosystems. By contributing to a more complete and fundamental understanding

of engineered nanomaterial behavior in the environment, the author hopes this research will promote the sustainable and responsible use of engineered nanomaterials.

Table of Contents

Acknowledgements	i
Dedication	iii
Abstract	iv
Table of Contents	xii
List of Tables	xxi
List of Figures	xxii
List of Abbreviations	xxvii
Chapter 1	
Analytical Aspects of Nanotoxicology.....	1
1.0 Introductory Chapter Overview	2
1.1 Introduction	3
1.2. Characterizing Dynamic Physical and Chemical Properties of Nanomaterials: Aggregation and Degradation	8
1.2.1 Microscopy	8
1.2.2 Dynamic Light Scattering	13
1.2.3 Nanoparticle Tracking Analysis	13
1.2.4 Tunable Resistive Pulse Sensing	14
1.2.5 Electrospray-Differential Mobility Analysis	17
1.2.6 Single Particle Inductively Coupled Plasma Mass Spectrometry	17
1.2.7 Differential Centrifugal Sedimentation	19
1.2.8 Ion-selective Electrodes	20
1.3 Characterizing Dynamic Physical and Chemical Properties of Nanomaterials: Nanomaterial Surface Adsorption	22

1.3.1 X-ray Photoelectron Spectroscopy	24
1.3.2 Attenuated Total Reflectance Fourier Transform Infrared Spectroscopy	24
1.3.3 Surface-Enhanced Raman Spectroscopy	26
1.3.4 Circular Dichroism	26
1.3.5 Nuclear Magnetic Resonance Spectroscopy	27
1.3.6 Mass Spectrometry	29
1.3.7 Small-Angle X-Ray Scattering	34
1.3.8 Electron and Atomic Force Microscopies	35
1.3.9 Fluorescence Correlation Spectroscopy	36
1.3.10 Isothermal Titration Calorimetry	38
1.4 Characterizing Dynamic Physical and Chemical Properties of Nanomaterials: Separating Nanomaterials from Complex Biological Matrices	39
1.4.1 Chromatography	39
1.4.2 Field-Flow Fractionation	40
1.5 Interactions of Nanomaterials with Biological Systems	43
1.5.1 Electron Microscopy and X-Ray Techniques	44
1.5.2 Atomic Force Microscopy	50
1.5.3 Hyperspectral Imaging	56
1.5.4 Super-Resolution Light Microscopy	58
1.5.5 Spectroscopy	59
1.5.6 Sum Frequency Generation	60
1.5.7 Raman Spectroscopy	61
1.5.8 ATR-FTIR Spectroscopy	64

1.5.9 Laser-Induced Breakdown Spectroscopy	65
1.5.10 Electron Paramagnetic Resonance Spectroscopy	65
1.5.11 Mass Spectrometry	67
1.5.12 Gravimetric Analysis	71
1.6 Nanomaterial-Induced Changes in Physiological Processes	75
1.6.1 Electrochemical	76
1.6.2 –Omic Methods Applied to Nanomaterial Toxicology	81
1.6.3 Transcriptomics	83
1.6.4 Proteomics	87
1.6.5 Metabolomics	90
1.7 Conclusions	93
1.8 Acknowledgements	97
Chapter 2	
Effects of Humic and Fulvic Acids on Silver Nanoparticle Stability, Dissolution, And Toxicity.....	98
2.1 Introduction	100
2.2 Experimental	103
2.3 Results and Discussion	104
2.3.1 Impact of NOM and Nanoparticle Capping Agents on AgNP Colloidal Stability	104
2.3.2 Impact of NOM on AgNP Dissolution	114
2.3.3 Impact of NOM on AgNP Toxicity to Bacteria	120
2.4 Conclusions	122
2.5 Acknowledgements	123

2.6 Supporting Information	124
2.6.1 Characterization of AgNPs by TEM and Zeta-potential Measurements	124
2.6.2 Aggregation of Citrate-capped AgNPs in a High Ionic Strength Buffer Containing 10 mg/L NOM Observed by UV-vis Extinction Spectroscopy	125
2.6.3 NOM Elemental Compositions	126
2.6.4 Dark-field Microscopy and Hyperspectral Imaging Characterization of Citrate-capped AgNPs Exposed to NOM	126
2.6.5 Theoretical Responses of ISEs	128
2.6.6 ISE-measured Dissolution of Citrate-capped AgNPs in pH Buffer Containing 10 mg/L NOM	129
2.6.7 ISE-measured Complexation of Ag ⁺ and Citrate or Polyvinylpyrrolidone	130
2.6.8 Materials and Methods	130
Chapter 3	
Dynamic Silver Speciation as Studied with Fluorous-phase Ion-selective Electrodes: Effect of Natural Organic Matter on the Toxicity and Speciation of Silver.....	138
3.1 Introduction	140
3.2 Experimental	144
3.3 Results and Discussion	145
3.3.1 Ion-Selective Electrodes	145
3.3.2 Interference of the Sample Matrix on Ag ⁺ Binding to NOM	147
3.3.3 Binding of Ag ⁺ to NOM	151
3.3.4 Effect of NOM on Ag ⁺ Toxicity	156
3.4 Conclusions	161
3.5 Acknowledgements	162

3.6 Supporting Information	162
3.6.1 Effect of NOM on Toxicity of Ag ⁺ and Ag NPs	162
3.6.2 Measurements with Ion-Selective Electrodes with Fluorous Sensing Membranes	163
3.6.3 Solution Preparation and Binding Measurements	165
3.6.4 Kinetics of Ag ⁺ and NOM Binding	168
3.6.5 Effect of pH on Ag ⁺ Binding to SRHA, SRFA, and PLFA	172
3.6.6 Confirmation of Ag NP Formation as a Result of Ag ⁺ Reduction by PLFA using Dark-field Microscopy with Hyperspectral Imaging and Transmission Electron Microscopy, TEM	174
3.6.7 Silver Toxicity to <i>Shewanella oneidensis</i>	179
Chapter 4	
Facile Method to Stain the Bacterial Cell Surface for Super-Resolution Fluorescence Microscopy.....	181
4.1 Introduction	183
4.2 Experimental	185
4.2.1 Bacterial Culture Preparation	185
4.2.2 Cell Staining	186
4.2.3 Preparation for Imaging	186
4.2.4 Preparation of Nanomaterials	187
4.2.5 Cell Exposure to Nanomaterials	187
4.2.6 Microscopy Parameters	187
4.3 Results and Discussion	188
4.4 Conclusions	194
4.5 Acknowledgement	195

4.6 Supporting Information	195
4.6.1 Estimating the Localization Precision Achieved by STORM	195
4.6.2 Images of Cells and Nanomaterial-Cell Interactions	196
4.6.3 Commercial CdSe/ZnS Quantum Dot Size Characterization	198
Chapter 5	
Lipopolysaccharide Density and Structure Govern the Extent and Distance of Nanoparticle Interaction with Actual and Model Bacterial Outer Membranes.....	200
5.1 Introduction	202
5.2 Experimental	203
5.2.1 Gold Nanoparticle Preparation and Characterization	203
5.2.2 Bacterial Culture	204
5.2.3 Removal of LPS from Cells	205
5.2.4 Nanoparticle-Cell Attachment Experiments	205
5.2.5 Nanoparticle-Bilayer Attachment Experiments	206
5.2.6 Second Harmonic Generation	207
5.3 Results and Discussion	208
5.3.1 Nanoparticle-Cell Attachment	208
5.3.2 Attachment of Cationic and Anionic Gold Nanoparticles to LPS-Containing Bilayers	213
5.3.3 Proximity of MPNH ₂ -AuNPs to the Phospholipid-Solution Interface	218
5.3.4 Effect of Nanoparticle-Bilayer Association on Lipid Structure	222
5.4 Conclusions	222
5.5 Acknowledgements	224
5.6 Supporting Information	224

5.6.1 Chemicals	237
5.6.2 Bacterial Culture Media	238
5.6.3 Cell Sorting by Flow Cytometry	238
5.6.4 Preparation of Lipid Vesicles	239
5.6.5 Quartz Crystal Microbalance with Dissipation (QCM-D) Monitoring	241
5.6.6 Estimation of Masses Measured by QCM-D	242
5.6.7 Preparation of Solid-supported LPS-containing Lipid Bilayers	243
5.6.8 Second Harmonic Generation	244
5.6.9 Super-resolution Fluorescence Microscopy	246
Chapter 6	
Impact of Nanoscale Lithium Nickel Manganese Cobalt Oxide (NMC) on the Bacterium <i>Shewanella oneidensis</i> MR-1.....	247
6.1 Introduction	249
6.2 Experimental	251
6.2.1 NMC Synthesis	251
6.2.2 Inductively Coupled Plasma Optical Emission Spectroscopy (ICP-OES) characterization of NMC stoichiometry and of metal release into growth medium	252
6.2.3 X-ray Photoelectron Spectroscopy	253
6.2.4 Scanning Electron Microscopy	253
6.2.5 Transmission Electron Microscopy	253
6.2.6 Bacterial Response to NMC Exposure	254
6.3 Results and Discussion	256
6.3.1 Preparation and Characterization of Nanoscale NMC	256
6.3.2 Impact of NMC on <i>Shewanella oneidensis</i> MR-1	257

6.3.3 Mechanism of Interaction	269
6.4 Conclusions	274
6.5 Acknowledgements	274
6.6 Supporting Information	275
6.6.1 Cycling Induced Fracture of Commercial NMC	275
6.6.2 Atomic Force Microscopy of NMC	276
6.6.3 Transmission Electron Micrographs of NMC	277
6.6.4 Variable Recovery of Exponential Growth for <i>S. oneidensis</i> Exposed to 5 mg/L NMC	278
6.6.5 Negligible impact of NMC on oxygen consumption independent of cellular respiration	280
6.6.6 Modeling the Effect of Initial Cell Population Size on Population Growth	281
6.6.7 Suspension Turbidity Due to NMC in Cell-free Media	282
6.6.8 Time-dependent Changes in Chemical Composition of Aqueous Phase	283
6.6.9 X-ray Photoelectron Spectroscopy of Co, Ni, and Mn in NMC	283
6.6.10 Growth and Respiration Profiles for Li ⁺ and Mn ²⁺ Exposures	284
6.6.11 Powder X-ray Diffraction	285
6.6.12 Oxygen Uptake Rate Profiles for NMC and Metal Ion Exposures	286
6.6.13 Visual Minteq Modeling of Solution Speciation	287
Chapter 7	
Ongoing and Future Research.....	290
7.1 Lipopolysaccharide-Mediated Interactions between Nanoparticle and Gram-negative Bacteria	291
7.2 Nanoscale Battery Cathode Material Toxicity to Bacteria	295

References.....	303
Curriculum Vitae.....	321

List of Tables

Chapter 1

Table S1. Elemental compositions of three NOM models	126
--	-----

Chapter 5

Table S1. Areal acoustic mass densities ($\Delta m_{\text{QCM-D}}$) of SiO ₂ -supported bilayers composed of POPC and lipopolysaccharide	236
---	-----

Table S2. Final frequency shifts ($\Delta f_5/5$) following AuNP association with LPS-amended POPC bilayers	236
---	-----

Table S3. Estimated final acoustic areal mass densities ($\Delta m_{\text{QCM-D}}$) following AuNP association with LPS-amended POPC bilayers	236
---	-----

Chapter 6

Table 1. Measured concentrations of ions produced in solution by dissolution of NMC, and expected concentration if NMC dissolved completely	261
---	-----

Table S1. Speciation of soluble metals in bacterial growth medium with added 0.270 mM LiCl, 0.062 mM NiCl ₂ , 0.021 mM for CoCl ₂ , and 0.0078 mM MnCl ₂	287
---	-----

List of Figures

Chapter 1

Figure 1. Returns for the search term “nanotoxicology” on SciFinder from 1995-2015	4
Figure 2. Physical and chemical transformations of nanomaterials	5
Figure 3. Darkfield hyperspectral images of suspected individual Ag nanoparticles	12
Figure 4. Comparison of DLS- and TRPS-measured size-distributions of carbon nanohorns	16
Figure 5. ToF-SIMS images of inkjet-printed droplets of Ag nanoparticles	33
Figure 6. STXM and fluorescence overlay STXM images of epithelial cells exposed to CeO ₂ nanoparticles	48
Figure 7. Average approach and pull-off force curves for an AFM probe to and from an <i>Escherichia coli</i> cell surface	54
Figure 8. Raman spectra and intensity maps of epithelial carcinoma cells exposed to carbon nanotubes	63
Figure 9. Association of cationic gold nanoparticles to POPC lipid bilayers and <i>Shewanella oneidensis</i> cells containing variable lipopolysaccharide content	74
Figure 10. Differential gene expression of zebrafish embryos exposed to various forms of silver	87

Chapter 2

Figure 1. UV-visible extinction spectra of AgNPs exposed to NOM	106
Figure 2. Average hydrodynamic diameters of AgNPs exposed to NOM	112
Figure 3. Dissolution of AgNPs exposed to NOM and toxicity to <i>Shewanella oneidensis</i>	117
Figure S1. TEM micrographs and zeta potential measurements of AgNPs	124
Figures S2. UV-visible extinction spectra of pristine AgNPs and AgNPs in NOM solution	125

Figure S3. Dark-field micrographs and UV-visible spectral features of AgNPs exposed to NOM	127
Figure S4. Calibration curve of a fluoruous-phase Ag ⁺ ISE	128
Figure S5. Dissolution of AgNPs in NOM solution	129
Figure S6. Complexation of Ag ⁺ and citrate or polyvinylpyrrolidone	130

Chapter 3

Figure 1. Fluorous-phase Ag ⁺ ISE setup and preparation of a calibration curve	147
Figure 2. Interference of buffer components on Ag ⁺ binding to NOM	150
Figure 3. Ag ⁺ and NOM binding and its effect on Ag ⁺ toxicity	160
Scheme S1. Structure of HEPES and MOPS	165
Figure S1. Ag ⁺ complexation with buffer components	167
Figure S2. Emf response of a fluoruous-phase Ag ⁺ ISE in a solution containing 5.0 μM Ag ⁺ and 51 mg/L PLFA	168
Figure S3. Kinetics of Ag ⁺ binding to NOM at pH 9	170
Figure S4. Emf response of a fluoruous-phase Ag ⁺ ISE in AgCH ₃ COO solution with and without PLFA	172
Figure S5. Effect of pH and NOM source on Ag ⁺ and NOM complexation	173
Figure S6. Dark-field microscopy and hyperspectral images of silver nanoparticle formation in a solution of Ag ⁺ with and without PLFA	176
Figure S7. TEM images of buffered solutions containing Ag ⁺ and/or PLFA indicating the presence or absence of nanoparticles	178
Figure S8. Toxicity of Ag ⁺ to <i>Shewanella oneidensis</i>	180

Chapter 4

Figure 1. Confocal and SIM images of fluorescently stained <i>Bacillus subtilis</i>	189
---	-----

Figure 2. SIM and STORM images of fluorescently stained <i>Shewanella oneidensis</i>	191
Figure 3. SIM image of <i>Shewanella oneidensis</i> with associated amino-PEG quantum dots	193
Figure 4. Laser-scanning confocal microscopy image of <i>Shewanella oneidensis</i> with associated amino-PEG quantum dots	194
Figure S1. Wide-field and STORM images of fluorescently stained <i>Shewanella oneidensis</i>	197
Figure S2. SIM image of fluorescently stained <i>Shewanella oneidensis</i>	198
Figure S3. Representative TEM images and size-distribution of CdSe/ZnS nanoparticles	199
 Chapter 5	
Figure 1. Number-average hydrodynamic diameters and electrophoretic mobilities of MPA- and MPNH ₂ -functionalized gold nanoparticles	210
Figure 2. Gold nanoparticle association with bacterial cells as a function of LPS content	213
Figure 3. Hydrodynamic diameters, electrophoretic mobilities, and LPS content of lipid vesicles	215
Figure 4. Normalized maximum frequency shifts following MPNH ₂ -AuNP introduction to LPS-containing lipid bilayers	216
Figure 5. SHG signal intensity following MPNH ₂ -AuNP introduction to LPS-containing or LPS-free lipid bilayers	220
Figure S1. General LPS structure for gram-negative bacteria	225
Figure S2. LPS content of native and LPS-depleted <i>Shewanella oneidensis</i>	226
Figure S3. Dark-field micrograph and visible-near infrared spectral map of <i>Shewanella oneidensis</i> exposed to MPNH ₂ -AuNPs	227
Figure S4. Representative QCM-D response during lipid bilayer formation	228
Figure S5. MPNH ₂ -AuNP association to <i>Shewanella oneidensis</i> as a function of cell LPS content, observed by flow cytometry	230

Figure S6. Molecular mass distribution of LPS from <i>Salmonella enterica</i> and <i>Shewanella oneidensis</i>	232
Figure S7. Apparent ζ -potentials of lipid vesicles incorporating various mole percent smooth or rough LPS	233
Figure S8. SHG signal intensity following introduction of MPNH ₂ -AuNPs to lipid bilayers with various mole percent smooth or rough LPS	234
Figure 9. Fluorescence micrographs of lipid bilayers incorporating fluorescently labeled POPC before and after MPNH ₂ -AuNP introduction	235
Chapter 6	
Figure 1. SEM- and TEM-micrographs of NMC nanoparticles	257
Figure 2. <i>Shewanella oneidensis</i> respiration and growth in the presence or absence of NMC nanoparticles	258
Figure 3. Concentration of dissolved species produced from 5 mg/L NMC nanoparticles in growth medium and fractional composition of Co, Ni, and Mn at the NMC nanoparticle surface	264
Figure 4. <i>Shewanella oneidensis</i> respiration in the presence or absence of Ni ²⁺ or Co ²⁺	266
Figure 5. <i>Shewanella oneidensis</i> respiration and growth in the presence or absence of Ni ²⁺ and Co ²⁺	268
Figure 6. Transmission electron micrographs of <i>Shewanella oneidensis</i> exposed to NMC nanoparticles	271
Figure S1. SEM image of commercial NMC material	275
Figure S2. AFM image and height profiles of NMC nanoparticles	277
Figure S3. Edge-on transmission electron micrographs of stacks of NMC nanosheets	278
Figure S4. Respiration profiles of <i>Shewanella oneidensis</i> in growth medium with or without NMC nanoparticles	279
Figure S5. Oxygen consumption in cell-free growth medium in the absence or presence of NMC nanoparticles	280

Figure S6. Modeled population growth over 60 generations for a bacterial cell culture with various initial cell densities	281
Figure S7. Turbidity of NMC nanoparticle suspensions in growth medium	282
Figure S8. Concentration of dissolved species produced from 50 mg/L NMC nanoparticles in growth medium	283
Figure S9. XPS spectra of NMC before and after exposure to growth medium	284
Figure S10. <i>Shewanella oneidensis</i> respiration and growth in the presence or absence of Mn^{2+} or Li^+	284
Figure S11. Powder X-ray diffraction of NMC nanoparticles	286
Figure S12. Oxygen uptake rate of <i>Shewanella oneidensis</i> in the presence or absence of NMC nanoparticles, Ni^{2+} and Co^{2+} , Ni^{2+} , Co^{2+} , Li^+ , or Mn^{2+}	287
 Chapter 7	
Figure 1. Characterization of LPS extracted from <i>S. oneidensis</i> by SDS-PAGE	294
Figure 2. Concentration of dissolved species produced from 5 mg/L NMC nanoparticles in growth medium	296
Figure 3. Response of <i>S. oneidensis</i> to NMC exposure as a function of Mn-enrichment	297
Figure 4. Response of <i>S. oneidensis</i> to Ni^{2+} and Co^{2+} , Ni^{2+} , Co^{2+} , Mn^{2+} , and Li^+ , or NMC exposure as a function of Mn-enrichment	300

List of Abbreviations

A_i	measured XPS area for the element i
$a(x)$	activity of x
AF4	asymmetric flow field-flow fractionation
AFM	atomic force microscopy
AgNP	silver nanoparticle
ANOVA	analysis of variance
ATP	adenosine triphosphate
ATR	Attenuated total reflectance
BSA	bovine serum albumin
C	mass sensitivity constant for quartz crystal microbalance with dissipation sensor crystal
$c(x)$	concentration of x
CCD	charge coupled device
cDNA	complimentary deoxyribonucleic acid
CD spectroscopy	circular dichroism spectroscopy
Cryo-TEM	cryogenic transmission electron microscopy
CTAB	cetyltrimethylammonium bromide
DLS	dynamic light scattering
DMPC	1,2-dimyristoyl- <i>sn</i> -glycero-3-phosphocholine
DMSO	dimethyl sulfoxide
DMTAP	dimyristoyl trimethylammonium propane
DNA	deoxyribonucleic acid
DOPC	1,2-dioleoyl- <i>sn</i> -glycero-3-phosphocholine
DOSY	diffusion-ordered spectroscopy
D-PBS	Dulbecco's phosphate buffered saline
E°	standard reduction potential
EDS, EDX	energy-dispersive x-ray spectroscopy
EDTA	ethylenediaminetetraacetic acid
EELS	electron energy loss spectroscopy
EM	electron microscopy
emf	electromotive force
ENVI	environment for visualizing images
EPR	electron paramagnetic resonance
ES-DMA	electrospray-differential mobility analysis
F	Faraday constant
F4	flow field-flow fractionation
FA	fulvic acid
FACS	fluorescence-activated cell sorting
FCS	fluorescence correlation spectroscopy
FE-SEM	field emission scanning electron microscopy
FFF	field-flow fractionation
FITC-A	fluorescence emission intensity in the range 530 ± 10 nm

FRAP	fluorescence recovery after photobleaching
FSC-A	forward-scattered light intensity
FTIR spectroscopy	Fourier transform infrared spectroscopy
FWHM	full width at half maximum
f_x	fractional composition of element x
g	standard gravitational acceleration
GC-MS	gas chromatography-mass spectrometry
GO	graphene oxide
HA	humic acid
HAADF-STEM	high angle annular dark field scanning transmission electron microscopy
HDC	hydrodynamic chromatography
HEPES	4-(2-hydroxyethyl)piperazine-1-ethanesulfonic acid
HPLC	high-performance liquid chromatography
HSA	human serum albumin
I	ionic strength
I/I_0	transmitted beam intensity/incident beam intensity
ICP-MS	inductively coupled plasma mass spectrometry
ICP-OES	inductively coupled plasma-optical emission spectroscopy
ISDD	<i>in vitro</i> sedimentation, diffusion and dosimetry
ISE	ion-selective electrodes
ITC	isothermal titration calorimetry
Kdo	3-deoxy-D-manno-octulosonic acid
LB	Lysogeny broth
LC	liquid chromatography
LDI	Laser desorption/ionization
LIBS	laser-induced breakdown spectroscopy
LPS	lipopolysaccharide
LSPR	localized surface plasmon resonance
MOPS	<i>N</i> -morpholino-3-propanesulfonic acid
MPA	3-mercaptopropionic acid
MPNH ₂	3-mercaptopropyl amine
mRNA	messenger ribonucleic acid
MS	mass spectrometer
MTS	3-(4,5-dimethylthiazol-2-yl)-5-(3-carboxymethoxyphenyl)-2-(4-sulfophenyl)-2H-tetrazolium
MTT	3-(4,5-dimethylthiazol-2-yl)-2,5-diphenyltetrazolium bromide
MWCNT	multi-walled carbon nanotube
MWCO	molecular weight cut-off
NA	numerical aperture
NIR	near infrared
NIST	National Institute of Standards and Technology
NMC	nickel manganese cobalt oxide
NMR	nuclear magnetic resonance

NOM	natural organic matter
NTA	nanoparticle tracking analysis
OD	optical density
OUR	oxygen uptake rate
PALM	photoactivated localization microscopy
PBS	phosphate buffered saline
PCA	principal component analysis
PDA	polydopamine
PEG	polyethylene glycol
PLFA	Pony Lake fulvic acid
PLL	poly-L-lysine
PLS-DA	partial least squares discriminant analysis
POPC	1-palmitoyl-2-oleoyl- <i>sn</i> -glycero-3-phosphocholine
POPG	1-palmitoyl-2-oleoyl- <i>sn</i> -glycero-3-phosphoglycerol
POPS	1-palmitoyl-2-oleoyl- <i>sn</i> -glycero-3-phospho-L-serine
PPHA	Pahokee Peat humic acid
PVP	polyvinylpyrrolidone
PVP-10	polyvinylpyrrolidone average molecular weight 10,000 g/mol
QCM-D	quartz crystal microbalance with dissipation
qRT-PCR	quantitative real-time polymerase chain reaction
Q-SAR	quantitative structure-activity relationship
R	universal gas constant
RCF	relative centrifugal force
RF	radio frequency
rLPS	rough lipopolysaccharide
RNA	ribonucleic acid
ROS	reactive oxygen species
RPM	revolutions per minute
SAXS	small-angle X-ray scattering
SDS	sodium dodecyl sulfate
SDS-PAGE	sodium dodecyl sulfate-polyacrylamide gel electrophoresis
SEM	scanning electron microscopy
SERS	surface-enhanced Raman spectroscopy
SFG	sum frequency generation
SHG	second harmonic generation
S_i	atomic sensitivity factor for element i
SILAC	stable isotope labeling by amino acids in cell culture
SIM	structured illumination microscopy
SIMS	secondary ion mass spectrometry
sLPS	smooth lipopolysaccharide
SNMS	secondary neutral mass spectrometry
SOD	superoxide dismutase
sp-ICP-MS	single particle inductively coupled plasma mass spectrometry
SRFA	Suwannee River fulvic acid

SRHA	Suwannee River humic acid
SRNOM	Suwannee River aquatic natural organic matter
SSC-A	orthogonal light scattering intensity
STD	saturation transfer difference
STED	stimulated emission depletion
STORM	stochastic optical reconstruction microscopy
STXM	scanning transmission x-ray microscopy
SWCNT	single-walled carbon nanotube
T	absolute temperature
TEM	transmission electron microscopy
ToF	time of flight
TRPS	tunable resistive pulse sensing
UV	ultraviolet
UV-vis	ultraviolet-visible
XANES	X-ray absorption near edge structure
XPS	X-ray photoelectron spectroscopy
XRD	X-ray diffraction
Y_0	initial cell count
$\Delta m_{\text{QCM-D}}$	shift in quartz crystal microbalance with dissipation adlayer areal mass density
ΔD_n	energy dissipation shift for harmonic number n
Δf_n	frequency shift for harmonic number n
λ_i	inelastic mean free path for element i
μ -XANES	micro-X-ray absorption near edge structure
μ -XRF	microfocused X-ray fluorescence

Chapter 1

Analytical Aspects of Nanotoxicology

Adapted from:

Gunsolus, I. L.; Haynes, C. L. *Anal. Chem.* **2016**, 88, 451-479

Copyright ©2016 American Chemical Society. All rights reserved.

1.0 Introductory Chapter Overview

Chapter 1 reviews and critically analyzes the applications of analytical methods in nanotoxicology research. It provides the reader with perspective on the field of nanotoxicology that will aid in understanding the subsequent experimental thesis chapters (Chapters 2-6). Chapter 1 is divided into two main sections: the first focuses on methods used to characterize the dynamic physical and chemical properties of nanomaterials themselves while the second focuses on methods used to characterize nanomaterial interactions with biological systems. This structure was chosen in part to emphasize the importance of linking specific physical and chemical properties of nanomaterials with their toxicity to organisms. While the need for establishing this link may seem obvious, researchers face many experimental challenges in doing so. Whereas a molecular toxicologist can assume that a mole of molecules under consideration is chemically uniform, a nanomaterial toxicologist cannot; nanomaterials, no matter how carefully synthesized, display a distribution of chemical and physical properties. In addition, nanomaterials routinely undergo chemical and physical transformations in both laboratory and natural environments. The dynamic behavior of nanomaterials makes it challenging for nanotoxicologists to define the physical and chemical properties that contribute to their toxicity. Chapter 1 aims to assist researchers in this endeavor by reviewing the available analytical methods for characterizing the dynamic behavior of nanomaterials and highlighting deficiencies. The chapter then shifts attention to the characterization of nanomaterials within biological systems. The analytical methods reviewed in this section address two major experimental challenges facing

nanotoxicologists: the difficulty of visualizing nanomaterial interactions with biological systems given the small size of nanomaterials, and the difficulty of extracting changes in chemical signal from noise given the chemical complexity of biological environments. Chapter 1 concludes with perspective on how nanotoxicology research can impact nanotechnology development, considering the links between experimental and mathematical/computational approaches to characterize nanomaterial toxicity, the need for causal, as opposed to correlative, knowledge of nanomaterial-biological interactions, and the need for collaborative research efforts across the physical and biological sciences.

1.1 Introduction

Nanotoxicology, the study of nanomaterial toxicity to biological systems, has become a vibrant area of research over the past ten years. Two main factors drive this enthusiasm: (1) industrial interest in engineered nanomaterials,¹ leading to their increasing use in consumer products^{2,3} and increasing possibility of human and environmental exposure;⁴ and (2) the unique physical and chemical properties of nanomaterials relative to their bulk counterparts. The rapid growth of academic research in nanotoxicology is evidenced by the sharp increase in the number of articles published on this subject over the past approximately ten years (Figure 1). The following review highlights the analytical methods used in nanotoxicology research, encompassing methods that probe the dynamic physical and chemical properties of nanomaterials (section 1) as well as methods that assess interactions between nanomaterials and biological systems (section 2). We will restrict our discussion to the toxicity of engineered nanomaterials, the subjects of the vast

majority of nanotoxicity studies to date, as opposed to naturally occurring nanomaterials. The content of this review will be weighted towards work that has been published within the past three years; almost 50% of the citations fall in the period 2013-2015.

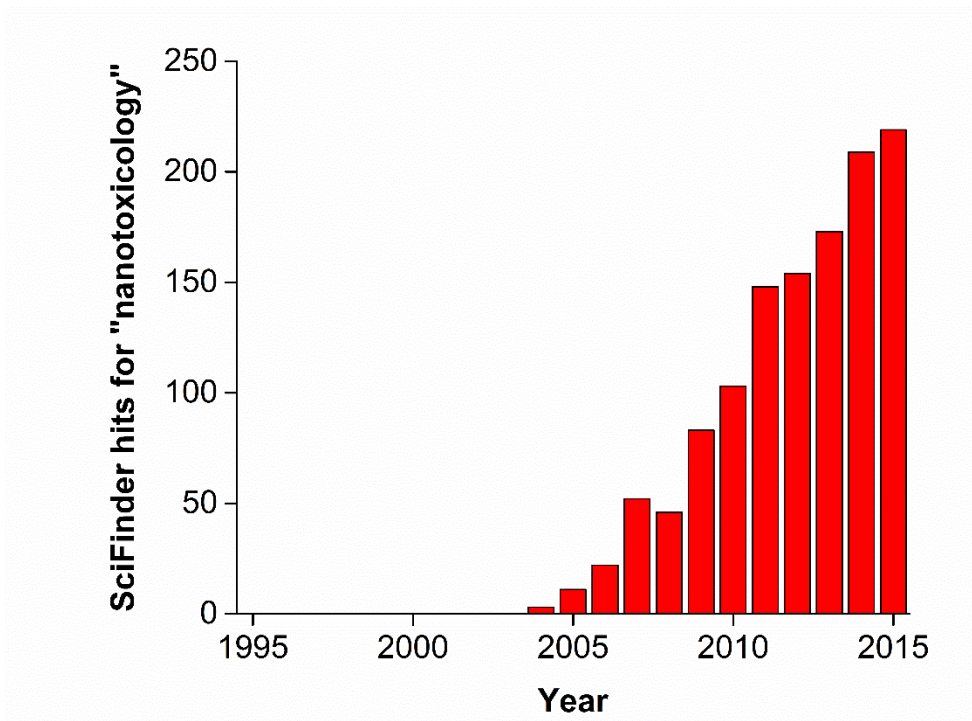


Figure 1. Returns for the search term “nanotoxicology” on SciFinder as of Oct. 14, 2015, organized by publication year.

Unique experimental challenges distinguish nanotoxicology research from the more classical field of molecular toxicology. Among these are the highly dynamic chemical composition and physical properties of nanomaterials (Figure 2). Nanomaterials routinely undergo both chemical and physical transformations even under controlled laboratory conditions through mechanisms including dissolution, release of ligands that decorate their surface, adsorption of secondary species (e.g., proteins), and aggregation.

Characterizing these dynamic chemical and physical properties is crucial to identifying the mechanism of interaction with biological systems and the nanomaterial toxicity. Even in the absence of these transformations, a population of nanomaterials does not have a uniform chemical or physical identity. While a mole of a particular molecule is composed of chemically identical units and is thus chemically uniform, a mole of a particular nanomaterial exhibits a distribution of chemical and physical parameters like oxidation state, size, and shape.

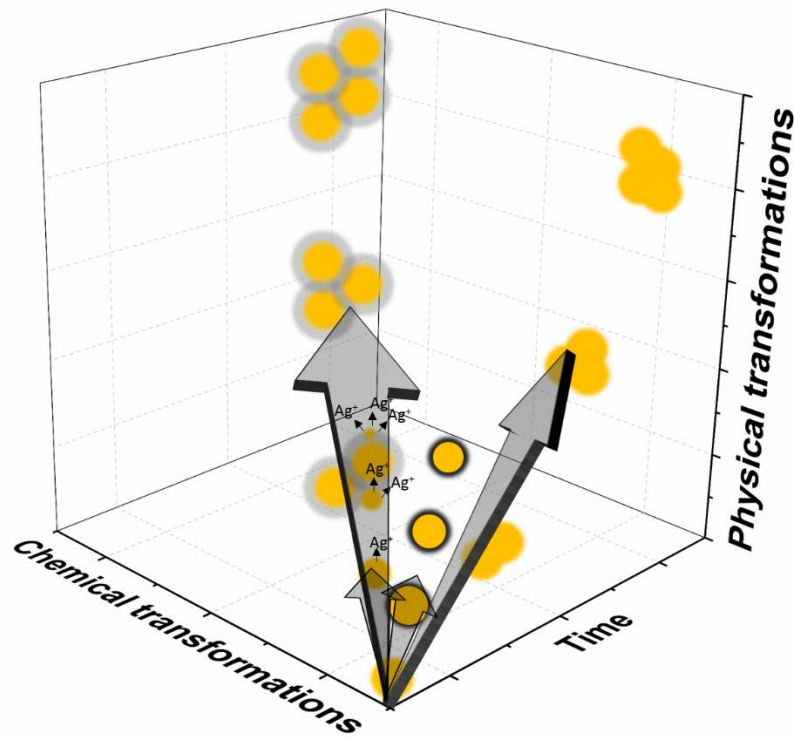


Figure 2. Physical and chemical transformations of silver nanoparticles are depicted to illustrate the dynamic properties of nanomaterials in general. Arrows are used to guide the eye along the progression of a particular transformation over time. Depicted from left to right: agglomeration of protein-coated nanoparticles (containing a diffuse layer around

the nanoparticle core); oxidation of nanoparticles to release ionic silver; oxidation of the nanoparticle surface to form a layer of silver oxide; and agglomeration of pristine nanoparticles.

An additional, and equally important, set of experimental challenges arises from the great variability in chemical composition and structural complexity of commercially used nanomaterials. In commercial products, nanomaterials are used as chemically inert or active additives that impart desired qualities, such as increased hardness or surface area, antimicrobial behavior, UV protection, and coloring.⁵ In some important emerging applications, nanomaterials serve not just as useful additives, but form the basis of product performance. This includes drug-delivery for cancer therapy,⁶ energy conversion,⁷ and energy storage materials.⁸ Nanomaterials used in these and other commercial applications are highly variable in size, shape, chemical composition, surface functionalization, crystallinity, and incorporation into secondary structures (e.g., polymer films). The chemical and structural diversity of nanomaterials, which is likely to increase as new generations of nanomaterials are developed, leads to highly variable modes of interaction with biological systems, challenging the establishment of standard toxicological methods. This challenge has been addressed in two primary ways in the nanotoxicology literature.

In the first approach, known routes of nanotoxicity, including disruption of cell membrane integrity, DNA damage, and oxidative stress, are assessed. Commercially available cytotoxicity assays, primarily based on small molecule probes of a particular

biological pathway or endpoint, have been frequently employed for this purpose. However, some assays experience significant interference resulting from probe interactions with nanomaterials;⁹ implicated nanomaterials include silver, titania, copper, and iron oxide nanoparticles as well as carbon nanotubes.¹⁰⁻¹⁴ While these assays provide extensive insights into the toxicological effects of nanomaterials on biological systems, their specificity dictates that only a small set of hypotheses related to the nanomaterial-biological interaction can be tested. Methods with more general analytical capabilities are also needed to enable hypothesis-driven investigations of nanomaterial-biological interactions that are not limited to already known routes of toxicity. Such methods are more likely to reveal unknown or unexpected mechanisms of nanomaterial-biological interaction, a critical step towards predicting nanomaterial risk and developing sustainable nanomaterials.

In a second approach, nanotoxicologists are increasingly adapting analytical methods with origins in the chemical sciences (e.g., spectroscopy, mass spectrometry, and electrochemical methods) and the biological sciences (e.g., genomics, proteomics, and metabolomics) to assess the response of biological systems to nanomaterial exposure. This review focuses on the application of analytical methods in two broad categories. The first is methods used to characterize the physical interaction of nanomaterials with biological systems based on uptake and distribution in cells and tissues and biophysical changes in cell membrane integrity, and DNA and protein structure. The second is methods used to characterize changes in biological function following exposure to

nanomaterials. These include changes in cell and organism survival and reproduction; mobility; signaling; and gene, protein, and small molecule expression.

Continuing to develop analytical methodology that probes the dynamic interface between nanomaterials and biological systems, rather than just the toxicological outcome of this interaction, remains a fundamental challenge in the field of nanotoxicology, but will enable discovery of more causal, as opposed to correlative, mechanisms of nanotoxicity.¹⁵ We suggest that causal, mechanistic knowledge of nanotoxicity is necessary to design functional nanomaterials with controlled biological impacts and to keep pace with the rate of new and increasingly complex nanomaterial incorporation into consumer products.

Section 1.2 will focus nanomaterials themselves, reviewing methods that facilitate characterization of nanomaterial aggregation, degradation, and molecular surface adsorption.

1.2 Characterizing Dynamic Physical and Chemical Properties of Nanomaterials: Aggregation and Degradation

1.2.1 Microscopy. Transmission electron microscopy (TEM) remains the gold-standard for characterizing the primary size and structure of nanomaterials based on its high spatial resolution. Chemical information about a nanomaterial can also be obtained through parallel analysis using spectroscopic methods such as electron energy loss spectroscopy (EELS) or energy-dispersive x-ray spectroscopy (EDX). Despite this

versatility, sample preparation requirements for TEM traditionally limits its utility for characterizing nanomaterial dispersions in situ (i.e., under biologically or environmentally relevant conditions). In particular, the high-vacuum environment of electron microscopes can lead to sample preparation artifacts (e.g., nanomaterial aggregation induced by solvent evaporation) that do not reflect nanomaterial behavior in solution. However, advances in sample preparation are expanding the utility of electron microscopy for in situ nanomaterial characterization. Cryo-TEM, in which samples are imaged in a vitrified state, preserves the spatial arrangement of species as they exist in solution. This technique has been used, for example, to observe decreased packing density of poly(organosiloxane) nanoparticles in the presence of serum, indicating possible co-aggregation of nanoparticles and serum proteins.¹⁶ Cryo-TEM has also been used probe the molecular structure of hybrid perylene diimide/single wall carbon nanotube structures.¹⁷ Based on the observed distance between adjacent carbon nanotubes in cryo-TEM images, the authors concluded that a single molecular layer of perylene diimide derivative exfoliated the nanotubes. While cryo-TEM is a powerful probe of nanoscale packing, it cannot assess the dynamic behavior of nanomaterial dispersions. Liquid-cell TEM does preserve the fluid environment around the nanomaterial. In this technique, imaging electrons pass through a viewing window (typically composed of Si₃N₄) and encounter a liquid sample sealed in a chamber. Liquid-cell TEM has been used extensively to observe the crystal growth of metal nanoparticles, the subject of a recent review,¹⁸ and liquid-cell scanning TEM has been recently used to observe the hydration layer around alumina nanoparticles, representing the first time that the solvent

shell (i.e., the region of solvent which is restructured relative to the bulk solvent through its interaction with the nanomaterial surface¹⁹) has been directly visualized.²⁰ Recent development of a highly electron-transparent liquid cell made from graphene sheets has enabled liquid-cell TEM to observe the molecular motion of nano-bio conjugates (composed of Au nanoparticles and double-stranded DNA) in solution.²¹ While “soft” biological structures such as DNA are susceptible to damage from prolonged exposure to an imaging electron beam, liquid-cell TEM offers a means to observe dynamic behavior of nano-bio structures with very high spatial resolution. Despite these advances, long image acquisition and analysis times make these methods ill-suited for high-throughput, statistically significant characterization of nanomaterial properties.

Light microscopy is a less-invasive, simpler, and faster alternative to electron microscopy, but is generally unsuitable for characterizing nanomaterial dispersions due to its much lower spatial resolution. However, dark-field microscopy combined with hyperspectral imaging (e.g., the CytoViva® Hyperspectral microscope) is an emerging light microscopy method suitable for nanomaterial characterization. In the CytoViva® imaging system, a novel dark-field condenser illuminates a sample with highly collimated light at oblique angles, improving signal-to-noise and contrast over traditional dark field microscopy.²² Scattered light in the range 400-1000 nm is resolved using a microscope-mounted spectrophotometer and spectrophotometer-integrated CCD and analyzed using “environment for visualizing images” (ENVI) software. Badireddy et al. employed the CytoViva® imaging system to differentiate between silver, titania, and ceria nanoparticles in a mixed sample in pure water, and to detect and quantify the relative

amount of silver nanoparticles in complex aqueous samples containing natural colloidal species (i.e., simulated wetland ecosystem water and clarified wastewater).²³ Engineered nanoparticles were detected and classified by spectral similarity analysis; spectra collected from a sample were compared to a library of reference spectra collected for each nanoparticle in pure water, and matches were determined by setting an arbitrary similarity threshold of 90%. In another study, Badireddy et al. used similar methods to observe silver nanoparticle formation from silver ions in solutions containing chloride or bacterial cells and extracellular polymeric substances exposed to visible light (Figure 3).²⁴

Microscopy is best used in combination with ensemble measurements that can analyze a much larger population of nanomaterials while also characterizing their dynamic, hydrated behavior. Nanomaterials are prone to aggregation in high ionic strength solutions, including many with biological and environmental relevance (e.g., blood plasma and saltwater). Repulsive electrical double layer interactions between nanomaterials are reduced as ionic strength increases, and when attractive van der Waals forces dominate, aggregation occurs. Nanomaterials frequently exhibit time-variable mobility under the conditions of most toxicological assays, where aggregation reduces particle diffusion and can lead to particle settling. Dynamic changes in aggregation state and mobility can significantly affect nanomaterial toxicity by influencing the nanomaterial dose and effective size that comes in direct contact with a biological system. Consequently, it is imperative that nanomaterial aggregation and mobility be understood in order to identify the source of nanomaterial toxicity. There are a variety of

analytical methods available to characterize the dynamic, hydrated behavior of nanomaterials.

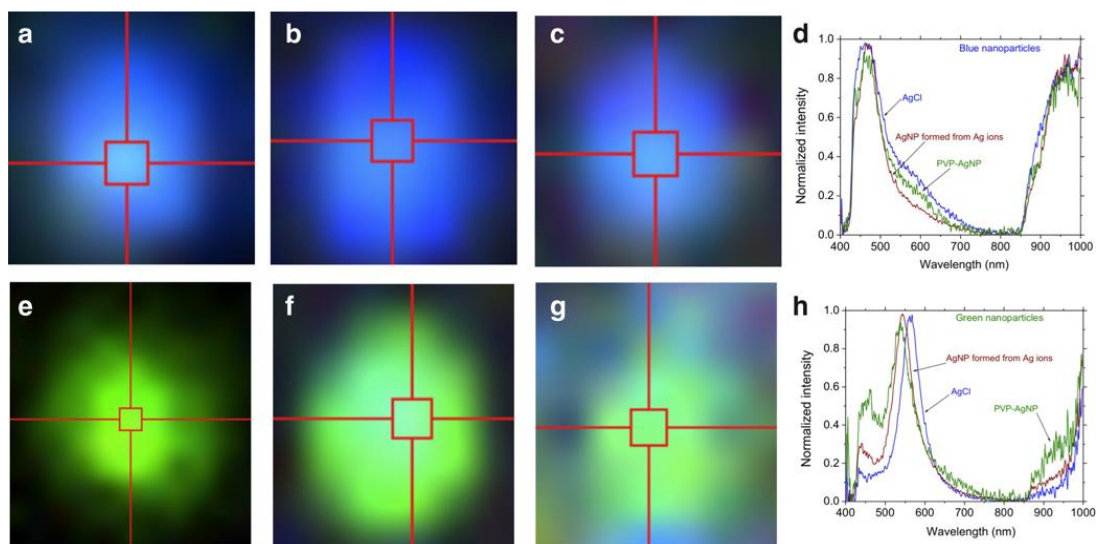


Figure 3. Darkfield hyperspectral images of suspected individual Ag nanoparticles are shown in panels a-c and e-g (400x magnification, scale bar not provided). Images were collected from a suspension of AgCl exposed to visible light (a, e) and a suspension of the bacterium *Pseudomonas aeruginosa* in medium containing NaCl and extracellular polymeric substances (b, f). Visible near-infrared spectra (d, h) collected from these suspected nanoparticles from the areas highlighted in crosshairs closely match those collected from polyvinylpyrrolidone-stabilized Ag nanoparticles prepared directly (c, g), suggesting nanoparticle formation under the conditions studied. Reprinted with permission from Badireddy, A. R.; Budarz, J. F.; Marinakos, S. M.; Chellam, S.; Wiesner, M. R. *Environ. Eng. Sci.* **2014**, *31*, 338–349 (ref 24). The publisher for this copyrighted material is Mary Ann Liebert, Inc. publishers.

1.2.2 Dynamic light scattering (DLS) is the most commonly used method to determine nanomaterial mobility, and is based on measurements of hydrated diameter in solution. Dynamic fluctuations in the intensity of light scattered by nanomaterials (due to Brownian motion) are monitored and fit to an autocorrelation function. From this fit, a nanomaterial's diffusion coefficient can be obtained and subsequent application of the Stokes-Einstein relation allows the hydrodynamic diameter to be calculated. Although DLS is most commonly used to probe static nanomaterial suspensions, it can also operate under continuous flow as, for example, when coupled with asymmetric field flow fractionation (*vide infra*) to simultaneously fractionate and characterize nanoparticle dispersions.²⁵

DLS assumes a spherical particle geometry and thus has limited utility for characterizing the behavior of non-spherical nanomaterials (e.g., commonly used materials such as gold nanorods and carbon nanotubes). In addition, DLS has greater sensitivity for larger particles than smaller ones,²⁶ decreasing its ability to resolve multiple particle size distributions. Light scattering from other colloidal species present in many biologically and environmentally relevant matrices (e.g., protein aggregates and dissolved organic matter) can interfere with DLS measurements of nanomaterial behavior since, like most methods used to track nanomaterial aggregation and mobility, DLS lacks chemical selectivity.²⁷

1.2.3 Nanoparticle tracking analysis (NTA) has better resolution than DLS for characterizing mobility and size of nanoparticles in dispersions. Like DLS, NTA detects

scattered light incident on the particles; unlike DLS, it uses a high-frame-rate digital camera to acquire images of nanoparticles in solution. The Brownian motion of individual particles is observed by tracking the evolution of their position across many images, and the Stokes-Einstein relation is applied to calculate the hydrodynamic diameter. Since NTA can discriminate between individual particles, it is typically better suited to resolving distinct particle populations in polydisperse samples than is DLS, which acquires an ensemble measurement of all particles simultaneously. Images obtained from NTA can also be used to visualize the sample and determine the approximate nanoparticle concentration.²⁸ NTA assumes, as does DLS, a spherical morphology to calculate particle size from diffusion rate, making it generally ill-suited to studying non-spherical nanomaterials. While the resolving power of NTA is generally considered superior to that of DLS, it is not adequate for all applications. For example, a study by Anderson et al. showed that NTA and DLS could not resolve populations of polystyrene nanoparticles in a dispersion containing 220- to 410-nm diameter particles.²⁹

1.2.4 Tunable resistive pulse sensing (TRPS) can be used when higher resolution is required to distinguish multiple particle populations in a polydisperse sample. The number density distribution of particle sizes obtainable with TRPS allows more accurate determination of particle mobility and morphology than is possible with DLS. This method relies on the Coulter principle, widely exploited in Coulter counters used to size and count cells.³⁰ The Coulter principle states that the flow of a particle through a pore containing conductive fluid transiently increases the electrical impedance across the pore

in a manner proportional to the particle's volume.³¹ While traditional Coulter counters utilize rigid pores of a fixed size, TRPS employs pores fabricated in an elastic membrane. Pore size can be precisely controlled by changing the tension across the membrane; this increases the resolving power and dynamic range of TRPS.³² Pal et al. have used TRPS to individually measure the hydrated size and aggregation behavior of populations of multiple nanomaterials with greater sensitivity and resolution than is possible with DLS (Figure 4).³³ Particles studied include non-spherical carbon-based nanomaterials, cerium oxide nanoparticles, and nickel nanoparticles. TRPS can be used to simultaneously monitor nanoparticle zeta-potential and size, based on a theoretical treatment of the forces acting on the particle which determine its velocity through a pore.³⁴ Analysis of the impedance peak traces resulting from TRPS analyses (e.g., half-width) may reveal additional information regarding dynamic changes in particle charge and other parameters, such as protein corona thickness.³³

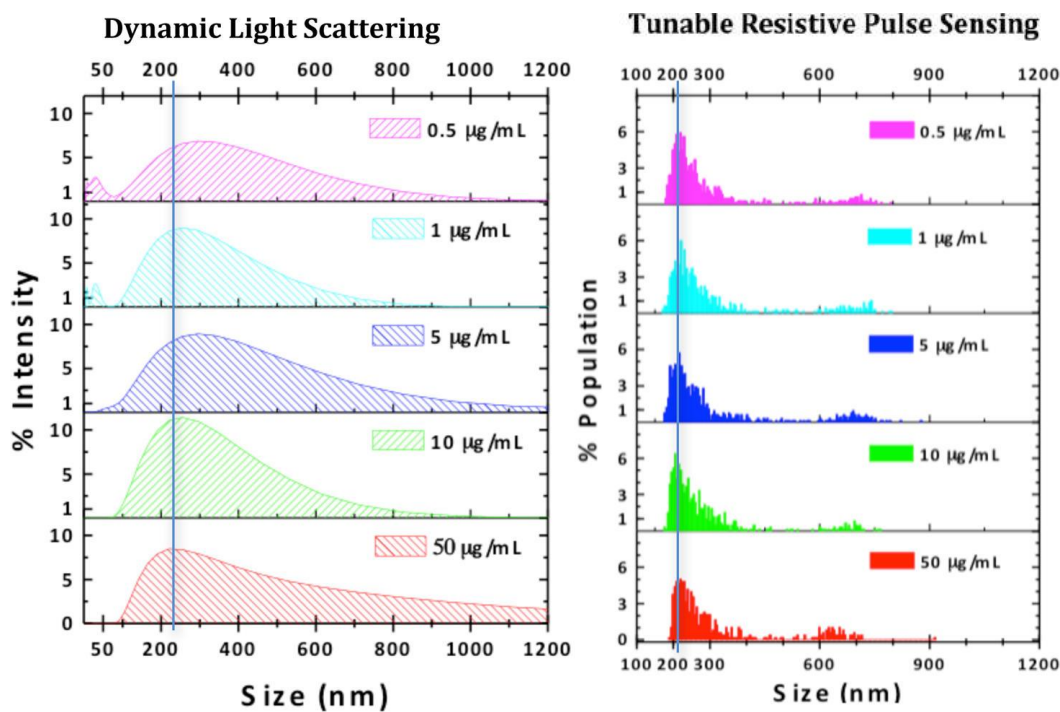


Figure 4. Comparison of DLS- and TRPS-measured size-distributions of H_2O_2 -oxidized single wall carbon nanohorns prepared in cell culture medium (RPMI medium) supplemented with 10% fetal bovine serum. Sequential dilutions of a $500 \mu\text{g/mL}$ stock solution of nanohorns in medium were prepared to achieve the concentrations listed. DLS analysis indicated a single, broad distribution of nanohorn sizes at most nanomaterial concentrations, though interfering signal in small size regimes due to serum proteins was observed at low nanohorn concentrations. In contrast, TRPS resolved two distinct nanohorn populations at all concentrations studied. Measured average nanohorn size varied with concentration when measured by DLS, while TRPS-measured averages showed limited concentration-dependence. Reprinted with permission from Pal, A. K.; Aalaei, I.; Gadde, S.; Gaines, P.; Schmidt, D.; Demokritou, P.; Bello, D. *ACS Nano* **2014**, 8 (9), 9003–9015 (ref 33). Copyright 2014 American Chemical Society.

1.2.5 Electrospray-differential mobility analysis (ES-DMA) has been used to characterize the aggregation behavior of spherical and non-spherical nanomaterials, including silver³⁵ and gold nanoparticles,^{27,36–38} gold nanorods,³⁹ graphene nanosheets,⁴⁰ and single-walled carbon nanotubes.⁴¹ This technique measures the electrical mobility of aerosolized nanoparticles in a sheath flow of air under an applied electric field of variable strength. To assess the properties of non-spherical particles, including nanosheet thickness, nanorod diameter and length, and nanotube length, extensive data fitting and correction parameters must be employed. These extensive data processing requirements limit the usefulness of ES-DMA in routine analysis of non-spherical nanomaterials.

1.2.6 Single particle inductively coupled plasma mass spectrometry (sp-ICP-MS) addresses the lack of chemical selectivity inherent in other nanomaterial aggregation and mobility analysis methods. Most methods used to track nanomaterial aggregation and mobility cannot distinguish between nanomaterials of interest and other colloidal species common to many biological matrices (e.g., lipid vesicles, dissolved organic matter, or protein aggregates), potentially decreasing the accuracy of nanomaterial size and mobility measurements due to signal interference. The sp-ICP-MS method significantly expands the capability of traditional ICP-MS for studying nanomaterials by incorporating time-resolution into elemental composition analysis. Ionized colloidal particles produce transient signals in the MS detector, assuming an optimized dwell-time and sufficiently dilute particle concentration such that particle ionization and detection events do not overlap. Transient signals are analyzed according to their frequency, intensity, and

elemental composition; from these data, colloidal concentration, size distribution, and chemical identity, respectively, can be calculated.⁴²⁻⁴⁵ Soluble species produce signals with more constant intensity, and their concentration can be separately quantified. The ability of sp-ICP-MS to distinguish colloidal species from soluble ions makes it a valuable tool for studying the toxicity of nanomaterials prone to chemical degradation, as these ions can contribute significantly to overall toxicity.⁴⁶⁻⁴⁸ The sp-ICP-MS method has been shown to have a similar accuracy to DLS for determining nanoparticle size distribution.⁴⁹

Peters et al. have recently demonstrated the robustness of sp-ICP-MS for nanoparticle detection in various complex matrices, including food, waste water, culture media, and biological tissue, using four commonly used nanoparticles (Au, Ag, TiO₂, and SiO₂).⁵⁰ Tuoriniemi et al. reported a size detection limit of 20 nm for Ag nanoparticles; below this, signal intensity spikes due to nanoparticle ionization overlapped with the background signal of dissolved silver ions.⁵¹ Liu et al. demonstrated a size detection lower limit of 10 nm for gold nanoparticles. This limit may vary by matrix or nanoparticle material since extent of dissolution will vary. An upper limit of 70 nm was obtained when using a pulse mode counting detector.⁵² Above this nanoparticle size, the signal spike produced upon nanoparticle ionization exceeded the linear dynamic range of the detector. Operating in a lower sensitivity analogue mode allowed the authors to extend the size detection maximum to 200 nm.

Liu et al.'s study also demonstrates the capability of sp-ICP-MS to simultaneously monitor nanomaterial size and chemical speciation. Dissolved Au ions released from gold nanoparticles contributed constant signal in the MS detector, while gold nanoparticles contributed spikes corresponding to individual nanoparticle events.⁵² Laborda et al. reported a similar ability to distinguish dissolved Ag ions and Ag nanoparticles.⁵³ In parallel, the authors measured the size distribution and number concentration of silver nanoparticles. Nanoparticle sizing by sp-ICP-MS generally assumes a spherical particle morphology and compares the signal intensity from an unknown sample to a series of standards. Nanoparticle diameter is calculated using the geometric relation between spherical particle mass and diameter.⁵⁴ To the best of our knowledge, sp-ICP-MS has not been applied to characterize non-spherical nanomaterials.

1.2.7 Differential centrifugal sedimentation is a very high-resolution method to determine nanoparticle size that relies on tracking nanoparticle transport through a density gradient.²⁹ Nanoparticles are introduced into a carrier solution (typically sucrose), which establishes a density gradient as the solution spins and is subjected to centrifugal force. While this method has high resolution and a large dynamic range, it cannot be used for in situ measurement of nanoparticle transformations in biological matrices due to the requirement that nanoparticles be introduced into a carrier solution.²⁹ However, a centrifugal method for particle size discrimination that can be applied to nanoparticles suspended in biologically relevant matrices has been developed by DeLoid et al.⁵⁵ These researchers developed a standard method using volumetric centrifugation (pellet volume

determination) to determine the effective density of nanomaterials, which they applied to calculate delivered nanomaterial dose to surface-bound cell cultures, a common mode of toxicological assessment.⁵⁶ The latter calculation was achieved using the *in vitro* sedimentation, diffusion and dosimetry (ISDD) model created by Hinderliter et al, which uses nanomaterial hydrated size (measured by DLS) and density as inputs.⁵⁷

1.2.8 Ion-selective electrodes (ISEs) offer a means to monitor the chemical speciation of nanomaterials in complex matrices and are primarily useful for tracking the dissolution of chemically unstable nanomaterials. ISEs are potentiometric chemical sensors with high selectivity for a target ionic analyte and are routinely employed for *in situ* quantification in complex matrices such as plasma and whole blood.⁵⁸ The earliest ISE, the glass pH electrode, was based on the selective permeability of glass for hydrogen ions. State-of-the-art ISEs use ion receptors (i.e., ionophores).⁵⁹ ISEs employing ionophores present in matrices of highly fluorinated compounds have shown very high selectivities and stabilities, making them among the most selective chemical sensors.⁶⁰⁻⁶³

While ISEs are not capable of analyzing nanomaterial size in addition to chemical speciation, as is possible using sp-ICP-MS, their capacity to monitor chemical speciation with high selectivity and time-resolution is superior to that of sp-ICP-MS. Commercially available solid-state Ag/Ag₂S ISEs have been used to monitor silver nanoparticle speciation (i.e., to observe release of Ag(I) from Ag nanoparticles) in a number of studies.⁶⁴⁻⁶⁶ Kakinen et al. monitored copper ion release from CuO nanoparticles in various media commonly used for biological toxicity testing using both a commercially

available Cu-ISE (sensitive only to Cu (II)) and a bioluminescent bacterial-based biosensor (sensitive to bioavailable copper ions).⁶⁷ The authors observed that more dissolved copper was detected by the bacterial biosensor than by the ISE, suggesting that copper was bioavailable in some form other than free Cu (II). This study suggests that both free and complexed metal ions may be bioavailable and contribute to overall organismal toxicity.

Custom-made ISEs also have been used to monitor nanoparticle dissolution. Maurer-Jones et al. employed a fluoruous-phase silver ISE to monitor silver nanoparticle dissolution in real-time in a biological matrix containing live bacterial cells (*Shewanella oneidensis* MR-1).⁶⁸ They observed altered nanoparticle dissolution kinetics and lower total silver ion release from nanoparticles in the presence of cells than in an identical cell-free matrix, demonstrating that the presence of organisms can alter nanoparticle dissolution behavior. Koch et al. similarly observed decreased silver nanoparticle dissolution in the presence of human alveolar epithelial cells versus in cell-free culture media using a commercially available solid-state membrane Ag/Ag₂S ISE.⁶⁹

As discussed here, multiple analytical methods are available to characterize the dynamic, hydrated behavior of nanomaterials. Given the increasingly common occurrence of nanomaterials with non-spherical morphologies (e.g., nanosheets, nanotubes, nanocubes), it is imperative that researchers move beyond light scattering techniques that assume spherical geometry as the primary means to characterize nanomaterial aggregation behavior. Electron microscopy remains the most readily available option for many researchers to characterize both spherical and non-spherical nanomaterial aggregation or

size change due to dissolution, though its low throughput and small sampling size present significant limitations. TRPS and ES-DMA represent two higher-throughput options to characterize both spherical and non-spherical nanomaterials in complex, biologically relevant matrices, and commercial instruments are available. TRPS will be much more easily implemented by most nanotoxicologists, based on far lower data processing requirements than ES-DMA. ISEs provide a means to monitor the chemical speciation of nanomaterials with exceptionally high selectivity while sp-ICP-MS, though its application to nanomaterials with non-spherical morphology remains unexplored, offers the unique capability to simultaneously monitor nanomaterial size and chemical speciation.

1.3 Characterizing Dynamic Physical and Chemical Properties of Nanomaterials: Probes of Molecules at Nanomaterial Surfaces

Nanomaterials exhibit not only dynamic colloidal behavior under biologically relevant conditions, but dynamic changes in surface chemistry as well. Components of biological and environmental matrices, including proteins,^{70,71} lipoproteins,⁷² and dissolved organic matter,^{73,74} can adsorb onto nanomaterial surfaces under realistic exposure scenarios, forming a molecular “corona”. Protein coronas, being the most widely studied, have been shown to significantly alter nanomaterial colloidal behavior and interaction with biological systems relative to the pristine nanomaterial by modifying factors such as nanomaterial size, surface charge, and surface chemistry.⁷⁵ The composition of the protein corona, e.g. the glycosylation state of adsorbed proteins, can influence the extent

of nanomaterial internalization by cells.^{76,77} Adsorbed proteins can also influence immune response in cells, a subject that has been recently reviewed.⁷⁸ Adsorption of other molecules, including humic and fulvic acids, has also been shown to alter nanomaterial colloidal behavior and toxicity.⁷⁹⁻⁸¹ Detailed characterization of the dynamic composition of the protein corona, as well as coronas formed from less-studied molecules like dissolved organic matter, is necessary to understand the interface between nanomaterials and biological systems under biologically and environmentally relevant exposure scenarios.

The binding constants controlling molecular adsorption to nanomaterial surfaces and the composition, surface-coverage, thickness, and orientation of molecules on the nanomaterial surface have been studied using a number of analytical techniques. A significant barrier to characterization of molecular adsorption to nanomaterial surfaces *in situ* is signal interference due to the high chemical complexity of biologically relevant media (which may contain proteins, lipids, and dissolved organic matter). Additionally, discriminating between species adsorbed to the nanoparticle surface and those in solution can be difficult due to their similar chemical signatures. These problems can be ameliorated by isolating subpopulations of nanomaterials or by isolating nanomaterials from interfering colloidal species in the sample matrix prior to analysis; however, separation methods have been infrequently employed in published studies. Currently available separation methods include column chromatography and field flow fractionation and its derivatives (see Section 1.4). Development of more rapidly

implementable and generalizable methods to separate nanomaterials from complex biological matrices would facilitate accurate nanomaterial characterization.

1.3.1 X-ray photoelectron spectroscopy (XPS) is widely used to probe the chemical environment of planar surfaces, but is more difficult to perform on nanoparticle surfaces due to their non-planar geometry and small size.⁸² Torelli et al. have recently developed a quantitative method to correct XPS data obtained from small, spherical, surface-functionalized nanoparticles by accounting for the effects of surface curvature on spectral intensities. Their geometric correction method can be applied to quantitatively measure ligand density on the surface of nanoparticles smaller than 20 nm using XPS, which would otherwise give aberrant quantitative data.⁸²

1.3.2 Attenuated total reflectance Fourier transform infrared (ATR-FTIR) spectroscopy is used to assess the adsorption of molecules to nanomaterial surfaces both qualitatively (identity and structure of surface-adsorbed ligands) and quantitatively (kinetics of adsorption).⁸³ ATR-FTIR can be used to study the interactions of both small molecules (e.g., carboxylic acids,^{84,85} and catechols⁸⁶) and large molecules (e.g., proteins) with nanomaterials, though studies of larger molecules are less common. Nanomaterials are introduced to the ATR crystal surface by drop casting, which creates a thin film, and molecules of interest are then introduced using a flow-cell placed on the crystal's surface. An evanescent infrared wave, produced as a result of total internal reflection at the crystal surface, serves as a probe of the chemical environment within a short (~ 1 μm) distance

from the crystal-solution interface. This short penetration depth limits signal contributions from the bulk solution (i.e., from species not bound to the nanomaterial surface), although interfering signal from the bulk may still be significant enough to complicate analysis in complex solution environments.

Qualitative characterization of ATR-FTIR spectra requires assigning vibrational peak modes and monitoring relative changes in peak position, width, and intensity. For example, Tsai et al. used ATR-FTIR to qualitatively assess BSA adsorption to PEG-functionalized gold nanoparticles.²⁷ The authors monitored observed peak broadening and decreased intensity in the amide I region, which they attributed to a loss of secondary structure (α -helices). Quantitative characterization was achieved by monitoring changes in peak intensity in the amide II region as a function of BSA concentration introduced to the flow cell housing the gold nanoparticles. This vibrational region is relatively insensitive to protein secondary structure and can be used to quantify total protein adsorption. Using the Langmuir adsorption model, the authors used these data to determine the adsorption density and surface binding constant of BSA on PEG-functionalized gold nanoparticles. They found fairly good agreement between these parameters as determined by ATR-FTIR, a fluorescence assay of adsorbed protein concentration, and electrospray-differential mobility analysis.

Quantitative analysis of protein adsorption to or desorption from nanomaterials can, however, be significantly complicated by spectral artifacts such as experimental drift, commonly introduced during blank subtraction.⁸³ In addition, distinguishing spectral intensity changes resulting from protein exchange with the nanomaterial surface versus

protein conformational changes can be difficult, as has been described in the case of human plasma protein adsorption to super-paramagnetic iron oxide nanoparticles.⁸⁷ For these reasons, ATR-FTIR is best used in combination with other techniques to probe molecular adsorption to nanomaterial surfaces.

1.3.3 Surface-enhanced Raman spectroscopy (SERS) is another surface-sensitive method capable of probing biomolecule interactions with nanomaterials. SERS relies on the significant enhancement of Raman scattering intensity that occurs within a nanometer-length region of a plasmonically active surface (like a noble metal nanoparticle). Consequently, this technique is inherently limited in scope and has been infrequently employed to characterize biomolecule-nanomaterial interactions. However, by exploiting the fact that surface enhancement occurs over a nanometer length scale, SERS can be used to probe biomolecule binding distance from a plasmonically active surface. For example, Treuel et al. observed that Raman features of proteins adsorbed to citrate-functionalized silver and gold nanoparticle surfaces diminished when the capping agent was replaced with a thicker polymer coating.⁸⁸

1.3.4 Circular Dichroism. Protein adsorption to nanomaterial surfaces commonly results in a loss of secondary structure. Consequently, circular dichroism (CD) spectroscopy can be applied to quantify protein adsorption to nanomaterial surfaces by monitoring loss of protein secondary structure in the bulk solution.⁸⁹ A theoretical treatment of the effects of protein-to-nanoparticle adsorption on protein secondary structure has been developed by

Li et al.⁹⁰. The authors used coarse-grained molecular dynamics simulations to model the interaction of apolipoprotein A-1, the main component of high-density lipoprotein, with silver nanoparticles, and validated these simulations against direct CD measurements.⁹⁰ In both their simulations and experiments, the authors observed destruction of protein α -helices and increased β -sheet character following interaction with nanoparticles. Gagner et al. observed loss of both α -helix and β -sheet secondary structure in both lysozyme and α -chymotrypsin following their adsorption to gold nanospheres and nanorods.⁹¹ Lysozyme-nanoparticle conjugates showed greater losses in secondary structure (and protein activity, measured in parallel using enzymatic assays) than α -chymotrypsin-nanoparticle conjugates. Rotello et al. also observed loss of α -helix structure in BSA upon interaction with gold nanorods functionalized with amine-terminated polyethylene glycol.⁹² In contrast to these studies, Wang et al. observed that weak, reversible binding of Subtilisin Carlsberg, an enzyme representative of serine proteases, to silica nanoparticles resulted in no loss of secondary structure.⁹³ However, the authors observed altered near-UV CD spectra following enzyme interaction with nanoparticles, suggesting altered tertiary structure. Despite being weak, these enzyme-nanoparticle interactions decreased the catalytic efficiency of the enzyme, with smaller nanoparticles inducing a greater reduction than larger nanoparticles.

1.3.5 Nuclear magnetic resonance spectroscopy (NMR) is based on a more general detection principle than are the previously mentioned techniques, which complicates its use in complex biological matrices (e.g., those containing multiple amino acids or

proteins). However, its high chemical sensitivity and versatile detection platform, including the ability to be combined with measurement of diffusion coefficients, makes it a valuable method for probing biomolecule interactions with nanomaterial surfaces. Solid-state NMR can provide detailed information about the chemical environment at nanoparticle surfaces. For example, solid-state NMR has been used to characterize the orientation of L-cysteine on gold nanoparticle surfaces based on measurements of discrete ^1H , ^{13}C , and ^{15}N resonances.^{94,95} Both broad and sharp ^1H resonances were observed, with the former attributed to cysteine bound close to the nanoparticle surface and the latter attributed to cysteine present in an outer layer not chemisorbed to the nanoparticle surface.⁹⁵

Solution-based NMR has also been used to characterize adsorbed species. Hellstrand et al. used $^1\text{H}/^1\text{D}$ NMR to identify adsorbed lipids that had been extracted (into chloroform) from lipoproteins bound to the surface of copolymer nanoparticles.⁷² Giri et al. used 1D and 2D (DOSY) ^1H NMR to observe the strength of interaction between human serum albumin (HSA) and poly(amidoamine) dendrimers of various generations and with various terminal groups (e.g., NH_2 vs. OH).⁹⁶ Their experiments revealed overall weak interactions between the dendrimers and HSA, indicated by small chemical shifts and changes in diffusion constants. The authors also employed saturation transfer difference (STD) NMR to identify protein domains displaying the strongest interactions with dendrimers. In STD NMR, short RF pulses are used to saturate host molecule (e.g., protein) resonances without affecting other molecules in solution.⁹⁷ Guest molecules that bind to the host experience saturation through intermolecular saturation transfer, while

molecules that do not bind remain unsaturated. The difference spectrum resulting from pre- and post-saturation NMR spectra reveals the chemical environment of only the bound guest molecules. Protons closer to the dendrimer core were more saturated (as a result of saturation transfer from HSA) than those farther from the core, indicating stronger interactions between HSA and inner dendrimer protons than outer protons.⁹⁶

1.3.6 Mass Spectrometry provides a more sensitive and quantitative means to identify biomolecules adsorbed to nanomaterials than does NMR spectroscopy. Multiple mass spectrometry platforms have been applied to characterize molecules adsorbed to nanomaterial surfaces; these vary in their sample preparation requirements (e.g., need to separate sample components prior to mass spectral analysis), which subsequently determines their time resolution.

Sisco et al. used 2D gel electrophoresis and LC-MS/MS to identify proteins adsorbed to polymer-wrapped gold nanorods.⁹⁸ Nanorods terminated with negatively or positively charged head groups or polyethylene glycol were incubated in rat cardiac fibroblast cell culture media, allowing proteins to adsorb to the nanorod surface overnight. Adsorbed proteins were eluted by increasing the solution salt concentration, separated by 2D gel electrophoresis, and identified using LC-MS/MS. Adsorption of biglycan, a protein that influences cellular interactions with the extracellular matrix, was found to correlate with the impact of nanorod exposure on fibroblast contractile ability: negatively and positively charged nanorods adsorbed biglycan and decreased contractile ability, while polyethylene

glycol-functionalized nanorods resisted biglycan adsorption and had no effect on contractile ability.

Similar methods based on protein separation by 2D gel electrophoresis and detection by LC-MS have been employed to characterize the nanoparticle protein corona in other studies.^{99,77,100–102} However, these methods generally lack the time-resolution required to observe the dynamics of protein corona evolution; unbound proteins are typically separated from nanoparticles and nanoparticle-protein complexes via centrifugation or size-exclusion chromatography, and the length of this separation procedure determines the time-resolution of the technique. Higher time-resolution has been obtained by centrifuging nanoparticles and proteins through a sucrose cushion to isolate nanoparticle-protein complexes.¹⁰³ Subsequently, label-free LC-MS proteomics was used to qualitatively and quantitatively characterize protein adsorption to silica and polystyrene nanoparticles. The high time-resolution of this approach allowed for observation of rapid (<0.5 min) adsorption of hundreds of distinct proteins. With continued incubation time, changes were primarily observed in the quantity (rather than the identity) of adsorbed proteins. Subsequent evaluation of the impact of silica nanoparticle exposure to thrombocytes, erythrocytes, and endothelial cells (measured as cell aggregation, hemolysis, and ATP content, respectively) showed that even short (0.5 min) nanoparticle exposure to proteins reduced their biological impact. Previously employed methods to characterize protein-polystyrene nanoparticle interactions, including differential centrifugal sedimentation, dynamic light scattering, and transmission electron

microscopy,¹⁰⁴ have less control over the nanoparticle-protein interaction time than the proteomic approach employed by Tenzer et al., resulting in lower time-resolution. Laser desorption/ionization mass spectrometry (LDI-MS) has been used to rapidly characterize the structure of monolayer and mixed monolayer ligands on magnetic nanoparticles (FePt and Fe₃O₄ nanoparticles).¹⁰⁵ Though LDI-MS has not yet been applied to study biomolecule adsorption to nanoparticles (to the best of our knowledge), it provides a rapid means to analyze pristine nanoparticle surface chemistry, a key determinant of nanoparticle-biomolecule interactions. In the study by Yan et al., sample preparation for mass spectral analysis required only spotting nanoparticle suspensions on a steel target plate and allowing them to air-dry; subsequent analysis consumed a very small amount of sample (2 µg).¹⁰⁵ In addition to qualitative characterization of ligand structure, quantitative analysis of ligand composition on the nanoparticle surface was also performed. Six mixed monolayer FePt nanoparticle populations were prepared, each containing a different ratio of two ligands. Following mass spectral analysis, signal intensities from ions unique to each ligand were summed and corrected for differing ionization efficiencies based on analysis of a nanoparticle with a 1:1 ligand ratio (verified by ICP-MS). The resulting ligand compositions (expressed as a ratio of ligand concentrations) were compared to those measured using HPLC-MS following digestion of the nanoparticle core. The two methods showed good agreement, though LDI-MS analysis was performed in one hour while HPLC-MS analysis required 18 hours. Szakal et al. developed a time-of-flight secondary ion mass spectrometry (ToF-SIMS) method to characterize nanoparticle surface chemistry in simple and complex matrices.¹⁰⁶

Using TiO₂ nanoparticles as a model, they deposited nanoparticles as aggregate rings onto silica substrates using ink-jet printing technology; aggregate rings were subsequently scanned using ToF-SIMS. In this technique, an energetic ion beam sputters atoms and molecules off a sample surface; the fraction liberated as ions are subsequently mass analyzed in ToF mass spectrometer. Nanoparticles exposed to natural organic matter prior to deposition showed lower ratios of Ti⁺ to C₃H₅⁺ than did pristine nanoparticles, indicating greater adsorption of organic material to the nanoparticle surface in this case. Repeated scanning using ToF-SIMS removed material from the nanoparticle surface, allowing the authors to probe the chemical environment both at the nanoparticle surface and in the core. In subsequent work, Szakal et al. applied ToF-SIMS with ink-jet printing to visualize Ag nanoparticle dissolution (Figure 5).¹⁰⁷ Nanoparticles and ions produced distinct chemical distribution maps after deposition onto silica substrates which allowed nanoparticle dissolution to be visualized.

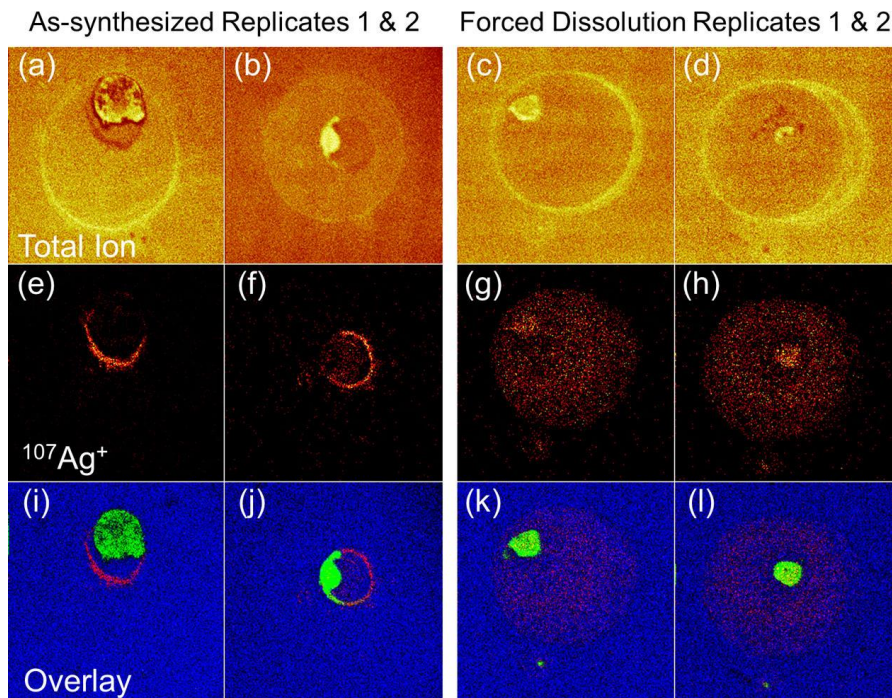


Figure 5. ToF-SIMS images of inkjet-printed droplets of as-synthesized Ag nanoparticle suspension (panel columns a, e, i and b, f, j) and Ag nanoparticle suspension treated with 300 nm UV light to force nanoparticle dissolution (panel columns c, g, k and d, h, l). Panel rows depict the spatial distribution of the sum of all signal intensities across all secondary ions measured (a-d), the signal intensity of $^{107}\text{Ag}^+$ (e-h), and the signal intensities of $^{107}\text{Ag}^+$ in red, Na_2OH^+ (indicative of non-silver ionic species in solution) in green, and $^{28}\text{Si}^+$ (indicative of the silicon substrate) in blue (i-l). The $^{107}\text{Ag}^+$ signal was concentrated in a ring around the perimeter of the dried as-synthesized Ag nanoparticle droplet (e, f) and showed no overlap with Na_2OH^+ (i, j), consistent with separation of intact Ag nanoparticles from water-soluble species. In contrast, $^{107}\text{Ag}^+$ signal was more evenly dispersed throughout the droplet of UV-treated Ag nanoparticles (g, h), suggesting that nanoparticle dissolution occurred. However, $^{107}\text{Ag}^+$ signal was not entirely co-localized with that of other water-soluble ionic species (indicated by Na_2OH^+ signal),

suggesting that dissolved Ag species were of only partially ionic character or consisted of a mix of soluble and insoluble species. Images show an area of $500 \times 500 \mu\text{m}$. Reprinted with permission from Szakal, C.; Ugelow, M. S.; Gorham, J. M.; Konicek, A. R.; Holbrook, R. D. *Anal. Chem.* **2014**, 86 (7), 3517–3524 (ref 107). Copyright 2014 American Chemical Society.

1.3.7 Small-angle x-ray scattering (SAXS) has been used to study the interactions of colloidal systems with biomolecules; however, it requires a significant amount of data processing. Elastic X-ray scattering intensity is measured as a function of the incident X-ray beam angle (i.e., the scattering vector). The resulting data are fit to one of several particle scattering models (e.g., for spherical polymer micelles^{108,109}) that can account for particle size, shape, and presence of adsorbates. Henzler et al. used SAXS to analyze the spatial distribution of proteins (bovine β -lactoglobulin) adsorbed to polystyrene nanoparticles functionalized with poly(styrene sulfonate) (so-called polyelectrolyte brushes).¹¹⁰ Modeling the SAXS data as a function of the scattering vector as well as nanoparticle and protein concentration, these authors observed protein adsorption within the polyelectrolyte chains rather than at the particle core. SAXS analysis was also used to quantify total protein adsorption; results were compared to those obtained by isothermal titration calorimetry (ITC) and ultrafiltration characterization. SAXS and ITC showed good agreement, while ultrafiltration, which removes weakly adsorbed protein and thus provides quantitative information on only the “hard” protein corona, showed lower protein adsorption.

1.3.8 Electron and Atomic Force Microscopies. While electron microscopy alone cannot quantitatively assess adsorption processes on the surface of nanomaterials, it can provide high-resolution images of labeled adsorbed species. Kelly et al. studied the spatial distribution of transferrin protein on polystyrene nanoparticles by subjecting the protein-coated nanoparticles to treatment with small (5-nm) gold nanoparticles bearing antibodies for transferrin epitopes.¹¹¹ The spatial distribution of protein was inferred from the location of the gold nanoparticles under saturation conditions (i.e., when all accessible transferrin epitopes had been labeled, as determined by differential centrifugal sedimentation analysis of particle size over a range of gold label concentrations); the relatively small number of epitopes available for interaction with antibodies reduced the likelihood that gold nanoparticles (due to their size) would block neighboring interaction sites. Protein distribution appeared random, a result consistent with stochastic adsorption. Though difficult to apply when studying small, electron-dense nanomaterials, biomolecule-targeted labeling combined with high-resolution electron microscopy imaging remains one of the few methods available (in addition to super-resolution fluorescence microscopy) to visualize biomolecule adsorption to nanomaterials with nanometer spatial resolution.

Atomic force microscopy (AFM) has been used in one study to observe the binding modes of various proteins to single-walled carbon nanotubes.¹¹² While AFM can readily achieve sub-nanometer resolution along the z-axis (vertical resolution), its resolution in the x-y plane (lateral resolution) is limited by the size of the instrument tip, and is

typically tens of nanometers. Consequently, AFM cannot resolve the spatial distribution of individual proteins on a nanoparticle surface, though it can be used to visualize the spatial distribution of protein aggregates. In work by Ge et al., bovine fibrinogen and gamma globulin aggregated non-uniformly, transferrin aggregated in uniform nodes, and bovine serum albumin bound uniformly.¹¹² Molecular dynamics modeling was used to examine the mechanism of protein to nanotube binding and identified tyrosine and phenylalanine as the dominant amino acid residues in contact with the nanotube surface.

1.3.9 Fluorescence correlation spectroscopy (FCS) can be used to calculate diffusion constants of fluorescently labeled nanoparticles or biomolecules by measuring fluctuations in the number of fluorescent particles within a small (typically femtoliter)¹¹³ probe volume. Since FCS is sensitive only to fluorescent species, it can be used to measure diffusion constants in complex matrices, where the presence of multiple species may interfere with light scattering techniques (e.g., DLS). While FCS cannot directly reveal protein conformation, binding constants and surface coverages can be calculated from changes in diffusion coefficients of interacting species. Milani et al. used FCS to measure changes in the diffusion time of fluorescently labeled transferrin (a major protein component of blood) upon binding to polystyrene nanoparticles.¹¹⁴ The fraction of bound transferrin was determined by fitting the autocorrelation function describing its time-dependent diffusion with a two-component function previously described by Rusu et al.¹¹⁵ By tracking the fraction of nanoparticle-bound transferrin as a function of the protein-to-nanoparticle concentration ratio, Milani et al. determined that protein

adsorption occurred in two distinct phases: in the first phase, proteins adsorbed irreversibly to the nanoparticle surface until surface-saturation was achieved (forming a so-called hard protein corona); in the second phase, additional proteins bound reversibly to those already adsorbed to the particle surface, forming a “soft corona” that exchanged dynamically with solution proteins.

Treuel et al. observed completely reversible adsorption of human serum albumin to dihydrolipoic acid-functionalized CdSe/ZnS core-shell quantum dots using FCS.¹¹⁶ The extent of adsorption was determined as a function of the protein surface charge (made more negative by addition of carboxyl groups or less negative by addition of amino groups). They observed larger increases in nanoparticle hydrodynamic radii (calculated from the diffusion coefficient using the Stokes-Einstein relation) when nanoparticles were exposed to charge-modified vs. native human serum albumin. Charge-modified and native proteins were suggested to adopt different conformations when binding to the quantum dots, resulting in a more- or less-compact protein corona and, consequently, hydrated radius. The authors acknowledge that previous studies (including their own) had demonstrated irreversible (compact) protein adsorption to other nanoparticles (including silver^{117,118} and gold¹¹⁸), underscoring the lack of mechanistic knowledge on the reversibility of protein adsorption.¹¹⁶ We note that nanoparticle polymer coatings, at least for some noble metal nanoparticles, have been shown to favor soft protein corona formation, due to weak polymer-protein interactions relative to polymer-polymer interactions at the nanoparticle surface.⁸⁸ In contrast, polymer-nanoparticle entanglement, which is more likely to occur with increasing polymer length, may lead to reduced

protein desorption, or formation of a hard corona.¹¹⁶ It is likely that nanomaterial surface functionalization plays a role in determining the reversibility of binding interactions with proteins.

1.3.10 Isothermal titration calorimetry (ITC) provides a means to directly probe the enthalpy change associated with biomolecule adsorption to a nanomaterial surface, from which multiple thermodynamic parameters can be calculated. Zeng et al. measured the thermodynamic parameters controlling the interaction of acrylamide-based polymer nanoparticles with the polysaccharide heparin.¹¹⁹ Titration of heparin into a nanoparticle solution released heat when binding occurred and, by fitting the titration curve resulting from multiple additions of heparin, the binding constant, stoichiometry, and enthalpy change were calculated. The entropy change was calculated according to Gibb's law. A series of nanoparticles composed of polymers with varying ionic character, hydrophobicity/hydrophilicity, and cross-linking were tested. The authors proposed that hydrogen bonding, ionic interactions, and dehydration of polar groups were the predominant modes of heparin and nanoparticle interaction and that nanoparticles with higher charge density and degree of cross-linking had greater affinity for heparin. Loosli et al. recently used ITC to measure the thermodynamic parameters controlling the adsorption of Suwannee River humic acids to TiO₂ nanoparticles and to elucidate the mechanism of the adsorption process.¹²⁰ Initial experiments were performed at a pH where nanoparticles had a positive surface charge and humic acids had a negative charge. Differing behavior was observed when humic acids were titrated into a suspension of

nanoparticles versus when nanoparticles were titrated into a suspension of humic acids. In the former case, humic acid adsorption to the nanoparticle surface was primarily enthalpically driven for most ratios of nanoparticle to humic acid concentration; small but also favorable entropy changes were observed. The reaction stoichiometry was calculated to be less than one, indicating incomplete coverage of the nanoparticle surface by humic acids. In the latter case, enthalpy changes upon nanoparticle association to humic acids were lower than in the former case. The authors suggest that greater homoagglomeration of humic acids in the former case (where the humic acid concentration is higher) leads to complexation of humic acids with more nanoparticles and a more enthalpically driven interaction. Nanoparticles were also titrated with humic acids at a higher pH, where each has a negative charge. Association was observed despite unfavorable electrostatic interactions, suggesting that van der Waals interactions were also present.

1.4 Separating nanomaterials from complex biological matrices

1.4.1 Chromatography. As mentioned above, nanomaterial characterization in complex matrices of biological and environmental relevance is complicated by the need to selectively monitor target nanomaterials or biomolecules in the presence of multiple interfering species (e.g., dissolved organic matter, lipid vesicles, or proteins). Improved methods to separate nanomaterials from interfering colloidal species would facilitate more accurate nanomaterial characterization in such complex matrices. Column chromatography, including high-performance liquid chromatography,¹²¹ size-exclusion chromatography,¹²² and gel-electrophoresis¹²¹ have been used previously to separate

nanoparticles based on their size, but have not until recently been applied to separate nanomaterials from complex matrices. Zhou et al. recently published a liquid chromatography method to separate silver nanoparticles and silver ions in complex matrices including naturally samples waters (i.e., lake water and waste water treatment plant influent and effluent).¹²³ An amine-terminated column was used as the stationary phase; FL-70 surfactant and sodium thiosulfate were added to the mobile phase to elute silver nanoparticles and ions, respectively. The column was connected to an ICP-MS for silver detection. Recoveries of ionic silver and silver nanoparticles in naturally sampled waters ranged from 84.7-96.4% and 81.3-106.3%, respectively. Hydrodynamic chromatography (HDC), wherein colloidal species are separated by size based on their flow velocities through the dead space of a column packed with nonporous beads, has been used to distinguish silver, gold, and polystyrene nanoparticles spiked into naturally sampled river water with non-baseline resolution.¹²⁴ Nanoparticles were identified by size analysis using both online DLS and offline DLS and single particle ICP-MS detection. Silver nanoparticles spiked into river water could not be detected by DLS due to the presence of multiple colloidal populations, but separation by HDC and subsequent DLS analysis allowed the nanoparticle population to be distinguished from natural colloids.

1.4.2 Field-flow fractionation. Though liquid chromatography has been used to separate nanoparticles from complex matrices, as described above, the most widely used method to separate nanoparticles from complex matrices is field-flow fractionation (FFF). Gray et al. showed that FFF can achieve significantly greater nanoparticle size resolution than

HDC; mixtures of Au nanoparticles with diameters between 5 and 100 nm could not be resolved by HDC, while FFF produced baseline resolution.¹²⁵ While FFF method development time can be significant,¹²⁶ this family of techniques is versatile both in the range of particles sizes that can be efficiently separated (from approximately 1 nm to 100 μm)¹²⁷ and the separation mechanism (not only size but also charge). In FFF, a field is applied perpendicular to fluid flow through a channel. The type of field used depends on the desired separation principle, but may be, e.g., a crossflowing fluid (as in the case of flow field-flow fractionation, F4), an electric field, or a thermal gradient.¹²⁷ Fluid flowing from the instrument inlet to outlet adopts a parabolic flow profile and thus contains distinct laminae having unequal flow velocities. Application of a perpendicular field drives suspended particles (e.g., nanomaterials) towards the edge of the channel. Subsequent diffusion drives particles into distinct laminae based on their mobility, causing particles to elute from the device at different times.

FFF has been employed to study nanomaterial transformations under biologically and environmentally relevant conditions. Ashby et al. used F4 to rapidly (<10 min.) separate serum proteins exposed to superparamagnetic iron oxide nanoparticles.¹²⁸ Separation was based on nanoparticle binding affinity. The later-eluting proteins (i.e., those with mild affinity for the nanoparticle surface, the so-called soft protein corona,¹¹⁴) were isolated and identified by LC-MS/MS analysis.

Asymmetric F4 (AF4), which utilizes a perpendicular flow field created by the continual exit of carrier fluid through the bottom of the device, has also been applied to separate nanoparticles from complex, environmentally relevant matrices. Koopmans et al.

separated citrate- and PVP-capped silver nanoparticles from sandy and clay soils and used in-line UV-vis spectroscopy to detect the concentration of eluted particles and DLS to determine nanoparticle size.¹²⁹ The authors found that a low concentration (0.01% w/v) of sodium dodecyl sulfate was required to separate nanoparticles from soil, demonstrating the critical role of the carrier fluid in F4 separations. Other in-line detection systems can be coupled with FFF. For example, Mitrano et al. have discussed the improved selectivity and sensitivity of FFF coupled with ICP-MS versus UV-vis spectroscopy and its advantages for analyzing nanomaterials in complex environmental samples.¹³⁰ As one example, FFF coupled with ICP-MS distinguished silver and gold nanoparticles by both size and chemical composition, while FFF coupled with UV-vis spectroscopy could only distinguish the nanoparticles by size.¹³¹

Johann et al. have recently expanded the utility of FFF beyond separations by combining AF4 and electrical FFF to measure nanoparticle or protein electrophoretic mobility as a function of size.¹³² Sequential AF4 experiments were performed with or without application of an electric field applied across the flow channel, and the electrophoretic mobilities of discrete nanoparticle populations were determined from the dependence of their retention times (and thus, flow velocities) on the magnitude of the applied electric field. By creating a parallel separation and measurement system, the authors have addressed an important theme within the field of nanomaterial toxicology, which is the need for rapid, parallel analysis of multiple nanomaterial physical and/or chemical properties.

Sections 1.2-1.4 have focused on analytical methods to characterize nanomaterials and their transformations relevant to nanotoxicity. Sections 1.5-1.6 will focus on analytical methods to directly characterize nanomaterial impacts on biological systems, including both the physical interaction between nanomaterials and membranes, cells, and organisms, and the physiological consequences of those interactions.

1.5 Interactions of Nanomaterials with Biological Systems

While the previous section focused on separating nanomaterials from a complex matrix for analysis, there are critical questions about nanomaterial-biological interactions that require direct visualization or measurement of these interactions in situ. To understand the mechanisms underlying nanomaterial-induced changes in survival of isolated cells or whole organisms, the interactions between nanomaterials and the biomolecules that compose the cell membrane and interior must be characterized. Reversible or irreversible adsorption of nanomaterials to cell membranes has potential consequences for membrane fluidity and integrity and membrane small molecule and ion transport, while nanomaterial internalization or endocytosis provides nanomaterial access to intracellular organelles and biomolecules. Release of ionic or radical species from nanomaterials in the biologic matrix may disrupt the cell membrane or intracellular biomolecules.

The two major obstacles to characterizing the physical interaction of nanomaterials with biological systems are the small scale of nanomaterials, which makes direct visualization of interactions difficult, and the chemical complexity of biological environments, from which it is difficult to extract any change in chemical signal from noise.

To address the first challenge, researchers have applied a variety of microscopy methods with nanometer-scale resolution, including electron microscopy, atomic force microscopy, and super-resolution fluorescence microscopy to visualize the nanomaterial-biological interface. To address the second challenge, researchers have applied methods with chemical selectivity (e.g., x-ray and infrared spectroscopies and mass spectrometry) to quantitatively and qualitatively characterize the impact of nanomaterial interactions with biological systems at the molecular scale.

1.5.1 Electron microscopy and x-ray techniques. Electron microscopies such as TEM and SEM provide very high resolution, making them useful for observing the interface of biological systems with nanomaterials, most of which are smaller than the diffraction limit of visible light (~200 nm);¹³³ however, electron microscopies typically have low contrast for low molecular weight, i.e. carbonaceous, species. Another limitation is that these techniques use ultra-high vacuum conditions that usually require extensive sample preparation (e.g., fixation, dehydration, embedding into resin, sectioning, staining, and/or application of a conductive coating); these conditions preclude image acquisition under native, hydrated conditions. Advances in sample preparation for electron microscopy, such as high pressure freezing, facilitate more rapid characterization of nanomaterial-biological interactions and with fewer sample preparation artifacts than is possible using traditional sample preparation methods (i.e., fixation with glutaraldehyde, dehydration, and staining).¹³⁴

Opportunities for in-line chemical analysis using, e.g., x-ray spectroscopies, further expand the utility of electron microscopy for nano-bio characterization to include chemical sensitivity. Omajali et al. observed that biosynthesized Pd nanoparticles localized in *Desulfovibrio desulfuricans* bacterial cells exposed to Pd (II) were not readily visible by traditional TEM, but could be easily visualized by electron backscattering measurements using high angle annular dark field scanning transmission electron microscopy (HAADF-STEM). Energy dispersive x-ray spectroscopy (abbreviated EDX or EDS) was performed in-line with HAADF-STEM imaging to create an elemental map of the environment within the cell and to unequivocally identify intracellular Pd.¹³⁵ HAADF-STEM produces images with high-signal-to-noise and high-contrast by detecting only electrons that are highly scattered following interaction with high-mass areas in a sample. Klein et al. have suggested that HAADF-STEM may be unable to distinguish native high-mass species within a cell from nanomaterials, since both would produce high scattering.¹³⁶ They suggest that dark-field TEM, which achieves contrast based on sample crystallinity rather than mass, may be more suitable than HAADF-STEM for distinguishing biological material from inorganic (crystalline) nanomaterial in biological samples. The authors used dark-field TEM to produce high-signal-to-noise, high-contrast images of gold nanoparticles associated with the surface of *Bacillus subtilis* bacterial cells and iron oxide nanoparticles internalized by peripheral blood mononuclear cells. Iron oxide nanoparticles were distinguished from biological material stained with osmium tetroxide and uranyl acetate by tilting the incident electron beam to an angle that produced diffraction selectively from nanoparticles.

Like Omajali et al., several other studies have used x-ray microscopies to track nanomaterial distribution in tissues, identify nanomaterials internalized by or associated with cells, and track nanomaterial chemical speciation. Plascencia-Villa et al. used field emission scanning electron microscopy (FE-SEM) and scanning transmission electron microscopy (STEM) in combination with EDX to characterize the interaction of CeO₂, TiO₂, and ZnO nanoparticles with unstained, uncoated mouse macrophages.¹³⁷ FE-SEM images showed that CeO₂ and TiO₂ nanoparticles induced small protrusions in the cell surface, while ZnO nanoparticles induced larger protrusions. Using EDX, the authors quantified the weight percent of nanoparticles associated with cells by comparing metal peak area (arising from nanoparticles) to those of C, N, and O (arising from biological material). Bright-field and dark-field STEM images of thin sections of cells were acquired to visualize nanomaterial uptake by cells, and EDX chemical mapping confirmed the location of nanoparticles inside cells. Mu et al. used EDX to observe the distribution of silica nanoparticles within adenocarcinomic human alveolar basal epithelial (A549) cells; the particles were too small and electron poor to conclusively identify using TEM alone.¹³⁸

Hernandez-Viezcas applied synchrotron microfocused X-ray fluorescence (μ -XRF) and micro-X-ray absorption near edge structure (μ -XANES) to probe the distribution and chemical speciation of ZnO and CeO₂ nanoparticles within soybeans grown in nanoparticle-enriched soil.¹³⁹ μ -XRF was used to map the spatial distribution of Zn and Ce in soybean tissue with micrometer resolution, while μ -XANES was used to determine

metal speciation (i.e., metal coordination environment); the latter was achieved by fitting XANES spectra obtained from metal-containing locations within soybean tissue with linear combinations of spectra obtained from reference metal compounds. Results showed that CeO₂ nanoparticles were taken up into soybean pods while ZnO nanoparticles were not; Zn accumulated in pods in a form that could not be directly identified based on reference compounds, but resembled Zn-citrate. Similarly, Gilbert et al. used μ -XRF and μ -XANES to probe ZnO nanoparticle accumulation and speciation in human bronchial epithelial cells.¹⁴⁰ Zn signals were detected in cells, but intracellular Zn localization could not be determined due to the micrometer spatial resolution of μ -XRF. Parallel XANES analysis showed that intracellular Zn was present in the form of free Zn²⁺ or Zn²⁺ complexes rather than intact nanoparticles. Control studies performed using Fe-doped ZnO nanoparticles, which had higher chemical stability than undoped ZnO nanoparticles and served as markers of cellular internalization of nanoparticles, provided further evidence that ZnO nanoparticles dissolved after being internalized by cells, rather than before internalization. Szymanski et al. used scanning transmission x-ray microscopy (STXM) to quantify the oxidation state of CeO₂ nanoparticles (i.e., ratio of Ce³⁺ to Ce⁴⁺) within and outside of hydrated, fixed mouse alveolar epithelial cells (Figure 6).¹⁴¹ Maps of nanoparticle distribution within cells were obtained with 50 nm spatial resolution. Subsequent line-scans across intracellular and extracellular nanoparticle aggregates revealed their oxidation state. Internalization of nanoparticles by cells led to their net reduction (i.e., an increase in the Ce³⁺ to Ce⁴⁺ ratio); correlated measurements of intracellular reactive oxygen species, a general indicator of oxidative stress, showed

reduced oxidative stress following cell exposure to some concentrations of CeO₂ nanoparticles. The authors postulated that CeO₂ nanoparticles may reduce cellular oxidative stress through superoxide dismutase- or catalase-like reactions, though they are also capable of increasing oxidative stress at some exposure concentrations.

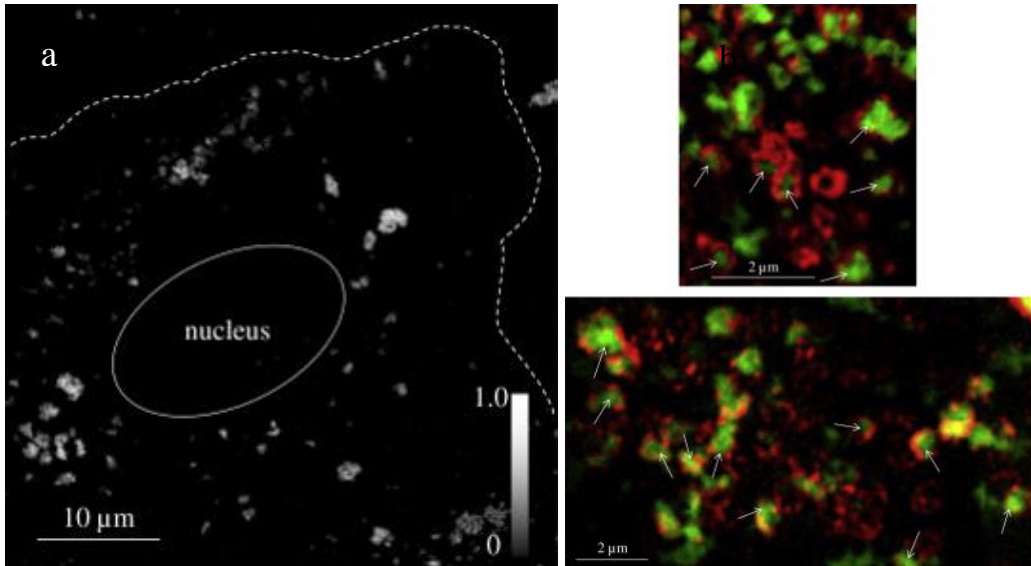


Figure 6. STXM (a) and fluorescence-overlay STXM (b) images of mouse alveolar type II epithelial cells exposed to CeO₂ nanoparticles. Cerium distribution within a cell was observed using STXM by subtracting a scan acquired below the cerium x-ray absorption edge from that acquired above it (a). The cell perimeter and nucleus were observed in scans acquired above the cerium x-ray absorption edge and are indicated with white lines. Cerium absorbance intensity is indicated in the gray scale-bar. Cerium distribution was also observed with respect to fluorescently labeled lysosomes present in the cell cytoplasm (b). Cerium (green, observed using STXM) was observed to be encased by lysosomes (red, observed using structured illumination microscopy) in overlaid STXM and fluorescence images, indicated by white arrows. Reprinted with permission from

Szymanski, C. J.; Munusamy, P.; Mihai, C.; Xie, Y.; Hu, D.; Gilles, M. K.; Tyliczszak, T.; Thevuthasan, S.; Baer, D. R.; Orr, G. *Biomaterials* **2015**, *62*, 147–154 (ref 141).

Copyright 2015 Elsevier.

Because X-rays easily penetrate biological material, X-ray microscopies typically lack the ability to discriminate nanomaterial distribution in three-dimensions. However, James et al. combined μ -XRF with focused ion beam ablation and SEM to determine the three-dimensional distribution of ZnO nanoparticles in human macrophages.¹⁴² Two-dimensional nanoparticle distributions were acquired by μ -XRF in parallel with SEM scans of sample topography. The sample surface was subsequently ablated to remove cellular material and nanomaterials using a focused Ga⁺ beam, and its topography was again probed by SEM. By repeating this process serially, a three-dimensional mapping of nanoparticle distribution in the cell was obtained. Drescher et al. observed the three-dimensional distribution of silica-coated silver nanoparticles in vitrified mouse fibroblasts and macrophages using cryogenic synchrotron X-ray tomography.¹⁴³ Nanometer spatial resolution was achieved without the need for extensive sample preparation or microtome slicing, as is required for electron microscopy; previous work has shown that synchrotron x-ray tomography using soft x-rays can achieve spatial resolution of 36 nm by the Rayleigh criterion¹⁴⁴ while imaging through samples 5 to 10 μ m in thickness.^{144,145} Descher et al. observed that cellular uptake of nanoparticles induced aggregation that was not observed in cell-free media. Nanoparticle association to

the nuclear membrane and other organelles was observed, though nanoparticles did not appear to move into the nucleus.

1.5.2 Atomic force microscopy (AFM) has a few advantages over electron microscopy for characterizing interactions between nanomaterials and biological systems. These include its high spatial resolution in three dimensions, compatibility with imaging under ambient pressure in liquids and in air, and ability to probe the physical properties of a sample, like stiffness and adhesion strength. Unlike electron microscopy, however, AFM cannot be easily combined with secondary spectroscopic methods to analyze chemical composition; chemical information can be obtained by measuring interaction forces between a sample (e.g., live bacterial cells) and an AFM tip decorated with specific functional groups, though this method has not been widely applied to study nanomaterial-biological interactions (see Fig. 7 for a related example). Image acquisition time is typically greater for AFM than for electron microscopy because it is a scanning method. AFM has been applied to study the interactions of both model biological systems (i.e., supported lipid bilayers, models of cell membranes) and living organisms with nanomaterials.

Troiano et al. used AFM to observe association of negatively charged gold nanoparticles with negatively charged lipid bilayers, in contrast to the expectation for electrostatic repulsion between these two systems.¹⁴⁶ Combined with other surface characterization methods, notably second harmonic generation, their results suggest that multivalent interactions can lead to associative nanoparticle-bilayer interactions that are not expected

from average charge density measurements. Beyond assessment of nanoparticle-bilayer association, Bhattacharya et al. studied the penetration of dendrimer nanoparticles into supported lipid bilayers and the consequences on membrane ordering using AFM, high resolution X-ray scattering and diffraction, and molecular dynamics simulations.¹⁴⁷ Three- and four-generation poly(ether imine) dendrimers were incubated with DMPC supported lipid bilayers, and AFM images showed that third-generation dendrimers induced formation of barrel structures in the bilayers without penetrating, while fourth-generation dendrimers penetrated into the bilayers, leaving less dendrimer material protruding from the membrane surface. As lipid packing density increased, penetration depth decreased. X-ray scattering analysis of the membrane electron density profiles further confirmed that fourth-generation dendrimers disrupted membranes to a greater extent than third-generation dendrimers, as evidenced by increased reduction of the lipid head group density and top leaflet thickness.

Carbonaceous nanomaterials are difficult to observe by electron microscopy due to their low electron density (resulting in low mass-contrast), but can be observed readily using AFM. Spurlin et al. observed that fullerene (C₆₀) nanoparticle aggregates associated with the surface of cationic DMTAP lipid bilayers without inducing changes in lipid packing density (based on phase-transition temperature measurements).¹⁴⁸

In contrast to the negligible effects of fullerene nanoparticles on lipid packing density, Leroueil et al. observed the formation or expansion of defects in DMPC lipid bilayers exposed to a variety of cationic nanoparticles of variable size, charge density, shape, chemical composition, and rigidity using AFM.¹⁴⁹ Their results demonstrate that

cationic nanoparticles present above a threshold concentration disrupt lipid bilayers, suggesting that membrane disruption may be a generalized mechanism of cationic nanoparticle toxicity to cells.

Work by Van Lehn et al. using AFM combined with atomistic simulations and quartz crystal microbalance measurements suggests that nanoparticle insertion into lipid bilayers required the presence of membrane defects, the edges of which acted as the primary binding sites for nanoparticles.¹⁵⁰

AFM has also been used to study nanomaterial interactions with whole cells. Dorobantu et al. acquired AFM images of the bacteria *Pseudomonas aeruginosa* and *Staphylococcus aureus*, the yeast *Saccharomyces cerevisiae*, the alga *Chlorella protothecoides*, and the unicellular flagellate *Euglena gracilis* following exposure to equimolar concentrations of silver nanoparticles or silver nitrate.¹⁵¹ Aliquots of cell suspension were loaded onto glass slides coated with 3-aminopropyltrimethoxysilane, and AFM images were acquired in tapping mode after allowing cells to settle for 60 minutes. The AFM images identified adsorbed nanoparticles on the cell surface and also demonstrated changes in cell morphology and membrane integrity following nanoparticle or chemical exposure. Silver ions and nanoparticles induced the greatest damage in *Euglena gracilis* among the organisms studied; release of silver ion was determined to be the major route of silver nanoparticle toxicity, consistent with previous reports.^{46,47,152,153}

As mentioned above, AFM can probe the physical properties of biological samples, including physical changes induced by exposure to nanomaterials. For example, Liu et al.

used AFM to study changes in *Escherichia coli* and *Bacillus subtilis* morphology and mechanical properties following interaction with single-walled carbon nanotubes.¹⁵⁴ Cell morphology was evaluated by drying cells suspensions on glass slides and acquiring AFM images in tapping mode. Nanotubes accumulated on the cell surface and induced membrane damage, which progressed from increased surface roughness to release of cytoplasm and cell collapse over 2 h. Spring constants of cell surfaces were obtained by measuring force-distance curves of cells immobilized on poly-L-lysine-coated glass slides immersed in saline solution. Nanotube exposure reduced the cell surface spring constant, which the authors speculated may be due to a loss of cell turgor pressure caused by membrane damage and leakage of cytoplasm. Liu et al. showed that well-dispersed single-walled carbon nanotubes can puncture the cell surface of multiple species of bacteria, acting as so-called “nano-darts”.¹⁵⁵ Differences in the relative susceptibilities of bacterial species to puncture by nanotubes were correlated with differences in bacterial surface stiffness, measured by AFM. Force-distance profiles of bacterial cells immersed in aqueous solution showed that gram-negative bacterial cells were stiffer than gram-positive cells, and bacterial activity tests showed that gram-negative cells were also more resistant to puncture by nanotubes.

AFM can also be applied to directly probe the physical interaction between nanomaterials and cells, not just the biological consequences of this interaction. For example, Castrillón et al. functionalized an AFM probe with graphene oxide nanosheets and used force spectroscopy to measure the adhesion force between them and the surface of *Escherichia coli* cells immobilized on a poly-L-lysine-coated glass slide through amine-coupling and

electrostatic attraction (Figure 7).¹⁵⁶ Repulsive forces were observed when the probe approached the cell surface, and were also observed when the probe was pulled off the cell surface. Attractive forces were observed irregularly in pull-off events. The authors acknowledged that immobilized graphene oxide nanosheets cannot change their orientation relative to the cell surface to adopt more energetically favorable orientations, as they can in solution. However, they maintain that physical disruption of the cell membrane is unlikely to be the dominant mechanism of graphene oxide nanosheet toxicity given the overall repulsive interactions observed. They suggest, instead, that graphene oxide-induced oxidative stress, which they demonstrated by measuring glutathione oxidation in the absence of cells, may play a role in toxicity. This suggestion is consistent with previous reports showing that graphene oxide induces oxidative stress in the bacterium *Pseudomonas aeruginosa*¹⁵⁷ and that direct contact between graphene oxide and cells is not a prerequisite for toxicity.¹⁵⁸

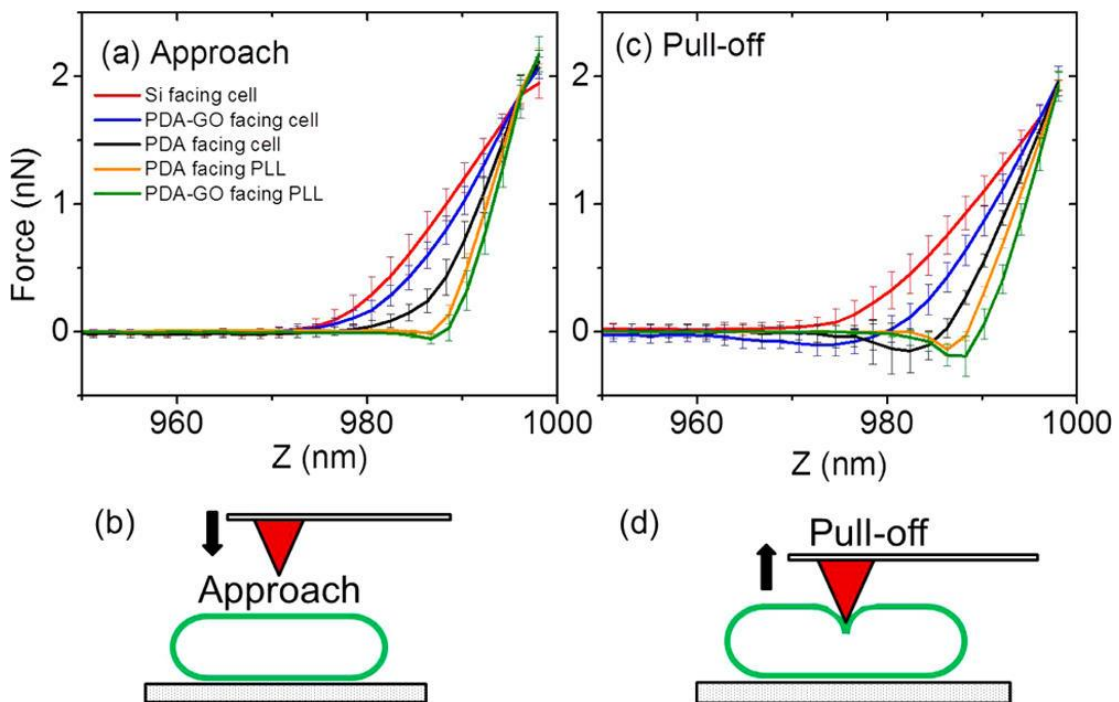


Figure 7. Average force curves for the approach (a) and pull-off (b) of an AFM probe to and from an *Escherichia coli* cell surface as a function of the tip position (Z). Tip position ranges from $Z=0$ (fully retracted probe) to $Z=1\ \mu\text{m}$, at which the maximum force is applied. The top three force curves (red, blue, black) were collected by measuring the interaction force between the cell surface and AFM tips of different surface chemistries; tips were composed of silicon, silicon coated with polydopamine and graphene oxide (PDA-GO), and silicon coated with polydopamine alone (PDA). The bottom two curves (orange, green) were collected by measuring the interaction force between PDA or PDA-GO probe tips and a cell-free, poly-L-lysine (PLL)-coated glass slide. Repulsive interaction (positive adhesive force) was observed between *Escherichia coli* cells and Si, PDA-GO, and PDA probe tips upon approach; in the case of PDA-GO probe tips, the authors suggest that electrostatic repulsion occurs between the negatively charged cell surface and negatively charged carboxylate groups in GO nanosheets, and that steric repulsion occurs between lipopolysaccharides in the cell outer membrane leaflet and GO (a). Some attractive interaction (negative adhesive force) was observed between the PDA-GO probe and the cell surface during pull-off (b), which the authors attribute to lipopolysaccharide molecules bridging the probe and cell surface. Reprinted with permission from Romero-Vargas Castrillón, S.; Perreault, F.; de Faria, A. F.; Elimelech, M. *Environ. Sci. Technol. Lett.* **2015**, 2 (4), 112–117 (ref 156). Copyright 2015 American Chemical Society.

1.5.3 Hyperspectral Imaging. Dark-field microscopy combined with hyperspectral imaging, introduced in Section 1.1, has been used to rapidly detect engineered nanomaterials bound to or internalized by cells and organisms with minimal sample preparation. For example, Pratsinis et al. acquired dark-field micrographs of murine macrophages exposed to silver nanoparticles and measured the extinction spectrum from 400-1000 nm within each pixel of the dark-field image using the Cytoviva® imaging system.¹⁵⁹ Visible-near-infrared spectra indicated partial nanoparticle agglomeration upon internalization by cells. Though hyperspectral imaging has been most-frequently employed to study noble metal nanoparticles, carbonaceous nanomaterials have also been studied by this technique. For example, Smith et al. used Cytoviva® dark-field and hyperspectral imaging to observe single wall carbon nanotube uptake into circulating mouse blood cells following nanotube injection into the mouse tail vein.¹⁶⁰ Additional flow cytometry experiments showed that nanotube uptake occurred selectively in Ly-6C^{hi} monocytes over other blood cells, and intravital microscopy showed that monocytes delivered nanotubes to the tumor site. Schwab et al. also used Cytoviva® dark-field and hyperspectral imaging to observe carbon nanotube attachment to the surface of *Chlorella vulgaris* algal cells; no spectral matches for nanotubes were observed in the cell interior, suggesting no nanotube uptake by cells.¹⁶¹ Mortimer et al. recently assessed the capability of the Cytoviva® dark-field and hyperspectral imaging system to detect and quantify the uptake of a variety of nanomaterials (including Ag, Au, CuO, and TiO₂ nanoparticles and CdSe/ZnS core-shell quantum dots) into a model organism (the protozoan *Tetrahymena thermophila*).¹⁶² Reference spectra of each nanoparticle type were acquired after

suspending nanoparticles in a solution containing extracellular substances isolated from the protozoan culture; this was done to account for the potential effects of nanomaterial transformations upon incubation with cells on nanoparticle spectral features.

Hyperspectral images of cells exposed to each nanoparticle type were then compared to the corresponding nanoparticle reference to detect internalized nanoparticles. In all cases, internalized nanoparticles were detected; false-positives (i.e., detection of nanoparticles in unexposed cells) were observed only in the case of TiO₂ nanoparticles, whose spectral features were similar to those of protozoan cells. In cases where nanoparticles showed sufficiently distinct spectral profiles (as was observed for, e.g., CdSe/ZnS quantum dots and Ag nanoparticles), hyperspectral imaging was able to discriminate between two nanoparticle types simultaneously internalized by cells. While the diffraction-limited spatial resolution of dark-field microscopy presents challenges for characterizing nanomaterial interactions with small cells, such as bacteria, or sub-cellular features, Badireddy et al. have demonstrated the ability to observe silver nanoparticle localization near the surface of the bacterium *Pseudomonas aeruginosa* using the Cytoviva® dark-field and hyperspectral imaging system; in this case, the nanoparticle localization at cell surfaces was confirmed using scanning electron microscopy.²⁴ Though the Cytoviva® imaging system has been the most commonly used hyperspectral imaging system in the nanotoxicity literature, alternative systems are available; the features and capabilities of commercially available systems have recently been compiled by Roth et al.²²

1.5.4 Super-resolution light microscopy techniques are not constrained by the diffraction limit of light. Since they do not require ultra-high vacuum conditions, they can be used to image cells in the hydrated state. These techniques are inherently fluorescence-based, and they typically rely on the selective excitation of fluorophores within a sub-diffraction-limited area (e.g., stimulated emission depletion [STED] microscopy), calculation of the center of the point-spread-function of individual, photo-switchable fluorophores (e.g., stochastic optical reconstruction microscopy [STORM]), or interaction of a sample with structured light, producing interference patterns that contain sub-diffraction-limited information (e.g., structured illumination microscopy [SIM]).

Limitations to the use of super-resolution microscopy in nanotoxicology research are that the instrumentation is not widely available and that the nanomaterials and some feature of the biological system must be fluorescent and distinct from one another. However, some nanomaterials of interest to the nanotoxicology community have inherent fluorescence and have been successfully imaged using super-resolution methods. These materials include nanodiamond incorporating nitrogen-vacancy centers¹⁶³ as well as carbon quantum dots¹⁶⁴ and CdSe/ZnS core-shell quantum dots.¹⁶⁵ Leménager et al. used STED to determine the location of 5 nm luminescent carbon dots within fixed and living MCF-7 breast cancer cells with more than six-times greater spatial resolution than confocal microscopy.¹⁶⁴ Szymanski et al. used SIM to observe fluorescently labeled lysosomes within hydrated, fixed mouse alveolar epithelial cells with 120-130 nm lateral resolution (see Figure 6).¹⁴¹ Images of lysosome locations were overlaid with STXM images of intracellular CeO₂ nanoparticles, as described in a preceding section of this review. The

oxidation state distribution of nanoparticles within lysosomes was overall similar to that of nanoparticles within cells outside of lysosomes; this result suggests that the overall reduction of nanoparticles observed upon internalization by cells occurred via a mechanism upstream from movement into lysosomes. In addition to locating nanomaterials within cells, super-resolution microscopy can provide novel insight into the structure of biological systems in the context of nanotoxicology research. For example, Melby et al. used SIM to observe formation of lipid-ordered and lipid-disordered domains in supported lipid bilayers containing unlabeled and fluorescently labeled phospholipids, sphingolipid, and cholesterol.¹⁶⁶ Bilayers containing phase-segregated lipid domains were then exposed to gold nanoparticles and studied by quartz-crystal microbalance with dissipation monitoring (vide infra) to determine the influence of these domains (representative of those present in eukaryotic cells) on nanoparticle attachment to membranes. Bilayers containing ordered lipid domains showed greater cationic gold nanoparticle association than those lacking lipid ordered domains under high ionic strength conditions.

1.5.5 Spectroscopy. Intrinsic spectroscopic methods have been applied to study the interactions of nanoparticles with a range of biological systems, including whole organisms, cells, and model cell membranes (i.e., supported lipid bilayers). As label-free probes of biomolecule structure, spectroscopic techniques have advantages over cytotoxicity assays that employ colorimetric or fluorescent dyes to assess cell membrane integrity, metabolic activity, or oxidative stress. Such assays are subject to interference

by nanoparticle interactions with dyes or dye products, as discussed previously in this review.

1.5.6 Sum frequency generation (SFG) is a nonlinear optical process sensitive to asymmetric matter.¹⁶⁷ SFG spectroscopy has been applied to selectively probe the chemical environment at many types of asymmetric interfaces, including the interface of biological membranes and nanomaterials in the context of nanomaterial toxicity research. Doğangün et al. used SFG to detect changes in the structure of phospholipid membranes exposed to lithium-intercalating nanomaterials, which are used as cathode materials in lithium-ion batteries.¹⁴⁶ When phospholipid bilayers composed of mixtures of zwitterionic and anionic lipids were exposed to LiCoO₂ nanosheets, the SFG intensity of a methyl symmetric stretch in lipid acyl chains increased. Control experiments were performed using bilayers composed of various ratios of these lipids. Together, these experiments suggested that bilayer exposure to LiCoO₂ nanosheets (which had positive or near-neutral zeta-potentials depending on their lithiation state) caused negatively charged lipids to preferentially move to the leaflet closer to the particles, increasing bilayer asymmetry and enhancing SFG signal intensity. In contrast, phospholipid bilayers exposed to a related lithium-intercalating nanosheet with a negative zeta-potential, LiNi_{1/3}Mn_{1/3}Co_{1/3}O₂, showed no changes in SFG intensity.

Troiano et al. probed the association of gold nanoparticles with zwitterionic supported lipid bilayers as a function of nanoparticle charge and solution ionic strength by using resonantly enhanced second harmonic generation (SHG), a special case of SFG where

photons of identical frequency combine to produce photons of twice the frequency.¹⁴⁶ By monitoring the enhancement of SHG intensity at the bilayer-solution interface, they demonstrated that while Coulombic interactions largely determine the overall magnitude of nanoparticle association to bilayers, particle-bilayer interaction strength is largely independent of particle charge, indicating a likely role of multivalent interactions.

1.5.7 Raman spectroscopy can probe the molecular environment of biological systems under hydrated conditions since water has a low Raman scattering cross-section and, thus, contributes little interfering signal to analytes in water. Candeloro et al. used Raman spectroscopy to individually analyze un-fixed, live HeLa cells directly injected with Ag and Fe₃O₄ nanoparticles, achieving a spatial resolution of approximately 1 μm (based on the laser spot size).¹⁶⁸ Direct injection into HeLa cells was used to avoid nanoparticle transformations, such as aggregation and protein adsorption, which can occur in biological exposure media and may impact biological response. Following multivariate statistical analysis, distinctions between control and nanoparticle-treated cell populations were attributed to biochemical changes induced by oxidative stress (i.e., decreased concentrations of glycogen and fructose-6-phosphate in cells exposed to nanoparticles). Raman spectroscopy can also be employed to track nanomaterial localization within cells. Shah et al. used confocal Raman microscopy to dynamically monitor gold nanoparticle uptake into human prostate cancer LNCaP pro5 cells with approximately 250 nm lateral resolution and 500 nm vertical resolution.¹⁶⁹ Using this method, Raman spectra were acquired as a laser scanned across a sample mounted on a glass slide placed in modified

confocal microscope; an image was then created by mapping the intensity of chosen Raman lines among the pixels in the sampled area. Gold nanoparticles were detected by monitoring the photoluminescence arising from laser excitation. Cellular features were detected by monitoring a Raman-active C-H stretching mode, used as a generic reporter of organic material. Images collected 2, 12, and 24 h after incubating cells with nanoparticles showed increasing nanoparticle uptake and movement towards the nucleus, whose position within the cell was inferred from contrast in Raman signal intensity relative to the rest of the cell.

Raman spectroscopy has also been used to detect carbonaceous nanomaterials. For example, Lamprecht et al. used confocal Raman microscopy to locate double-walled carbon nanotubes within human urinary bladder carcinoma cells with lateral resolution of 259 nm (based on the Rayleigh criterion) and vertical resolution of about 1 μm .¹⁷⁰ The intracellular location of carbon nanotubes was mapped without the use of chemical labels (e.g., fluorescent labels) by monitoring their Raman-active G mode (Figure 8). Cellular features were also identified and mapped by tracking Raman-active C-H stretching modes. Images showed that carbon nanotubes preferentially localized near the cell nucleus, which was distinguished from surrounding cell material by its higher C-H mode Raman signal intensity.

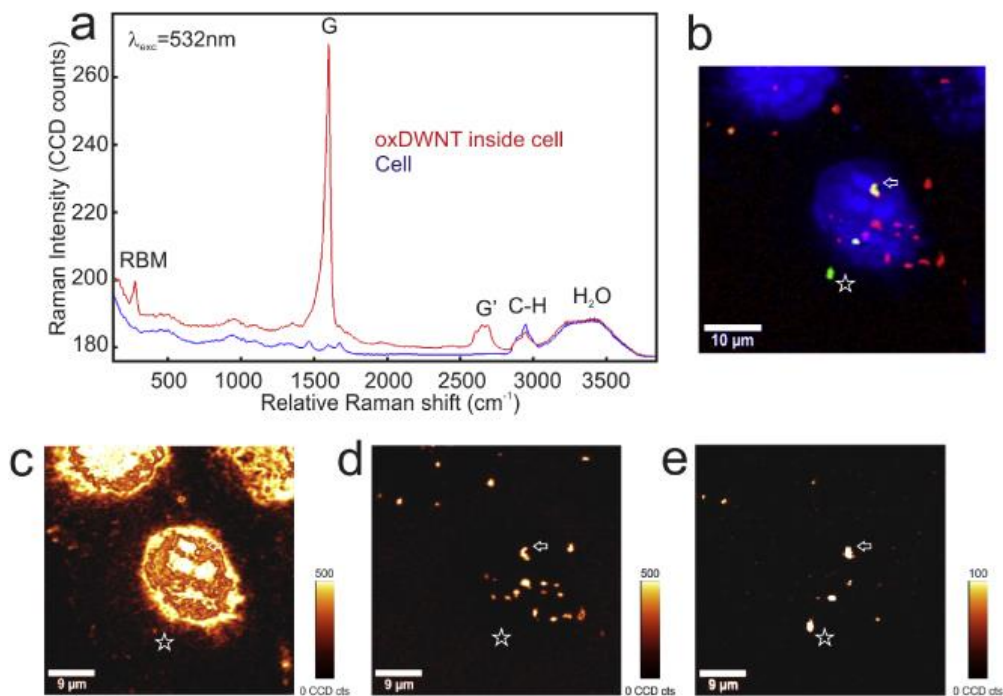


Figure 8. Raman spectra and intensity maps of fixed epithelial urinary bladder carcinoma cells exposed to oxidized double walled carbon nanotubes. Internalized nanotubes were detected using the G' vibrational mode of C-C bonds, though the radial breathing mode (RBM) was observed in some cases (a). Cellular material was identified using a C-H bond stretching mode at $\sim 3000\text{ cm}^{-1}$ shift, which was present in both cellular material (e.g., lipids) and in nanotubes (a). A spectral intensity map was produced by integrating the C-H peak intensity (blue), G' peak intensity (red), and RBM peak intensity (green); overlapping G' and RBM peaks appear yellow (b). Using the same field of view used in panel b, spectral intensity maps of C-H, G', and RBM, respectively, were produced (c-e). Reprinted with permission from Lamprecht, C.; Gierlinger, N.; Heister, E.; Unterauer, B.; Plochberger, B.; Brameshuber, M.; Hinterdorfer, P.; Hild, S.; A Ebner. *J. Phys. Condens. Matter* **2012**, 24 (16), 164206 (ref 170). © IOP Publishing. Reproduced with permission. All rights reserved.

Higher-spatial-resolution Raman methods are needed to probe nanoparticle interactions with smaller biological systems (e.g., microorganisms, organelles) and to distinguish local from distributed effects of nanoparticles on the chemical signatures of biological systems. Raman spectra of biomolecules have been collected with sub-diffraction-limited spatial resolution (20 nm) by applying stochastic reconstruction methods (also applied in super-resolution fluorescence microscopy¹⁷¹) to temporal fluctuations of surface-enhanced Raman scattering (SERS) signal intensity.¹⁷² Further development of sub-diffraction-limited Raman spectroscopy will enable more widespread application of this technique to the study of biological systems.

1.5.8 ATR-FTIR spectroscopy. Infrared spectroscopy provides complementary information to Raman spectroscopy, since it is sensitive to some non-Raman-active molecular vibrations; however, it suffers from interference in aqueous environments due to the large infrared absorption by water. To study biological systems under hydrated conditions using infrared spectroscopy, an ATR crystal can be used to probe a small depth into a sample (described in more detail in Section 1.2) and limit interference of bulk water. Li et al. used ATR-FTIR to assess the impacts of carbon-based nanomaterials, including C₆₀, multi-walled carbon nanotubes (MWCNTs), and single-walled carbon nanotubes (SWCNTs), on both MCF-7 breast cancer cells¹⁷³ and zebrafish.¹⁷⁴ Cancer cells were exposed to low concentrations (0.0025 to 0.1 mg/L) of MWCNTs, and changes in cellular lipid, protein, and DNA/RNA structure were assessed.¹⁷³ Nanomaterial-

induced damage to cell membrane components was suggested as a major route of toxicity, as protein and lipid spectral regions were most significantly altered. Raman spectroscopy was used in parallel with ATR-FTIR to quantify the ratio of oxidized cysteine to total protein in the cancer cells, a marker of oxidative stress. Short MWCNTs induced greater oxidative stress in cancer cells than did long MWCNTs. Zebrafish exposed to carbon nanomaterials showed altered lipid-to-protein ratios (probed by ATR-FTIR) and lipid unsaturation levels (probed by Raman spectroscopy) in various tissues, including the brain and gonads, demonstrating that these materials can exert system-wide stress.¹⁷⁴

1.5.9 Laser-induced breakdown spectroscopy (LIBS) was used by Sancey et al. as a label-free method to locate and quantify gadolinium-based nanoparticles in whole mouse kidneys.¹⁷⁵ Given its general detection scheme based on atomic emission, LIBS can be applied to study nanomaterials with any chemical composition. However, LIBS is inherently destructive, and its low spatial resolution (reported by Sancey et al. to be 10 μm) makes it applicable only for very large biological systems, such as whole organs.

1.5.10 Electron paramagnetic resonance (EPR) spectroscopy (also referred to as electron spin resonance). Generation of reactive oxygen species (ROS) and the oxidative damage they subsequently induce is a frequently described mechanism of nanomaterial toxicity to living organisms. Nanomaterial-induced ROS generation is frequently monitored *in vitro* and *in vivo* using fluorescence imaging (e.g., using ROS

probes such as dichlorofluorescein diacetate¹⁷⁶⁻¹⁷⁹), but this approach can suffer from signal interference due to probe interactions with nanomaterials and components of complex biological matrices, complicating quantitative analysis. EPR spectroscopy provides a more quantitative means to detect free radicals, a category into which many ROS, including $O_2^{\cdot-}$ and HO^{\cdot} fall, as this method is less susceptible to matrix interference.¹⁸⁰ EPR spectroscopy detects short-lived free radicals that have been trapped as longer-lived spin-adducts through reaction with spin-trapping agents such as nitrones.¹⁸¹ Yin and coworkers have recently reviewed the application of EPR spectroscopy to quantify ROS production from nanomaterials.¹⁸²

Perelshtein et al. used EPR spectroscopy to measure free radical production in water by commercial and sonochemically prepared CuO and ZnO nanoparticles, and correlated free radical production with nanoparticle toxicity to bacterial cells and human alveolar epithelial cells.¹⁸³ These authors observed increased generation of free radicals by nanoparticles incorporating more defects in their crystal structure, and overall higher toxicity of nanoparticles with more defects. Ahlberg et al. used EPR spectroscopy to measure intracellular free radical production by Ag nanoparticles in human keratinocyte cells.¹⁸⁴ In this study, Ag nanoparticles were stored under air or argon prior to use; storage under argon reduces their oxidative dissolution to Ag^+ . Lower free radical production was observed by particles stored under argon, suggesting nanoparticle dissolution induced intracellular ROS production.

Though free radical production is a widely cited source of nanomaterial toxicity, chemically inert nanomaterials are less likely to produce free radical species; for

example, Nelson et al. observed no formation of free radicals from NIST gold nanoparticle reference materials with diameters of 10, 30, and 60 nm either alone, in the presence of DNA, or after UV-irradiation.¹⁸⁵ Some nanoparticles are also capable of scavenging free radical species through redox reactions. Dunnick et al. used EPR spectroscopy to measure free radical scavenging by CeO₂ nanoparticles with different valence state ratios (Ce³⁺/Ce⁴⁺) in both cell culture media and in the presence of rat alveolar epithelial cells.¹⁸⁶ They observed decreased radical scavenging with increasing doping of Gd₂O₃ into the nanoparticles, where doping was suggested to decrease the particles' ability to transition between the Ce³⁺ and Ce⁴⁺ states. This result suggests that the radical scavenging capacity of CeO₂ nanoparticles is determined by their ability to transition between valence states. In a related study, Celardo et al. showed that doping CeO₂ nanoparticles with Sm decreased their radical scavenging capacity. Since Sm doping decreased the Ce³⁺ concentration, this result suggests that redox reactions between Ce³⁺ and Ce⁴⁺ were key to nanoparticle radical scavenging capacity.¹⁸⁷

1.5.11 Mass spectrometry methods differ greatly in their spatial resolution, with significant consequences for their applications in nanomaterial toxicity research.

Electrospray ionization mass spectrometry methods require that chemically heterogeneous samples be chromatographically separated prior to analysis. In the context of biological samples (e.g., cells, tissues, or organisms exposed to nanomaterials), this requirement severely limits spatial resolution, since samples must be homogenized and species of interest extracted prior to analysis. Despite low spatial resolution, chemical

labeling methods can be employed to selectively monitor species of interest to the nanomaterial-biological interface. For example, Nelson et al. used isotope-dilution LC-MS/MS to quantify the formation of oxidatively induced DNA lesions in both HepG2 cells (a human liver carcinoma cell line) and calf thymus DNA exposed to Au nanoparticles.¹⁸⁵ Four ¹⁵N-labeled nucleosides served as stable isotope standards, and subsequent quantification of natural DNA lesions relative to their labeled counterparts revealed no significant lesion formation induced by nanoparticle exposure. The gold nanoparticles used here may therefore serve as negative nanoparticle controls for toxicity studies targeting DNA damage. The authors note that mass spectral techniques have significant advantages over more commonly used DNA damage assays (e.g., the comet assay), in particular their ability to discriminate between multiple DNA lesions and to avoid interference from the presence of nanoparticles. We note that the much greater expense of mass spectrometry analysis over that of commercially available assays can present a barrier to the application of this technique.

Like electrospray ionization mass spectrometry methods, inductively coupled plasma mass spectrometry (ICP-MS) lacks spatial resolution. However, ICP-MS remains one of the most common means to quantify nanoparticle internalization into cells and tissues (along with related methods coupling an optical detector to an inductively coupled plasma source). Recent advancements in this technique have permitted single particle detection (see also Section 1.1). Single particle ICP-MS provides a more quantitative means to characterize nanoparticle uptake into cells and tissues and nanoparticle transformations (i.e., aggregation and dissolution) within biological environments than

microscopy techniques. Dan et al. used single particle ICP-MS to monitor gold nanoparticle uptake by tomato plants while simultaneously monitoring nanoparticle size distribution and dissolved gold concentration.¹⁸⁸ Nanoparticles were extracted from plant tissue by treatment with macroenzyme R-10, which was shown to have no significant impact on nanoparticle size and dissolution state. Uptake into plant tissue had no significant effect on nanoparticle size distribution following four day's exposure, and no significant oxidation of nanoparticles to Au ions was observed. Single particle ICP-MS has also been used to determine gold nanoparticle uptake by *Caenorhabditis elegans*, using tetramethylammonium hydroxide to extract nanoparticles from biological material.¹⁸⁹

Scanlan et al. applied single particle-IPC-MS to quantify silver nanowire uptake by *Daphnia magna* and to analyze the length and dissolution state of the nanowires.¹⁹⁰ *Daphnia* hemolymph was removed with a needle syringe and analyzed directly. Internalized silver nanowires were distinguished from dissolved silver by setting an intensity cut-off. A silver signal that occurred as a distinct spike was considered indicative of nanowires while a silver signal that was approximately constant was considered indicative of dissolved silver. Particulate silver was observed in all *Daphnia* samples exposed to silver nanowires; *Daphnia* receiving higher nanowire concentrations also contained significant concentrations of dissolved silver. Preferential uptake of shorter nanowires was observed by calculating the nanowire size-distribution resulting from ICP-MS-measured silver count rates.

Laser ionization methods, which have become more common over the past thirty years, can ionize select areas of a sample, and when coupled with mass spectral detection, can provide sufficient spatial resolution to locate nanomaterials within some biological systems. Spatial resolution is determined by the laser spot size and is typically single or tens of micrometers. Time of flight mass spectrometers are commonly used,^{191–194} though the laser ionization source can also be coupled to an ICP-MS.^{143,195} Laser desorption/ionization mass spectrometry (LDI-MS) can be used in an imaging format by rastering the incident laser beam across the sample of interest; this method has been used to detect and analyze many types of nanomaterials in cells and tissues, including carbon-based nanomaterials, where anionic carbon clusters containing 2-10 carbon atoms have been detected as markers for larger carbon nanomaterials,¹⁹¹ as well as gold and silver nanoparticles.^{143,193,195} LDI-MS has also been used in a non-imaging platform to detect nanoparticles extracted from cell lysates. In a handful of studies, ionizable ligands on the nanomaterial surface have been detected in place of the core material. So-called “mass barcodes” (commonly thiol-containing molecules) attached to the nanoparticle surface allow nanoparticles of the same core material but different surface chemistries to be distinguished.^{192–194}

Laser-secondary neutral mass spectrometry (laser-SNMS) is a useful tool for elemental- and molecular-level analysis in complex biological samples^{196,197} and holds promise for analysis of nanomaterial distribution in cells and tissues. Related to ToF-SIMS, introduced in Section 1.2.1, laser-SNMS also relies on sputtering a sample surface with an energetic ion beam; neutral atoms and molecules liberated from the surface are

subsequently ionized using a laser beam and are then mass analyzed.¹⁹⁶ The tunable penetration depth of the ion beam used in both SNMS and SIMS provides selectivity for the chemical environment at surfaces, making these techniques capable of probing the chemical environment at the interface of nanomaterials with cell membranes without the need for labels. Haase et al. used laser-SNMS to quantify silver nanoparticle uptake by human macrophages, while simultaneously imaging the spatial distribution of extracellular sodium and intracellular carbon and silver.¹⁹⁸ The authors also performed complementary confocal Raman microscopy characterization in an effort to maximize quantitative and qualitative information on nanoparticle distribution. Laser-SNMS was performed on cryogenically prepared cells, and resolved nanoparticle localization to within 100 nm. Confocal Raman required less sample preparation but achieved resolution of 400-500 nm for the silver nanoparticles. In parallel with SNMS analysis, the authors used ToF-SIMS as a label-free method to observe silver nanoparticle-induced changes in human macrophage membrane lipid composition, characteristic of oxidative stress and altered membrane fluidity. Three-dimensional images of cellular chemical composition were obtained by successively removing layers of biological material using ion sputtering.

1.5.12 Gravimetric Analysis. Quartz crystal microbalance with dissipation (QCM-D) has been used within the nanotoxicology community to study the interactions of nanomaterials with biological species ranging from collagen¹⁹⁹ to supported lipid bilayers^{14,146,200,201} to whole cells.²⁰² Based on the reverse piezoelectric effect in a quartz

crystal, addition of mass to the crystal decreases its resonance frequency, providing a label-free mechanism to detect, for example, nanoparticle adsorption to a biological species immobilized on the crystal surface. Most commonly, a supported lipid bilayer or whole cells are immobilized on the surface of a quartz crystal present in a flow cell, and nanomaterials are introduced in fluid flow. Mass addition to the crystal surface, via association with the immobilized biological material, is observed by a decrease in the crystal resonance frequency, and changes in the viscoelastic properties of biological material can be simultaneously observed by monitoring changes in the frequency dissipation. Some QCM-D instruments have the capacity to monitor frequency and dissipation changes at multiple harmonics. Since the penetration depth of the shear wave resulting from the crystal resonance is dependent on the harmonic number, such instruments allow the distance-dependence of nanoparticle-biological interactions to be probed. . In the nanotoxicology literature, QCM-D has been most commonly applied to study nanomaterial interactions with supported lipid bilayers, which serve as simplified models of biological membranes.

For example, Karlsson et al. studied the toxicity of copper-based nanoparticles (Cu, CuO, and Cu-Zn alloy nanoparticles) towards alveolar epithelial cells and red blood cells using standard cytotoxicity assays (Trypan blue and hemolysis assays) while also measuring nanoparticle adsorption to mixed lipid bilayers containing the lipids POPC and POPS or POPG using QCM-D.¹⁴ The more cytotoxic nanoparticles (Cu and Cu-Zn) induced small negative changes in frequency, indicating mass association to the bilayers, while the less cytotoxic nanoparticle (Cu) induced larger positive changes in frequency, indicating loss

of mass from the bilayer. The authors attributed this mass loss to lipid extraction from the membrane as a result of adsorption to the nanoparticle. By correlating lipid bilayer studies with cellular toxicity studies, the authors suggest that nanoparticle-induced oxidative stress (the suspected source of Cu and Cu-Zn nanoparticle toxicity) was more damaging under these conditions than lipid extraction by nanoparticles.

In another study, Jacobson et al. used QCM-D to detect gold nanoparticle association to supported lipid bilayers prepared from POPC and lipopolysaccharides, a component of the gram-negative bacterial cell membrane.²⁰¹ Nanoparticle association increased with lipopolysaccharide concentration in the bilayer and association was greater on a per-molecule-basis for lipopolysaccharides bearing long saccharide chains than short saccharide chains (Figure 9 a, b). Parallel studies using bacterial cells with variable LPS content also showed that nanoparticle association depended directly on lipopolysaccharide concentration in the cell membrane, suggesting a key role for this species in mediating bacterial cell-nanoparticle interactions (Figure 9 c).

QCM-D can be combined with impedance spectroscopy to probe the electrochemical behavior of supported lipid bilayers. For example, Mu et al. used electrochemical impedance spectroscopy to study ion transport through lipid bilayers exposed to silica nanoparticles.¹³⁸ No change in ion transport was observed, suggesting that membrane integrity was unaffected by the irreversible nanoparticle adsorption observed in QCM-D experiments. However, based on a parallel experiment that showed leakage of fluorescent dye from dye-encapsulating liposomes following nanoparticle exposure, the authors

suggested that silica nanoparticle adsorption to the membrane induced transient pore formation.

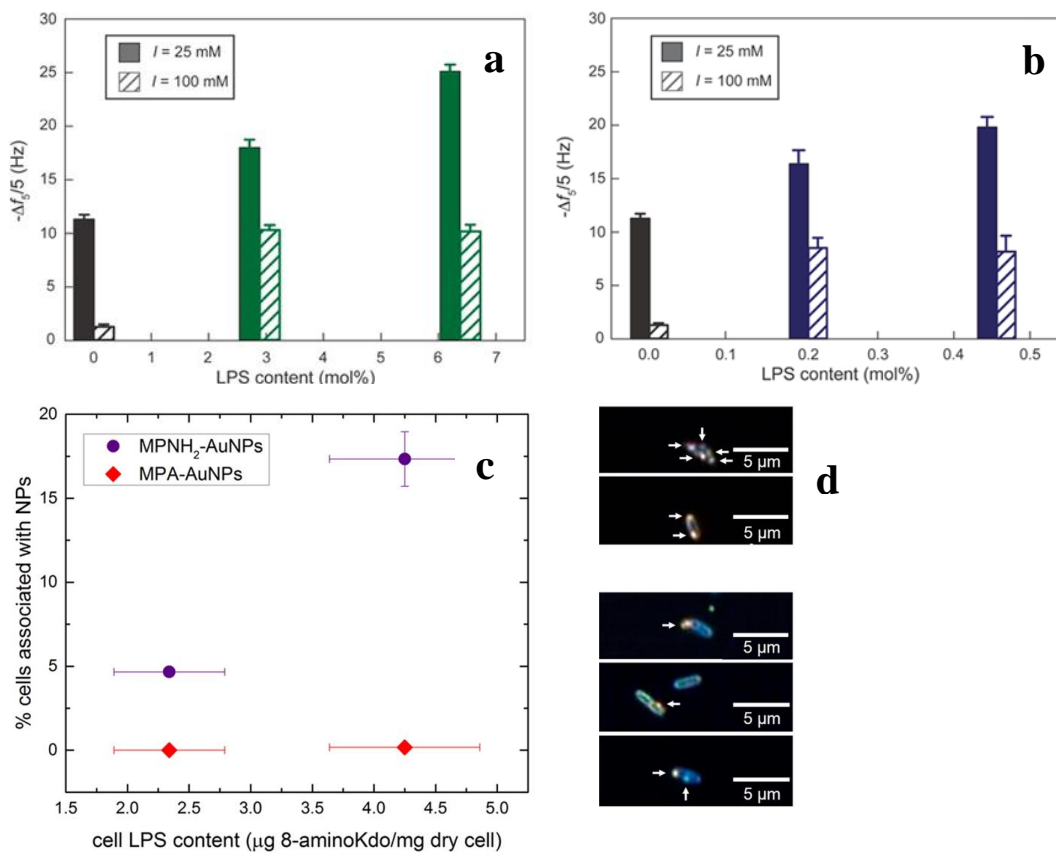


Figure 9. Association of cationic gold nanoparticles to POPC lipid bilayers containing variable lipopolysaccharide content was monitored using QCM-D (a, b). Nanoparticle association to the bilayer is indicated by negative frequency shifts for the 5th harmonic ($\Delta f_5/5$). Bilayers contained either rough lipopolysaccharide (a), which bears a short polysaccharide chain, or smooth lipopolysaccharide (b), which bears a long polysaccharide chain. Experiments were performed using solution conditions of either 25 or 100 mM total ionic strength. Association of cationic (purple) and anionic (red) gold nanoparticles to live bacterial cells (*Shewanella oneidensis* MR-1) was monitored as a

function of cell surface lipopolysaccharide content using flow cytometry (c).

Nanoparticle association to cells was confirmed visually using the CytoViva®

Hyperspectral microscope, where arrows indicate cell-associated material that was a spectral match for gold nanoparticles (d). Reprinted with permission from Jacobson, K.

H.; Gunsolus, I. L.; Kuech, T. R.; Troiano, J. M.; Melby, E. S.; Lohse, S. E.; Hu, D.;

Chrisler, W. B.; Murphy, C. J.; Orr, G.; Geiger, F. M.; Haynes, C. L.; Pedersen, J. A.

Environ. Sci. Technol. **2015**, *49* (17), 10642–10650. (ref 201). Copyright 2015 American Chemical Society.

QCM-D has been less-commonly applied to probe interactions of nanomaterials with whole cells. In one study, Wang et al. observed phagocytosis and later expulsion of large polystyrene beads (800 nm diameter) by macrophages immobilized on a QCM-D sensor in real-time.²⁰² Concentration-dependent frequency responses were observed when macrophages were exposed to SWCNTs, and these could be used to distinguish between nanomaterial exposure conditions that triggered no response, stress-response and recovery, and cellular toxicity (i.e., apoptosis).

1.6 Nanomaterial-Induced Changes in Physiological Processes

Developing a complete understanding of nanomaterial toxicity requires that the impacts of nanomaterials on the biomolecular components of cells, considered in Section 1.5 (Interactions of Nanomaterials with Biological Systems), be considered in parallel with their system-wide impacts on physiological function. Perturbations to processes such as

DNA replication, protein biosynthesis, and exocytosis can have significant consequences for cell or organism health and should be understood to ensure the responsible use of engineered nanomaterials. Understanding nanomaterial effects on physiological processes can also provide further insight into the mechanisms underlying nanomaterial-induced toxicity. Analytical methods adopted from areas within the chemical and biological sciences are enabling investigations of nanomaterial perturbations to physiological processes across a range of organismal complexity, from single-celled organisms like bacteria to primary human cells lines and multicellular organisms like water fleas. Linking nanomaterial impacts on physiological function to underlying mechanisms of toxicity remains a major challenge for the nanotoxicity research community.

1.6.1 Electrochemical. In this section, we will discuss the applications of electrochemical methods for evaluating nanomaterial toxicity, a topic that has also been reviewed by Özel et al.²⁰³

Electrical impedance monitoring provides a continuous, real-time, label-free approach for measuring cellular proliferation, motility, permeability, and metabolism.²⁰⁴ Cells in contact with conductive materials (e.g., microelectrodes placed in a culture dish) act as capacitive elements and increase electrical impedance proportionally to their extent of contact with the electrode.²⁰⁵ Hondroulis et al. developed a chip-based electrical impedance measurement array to quantify the toxicity of gold, silver, and cadmium oxide nanoparticles and single-walled carbon nanotubes to human lung fibroblasts and rainbow trout gill epithelial cells.²⁰⁶ An array of gold electrodes installed on the chip allowed

multiple cytotoxicity experiments to be run simultaneously. In their studies, cadmium oxide and silver nanoparticles more significantly decreased cell proliferation rates than did gold nanoparticles and single-walled carbon nanotubes, indicated by lower impedance values when tracked over time. In another study, Zhu et al. used a similar device to observe rates of mouse epithelial cell detachment from electrodes (due to necrosis) following the introduction of copper (II) oxide, cadmium oxide, and titanium dioxide nanoparticles.²⁰⁷ The highest rate of detachment was observed after exposure to copper (II) oxide, where the measured impedance returned to baseline values observed in the absence of cells after about 25 h exposure. Exposure to cadmium oxide and titanium oxide nanoparticles induced lower, but still significant, cell detachment.

In addition to home-built devices, commercially available electrical impedance measurement systems have also been used to study nanomaterial toxicity. Cimpan et al., using the xCELLigence Real Time Cell Analyzer Dual Plate instrument, observed a small decrease in the proliferation rate of mouse fibroblasts exposed to TiO₂ nanoparticles.²⁰⁸ These results were in agreement with those obtained using two traditional toxicological measurements (Trypan Blue staining and optical microscopy), which also indicated a small cytotoxic effect. Chuang et al. also used the xCELLigence system to quantify gold nanorod toxicity to six mammalian cell lines, and compared results to those obtained using conventional *in vitro* cytotoxicity assays (including MTS and Trypan blue viability assays and apoptosis and cell-division assays).²⁰⁹ Impedance-based and conventional cytotoxicity measurements both suggested that gold nanorods were toxic to cells; IC₅₀ values (indicating the nanoparticle concentration inducing a 50% decrease in cell

viability) measured using impedance and MTS assays were similar for some nanoparticle-cell combinations, while others gave values differing by up to a factor of 3.5. Impedance-based measurements were readily made across all cell lines employed, while some conventional cytotoxicity assays were not compatible with all cell types.

Giaever and Keese were the first to report on impedance-based measurements of the motility of healthy, adherent cells using a cell-covered electrode operating at a fixed AC frequency.²¹⁰ Variability in impedance over time is observed for healthy cells as they undergo metabolically driven shape changes and cell-cell junction distance changes; a decrease in impedance variability over time indicates cellular toxicity. Tarantola et al. were the first to apply this principle to study nanomaterial toxicity.^{211,212} In one study, the authors exposed MDCK II epithelial cells adhered to an electrode to CdSe/ZnS quantum dots, CTAB-coated gold nanorods, and polyethylene glycol-coated gold nanorods and monitored cell motion.²¹¹ Dose-dependent decreases in cell motion were observed for cells exposed to quantum dots and CTAB-coated gold nanorods, indicating nanoparticle toxicity, while polyethylene glycol-coated gold nanorods had a smaller and less dose-dependent effect on cell motion. Cell motion was suggested to be a more sensitive test of cell viability than a commonly used cytotoxicity assay (MTS-assay), since reduction of cell viability was seen at lower nanoparticle exposure concentrations with the former than the latter. Cell motion measurements were continuous, in contrast to many conventional cytotoxicity assays that probe toxicity only at discrete time points, enabling dynamic characterization of nanoparticle toxicity to cells.

Electrochemical impedance spectroscopy, in which electrical impedance is monitored as a function of frequency, has been applied by Zhang et al. to study the mechanism of silica nanoparticle interaction with DOPC lipid monolayers as a function of nanoparticle size.²¹³ Hydrophobic lipid tails were shown to physically associate with the surface of a mercury electrode at its point of zero charge, forming a lipid monolayer. As the electrode potential was made more negative, lipids began to desorb from the electrode; some remained within the Debye length of the electrode and could be electrochemically probed. Complex capacitance plots of the lipid desorption process indicated that smaller silica nanoparticles (18 nm diameter) more significantly stabilized lipids during desorption than did larger silica nanoparticles (182 nm diameter). In parallel studies, these authors performed confocal imaging and fluorescence recovery after photobleaching measurements on DOPC giant unilamellar vesicles. Their results demonstrated that smaller silica nanoparticles decreased the average lipid diffusion rate within the vesicles and induced vesicle hole formation, while larger silica nanoparticles increased the average lipid diffusion rate and extracted lipids from the membrane, wrapping the nanoparticle in lipids and leading to vesicle breakdown. These combined results were interpreted to mean that the process of wrapping membrane lipids around smaller nanoparticles is restricted by a larger energy barrier than exists for larger nanoparticles which have a lower surface curvature. Consequently, smaller particles, rather than extracting lipids from the membrane and becoming wrapped, would be expected adsorb to the membrane surface through van der Waals and electrostatic

interactions, increasing lateral tension within the membrane and leading to membrane stress-fractures, or holes.

Voltammetry has been adapted to study the impacts of nanomaterial exposure on living cells and organisms. Microelectrodes (approximately 10 μm in diameter) have been used to selectively probe electrochemical activity within tissues. Özel et al. exposed zebrafish embryos to CeO_2 nanoparticles and monitored the concentration of serotonin, a neurotransmitter involved in motility and digestive function, in the intestine using implanted carbon fiber microelectrodes and differential pulse voltammetry.²¹⁴ Intestinal serotonin levels decreased with multi-day exposure to 20-50 ppm of CeO_2 nanoparticles, likely due to depletion of serotonin from tissues by adsorption to the nanoparticle surface. Correlated *in vitro* experiments using UV-vis and FT-IR spectroscopies indicated that serotonin had adsorbed to the nanoparticle surface. In a separate study, Özel et al. used the same detection method to measure the intestinal concentration of nitric oxide, a physiologically important free radical biomolecule that can also induce cytotoxicity at high concentrations, in zebrafish embryos exposed to CeO_2 and CuO nanoparticles.²¹⁵ Exposure to CuO nanoparticles significantly increased intestinal nitric oxide concentrations. Some of this effect was attributed to release of copper (II) from the nanoparticles as a result of dissolution; control experiments showed that embryo exposure to CuSO_4 also increased nitric oxide levels. Low exposure concentrations of CeO_2 nanoparticles decreased intestinal nitric oxide concentrations, likely due to radical scavenging as a result of redox reactions with exposed $\text{Ce}^{3+}/\text{Ce}^{4+}$ sites on the nanoparticle

surface. However, the scavenging effect was concentration-dependent, as exposure to higher nanoparticle concentrations increased intestinal nitric oxide concentrations.

In two related studies, Maurer-Jones et al. and Love et al. measured the effects of nanoparticle exposure on exocytosis from individual cells by tracking the secretion of redox-active species.^{216,217} Microelectrodes were placed in contact with the surface of individual primary culture cells, and individual exocytosis events were observed as current spikes at the electrode, which was held at a constant potential capable of oxidizing the redox-active molecule of interest. Nanoparticle-induced changes in cell exocytosis were quantified by measuring the total concentration of secreted redox-active molecules and the kinetics of individual secretion events; the latter were calculated from the frequency and half-width of current spikes. Maurer-Jones et al. showed that serotonin exocytosis from murine peritoneal mast cells decreased in frequency and increased in duration following exposure to TiO₂ nanoparticles; lower total release of serotonin was also observed. These effects were attributed to increased concentrations of intracellular reactive oxygen species measured following nanoparticle exposure.²¹⁶ Love et al. showed that murine adrenal medullary chromaffin cells exposed to PEG-functionalized Au nanoparticles decreased the exocytosis of epinephrine and norepinephrine, while cells exposed to Ag nanoparticles showed unaltered exocytosis, despite significant cellular internalization.²¹⁷

1.6.2 -Omic Methods Applied to Nanomaterial Toxicology. Transcriptomics, proteomics, and metabolomics (sensitive to mRNA, protein, and small molecule

expression, respectively) are increasingly used to study the physiological consequences of nanomaterial exposure on a variety of cells and organisms. Known collectively as “–omics” methods, they encompass a wide range of biochemical and analytical techniques, including microarrays and next-generation sequencing technologies (transcriptomics), mass spectrometry (proteomics), and NMR (metabolomics). The –omics methods allow physiological perturbations induced by nanomaterial exposure to be assessed globally, that is, without targeting a particular physiological process. This untargeted nature enables novel modes of nanomaterial-biological interaction to be discovered and represents a significant advantage over many commercially available *in situ* cytotoxicity assays, which are often limited to probing one specific process (e.g., membrane integrity or enzymatic activity).

The –omics methods are compatible with a wide range of nanomaterial types and do not commonly suffer from the nanomaterial-induced interference that is common in many *in vitro* cytotoxicity assays.⁹ For example, transcriptomic approaches using DNA microarrays (vide infra) have been used to study differential gene expression in cells exposed to nanomaterials as diverse as carbon nanotubes,²¹⁸ high aspect ratio TiO₂ nanobelts,²¹⁹ TiO₂ nanoparticles,²²⁰ CeO₂ nanoparticles,²²¹ and mesoporous silica nanoparticle drug delivery systems.²²² The –omics methods often generate large, complex data sets that require significant processing to obtain meaningful biological conclusions. Multivariate analyses, such as principal component analysis, and bioinformatics techniques, including clustering algorithms and network analyses, are commonly employed for this purpose.

1.6.3 Transcriptomics. Transcriptomics quantifies RNA expression, which is indicative of gene regulation. Changes in mRNA expression induced by nanomaterial exposure are indicative of altered expression of the corresponding gene or gene cluster. Physiological impacts of nanomaterial exposure are then inferred based on that gene or gene cluster's known physiological function.

Two primary techniques are used to study the effects of nanomaterials on the cell transcriptome: microarrays, which consist of short DNA strands immobilized on a chip, and next-generation sequencing technology. In microarray experiments, mRNA is extracted from cells following nanomaterial exposure, reverse-transcribed to cDNA, functionalized with a fluorescent tag, and hybridized onto a microarray containing tens of thousands of complementary DNA fragments localized into distinct spots. The fluorescence intensity at a particular spot is indicative of the expression level of the corresponding gene. Microarrays have been most commonly used to study nanotoxicity in primary human cells and cell lines whose genomes are well-characterized; however, other well-characterized cell types, including *Escherichia coli*, have been used.^{220,223} In next-generation sequencing experiments using RNA-seq methodology, mRNA is extracted, reverse transcribed to cDNA, fragmented, and sequenced using a next-generation sequencing method (e.g., Illumina and SOLiD sequencing).

Fisichella et al. used human genome microarrays and quantitative real-time polymerase chain reaction (qRT-PCR) assays to study the response of intestinal Caco-2 cells to uncoated CeO₂ nanoparticles and citrate-coated CeO₂ nanoparticles.²²¹ Nanoparticles

were used in their pristine state and also after exposure to artificial daylight or treatment with acid, to simulate degradation expected to occur naturally in the intestine.

Differentially expressed genes were observed using microarrays and validated by parallel analysis by qRT-PCR. Ingenuity pathway analysis was subsequently used to identify the canonical biological pathways that contributed most significantly to the observed gene expression changes. Coated, pristine CeO₂ nanoparticles induced few changes in gene expression; however, uncoated nanoparticles and coated nanoparticles treated with light or acid induced significant changes in gene expression related to mitochondrial function, specifically the oxidative phosphorylation pathway. Fewer genes were significantly differentially expressed following exposure to pristine citrate-capped CeO₂ nanoparticles than uncoated or coated and degraded nanoparticles. Consequently, the authors suggested that citrate coating has protective effects towards Caco-2 cells.

While microarray technologies screen for differential expression among thousands of predetermined genes, next-generation sequencing techniques like RNA Seq sequence and analyze all extracted RNA sequences. Consequently, RNA-Seq can sample a larger array of physiological functions potentially impacted by nanomaterial exposure than can microarrays and so is more capable of discovering novel modes of nanomaterial impacts on physiological function. A few examples illustrate the application of next-generation sequencing technologies to study nanotoxicity. Huang et al. used the SOLiD RNA Seq platform to analyze differential microRNA expression (involved in regulating mRNA and protein expression) in human dermal fibroblasts as a function of silver nanoparticle exposure.²²⁴ In parallel, they measured differential gene expression using microarrays and

protein expression using 2-D gel electrophoresis and mass spectrometry. Publicly available gene annotation and visualization tools (i.e., Database for Annotation, Visualization and Integrated Discovery and The Gene Map Annotator and Pathway Profiler) were used to identify biological pathways impacted by nanoparticle exposure. Validation experiments using commercially available kits observed the functional response of cells to nanoparticle exposure (i.e., nanoparticle effects on cytoskeleton structure, ATP content, and apoptosis). These were performed to test the functional impact of changes in biological pathway regulation identified in mRNA expression studies. Such validation is a critical component of efforts to correlate differential gene, protein, or small molecule expression with nanotoxicity, as toxicological research must ultimately identify changes in cellular function, not just biomolecule expression. Through their combined analyses, Huang et al. determined that silver nanoparticles impaired cytoskeleton integrity, reduced cellular metabolism, and induced apoptosis.

Feliu et al. studied the toxicity of sub-lethal doses of poly(amidoamine) dendrimers to human bronchial epithelial cells using the Illumina RNA Seq platform for global RNA sequencing.²²⁵ Analysis of their sequencing data using a gene ontology bioinformatics package revealed that cationic, amine-terminated dendrimers significantly down-regulated genes related to cell division, while anionic, hydroxyl-terminated dendrimers induced no significant changes in gene expression. Subsequently, the authors directly measured changes in the cell cycle of cells exposed to cationic or anionic dendrimers using flow cytometry, and observed cell cycle arrest only in cells exposed to cationic

dendrimers. This work demonstrates the power of next-generation sequencing techniques to inform targeted, functional-level investigations of nanomaterial toxicity by detecting changes in cell pathway regulation with high sensitivity and without targeting. Finally, van Aerle et al. used the Illumina RNA Seq platform to investigate differential gene expression in zebrafish embryos in response to exposure to silver nanoparticles, bulk (non-nano) silver, and silver ions.²²⁶ Although some changes in gene expression were unique to silver nanoparticle exposure, disruption of the oxidative phosphorylation pathway was common following exposure to all silver materials. Changes in oxidative phosphorylation gene regulation were dependent on the duration of embryo exposure to silver, showing overall down-regulation between 0 and 24 h and up-regulation between 24 and 48 h (Figure 10); given the pronounced dependence of differential gene expression on nanomaterial exposure time, gene expression profiles should be collected at multiple time points following nanomaterial exposure. These time-dependent changes in gene regulation correlated well with changes in embryo oxygen consumption after exposure to silver ions; oxygen consumption was similarly reduced between 0 and 24 h after exposure to silver ions and recovered to control levels between 24 and 48 h. The authors concluded that dissolved silver ion is primarily responsible for the toxicity of silver nanoparticles and acts primarily through disruption of oxidative phosphorylation.

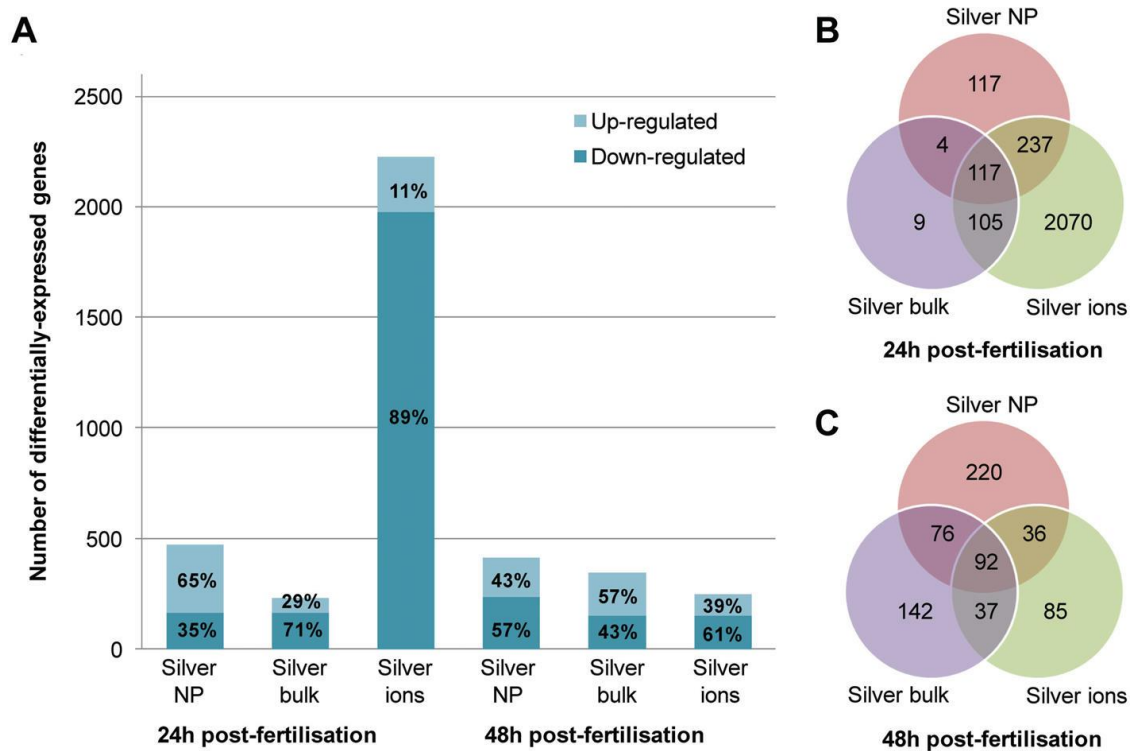


Figure 10. Zebrafish embryos exposed to various forms of silver showed time-dependent differential gene expression ($p < 0.05$) relative to unexposed embryos (a). The number of differentially expressed genes common between two or three distinct silver treatments are shown in overlapping areas of the Venn-diagrams (b, c). Reprinted with permission from van Aerle, R.; Lange, A.; Moorhouse, A.; Paszkiewicz, K.; Ball, K.; Johnston, B. D.; de-Bastos, E.; Booth, T.; Tyler, C. R.; Santos, E. M. *Environ. Sci. Technol.* **2013**, 47 (14), 8005–8014 (ref 226). Copyright 2013 American Chemical Society.

1.6.4 Proteomics. Protein expression, like mRNA expression, is indicative of the physiological state of a cell. Proteomics studies typically track relative differential protein expression as a function of nanomaterial exposure. Perturbations in physiological processes are inferred from known functions of differentially expressed proteins

identified using protein databases²²⁷ or from bioinformatics analyses that link patterns of differential protein expression to known biological pathways.^{228,229} Proteins are typically identified using mass spectrometry. Relative protein quantification is often achieved using label-free approaches, though improved quantification has been achieved using isotope labeling strategies such as “stable isotope labeling by amino acids in cell culture” (SILAC).²²⁹ More targeted protein analysis can also be achieved using protein microarrays based on antibody recognition.²³⁰ The range of cell and tissue types that can be analyzed by proteomics approaches is limited only by the knowledge of protein mass spectral signatures. Nanomaterial toxicity to bacteria (e.g., *Escherichia coli*^{220,231} and *Bacillus thuringiensis*),²³² human cells (e.g., alveolar-basal epithelial cells²²⁸ and epithelial cell-lung fibroblast co-cultures),²²⁹ and whole organisms (e.g., the water flea *Daphnia magna*²²⁷ and the blue mussel *Mytilus edulis*²³³) have all been assessed via proteomics methods. One recent article reviews and critically analyzes the application of proteomic approaches to study toxicology in general, including nanotoxicology,²³⁴ and another reviews the applications of proteomic approaches to study both protein-nanoparticle interactions (i.e., the protein corona) and nanomaterial toxicity.²³⁵

Pan et al. used LC-MS/MS to observe protein expression in human alveolar-basal epithelial A549 cells as a function of exposure to zinc oxide nanoparticles.²²⁸ Protein expression data were analyzed using PANTHER functional pathway analysis to determine specific cellular pathways perturbed by nanoparticle exposure. In parallel with proteomic analysis, changes in cell viability were observed using electrical impedance measurements. The authors showed that nanoparticle size and surface chemistry

(modulated by aluminum doping) influenced cell viability and biological pathway regulation. While proteomic analysis indicated that many biological pathways were perturbed by nanoparticle exposure, additional characterization of nanomaterial-induced changes in targeted cell functions are likely needed to validate these proteomic data and to draw generalizable conclusions regarding the mechanism of nanomaterial toxicity. Though protein and mRNA expression are related through the process of protein translation, their relationship in real systems is known to be complex; in some cases, poor correlation between the two has been observed.^{236,237} A more complete understanding of the physiological perturbations induced by nanomaterial exposure can be achieved by combining proteomics and transcriptomics approaches to monitor both protein and mRNA expression.²³⁸ Sohm et al. evaluated the response of *Escherichia coli* to Degussa P25 TiO₂ nanoparticles using a combination of cytotoxicity assays and transcriptomic and proteomic approaches.²²⁰ These authors observed differential expression of genes and proteins involved in many distinct biological pathways, including the osmotic stress response; fatty acid, polysaccharide, and peptidoglycan metabolism; redox homeostasis; and DNA replication. The physiological consequences of these changes in pathway regulation were assessed by cell viability, membrane potential, and membrane integrity assays. Their combined results suggested that TiO₂ nanoparticles reduced cell membrane integrity, leading to leakage of intracellular components and triggering an osmotic stress response.

Tilton et al. also combined transcriptomics and proteomics to quantify the response of three cell types (human macrophage-like immune surveillance cells, human small airway

epithelial cells, and a cell co-culture representing the gastrointestinal tract) to TiO₂ nanobelts and multi-walled carbon nanotubes.²¹⁹ Following nanomaterial exposure, global transcriptome analysis was conducted using a human genome microarray, and global proteome analysis was conducted using LC-MS/MS. Differential expression patterns were analyzed using bioinformatics methods across three dimensions: cell type, nanoparticle type, and expression type (transcriptome vs. proteome). No differentially expressed genes or proteins were common across all three cell types. However, common biological processes (or pathways) impacted by exposure to each nanomaterial type were identified by overlaps in the differential expression of genes and proteins. For example, the nuclear apoptotic process signaling network, involved in regulating apoptosis, cell cycle arrest, and DNA repair, was found to be significantly up-regulated by TiO₂ nanobelt exposure across all cell types, suggesting that this nanomaterial may exert genotoxicity to cells. The authors observed no correlation between the number of differentially expressed genes and cytotoxicity, leading them to suggest that global – omics measurements are indicative of the mechanisms of nanomaterial toxicity rather than overall cytotoxicity.

1.6.5 Metabolomics. The study of metabolites in biological systems is beginning to be used to track the physiologic impact of nanomaterials on cells, tissues, and organisms. Metabolite expression is not directly traceable to genome regulation through conserved pathways such as transcription and translation that control mRNA and protein expression. Rather, it is influenced by all metabolic processes within a cell and provides phenotypic

information. The two primary analytical tools used for metabolomics studies are ^1H -NMR and mass spectrometry. Although most metabolomic nanotoxicology studies have used only one of these techniques, they have complimentary capabilities and may be used effectively in combination. ^1H -NMR has greater quantitative capability and reproducibility than mass spectrometry, but its sensitivity is lower.²³⁹ The term metabonomics, which refers specifically to the quantitative study of metabolic response to stimuli,²³⁹ is often used to describe nanotoxicology studies conducted through ^1H -NMR investigation of metabolites. By tracking changes in metabolite expression with respect to nanomaterial exposure, biomarkers of nanomaterial stress can be identified and diagnostic mechanisms of nanomaterial toxicity can be discovered.

^1H -NMR metabolic profiling is sensitive to biological perturbations in the absence of apparent cytotoxicity. Åslund et al. used ^1H -NMR metabolic profiling to demonstrate that TiO_2 nanoparticles induced metabolic perturbations in the earthworm *Eisenia fetida*, despite previous studies having shown no nanoparticle impact on earthworm survival, reproduction, or growth at similar exposure concentrations.²⁴⁰ ^1H -NMR spectra of metabolites extracted from lyophilized earthworm tissue were analyzed by principal component analysis (PCA) and partial least squares discriminant analysis (PLS-DA). PCA loadings (a measure of a component's contribution to variation in a dataset) were plotted as a function of chemical shift detected by ^1H -NMR to identify metabolites with altered expression following organism exposure to TiO_2 nanoparticles. PLS-DA was used to test for significant separation between treatments. These authors hypothesized that observed metabolic perturbations may have been caused by oxidative stress, but

acknowledged that more targeted tests beyond global metabolic profiling are required to evaluate this hypothesis.

Bu et al. also used $^1\text{H-NMR}$, PCA, and PLS-DA to analyze the metabolic profile of rat urine and serum as a function of oral exposure to TiO_2 nanoparticles. Histological analysis provided no evidence of organ damage, but significant changes in metabolite concentrations were induced by nanoparticle exposure, consistent with perturbed energy and amino acid metabolism and altered gut microorganism composition. The authors suggested that nanoparticles may have acted through these mechanisms to induce slight injury to heart tissue, which was observed as mitochondrial swelling using TEM.²⁴¹

Carrola et al. also observed significant changes in the metabolic profiles of HaCaT cells exposed to silver nanoparticles at concentrations that were either below or above the threshold of acute cytotoxicity, determined using the MTT assay.²⁴² Metabolic analysis revealed significant increases in intracellular glutathione concentrations and significant decreases in intracellular concentrations of glutathione amino acid precursors. Given the role of glutathione in cells as an antioxidant, these results suggest that oxidative stress was a significant mechanism of silver nanoparticle toxicity.

Hu et al. recently employed GC-MS to analyze changes in expression of 66 metabolites in algal cells exposed to graphene oxide and SWCNTs.²⁴³ Analysis of variance (ANOVA) showed that cells exposed to either nanomaterial had significantly altered metabolic profiles relative to unexposed cells. Nanoparticle-induced oxidative stress was observed by measuring intracellular reactive oxygen species concentrations (using the fluorescence probe dichlorodihydrofluorescein diacetate) and superoxide dismutase

activity (using a commercial assay); greater oxidative stress was observed in cells exposed to SWCNTs than to graphene oxide. Orthogonal partial least-squares discriminant analysis was used to determine the relationship between oxidative stress and changes in metabolite expression. Thirteen metabolites were identified to have a strong, positive correlation with oxidative stress, and the authors suggested that these may serve as biomarkers of oxidative stress. Metabolomic analysis also revealed decreased unsaturated fatty acid content following nanomaterial exposure, consistent with osmotic stress; this result supported qualitative evidence from TEM images that cells exposed to nanomaterials displayed plasmolysis. This study demonstrates that pairing global metabolic analysis with targeted analysis of biological endpoints (i.e., oxidative stress and cell morphology) provides better-validated insight into mechanisms of nanomaterial toxicity than is possible using metabolic analysis alone.

1.7 Conclusions

This review has been organized around two central themes of nanotoxicity research: (1) nanomaterial physicochemical properties and transformations and (2) nanomaterial interactions with biological systems and corresponding physiological impacts. This structure was adopted in part to recognize the important roles that both nanomaterial and biological factors play in determining the outcome of nano-bio interactions. A key challenge for the nanotoxicity research community is linking nanomaterial physicochemical properties with biological outcomes; for nanotoxicity research to have a tangible impact on the course of nanotechnology development, specific nanomaterial

physicochemical properties that are predictive of toxicity must be identified such that industrial and regulatory bodies can take tangible steps towards designing and implementing safer nanomaterials.

To achieve this aim, nanotoxicity research must become more generalizable. Given the huge number of potential interaction pairings between industrially relevant nanomaterials and biological systems, a case-by-case approach to assessing nanotoxicity is unlikely to keep pace with advances in nanotechnology. Two approaches already beginning to be adopted by the field can improve the generalizability of nanotoxicity research. The first approach seeks to identify fundamental mechanisms of nanomaterial-biological interaction and toxicity by probing the molecular character of the nano-bio interface directly. This approach requires the continued development and application of highly sensitive and selective analytical tools, such as those described in this review, capable of probing the chemically complex environments of many nanotoxicity studies. The second approach, which has received less attention in this review, seeks to identify generalizable relationships between nanomaterial structure and biological activity by applying high throughput analyses paired with mathematical and computational approaches to analyze toxicological datasets.

As an example of the latter approach, Kaweeteerawat et al. analyzed a dataset consisting of the toxicological response of *Escherichia coli* to 24 metal oxide nanoparticles.²⁴⁴ Nanoparticle impacts on bacterial growth and intracellular and extracellular reactive oxygen species concentrations were measured, and a set of 30 physicochemical descriptors (some measured directly and some calculated) was created for each

nanoparticle. The physicochemical descriptors most-responsible for observed toxicity were then identified by constructing nano-structure activity relationships using statistical and machine-learning approaches. The authors observed that nanomaterial conduction band energy and metal ion hydration enthalpy had the highest correlation with toxicity to *Escherichia coli*, consistent with previous work studying metal oxide nanoparticle toxicity to mammalian cells.²⁴⁵

A related but more quantitative approach towards predicting nanomaterial-induced changes in biological function involves developing mathematical models, referred to as quantitative structure-activity relationships (Q-SARs), to relate nanomaterial structure and composition descriptors to biological endpoints informed by experimental data. The potential for these models to provide toxicological insight where purely experimentally derived data is impractical due to limitations of time or cost, have been recognized for over five years,^{246–248} and was the subject of a recent review.²⁴⁹ We agree with Oksel et al. that Q-SARs have the potential to identify significant routes of nanotoxicity and inform the design of safer nanomaterials. However, we suggest that direct measurements of molecular-scale phenomena at the interface of nanomaterials and biological systems are also needed to develop a fundamental understanding of nanotoxicology that is applicable to a diversity of biological systems. Our assertion is primarily based on the idea that Q-SAR methods are limited by the availability of large-scale cytotoxicity data, which may not be representative of all relevant modes of nanomaterial-biological interactions due to the inherently targeted nature of array-based cytotoxicity assays.

Whatever the approach used to characterize the interface of nanomaterials with biological systems, the goal should be causal, as opposed to correlative, knowledge of this interaction, given the superior predictive capability of the former. The ability to predict nanotoxicity from fundamental principles, though not yet realized in general, is needed in order to strategically design safe nanomaterials, since the large number of distinct nanomaterial types (e.g., of variable chemical composition, size, shape, morphology, crystallinity, surface modification, and incorporation into secondary structures) prohibits even high-throughput approaches from tracking nanomaterial toxicity on a case-by-case basis. Developing generalizable guidelines to support the development of safe nanomaterials remains a key challenge for the field. We postulate that application of analytical methods to probe molecular-level phenomena governing nanomaterial-biological interactions is critical to tackling this challenge.

Probing the nanomaterial-biological interface at multiple levels, from nanomaterial-biomolecule or -membrane interactions to nanomaterial effects on viability and function, typically requires the application of multiple analytical methodologies and is beyond the capabilities of many individual laboratories. Collaborative research efforts involving multiple areas of expertise in, e.g., the physical, chemical, and biological sciences, are therefore needed to understand the complex nanomaterial-biological interface.

Knowledge of complex data processing and statistical analysis methods is also increasingly needed to draw conclusions from large datasets describing the response of complex biological systems. Thus, this review serves as an invitation and a challenge to analytical chemists – push the limits of analytical methodology to achieve sensitive

detection schemes that yield molecular signatures in complex environments with high temporal and spatial resolution. The reward will likely be exciting, new, and sustainable nanomaterial-enabled technology.

1.8 Acknowledgements. The authors acknowledge funding from the National Science Foundation Center for Chemical Innovation: Center for Sustainable Nanotechnology (CHE-1503408). ILG gratefully acknowledges support from a Minneapolis Torske Klubben Fellowship and University of Minnesota Doctoral Dissertation Fellowship.

Chapter 2

Effects of Humic and Fulvic Acids on Silver Nanoparticle Stability, Dissolution, and Toxicity

Adapted from:

Gunsolus, I. L.; Mousavi, M. P. S., Hussein, K., Bühlmann, P., Haynes, C. L. *Environ.*

Sci. Technol. **2015**, *49*, 8078-8086

Copyright ©2015 American Chemical Society. All rights reserved.

This work was a joint effort of this author and Maral Mousavi, who performed characterization of silver nanoparticle dissolution using silver ion-selective electrodes. Kadir Hussein assisted this author with characterizing silver nanoparticle toxicity to *Shewanella oneidensis*.

The colloidal stability of silver nanoparticles (AgNPs) in natural aquatic environments influences their transport and environmental persistence, while their dissolution to Ag^+ influences their toxicity to organisms. Here, we characterize the colloidal stability, dissolution behavior, and toxicity of two industrially relevant classes of AgNPs (i.e., AgNPs stabilized by citrate or polyvinylpyrrolidone) after exposure to natural organic matter (NOM, i.e., Suwannee River Humic and Fulvic Acid Standards and Pony Lake Fulvic Acid Reference). We show that NOM interaction with the nanoparticle surface depends on (i) the NOM's chemical composition, where sulfur- and nitrogen-rich NOM more significantly increases colloidal stability, and (ii) the affinity of the capping agent for the AgNP surface, where nanoparticles with loosely bound capping agents are more effectively stabilized by NOM. Adsorption of NOM is shown to have little effect on AgNP dissolution under most experimental conditions, the exception being when the NOM is rich in sulfur and nitrogen. Similarly, the toxicity of AgNPs to a bacterial model (*Shewanella oneidensis* MR-1) decreases most significantly in the presence of sulfur- and nitrogen-rich NOM. Our data suggest that the rate of AgNP aggregation and dissolution in aquatic environments containing NOM will depend on the chemical composition of the NOM, and that the toxicity of AgNPs to aquatic microorganisms is controlled primarily by the extent of nanoparticle dissolution.

2.1 Introduction

Silver nanoparticles (AgNPs) are the most commonly used engineered nanomaterial in consumer products, serving primarily as antimicrobial agents (e.g., in fabrics and ointments).²⁵⁰ Common product uses can result in leaching of AgNPs into water (e.g., through laundering or skin cleansing), which is expected to be the major route for AgNPs to enter the wastewater supply.^{251,252} While a recent study demonstrated high removal efficiency of AgNPs in municipal waste water treatment plants,²⁵³ AgNPs are also expected to enter natural environments through direct discharge from manufacturing and disposal of consumer and medical products that may circumvent wastewater treatment.^{252,254,255} Given the potential for AgNP entry into environments and their known toxicity to microorganisms,²⁵⁶ significant efforts are being made to identify the material and environmental parameters that control AgNP behavior and environmental impact.

AgNPs that enter natural aquatic environments encounter variable temperature, pH, light illumination, ionic strength, dissolved molecular oxygen concentration, and natural organic matter (NOM) concentration and composition. Each of these parameters has the potential to influence nanoparticle colloidal stability. These factors can also influence AgNP dissolution to give Ag^+ (a process that depends on proton and molecular oxygen concentration),²⁵⁷ which is suggested to be the primary mode of AgNP toxicity to microorganisms.^{46,47,152,153} Among the potential transformations of AgNPs entering natural aquatic environments, the least understood are those affected by NOM. A survey of the literature reveals variable effects of NOM on AgNP stability and dissolution, which appears

to be caused by the high heterogeneity of NOM and the many AgNP models (in terms of size and surface chemistry) that have been employed.

Several studies demonstrated that addition of purified, naturally extracted NOM at low parts-per-million concentrations decreases homoaggregation rates (i.e., increases colloidal stability) of AgNPs; this applies to both AgNPs electrostatically stabilized with a citrate capping agent and sterically stabilized with polyvinylpyrrolidone (PVP) as the capping agent.^{74,258,259} Similarly, increased stability of citrate-capped AgNPs in unpurified NOM suspensions was observed.²⁶⁰ A few notable exceptions to this trend were reported. For example, fulvic acids isolated from a reference site in a Norwegian lake, despite having very similar elemental composition to Suwannee River fulvic acid models that were shown to stabilize AgNPs, had no effect on AgNP stability at equivalent or higher NOM concentrations.²⁶¹ Additionally, decreased colloidal stability of PVP-capped AgNPs following addition of cysteine (a simple model for protein-rich NOM) was observed in at least two studies.^{262,263} Our current understanding of NOM's impact on AgNP colloidal stability is complicated by results obtained using a wide range of nanomaterial-stabilizing agents and NOM types, and the general notion that NOM, despite its high chemical heterogeneity, can be considered as a class of molecules to have common patterns of interaction with AgNPs. Here, we identify the characteristics of NOM that most significantly impact the colloidal stability of AgNPs by employing in a single study a series of NOM types with variable chemical composition and nanoparticle capping agents.

The kinetics of AgNP dissolution, the equilibrium concentration of released Ag⁺, and complexation reactions of released Ag⁺ have been studied under variable solution

conditions and with variable AgNP types. Discrepancies exist in the literature regarding the effect of NOM (either macromolecular or small molecule NOM models) on the extent of AgNP dissolution. Liu et al. observed decreased AgNP dissolution in presence of thiol-containing species (e.g., cysteine and glutathione), which they attributed to a reduction in surface sites prone to oxidation.²⁶⁴ In contrast, Gondikas et al. demonstrated increased dissolution of citrate- and PVP-capped AgNPs in the presence of cysteine.²⁶² The latter authors attributed the discrepancy between the two studies to differences in sample preparation (specifically, the possibility for analyte retention and loss when using centrifugal filter units).²⁶² Further studies employing other NOM models observed either significantly increased^{265,266} or decreased^{257,267} dissolution of AgNPs with increasing NOM concentration. We note that the majority of dissolution studies employ measurements of total Ag concentration, without discriminating between free Ag⁺ and Ag⁺-NOM complexes, though related work of ours demonstrated that Ag⁺ binding to NOM can in some cases mitigate Ag⁺ toxicity to bacteria.²⁶⁸ In light of the important role of dissolved Ag⁺ (and Ag⁺-NOM complexes) to AgNP toxicity,^{47,268} and to address existing discrepancies in the literature, we used fluoruous-phase Ag⁺ ion-selective electrodes (ISEs) for in situ detection of AgNP dissolution by monitoring the Ag⁺ concentration. Fluorous-phase Ag⁺ ISEs were previously shown to be powerful tools for dynamic monitoring of AgNP dissolution in complex media.⁶⁸

Several studies observed reduced toxicity of AgNPs towards a number of organismal models in presence of NOM, but the mechanism of this effect remains unclear. Studies using bacterial models such as *Pseudomonas fluorescens*⁷⁹ and *Escherichia coli*²⁶⁷

suggested the primary mechanism to be complexation of Ag^+ with NOM, reducing its bioavailability or bactericidal activity. Other studies using *Pseudomonas fluorescens*²⁶⁹ and the nematode *Caenorhabditis elegans*⁸⁰ suggested that NOM adsorption to AgNP surfaces (possibly decreasing total Ag^+ release or modulating nanoparticle adsorption to or internalization by organisms) is the primary mechanism of toxicity mitigation. Through parallel measurements of Ag^+ concentration and AgNP toxicity to a bacterium (*Shewanella oneidensis* MR-1), this study provides a more direct means to evaluate the mechanism of NOM mitigation of AgNP toxicity than was previously possible. It seeks to provide new insight on the molecular interaction of NOM with commercially relevant AgNPs stabilized with citrate or PVP. By employing a series of NOM models to represent major NOM classes, we arrive at fundamental and generalizable conclusions about AgNP–NOM interactions. Using in situ characterization, we avoid sample preparation errors that may have contributed to conflicting interpretations of prior results.

2.2 Experimental

Citrate-capped AgNPs were prepared using a reported method.²⁶⁰ PVP-capped AgNPs were prepared by incubating citrate-capped AgNPs with excess PVP-10 (average molecular weight 10,000 g/mol, Sigma Aldrich), followed by purification. Ligand exchange was confirmed by zeta potential measurements, while particle size was determined using transmission electron microscopy. For details see the Supporting Information.

Stock solutions of 10 g/L NOM (Suwannee River Humic Acid Standard II, Suwannee River Fulvic Acid Standard II or Pony Lake Fulvic Acid Reference, International Humic Substances Society, St. Paul, MN) were prepared in deionized water and mixed with aliquots of purified and concentrated AgNP suspensions to achieve a 600 mg/L NOM concentration. Nanoparticles were incubated with NOM in the dark without mixing for 18 h followed by redispersion in 0.1 M ionic strength potassium phosphate buffer (pH 7.5, 5 mg Ag/L, 10 mg/L of NOM; acrylic cuvettes).

The colloidal stability of the resulting 3.0-mL AgNP samples was monitored over two days using UV-visible extinction spectroscopy and dark-field microscopy, and over eight days using dynamic light scattering (DLS). Dissolution was monitored over five hours in an identical buffer using fluoros-phase Ag⁺ ISEs, prepared as described elsewhere²⁶⁸ (see also the Supporting Information and Figure S4). Toxicity of AgNPs to *Shewanella oneidensis* MR-1 was evaluated using the LIVE/DEAD Cell Viability Assay (Invitrogen). For consistency, the cells were suspended in the buffer described above. For details see the Supporting Information.

2.3 Results and Discussion

2.3.1 Impact of NOM and nanoparticle capping agents on AgNP colloidal stability.

AgNPs were prepared with either a citrate or PVP-10 capping agent to represent two major classes of industrially relevant AgNPs. TEM micrographs (Supporting Information, Figure S1) reveal no appreciable change in AgNP morphology after exchanging citrate for PVP-10, demonstrating that nanoparticle surface functionalization can be varied independently

from morphology. The average particle diameters of citrate- and PVP-capped AgNPs were calculated to be 12.1 ± 2.4 nm and 15.5 ± 4.1 nm, respectively, based on TEM analysis of 500 nanoparticles, indicating a statistically significant ($p < 0.001$) but minor difference in nanoparticle size. Replacement of citrate by PVP-10 was probed by measuring the nanoparticle zeta potential; the zeta potential decreased significantly with exchange to PVP-10, from -32.8 ± 2.2 to -13.6 ± 3.6 mV. These values are consistent with at least partial replacement of negatively charged citrate with neutral PVP-10 (Figure S1) and are in agreement with literature values for PVP-capped AgNPs prepared directly.^{262,270,271}

Initially, AgNPs were exposed to 10 mg/L NOM, chosen to fall within the concentration range of natural freshwaters (1-60 mg/L).²⁷² Three types of NOM were used: Suwannee River fulvic acid (SRFA) and Suwannee River humic acid (SRHA) have similar elemental compositions²⁷³ (see Table S1) and represent NOM fractions derived primarily from decomposition of vegetation.²⁷⁴ Pony Lake fulvic acid (PLFA) represents NOM rich in sites with high affinity for metallic silver and Ag^+ (due to high sulfur and nitrogen content,²⁷⁵ a subset of which has a high affinity for silver and Ag^+ ;²⁶⁸ see Table S1). It is derived exclusively from microbial matter decomposition.²⁷⁴ None of these had a detectable effect on AgNP colloidal stability when present at a concentration of 10 mg/L, as determined by UV-visible extinction spectroscopy (Figure S2). This technique was used to demonstrate changes in AgNP aggregation by monitoring the intensity and position of size-dependent extinction peaks due to the localized surface plasmon resonance effect. In subsequent experiments, AgNPs were exposed to a larger concentration of NOM (600 mg/L) prior to colloidal stability assessment to promote NOM interaction with the AgNP

surface. This simulates, on an accelerated time-scale, particle acquisition of adsorbed NOM, which is expected to take place over longer time periods in natural aquatic environments containing lower NOM concentrations. Following redispersion in a high ionic strength (0.1 M) buffer, the bulk NOM concentration during colloidal stability assessment was 10 mg/L. The ionic strength was chosen to ensure that the interaction of NOM with the AgNP surface was not purely electrostatic while remaining representative of natural aquatic systems.²⁷⁶ Nanoparticle colloidal stability was monitored over two days again using UV-visible extinction spectroscopy (Figure 1).

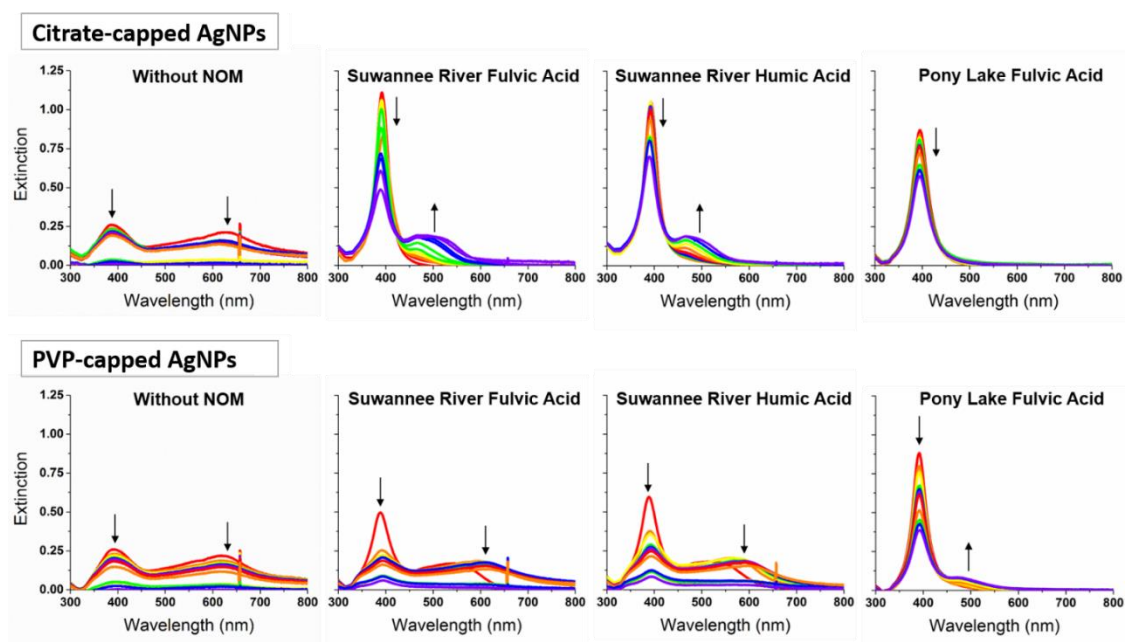


Figure 1. UV-visible extinction spectra show that NOM improves the colloidal stability of citrate-capped AgNPs more significantly than PVP-capped AgNPs, and that the degree of colloidal stabilization conferred by NOM for both particle types was SRFA < SRHA << PLFA. Spectra of citrate-capped (top) and PVP-capped (bottom) AgNPs in pH 7.5

phosphate buffer were collected after incubation of AgNPs with NOM type specified. Shown are spectra at 1-6 (red), 11, 20, 24, 30, and 46 h (violet) after particle redispersion; arrows indicate directions of peak intensity changes. The peak near 390 nm corresponds to extinction by the primary (12 nm-diameter) particle population and peaks at longer wavelengths correspond to aggregates. Aggregate settling decreases peak intensities as it removes particles from the probed sample volume. The feature observed around 650 nm is an instrumental artifact. Results were duplicated in independent experiments.

The plasmon resonance of spherical metal nanoparticles causes light extinction features that are sensitive to inter-particle interactions.²⁷⁷ Such interactions shift the particle plasmon extinction peak to higher wavelengths.²⁷⁷ In our study, a primary extinction peak attributable to the plasmon resonance frequency of non-agglomerated 12 nm-diameter AgNPs was observed at 391 and 394 nm for citrate- and PVP-capped AgNPs, respectively. The formation of variable-sized AgNP aggregates resulted in the appearance of a broader peak at longer wavelengths; larger aggregates produced broader and more red-shifted peaks. Similar observations of red-shifted UV-visible extinction spectra in response to AgNP aggregation were reported previously.²⁷⁸ Nanoparticle aggregation was further characterized using dynamic light scattering (DLS) to track hydrodynamic particle diameter over time following dispersion in buffer (Figure 2). Extinction spectroscopy and DLS demonstrate that incubation with NOM stabilized citrate- and PVP-capped AgNPs against homoaggregation in a high ionic strength buffer (0.1 M) relative to their pristine (no-NOM) counterparts. The aggregation behavior of AgNPs is known to depend on

surface characteristics, where surface coatings that promote steric repulsion are typically more effective at maintaining AgNP colloidal stability in high ionic strength environments than their counterparts promoting only electrostatic repulsion.^{279,280} However, surface coating-dependent behavior of AgNPs in the presence of NOM has not been studied thoroughly. It was observed that citrate- and PVP-capped AgNPs aggregated similarly with increasing ionic strength after addition of cysteine, which was used as a low molecular weight model for NOM.²⁶² However, higher molecular weight NOM, such as that used in our study, is expected to induce different effects, given its greater potential to increase steric repulsion between particles. In this study, the degree of AgNP stabilization conferred by NOM was dependent on both the NOM type and nanoparticle capping agent. Three primary effects were observed.

First, AgNPs exposed to high NOM concentrations had higher colloidal stability than pristine nanoparticles that were stabilized either electrostatically using citrate or sterically using PVP-10. Pristine citrate- and PVP-capped AgNPs aggregated immediately upon dispersion in phosphate buffer, as indicated by the low intensity of the primary extinction peak at 391 or 394 nm and the presence of a broad peak at longer wavelengths (Figure 1, left). The primary and secondary extinction peak intensities of citrate- and PVP-capped AgNPs decayed over time as the nanoparticles aggregated and fell out of suspension; particle dissolution (which was observed using ISEs and is discussed in more detail below) likely also contributed to decreasing intensity of the primary extinction peak. Rapid increases in the hydrodynamic particle diameters were observed over the first three hours following dispersion (Figure 2), consistent with rapid formation of large aggregates. In

contrast, citrate- and PVP-capped AgNPs that had been previously incubated with NOM showed a higher intensity primary extinction peak at early time-points, indicating a larger population of stable 12-nm nanoparticles. Appearance of a broader, secondary extinction peak at red-shifted wavelengths was also slower, suggesting slower aggregate formation. In most cases, the average hydrodynamic particle diameter increased following dispersion in buffer, but increases were dramatically slower than for pristine nanoparticles. This result suggests that ligand-stabilized AgNPs that encounter high concentrations of NOM have significantly higher colloidal stability than their pristine counterparts. While nanoparticle transport in natural aquatic environments depends not only on homoaggregation as evaluated here, but also on heteroaggregation and nanoparticle adsorption onto collector surfaces, our result suggests that AgNPs stabilized by NOM may be transported more efficiently through aquatic environments than their pristine counterparts, since homoaggregation and nanoparticle settling is reduced.

Second, the extent to which NOM increases AgNP colloidal stability depends on the affinity of the original organic capping agent for the nanoparticle surface. A fraction of PVP-capped AgNPs previously incubated with SRFA or SRHA aggregated immediately after dispersion in NOM-free buffer, resulting in a broad extinction peak between 500 and 750 nm (Figure 1, bottom). Equivalently prepared citrate-capped AgNPs aggregated more slowly and formed smaller aggregates, as indicated by slower growth of a narrower secondary extinction peak between 500 and 600 nm (Figure 1, top) and DLS measurement of hydrodynamic diameters (Figure 2). These results indicate that PVP-capped AgNPs are less effectively stabilized by NOM than citrate-capped AgNPs, which may be caused by

the higher affinity of PVP than citrate for the AgNP surface. Citrate is generally thought to be weakly bound to the AgNP surface,²⁷⁸ and citrate-capping of AgNPs is widely used in industry to provide stable precursors for other functionalization schemes due to the labile nature of this agent. At the high NOM concentrations employed in the current study, NOM may displace citrate from the nanoparticle surface. In contrast, PVP coordinates with the AgNP surface through van der Waals interactions and direct bonding interactions with the Ag *d*-band.^{281,282} Computational studies showed that the latter occurs through bonding orbitals of the 2-pyrrolidone subunit, localized on the oxygen (~60%) and nitrogen (~25%).^{281,282} This is consistent with spectroscopic studies of PVP interaction with Ag, which suggested that direct bonding interactions occur through either only oxygen or a combination of oxygen and nitrogen.²⁸³⁻²⁸⁵ Due to direct bonding interactions with Ag, PVP is harder to displace than citrate, which may result in a greater barrier to NOM interaction with the nanoparticle surface. Alternatively, NOM might adsorb to either citrate or PVP on the AgNP surface, rather than displacing them. Under this assumption, our results suggest that more NOM binds to adsorbed citrate than to PVP since exposure to NOM induces a more significant increase in the colloidal stability of citrate- than PVP-capped AgNPs. However, at the pH of this system (pH 7.5), greater electrostatic repulsion exists between the negatively charged acidic residues of NOM and citrate (which carries three negative charges) than PVP (which is neutral). Based on our results, we conclude that AgNPs stabilized with easily displaceable organic capping agents will be more effectively stabilized by NOM.

Third, the extent to which NOM increases AgNP colloidal stability, regardless of the organic capping agent, depends on the concentration of sites with high affinity for metallic silver and Ag⁺ (e.g., sulfur and nitrogen groups)²⁸⁶ in the NOM. For both citrate- and PVP-capped AgNPs, the stabilizing power of NOM occurs in the order SRFA < SRHA << PLFA (Figures 1 and 2). Following dispersal of citrate-capped AgNPs exposed beforehand with SRFA or SRHA in NOM-free buffer (Figure 1, top middle), a broad, secondary extinction peak between 500 and 600 nm (due to variable size aggregates) appeared. This suggests that AgNPs previously incubated with SRFA and SRHA aggregate significantly, although less than AgNPs not treated with NOM. In contrast, no secondary extinction peak was observed following dispersion of AgNPs exposed beforehand with PLFA (top right), suggesting that no significant aggregation occurs in this case. In the case of PVP-capped AgNPs, PLFA is the only NOM type that eliminates immediate formation of a broad aggregate peak (Figure 1, bottom right). Due to the presence of both primary (12 nm diameter) and variable-size nanoparticle aggregates in these samples, it was not possible to accurately determine the average hydrodynamic particle diameter by DLS using a single normal distribution model. Despite this limitation, the observed relative changes in estimated average hydrodynamic particle diameter were consistent with the extinction spectroscopy results. The estimated average hydrodynamic diameter of particles previously incubated with NOM increased most significantly over time when SRFA was used; this was true for both citrate- and PVP-capped AgNPs (Figure 2). In the case of citrate-capped AgNPs, the SRHA and PLFA incubation had indistinguishable effects on hydrodynamic particle diameter, but PLFA was a more effective stabilizing agent than SRHA in the case

of PVP-capped AgNPs. Visual evidence for the relative stabilizing power of SRFA, SRHA, and PLFA is provided in Figure S3, which shows dark-field images and spatially resolved light scattering spectra of pristine and NOM-stabilized citrate-capped AgNPs 24 hours after redispersion in buffer. These qualitative and semi-quantitative results, respectively, confirm that citrate-capped AgNPs are increasingly stable when exposed to NOM in the order SRFA < SRHA << PLFA.

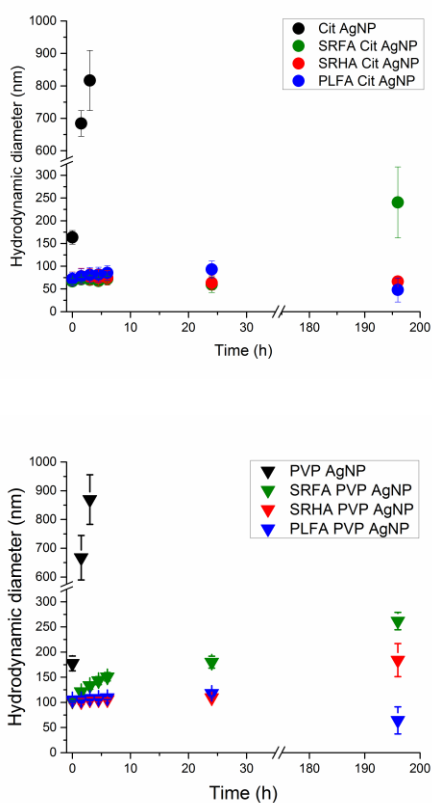


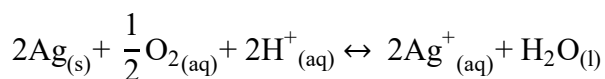
Figure 2. Average hydrodynamic diameters (Z-average particle size) of citrate-capped (top) and PVP-capped (bottom) AgNPs previously incubated with the NOM type specified after dispersion in buffer, as estimated with DLS. Error bars represent standard deviations of three independent replicates, each consisting of three analytical replicates.

The three NOM types used in the current study were chosen because they have similar average molecular weights (between 1300 and 1400 Da)²⁸⁷ but differ in sulfur and nitrogen content. Sulfur-containing species such as thiols have strong bonding interactions with metallic silver, and electron donating groups like sulfur and nitrogen may act as Ag⁺-coordinating sites²⁸⁸ when in the form, e.g., of thiols and amines. PLFA has approximately five to six times more total sulfur than either SRHA or SRFA (see Table S1),²⁷⁵ with approximately twice the fractional exocyclic sulfur content (e.g., thiol) of SRHA and SRFA.²⁸⁹ This results in an approximately eleven times higher thiol content of PLFA over SRHA and SRFA. Given the ability of thiols to form stable complexes with metals including silver²⁹⁰ and also with Ag⁺ (which was shown to adsorb to the nanoparticle surface²⁵⁷), the observed NOM ranking (PLFA >> SRHA > SRFA) may be partly attributable to their relative thiol contents. PLFA also has five to ten times more total nitrogen than SRHA or SRFA.²⁷⁵ This higher nitrogen content, present to a significant extent in the form of amides, amines, and heterocyclic nitrogens,²⁹¹ may also contribute to the greater stabilizing effect of PLFA. This explanation is also consistent with the latter ranking (SRHA > SRFA), since SRHA has an approximately two times higher nitrogen content than SRFA but is otherwise chemically similar (see Table S1). Given the lower oxygen content of PLFA than SRFA or SRHA (see Table S1), the relative NOM ranking observed here suggests that electron donating groups containing oxygen (e.g., carboxylic acids and phenols) have less influence on AgNP colloidal stability than electron donating

groups like sulfur and nitrogen. The relative NOM ranking observed here is consistent with that observed in a study considering Ag^+ only.²⁶⁸

We point out that while SRFA and SRHA have similar average molecular weights (1400 Da for SRHA, 1360 Da for SRFA),²⁹² their molecular weight distributions are different, with a larger fraction of higher molecular weight NOM in SRHA than SRFA.²⁹³ A previous study of citrate-capped gold nanoparticle stability with NOM suggested that high molecular weight fractions have much larger effects on nanoparticle stability than low molecular weight fractions separated from the same NOM source.²⁹⁴ Therefore, we suggest that preferential interaction of high molecular weight NOM fractions with AgNPs may also contribute to the increased colloidal stability of SRHA- over SRFA- stabilized AgNPs. PLFA has a similar molecular weight distribution as SRFA²⁹⁵ yet has a much greater effect on AgNP colloidal stability than SRFA or SRHA, as described above. Consequently, we suggest that sulfur and nitrogen content (i.e., sites with high affinity for metallic silver and Ag^+) plays a significant role in determining NOM's interaction with AgNPs in addition to molecular weight.

2.3.2 Impact of NOM on AgNP dissolution. The oxidative dissolution of AgNPs in natural aquatic environments is of interest due to the potential toxicity of released Ag^+ to microorganisms. In the absence of other oxidizing or reducing agents, AgNP dissolution proceeds with the following stoichiometry:²⁵⁷



The literature presents sometimes conflicting results regarding the effect of NOM on AgNP dissolution. For example, adsorption of thiol-containing species, such as cysteine, was shown to either inhibit^{264,270} or increase²⁶² AgNP dissolution. Such discrepancies may result from errors introduced during separation of AgNPs from dissolved Ag⁺ (e.g., from retention of Ag⁺ on centrifugal filters).²⁶² A separation step is necessary when monitoring AgNP dissolution by spectroscopic or spectrometric techniques, as these techniques cannot discriminate between Ag⁺ and AgNPs. In the current study, we employ fluoruous-phase Ag⁺ ISEs to monitor AgNP dissolution in situ, thereby eliminating the need for sample preparation and reducing potential sampling errors.⁶⁸

We investigated the effect of NOM composition on the dissolution of 12-nm-diameter citrate-capped AgNPs under an environmentally relevant condition (pH 7.5 phosphate buffer, as used above, and 10 mg/L NOM concentration in the bulk solution). Citrate-capped AgNPs that had been previously incubated with a high concentration of NOM (600 mg/L) were added to the pH buffer, yielding a silver concentration of 5 mg/L and a bulk NOM concentration of 10 mg/L. (Experiments were also conducted using AgNPs that had not been previously incubated with a high concentration of NOM, but the presence of 10 mg/L NOM in solution had no statistically significant effect on nanoparticle dissolution; see Figure S5.) Changes in the concentration of Ag⁺ were then monitored by measuring the electromotive force, emf, of the fluoruous-phase Ag⁺ ISE with respect to a reference electrode placed into the same solution. At a constant temperature, the emf of fluoruous-phase Ag⁺ ISEs increases linearly with the logarithm of the Ag⁺ activity. For example, at 20 °C a 10-fold increase in the activity of Ag⁺ results in a 58.2 mV increase in emf.⁵⁹ The

theoretical response and calibration of Ag^+ fluoruous-phase ISEs are explained in the Supporting Information and illustrated in Figure S4.

Figure 3a shows the results of ISE monitoring of nanoparticle dissolution. A sudden increase in the emf after addition of the AgNPs is caused by NP dissolution to give Ag^+ ions. The emf becomes stable one hour after AgNP addition, indicating that the concentration of Ag^+ in solution reached a steady state. The gradual increase in emf represents an increase in free silver concentration and not a slow response time of the electrode, as shown by the nearly instantaneous (less than 1 s) response of the ISE to changes in Ag^+ concentration caused by hydrogen peroxide and NaCl additions. While hydrogen peroxide oxidizes AgNPs and increases the Ag^+ concentration in solution, chloride precipitates Ag^+ , reducing the concentration of Ag^+ in solution. Both effects are detected quickly by the ISE, illustrating the advantage of this sensor for dynamic in-situ detection.

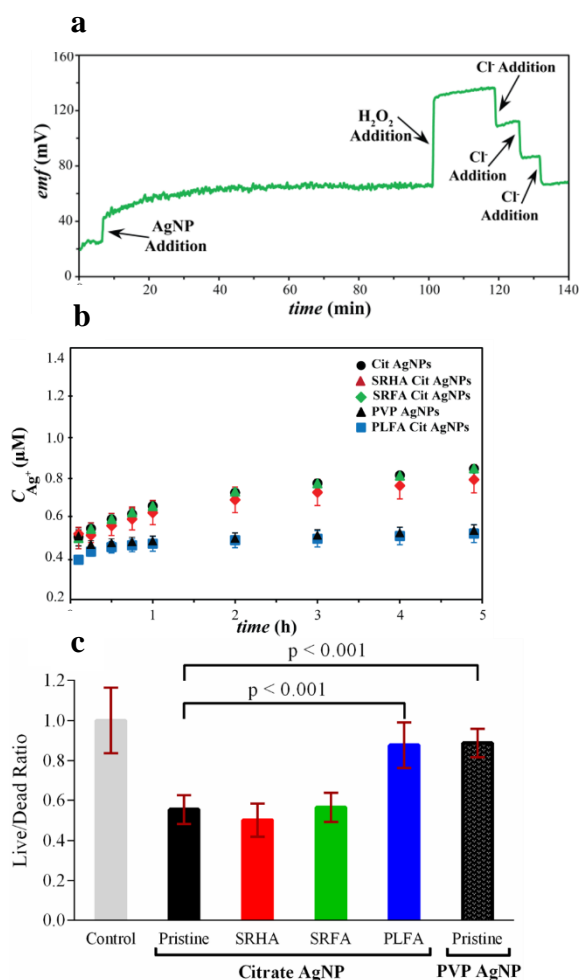


Figure 3. Continuous detection with fluoros-phase Ag⁺ ISEs: 5 mg Ag/L citrate-capped AgNPs were added to pH = 7.5 buffer while monitoring the Ag⁺ release. H₂O₂ was added to oxidize AgNPs, and Cl⁻ was added to reduce the Ag⁺ concentration (a). Dissolution of citrate-capped and PVP-capped AgNPs in pH 7.5 buffer (5 mg Ag/L) with or without prior incubation with NOM (non-surface bound NOM concentration 10 mg/L). Error bars represent standard deviations of three replicate measurements (b). Effect of AgNPs on *Shewanella* membrane integrity as a function of NOM type, as evaluated using fluorescent dyes (c); shown is the ratio of fluorescence emission intensities for a membrane permeable

dye (indicating live cells) and a membrane impermeable dye (indicating dead cells). Data collected from cells exposed to pristine nanoparticles (NP) and cells exposed to nanoparticles previously incubated with 600 mg/L NOM (PLFA-NP, SRFA-NP, and SRHA-NP) were normalized to a negative control from *Shewanella* not exposed to nanoparticles; values smaller than 1 indicate decreased membrane integrity following nanoparticle exposure. Error bars represent standard deviations of three biological replicates.

The effect of NOM with variable chemical composition on AgNP dissolution is presented in Figure 3b. SRHA- and SRFA-stabilized citrate-capped AgNPs showed equivalent Ag^+ release profiles over time to pristine nanoparticles (without NOM). Given the significantly increased colloidal stability of SRHA- and SRFA-stabilized AgNPs over pristine AgNPs, their similar dissolution profiles suggest that dissolution is relatively insensitive to nanoparticle aggregation state. This is consistent with previous reports, which suggested that AgNP aggregation only minimally decreases the surface area available for interaction with molecular oxygen.^{257,296} In contrast to SRHA- and SRFA-stabilized AgNPs, PLFA-stabilized citrate-capped AgNPs released over five hours approximately one-half the Ag^+ content of pristine nanoparticles. This result most likely reflects the high sulfur and nitrogen content of PLFA, as described above. Sulfur-containing functionalities, specifically thiol groups, have high affinities for silver surfaces, while thiolates and amines can form complexes with Ag^+ . NOM bound to the AgNP surface (e.g., through interaction of thiol-containing species with metallic silver or thiolates and amines with surface-adsorbed Ag^+) may exclude molecular oxygen from active sites and thereby limit oxidative

dissolution, as previously suggested in the case of thiols.²⁶⁴ Our results demonstrate that even when AgNPs are exposed to a very high NOM concentration (600 mg/L), there is a minimal effect on Ag⁺ release except when the NOM has a high concentration of strongly Ag-coordinating sites. Perhaps more surprising is the observation that prior incubation with SRHA or SRFA, which significantly stabilizes AgNPs against homoaggregation (as shown in our colloidal stability experiments), had no effect on the rate and total amount of Ag⁺ released.

We also compared the dissolution of citrate-capped and PVP-capped AgNPs. Exchanging a fraction of citrate for PVP-10 induced a significant decrease (~40%) in Ag⁺ release over five hours. Previous reports suggested that PVP may have high affinity for not only Ag surfaces but also Ag⁺,²⁹⁷ an effect that could trap Ag⁺ at the particle surface and buffer its release into solution.²⁶⁴ To directly test this hypothesis, we used Ag⁺ ISEs to monitor the concentration of free Ag⁺ in solution after addition of PVP. We observed no detectable changes in free Ag⁺ concentration after addition of up to 50 mg/L PVP (Figure S6), indicating that PVP has low affinity for Ag⁺ and is unlikely to trap Ag⁺ ions at the AgNP surface. An alternative mechanism to explain the observed PVP-induced decrease in AgNP dissolution is surface passivation. While it is beyond the scope of this work to directly assess the validity of this mechanism, we note Grubbs' suggestion that some polymer ligands can control access of molecular oxygen to the nanoparticle surface,²⁹⁸ which would decrease the oxidative dissolution rate of AgNPs. We note that the total dissolved Ag⁺ concentration in our experiments corresponds to approximately 1-2% (depending on the

capping agent) of the total silver content present in the original AgNP suspension, consistent with previous dissolution studies using larger (39 nm) PVP-capped AgNPs.²⁷⁰

2.3.3 Impact of NOM on AgNP Toxicity to Bacteria. Previous work suggested that AgNP toxicity to bacteria can be fully attributed to the bioavailable Ag^+ concentration resulting from nanoparticle dissolution.⁴⁷ A recent report suggested that, while AgNPs and Ag^+ may have similar effects on bacterial survival, they have distinct mechanisms of antibacterial activity.²⁹⁹ While questions remain regarding the relationship between AgNP dissolution and toxicity to bacteria, understanding AgNP dissolution in environmental matrices remains a critical step towards understanding the implications of their release into natural aquatic environments. To this end, a few studies assessed the role of Ag^+ -complexing agents, such as NOM, on resultant AgNP toxicity to bacteria. Fabrega et al. demonstrated reduced toxicity of citrate-capped AgNPs to *Pseudomonas fluorescens* with addition of 10 mg/L SRHA at pH 9.0, but no reduction of Ag^+ toxicity at an equivalent concentration.²⁶⁹ They hypothesized that reduction of AgNP toxicity caused by SRHA may be due to its role as a physical barrier to cell-NP contact or as a ROS-scavenger (antioxidant), while its lack of effect on Ag^+ toxicity may be due to insignificant binding with Ag^+ or continued bioavailability of Ag^+ in the complexed form. Zhang et al. demonstrated reduced bacterial disinfection performance of PVP-capped AgNPs following addition of 5 mg/L SRHA, an effect that they attributed to an observed reduction in Ag^+ release under these conditions.²⁶⁷ As these examples demonstrate, disagreements persist regarding the effect of NOM on AgNP dissolution and toxicity to bacteria, perhaps in part due to the use of indirect

measurements of AgNP dissolution and lack of Ag speciation information. Here, we coupled direct measurements of Ag⁺ dissolution from AgNPs in the presence of NOM (described above) with an assessment of AgNP toxicity to *Shewanella oneidensis* MR-1 to provide novel insight into the mechanism of NOM's effect on AgNP bactericidal efficacy.

In these toxicity experiments, as in previously described nanoparticle colloidal stability experiments, AgNPs were initially exposed to a high concentration of NOM, and were then redispersed in NOM-free buffer. *Shewanella oneidensis* MR-1 was mixed with NOM-treated citrate- or PVP-capped AgNPs and cellular membrane integrity was evaluated as a function of NOM type. Nanoparticle-induced membrane damage, a known mechanism of AgNP bactericidal activity,^{152,300} was observed by monitoring the relative fluorescence emission intensities of two nucleic acid probes, one of which is cell membrane-permeable, thus labeling all cells, and one which is cell membrane-impermeable, thus labeling only membrane-compromised cells. The relative fraction of membrane-compromised cells in a sample was then determined by calculating the ratio of fluorescence emission intensity of these probes normalized to a sample receiving no nanoparticle treatment.

Our results (Figure 3c) demonstrate that the bactericidal efficacy of citrate-capped AgNPs was reduced after exposure to PLFA, while SRFA and SRHA had no effect. This is consistent with the results of our ISE dissolution studies, which indicated that PLFA was the only NOM type to significantly reduce Ag⁺ release from AgNPs (Figure 3b). The relative impact of the NOM types used here on AgNP dissolution is also consistent with the results of our related study in which ISEs were used to measure Ag⁺ binding to NOM in the absence of AgNPs.²⁶⁸ Addition of PLFA to a Ag⁺ solution significantly decreased the

free Ag^+ concentration, indicating binding of NOM to Ag^+ , while SRHA and SRFA induced smaller decreases. In the present study, PVP-capped AgNPs were also observed to be less toxic than citrate-capped AgNPs, consistent with their significantly lower release of Ag^+ (Figure 3b). Complexation of Ag^+ with NOM on the nanoparticle surface or in the bulk may decrease its bulk concentration and lower the bactericidal efficacy of the nanoparticle. Passivation of the nanoparticle surface by adsorbed or covalently bound NOM may also suppress Ag^+ release in an analogous way to that described above for PVP. While direct evaluation of these proposed mechanisms is beyond the scope of this work, we note Liu et al.'s suggestion that both Ag^+ complexation with surface capping agents and AgNP surface passivation by ligands with high Ag-affinity are chemical approaches to control Ag^+ release from AgNPs.²⁶⁴ Some studies suggested that NOM may reduce AgNP toxicity indirectly, that is, by influencing processes other than nanoparticle dissolution (e.g., AgNP interaction with the bacterial cell surface or scavenging of reactive oxygen species).²⁶⁹ While our results do not exclude this possibility, they suggest that AgNP toxicity to bacteria is highly dependent on nanoparticle dissolution, a process that is in turn dependent on the chemical composition of the nanoparticle capping agent and, if present, NOM.

2.4 Conclusions

The results of our AgNP colloidal stability, dissolution, and toxicity studies suggest that NOM with high affinity for Ag (i.e., NOM rich in some sulfur and nitrogen compounds) will induce the greatest increase in AgNP colloidal stability, the greatest decrease in nanoparticle release of Ag^+ , and the greatest decrease in AgNP bactericidal efficacy. NOM

with lower affinity for Ag (i.e., NOM lower in reduced sulfur and nitrogen) will increase AgNP colloidal stability but have limited impact on nanoparticle release of Ag⁺ or bactericidal efficacy, potentially increasing the persistence and impact of AgNPs in natural aquatic environments. The magnitude of this effect is expected to depend on the relative concentrations of NOM in the bulk solution (where higher concentrations lead to greater complexation of NOM with Ag⁺ and may in some cases reduce AgNP bactericidal efficacy),²⁶⁸ and on the particle surface (where higher concentrations lead to greater colloidal stability but, in some cases, have no impact on Ag⁺ release relative to less colloidal stable AgNPs). In addition, our results indicate that exposure to NOM improves the colloidal stability of AgNPs by delaying the onset of aggregation rather than by eliminating it completely. We show that NOM can reduce the rate of AgNP aggregation over 1-8 days, but additional studies are needed to understand the longer-term aggregation behavior of AgNPs exposed to NOM. The present results and those of our study considering Ag⁺ only²⁶⁸ suggest that the effect of NOM on the bactericidal efficacies of Ag⁺ and AgNPs are not easily predicted by either the magnitude of NOM-Ag⁺ complexation or the extent of NOM association with the AgNP surface. Therefore, the consequences of AgNP release into natural aquatic ecosystems containing NOM must be evaluated in an environment-specific context.

2.5 Acknowledgements

This work was supported by a UMN Doctoral Dissertation Fellowship to M.P.S.M., UMN Biotechnology Institute Training Grant and Torske Klubben Fellowship to I.L.G.;

Heisig/Gleysteen Fellowship to K.H., and NSF Award #CHE-1152931. Parts of this work were performed at the UMN Characterization Facility, which receives partial support from the MRSEC NSF program. Thanks to Katie Hurley and Samuel Egger for acquiring TEM images.

2.6 Supporting Information

2.6.1 Characterization of AgNPs by TEM and Zeta-potential Measurements.

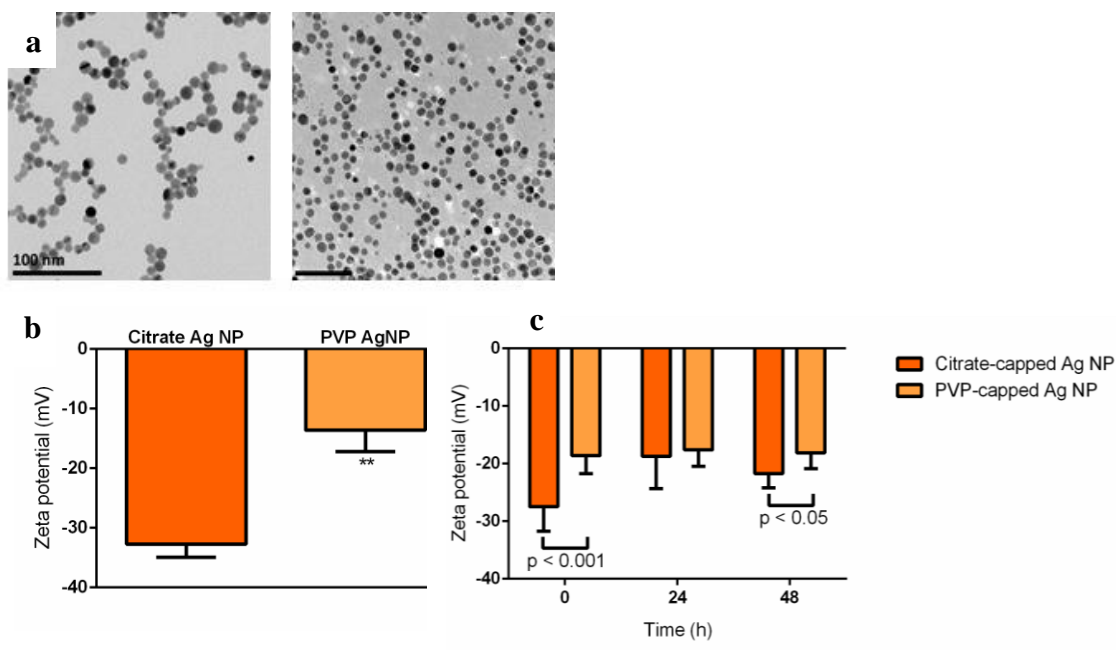


Figure S1. TEM micrographs of citrate-capped AgNPs (top left) and PVP-capped AgNPs (top right) reveal no change in nanoparticle size following exchange of the capping agent (a). Zeta potentials of freshly prepared AgNPs in deionized water (pH 6), where citrate- and PVP-capped AgNPs have average zeta potentials of -32.8 ± 2.2 mV and -13.6 ± 3.6 mV (b). Error bars represent the standard deviation of three independent replicates, each consisting of three zeta-potential measurements. Asterisks indicate $p < 0.01$ as calculated

by the unpaired t-test. Stability of citrate- and PVP-capped AgNP zeta potentials over 48 h in deionized water of pH 6 (c). P values shown were calculated by the unpaired t-test.

2.6.2 Aggregation of Citrate-capped AgNPs in a High Ionic Strength Buffer Containing 10 mg/L NOM Observed by UV-vis Extinction Spectroscopy.

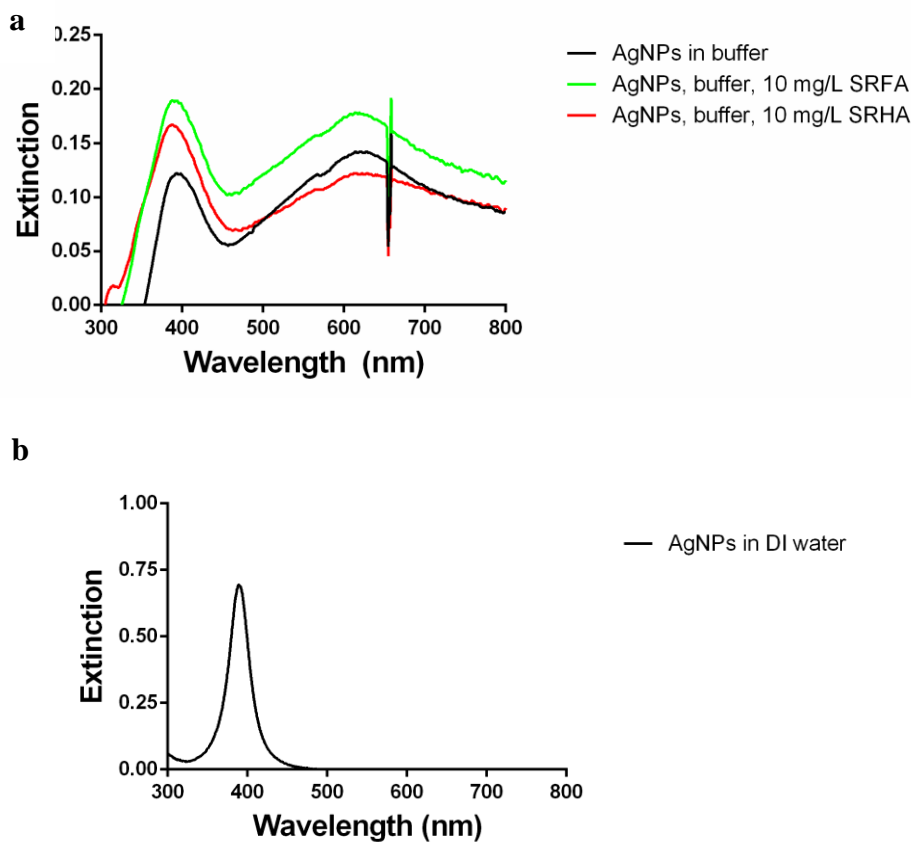


Figure S2. UV-vis extinction spectroscopy indicates that the addition of 10 mg/L NOM to a 0.1 M ionic strength phosphate buffer does not stabilize the AgNPs against homoaggregation, since the broad peak with maximum near 620 nm, attributable to variable-sized AgNP aggregates, is present in samples with and without NOM (a). Spectra of citrate-capped AgNPs exposed to no NOM, 10 mg/L Suwannee River Fulvic Acid

(SRFA), or 10 mg/L Suwannee River Humic Acid (SRHA) in pH 7.5 phosphate buffer are shown. The feature observed near 670 nm is an instrumental artifact. Prior to AgNP introduction to the high ionic strength buffer with or without NOM, the extinction spectrum showed a single peak centered at 391 nm, indicative of a lack of aggregates and a relatively narrow particle size distribution (b). A representative spectrum is shown.

2.6.3 NOM Elemental Composition

	C	H	O	N	S
Suwannee River Humic Acid Standard II	52.63	4.28	42.04	1.17	0.54
Suwannee River Fulvic Acid Standard II	52.34	4.36	42.98	0.67	0.46
Pony Lake Fulvic Acid Reference	52.47	5.39	31.38	6.51	3.03

Table S1. Elemental compositions of the three NOM models used in this study. Values shown are the percent (w/w) content of a dry, ash-free NOM sample.²⁷⁵

2.6.4 Dark-field Microscopy and Hyperspectral Imaging Characterization of Citrate-capped AgNPs Exposed to NOM.

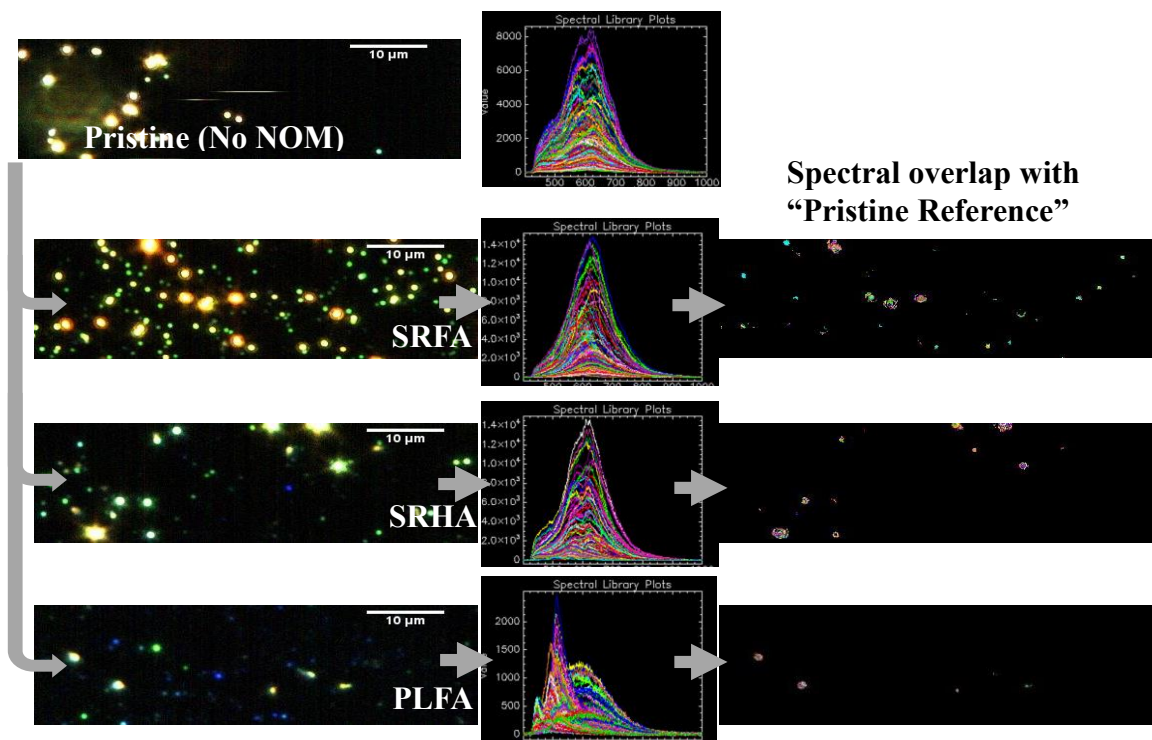


Figure S3. NOM-stabilized AgNPs are shown in order of increasing similarity (bottom to top on the right) to AgNPs without NOM (top left). Dark-field micrographs of citrate-capped AgNPs are shown on the left; these are stabilized with the NOM type indicated. In the images on the right, bright features correspond to areas within the micrographs on the left that have high spectral similarity to NOM-free nanoparticles. An increasing number of bright pixels indicates increasing similarity between the spectral features of the NOM-stabilized nanoparticle and those of NOM-free nanoparticles (i.e., increasing similarity to

heavily aggregated AgNPs). Pixel colors represent distinct wavelengths (within the UV-visible region) at which spectral matches were recorded.

2.6.5 Theoretical Responses of Ag⁺ ISEs.

Potentiometric measurements are performed by the determination of the electrical potential (typically referred to as electromotive force, emf) between the measuring electrode (here the fluoruous-phase Ag⁺ ISE) and a reference electrode, which are both in contact with the sample of interest. Note that the reference electrode provides a constant, sample-independent contribution to the measured emf. Ideally, the emf gives a response that can be described with the Nernst equation, i.e., $\text{emf} = E^\circ + (2.303 R T F^{-1}) \text{Log } a (\text{Ag}^+)$, where T represents the temperature in Kelvin, F is the Faraday constant, and R is the universal gas constant. For example, at 20 °C a tenfold increase in the Ag⁺ activity results in a 58.2 mV increase in the measured emf.⁵⁹ Calibration of the ISEs to determine the constant E° and check the prelogarithmic term (i.e., the response slope in a plot of emf vs $\text{Log } a (\text{Ag}^+)$) may be performed by addition of aliquots of concentrated AgCH₃COO solution (*aq*) to a more dilute solution and measurement of the emf. The emf response of an electrode to Ag⁺ addition provides the calibration curve resulting from that data. Note that the activity of an ion is the product of the ion concentration and an activity coefficient, which depends, in general, on the ionic composition of the sample solution. However, in solutions with a fixed ionic strength, the activity coefficient of Ag⁺ can be assumed to be constant and a plot of the emf vs $\text{Log } c (\text{Ag}^+)$ exhibits the same linearity as the plot of the emf vs $\text{Log } a (\text{Ag}^+)$. Therefore, emf data measured with a calibrated electrode can be converted to concentration

using the calibration equation experimentally determined for that electrode. Figure S4 demonstrates the ISE-measured response to Ag^+ additions to buffer (panel A), and the corresponding calibration curve (panel B).

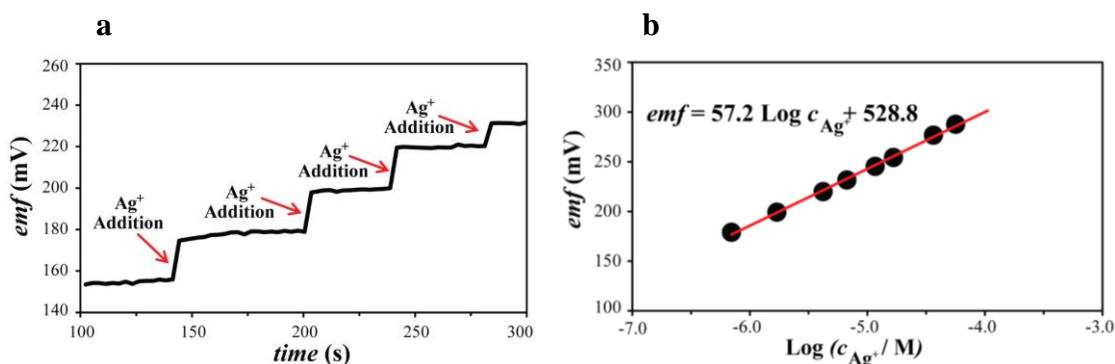


Figure S4: Representative calibration curve of a fluoros-phase Ag^+ ISE. Red arrows indicate additions of aliquots of 10.0 mM AgCH_3COO to the measuring solution. The emf of fluoros-phase Ag^+ ISEs increases after each Ag^+ addition (a). Only a portion of the calibration curve is shown for better visualization. The linear relationship between the emf and $\text{Log } c (\text{Ag}^+)$ can be used as the calibration equation for converting emf values to $[\text{Ag}^+]$ (b).

2.6.6 ISE-measured Dissolution of Citrate-capped AgNPs in pH Buffer Containing 10 mg/L NOM.

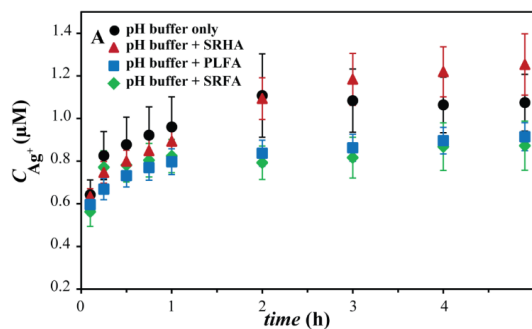


Figure S5. No significant effect of NOM on release of Ag^+ from 5 mg Ag/L citrate-capped AgNPs was observed at low NOM concentrations (10 mg/L) relative to NOM-free solutions. The Ag^+ released was measured with fluoros-phase Ag^+ ISEs in pH = 7.5 buffer with 10 mg/L SRHA, PLFA, or SRFA. Error bars represent the standard deviation of six replicate measurements.

2.6.7 ISE-measured Complexation of Ag^+ and Citrate or Polyvinylpyrrolidone.

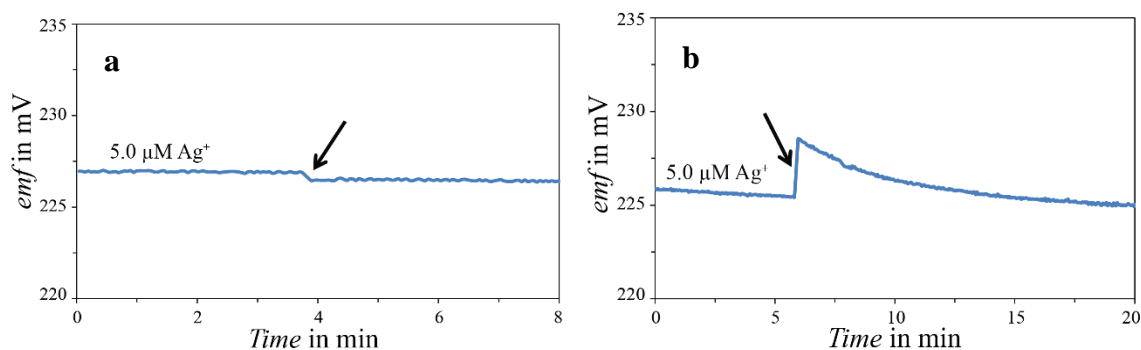


Figure S6. The emf of fluoros-phase Ag^+ ISEs in 5.0 μM AgNO_3 was monitored. (a) Addition of 50 mg/L trisodium citrate occurred at the time indicated by the black arrow and led to a 2% decrease in the Ag^+ concentration. (b) Addition of 50 mg/L polyvinylpyrrolidone (PVP-10) occurred at the time indicated by the black arrow, leading to an emf spike. After equilibration, no significant change in the Ag^+ concentration was observed.

2.6.8 Materials and Methods. *Nanoparticle Synthesis:* Citrate-capped AgNPs were synthesized according to the method used by Hackley and coworkers.²⁶⁰ All glassware was washed with aqua regia (3:1 HCl: HNO_3) and rinsed three times with deionized water (18

MΩ·cm specific resistance, EMD Millipore, Burlington, MA, USA) prior to use. First, 100 mL deionized water was brought to a boil. Then, 365 μL of 34 mM trisodium citrate dihydrate (Sigma Aldrich, St. Louis, MO, USA) and 211 μL of 58.8 mM AgNO₃ (Sigma Aldrich, St. Louis, MO, USA) were added with constant stirring. After 30 seconds, 250 μL of freshly prepared 100 mM aqueous NaBH₄ was added drop-wise, and the mixture was boiled with constant stirring for 15 minutes. The mixture was then removed from heat and allowed to cool to room temperature before beginning purification. To remove synthesis by-products and purify the nanoparticles, 15 mL aliquots of the mixture were loaded into regenerated cellulose (MWCO 50,000) centrifugal filter units (EMD Millipore, Carrigtwohill, Ireland), centrifuged 4 minutes at 1500 RCF, and then resuspended in 15 mL deionized water. Centrifugation and resuspension were repeated two more times. Following the final resuspension in deionized water, the mixture was centrifuged a final time to concentrate the nanoparticles. Nanoparticle concentration in units of silver mass per volume was determined by measuring the UV-visible extinction spectrum (USB2000, Ocean Optics, Dunedin, FL, USA) using the nanoparticle extinction coefficient and silver atom number value reported by Maurer-Jones et al.⁶⁸

Polyvinylpyrrolidone-capped AgNPs were prepared from the above citrate-capped AgNPs through ligand exchange, thus ensuring that nanoparticle core size and shape were preserved. Prior to centrifugal purification, a room temperature AgNP suspension, prepared as described above, was centrifuged for 30 minutes at 12500 RCF to pellet the nanoparticles. The supernatant was removed, replaced with 26 g/L PVP-10 (Sigma Aldrich, St. Louis, MO, USA), and incubated at room temperature in the dark with constant stirring

for four days. The AgNP suspension was then purified using centrifugal filter units as described above.

Transmission Electron Microscopy (TEM): Room temperature TEM images of AgNPs were acquired with a FEI Tecnai T12 microscope (FEI, Inc., Hillsboro, OR) operating at 120 kV. A 200 mesh copper grid with Formvar and carbon supports was dipped into a ~0.3 mg/mL NP suspension, then removed and allowed to dry before imaging. Image analysis was performed in ImageJ.³⁰¹

Zeta Potential Measurement: The zeta potential of citrate- and PVP-capped AgNPs was measured using a Brookhaven ZetaPALS Zeta-Potential and Particle Sizing Analyzer (Holtsville, NY). Three independent samples were prepared by diluting the purified nanoparticle suspensions to 5 mg Ag/L in deionized water (pH 6).

Buffer Preparation: The buffer used in all nanoparticle stability and dissolution experiments was prepared by combining 0.028 M K_2HPO_4 and 0.015 M KH_2PO_4 in deionized water and adjusting the pH to 7.5 by KOH additions.

UV-vis Extinction Spectroscopy: The AgNP aggregation state was tracked over 46 hours at room temperature by monitoring light extinction in the UV-visible range caused by the localized surface plasmon resonance (LSPR) effect using an OceanOptics USB2000 spectrometer coupled to a MicroPack DH-2000 UV-vis-NIR light source. Deionized water or deionized water with 10 mg/L NOM served as the blank references, and measurements were performed on two independent samples.

Dynamic Light Scattering Measurement: The Z-average particle size of citrate- and PVP-capped AgNPs was measured over 196 hours using a Brookhaven ZetaPALS Zeta-Potential and Particle Sizing Analyzer (Holtsville, NY). Three independent samples were analyzed using three analytical replicates per sample.

Dark-field Microscopy and Hyperspectral Imaging: While dark-field microscopy provides only qualitative information regarding AgNP stability, when performed in conjunction with hyperspectral imaging, it offers a semi-quantitative method to assess particle stability. In this work, hyperspectral scans consisting of hundreds of visible-near-infrared spectra were acquired within the field of view of a given dark-field image. These spectra are generated exclusively from light scattered at the nanoparticle surface and not absorbed light, since oblique-angle illumination is used. Scattered light intensity is dependent on the resonance frequency of localized surface plasmons at the nanoparticle surface, which in turn is dependent on the material dielectric properties (or refractive index), size, shape, and interparticle spacing. Aggregation of AgNPs results in a significant change in the localized surface plasmon resonance frequency (see Figure 1 in the main text), leading to shifts in hyperspectral features.

Hyperspectral scans acquired within the field of view of a given dark-field image were pooled into spectral libraries characteristic of each AgNP type (i.e., with different types of NOM). Spectral libraries of different nanoparticle conditions were compared using Spectral Angle Mapping similarity analysis software (ENVI 4.8, Exelis Visual Information Solutions, Boulder, CO). This similarity analysis yields plots (see Figure S3, right-hand side) in which the x- and y-axes indicate position within a corresponding dark-field image,

and the pixel brightness indicates spectral matches to a reference sample (here, AgNPs without NOM) above a defined threshold (here, 95% spectral similarity). No further normalization of these data are required, since the relative fraction of bright pixels (in the similarity plots) to total nanoparticles (in the dark-field images) indicates the degree of similarity between AgNPs exposed to NOM and pristine AgNPs in the reference sample.

Dark-field micrographs of AgNPs exposed to NOM were acquired on an Olympus BX43 microscope (Olympus America, Inc., Center Valley, PA) modified with a high signal-to-noise darkfield condenser unit from CytoViva (Auburn, AL). A 3 μ L sample aliquot was loaded onto a glass slide, covered with a coverslip, and imaged using a 150 W quartz-halogen lamp (Fiber-Lite DC-950, Dolan-Jenner Industries, Boxborough, MA), 100x 1.3 NA oil-immersion objective, and 12 bit CCD camera (pco.pixelfly, PCO, Kelheim, Germany). A hyperspectral imaging system consisting of a spectrophotometer (Specim, Oulu, Finland) and spectrophotometer-integrated CCD (pco.pixelfly, PCO, Kelheim, Germany) was then used to acquire hyperspectral images within the same field of view as the dark-field image.

Fabrication of Ag⁺-Selective Electrodes with Fluorous Sensing Membranes: Ion-selective electrodes (ISEs) were fabricated as reported.⁶⁰ Sensing phases were prepared by adding 0.5 mM ionic sites (sodium tetrakis[3,5-bis(perfluorohexyl)phenyl]borate) and 1.5 mM ionophore (1,3-bis(perfluorooctyl-ethylthiomethyl)benzene)⁶¹ into perfluoroperhydrophenanthrene (Alfa Aesar, Ward Hill, MA, USA). The mixture that resulted was stirred for at least a day to make sure that all the membrane components were completely dissolved. FluoroporeTM filters (porous poly(tetrafluoroethylene), 47 mm diameter, 0.45

μm pore size, 50 μm thickness, 85% porosity) from EMD Millipore (Bedford, MA, USA) were placed between two sheets of paper and cut with a 13-mm-diameter hole punch. This gave porous filter disks that were then used to mechanically support the sensing phase. Approximately 25 μL of this sensing phase was subsequently placed onto a stack of 2 porous filter disks. Complete penetration of the sensing phase into the porous supports was indicated by translucence of the filter disks.

The sensing membranes (i.e., the filter disks infiltrated with the fluoros sensing phase) were then mounted into custom-machined electrode bodies (prepared in house from poly(chlorotrifluoroethylene), as reported previously).⁶¹ For this purpose, a cap with a hole (8.3 mm diameter) in its center was screwed onto the electrode body, which positioned the sensing membrane between the cap and the electrode body but left all but the edge of the membrane exposed. Inner filling solution, 1 μM AgCH_3CO_2 (Sigma Aldrich, USA), was filled into the electrode bodies, and a AgCl -coated silver wire was inserted into this solution to act as the inner reference electrode. To replace the sodium ions in the thus prepared sensing membranes with silver ions, all electrodes were soaked prior to measurements for one day in 100 mL 0.1 mM AgCH_3CO_2 solution and then for another day in 100 mL 1.0 μM AgCH_3CO_2 . This process is typically referred to as membrane conditioning.

Experimental Details of the Potentiometric Measurements: An EMF 16 potentiometer (Lawson Labs, Malvern, PA, USA) with EMF Suite 1.02 software (Lawson Labs) was used for all potentiometric measurements, which were performed at room temperature in stirred solutions. The external reference electrode (relative to which all measurements with fluoros membrane ISEs were performed) was a double-junction AgCl/Ag electrode with

a AgCl saturated 3.0 M KCl reference electrolyte and 1.0 M LiOAc bridge electrolyte. All measurements were performed as at least 3 replicates. Successive addition of aliquots of 10 mM AgCH₃CO₂ solution to deionized water or the pH buffers was used to provide the data for calibration curves.

For the observation of nanoparticle dissolution, three ISEs were fabricated, calibrated, and inserted into 100 mL of the solution in which dissolution was going to take place. AgNPs were purified as described above and were added to the solution of interest to give AgNP concentrations of 5 mg Ag/L. Sensor monitoring was performed for 5 hours. All electrodes were calibrated once more after the NOM additions to confirm that the electrodes still exhibited stable responses to Ag⁺.

Bacterial Membrane Integrity Assay: Bacterial membrane integrity was evaluated after AgNP exposure using the LIVE/DEAD BacLight Viability Kit (Product L-7012, Life Technologies). Cells cultured in LB broth were centrifuged at 2000 RCF for 10 minutes and resuspended at a concentration of 2×10^8 cells/mL in pH 7.5 phosphate buffer. Then 1 mL of cell suspension was mixed with purified citrate- or PVP-capped AgNPs (5 mg Ag/L) that had been incubated overnight with or without NOM as described in the Materials and Methods. After 30 minutes of room temperature incubation, cells were centrifuged at 2000 RCF for 10 minutes, the supernatant was removed, and cells were resuspended in pH 7.5 phosphate buffer. Then 100 μ L of each sample was mixed with 100 μ L of a mixture of 3.34 mM Syto-9 and 20 mM propidium iodide provided in the BacLight Viability Kit in a 96 well plate. After a 15 minute room temperature incubation, fluorescence emission intensities at 528/20 nm (Syto-9 emission) and 635/32 nm (propidium iodide emission)

were measured on a Synergy 2 Multi-Mode Reader (BioTek, Winooski, VT) using an excitation wavelength of 485/20 nm. The response of cells exposed to NOM in the absence of AgNPs (at a concentration matching that present in samples exposed to AgNPs pre-incubated with NOM) was not significantly different from that of the negative control (cells exposed to neither AgNPs nor NOM).

Chapter 3

Dynamic Silver Speciation as Studied with Fluorous-Phase Ion-Selective Electrodes: Effect of Natural Organic Matter on the Toxicity and Speciation of Silver

Adapted from:

Mousavi, M. P. S., Gunsolus, I. L.; Perez de Jesus, C. E., Lancaster, M., Hussein, K.,
Haynes, C. L., Bühlmann, P. *Sci. Total Environ.* **2015**, 537, 453-461

Copyright ©2015 Elsevier. All rights reserved.

This work was a joint effort of this author and Maral Mousavi, who characterized silver speciation using silver-ion selective electrodes. Carlos Pérez de Jesús and Mitchell Lancaster assisted with electrode fabrication and solution preparation under the guidance of Maral Mosuvai, and Kadir Hussein assisted with assessment of silver toxicity to *Shewanella oneidensis* under the guidance of this author.

The widespread application of silver in consumer products and the resulting contamination of natural environments with silver raise questions about the toxicity of Ag^+ in the ecosystem. Natural organic matter, NOM, which is abundant in water supplies, soil, and sediments, can form stable complexes with Ag^+ , altering its bioavailability and toxicity. Herein, the extent and kinetics of Ag^+ binding to NOM, matrix effects on Ag^+ binding to NOM, and the effect of NOM on Ag^+ toxicity to *Shewanella oneidensis* MR-1 (assessed by the BacLight Viability assay) were quantitatively studied with fluoruous-phase Ag^+ ion-selective electrodes (ISEs). Our findings show fast kinetics of Ag^+ and NOM binding, weak Ag^+ binding for Suwannee River humic acid, fulvic acid, and aquatic NOM, and stronger Ag^+ binding for Pony Lake fulvic acid and Pahokee Peat humic acid. We quantified the effects of matrix components and pH on Ag^+ binding to NOM, showing that the extent of binding greatly depends on the environmental conditions. The effect of NOM on the toxicity of Ag^+ does not correlate with the extent of Ag^+ binding to NOM, and other forms of silver, such as Ag^+ reduced by NOM, are critical for understanding the effect of NOM on Ag^+ toxicity. This work also shows that fluoruous-phase Ag^+ ISEs are effective tools for studying Ag^+ binding to NOM because they can be used in a time-resolved manner to monitor the activity of Ag^+ in situ with high selectivity and without the need for extensive sample preparation.

3.1 Introduction

Silver has been estimated to be released into the environment at more than 2500 tons annually.³⁰² Since ionic silver, Ag^+ , is known to be highly toxic to bacteria, the sustainable use of silver-containing products, such as silver nanoparticles, requires a thorough understanding of the environmental toxicity of Ag^+ ions. Silver toxicity cannot be correlated to just the total silver present. Instead, the individual silver species must be considered for a correct assessment of toxicity. One of the main mechanisms of silver speciation is Ag^+ coordination with ligands that occur naturally in the environment. For example, Ag^+ is known to form stable complexes with Lewis bases such as amines, halides, and thiolates. Thiosulfate, sulfide, and chloride binding to Ag^+ have been shown to reduce the toxicity of Ag^+ .^{303–306} Consequently, the formation of silver complexes depends heavily on the environmental conditions.³⁰² For a meaningful assessment of Ag^+ toxicity, the coordinating ligands present in any particular environment must be identified, and their effect on the Ag^+ toxicity must be characterized.

One of the most common coordinating substances in natural soil and aquatic environments is natural organic matter (NOM; also commonly referred to as dissolved organic matter, DOM). There have been several reports of heavy metal ion binding to NOM, such as for Cu^{2+} , Pb^{2+} , Cd^{2+} , and Zn^{2+} .^{286,307–310} This binding results in the formation of new chemical species with altered toxicity and transport properties, which affects the bioavailability of these metals.^{307,311,312} NOM is found in environmental systems, such as surface waters, ground waters, soils, and sediments, in concentrations ranging from 1 up to more than 100 mg/L.^{269,313–316} NOM results from the decomposition of plant and animal residues and is

inherently a mixture of compounds without a well-defined molecular structure.³¹⁷ NOM consists largely of humic substances (humic acids, HA, and fulvic acids, FA) but also includes non-humic substances, such as fatty acids, sterols, natural sugars, amino acids, urea, and porphyrins.³¹⁸ Humic substances have molecular weights in the range from 300 to 300,000 and have a predominantly aromatic structure. Because they have many oxygen- and nitrogen-containing functional groups, such as carboxylic, phenolic, and amino groups, they exhibit an acidic and hydrophilic character and have high metal coordinating abilities.^{315,319} Due to their abundance in the hydrosphere, biosphere, and lithosphere, and their ability to form stable complexes with metals from both natural and anthropogenic sources, humic substances are commonly used as models for studying metal and NOM speciation.^{269,307,317,320} In this study, we utilized humic substances as models for studying the effect of NOM on Ag^+ speciation and toxicity.

Analytical methods that have been used in NOM/ Ag^+ speciation studies have been based on ion exchange equilibrium,^{321,322} equilibrium dialysis,^{259,318,321} atomic absorption and emission spectroscopy, mass spectrometry,^{313,316,323} ion-selective potentiometry,^{81,286,313,324} and the assessment of Ag^+ and Ag^+ -NOM complex toxicity towards organisms.^{269,322} Several reports suggest that NOM samples from various sources decrease the toxicity of Ag^+ to various organisms.^{79,306,311,325-329} This effect is usually attributed to Ag^+ binding to NOM, which lowers the free Ag^+ activity and, thereby, mitigates the ability of silver to act at the sites of toxic action in organisms.^{304,311} On the contrary, some NOM samples were reported to have no significant effect on the toxicity of Ag^+ to multiple organisms, and in these cases Ag^+ binding to NOM was concluded to be insignificant.^{269,322} Surprisingly,

there has been no report to date that quantitatively investigates the correlation between the extent of Ag^+ binding to NOM and Ag^+ toxicity. Clearly, to investigate this correlation, it is advantageous to use techniques that directly probe Ag^+ speciation without the added complexity introduced by the choice of organism, cell culture medium, and the type of toxicity assay as it is necessary in an indirect toxicology assessment.

A challenge in direct Ag^+ speciation studies is distinguishing different silver species, i.e., Ag NPs, free Ag^+ , and Ag^+ -NOM complexes. Except for ion-selective potentiometry, all the techniques mentioned above lack this ability. To account for this lack of selectivity, specific silver species are usually isolated by several sample preparation steps, e.g., by using molecular cut-off filters³²³ or centrifugation.³²³ Unfortunately, this sample preparation can introduce further complexity and potential errors in measurements and the interpretation of results. Such complications include silver adsorption to sample containers and interference from positively charged complexes (in the case of the ion exchange equilibrium method). Moreover, these methods cannot be used for in situ or kinetic studies due to the long analysis time resulting from the need for sample preparation (e.g., analysis times are approximately 2 h for ion exchange equilibrium methods³²¹ and 3 days for equilibrium dialysis³²¹). Even though binding of Ag^+ to NOM has been studied for more than a decade, and several hypotheses about its kinetics have been proposed, the kinetics of this reaction have not been investigated directly, possibly due to the lack of appropriate methodology.^{310,324,327}

Potentiometry with ion-selective electrodes, ISEs, offers selective and sensitive in situ Ag^+ detection, requires no substantial sample preparation, is non-destructive, has fast response

times, detects only non-complexed ions, and can be used for speciation and kinetics studies.⁵⁹ There have been few literature precedents for use of commercially available solid-state ISEs to study Ag^+ speciation,^{68,286,313,324,330} possibly due to the common issue of solid state ISE biofouling in biological samples (biological molecules such as proteins adsorb strongly through sulfur groups to silver halide and sulfide electrodes).^{331–334} ISEs with polymeric sensing membranes suffer less from adsorption but extraction of lipophilic biological interferents into their sensing membranes is still causing biofouling of these ISEs.^{335,336} In this work, we used ionophore-doped ISEs with fluoruous sensing membranes that are less susceptible to biofouling effects. Fluorous phases prepared from perfluorocarbon derivatives have low polarity and polarizability, are both hydrophobic and lipophobic (i.e., alkanes are not miscible with perfluoroalkanes), limit extraction of lipophilic interferents into the sensing membrane, and thus are less susceptible to biofouling than other polymeric membrane ISEs.⁶² Moreover, fluoruous-phase Ag^+ ISEs offer exceptional Ag^+ selectivity due to the non-coordinating and poorly solvating properties of the fluoruous phase. They also exhibit a fast response times (less than 1 s), making them a unique tool for environmental Ag^+ speciation studies.^{60,61,68} We used these sensors to study open questions regarding the interaction of Ag^+ and NOM, specifically the kinetics of Ag^+ and NOM binding and the correlation between the extent of Ag^+ binding to NOM and the resulting Ag^+ toxicity. While the current study focuses on Ag^+ binding to NOM, the effect of NOM on the toxicity of silver nanoparticles is also crucial for a thorough risk assessment of silver-containing products and was addressed in parallel work.⁸¹

3.2 Experimental Section

NOM samples: Suwannee River humic acid II, SRHA (Cat. No. 2S101H), Suwannee River fulvic acid II, SRFA (Cat. No. 2S101F), Pony Lake fulvic acid, PLFA (Cat. No. 1R109F), Pahokee Peat humic acid standard, PPHA (Cat. No. 1S103H), and Suwannee River Aquatic NOM, SRNOM (Cat. No. 2R101N) were purchased from the International Humic Substances Society, IHSS (St. Paul, MN). The fabrication and calibration of fluoros-phase Ag^+ ISEs was reported previously⁶⁸ and is discussed in the Supporting Information along with a description of the data analysis methods. Buffer preparation and toxicity assessments are also explained in detail the Supporting Information. All the solutions were prepared with deionized water (18 M Ω cm specific resistance, EMD Millipore, Burlington, MA). For preparation of the pH = 6.0 buffer, 0.100 M NaCH_3CO_2 and 0.006 M $\text{CH}_3\text{CO}_2\text{H}$ were mixed at room temperature, followed by adjustment of the pH by addition of aliquots of NaOH or $\text{CH}_3\text{CO}_2\text{H}$. The components of the pH = 7.5 buffer were 0.028 M K_2HPO_4 and 0.015 M KH_2PO_4 . The pH of the solution was adjusted to 7.5 by addition of aliquots of KOH. The pH = 9.0 buffer contained 0.087 M NaHCO_3 and 0.044 M Na_2CO_3 , and the pH was adjusted by addition of aliquots of NaOH. The HEPES buffer with pH = 7.5 was prepared by dissolving 0.20 M HEPES, 4-(2-hydroxyethyl)piperazine-1-ethanesulfonic acid, in deionized water, and the pH of the solution was adjusted to 7.5 by addition of aliquots of KOH. The MOPS buffer with pH = 7.5 was prepared by dissolving 0.30 M MOPS, *N*-morpholino-3-propanesulfonic acid, in deionized water, and the pH of the solution was adjusted to 7.5 by addition of aliquots of KOH.

The components of the phosphate (pH=7.5), carbonate (pH=9.0), and acetate (pH=6.0) pH buffers were chosen to interact minimally with Ag^+ and thus minimize the interference with respect to Ag^+ binding to NOM. The latter was assessed by measurements of the potentiometric response to Ag^+ by fluoruous-phase Ag^+ ISEs in deionized water and in pH buffers. The response for deionized water and all the pH buffer solutions were very similar, which confirmed that Ag^+ did not bind significantly to the pH buffer components (less than 15 mV and 2 mV change in the intercept and slope of the calibration equation, respectively). In the case of Ag^+ binding to the pH buffer components, the calibration equation would have shifted to lower emf values because of the lowering of the concentration of free Ag^+ ions as a result of complexation,⁶⁸ which must be prevented to avoid errors and an unrealistic evaluation of Ag^+ binding to NOM. Silver toxicity to the test organism, *Shewanella oneidensis* MR-1, assessed by evaluating bacterial membrane integrity after exposure to Ag^+ using the LIVE/DEAD BacLight Viability Kit (Product L-7012, Life Technologies).

3.3 Results and Discussion

3.3.1 Ion-Selective Electrodes. The electrical potential of an ISE is measured with respect to a reference electrode and is referred to as emf (see Figure 1). At a constant temperature, the emf increases linearly with the logarithm of the Ag^+ activity. For example, at 20 °C, a 10-fold increase in the activity of Ag^+ results in a 58.2 mV increase in the emf.^{59,337,338} The fluoruous-phase Ag^+ ISEs were calibrated by addition of aliquots of concentrated AgCH_3COO (aq), followed by measurements of the emf. As predicted by theory, a linear

relationship between the emf and $\text{Log } c(\text{Ag}^+)$ was observed for solutions with a fixed ionic strength, where activity coefficients are assumed to be constant (see Figure 1). The experimentally obtained emf data can be easily converted to Ag^+ concentrations using the calibration equations. The inherent response time of an ionophore-based ISE for the target ion is determined by ionic redistribution across the nanometer-sized charge separation layer at the interface of the sample and the ISE sensing membrane. In a typical experiment, the response time of the ISE measurement is, therefore, determined by how quickly an old sample can be replaced by a new one and not by a property of the electrode itself. In this work, all solutions were stirred, resulting in response times of less than one second (see Figure 1). The detection limit of the fluorous-phase Ag^+ ISEs used in this work was 0.05 μM . This is not an inherent limitation of these ISEs and with proper optimization, detection limits as low as 4.0×10^{-11} M have with been achieved with fluorous sensing membranes (Lai et al., 2010). It should be noted that ISEs selectively detect un-complexed (“free”) Ag^+ . This allowed us, in previous work, to utilize fluorous-phase Ag^+ ISEs to quantify the Ag^+ speciation in bacterial growth media and show that, in cell culture media that are rich in coordinating ligands, less than 5% of the silver is in the free Ag^+ form.⁶⁸ We also showed that these sensors can be used for dynamic monitoring of Ag^+ release from silver nanoparticles in the presence of interfering capping agents such as trisodium citrate.^{68,81} That work suggested that these sensors would very likely also be useful analytical tools for probing Ag^+ binding to NOM.

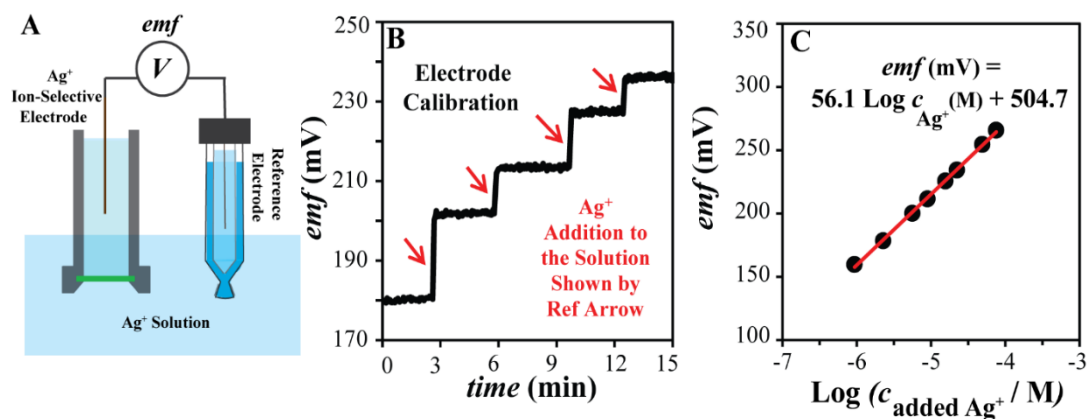


Figure 1. Fluorous-phase Ag^+ ISE setup and preparation of a calibration curve. Experimental Setup (A). Red arrows indicate additions of AgCH_3COO aliquots to the measuring solution (B). The emf of the fluorous-phase Ag^+ ISE increases after each rise in Ag^+ concentration. For better visualization, only a snapshot of the addition experiment is shown. The linear relationship between the emf and $\text{Log } c_{\text{Ag}^+}$ can be used as the calibration equation for converting emf values to Ag^+ concentrations (C).

3.3.2 Interference of the Sample Matrix on Ag^+ Binding to NOM. NOM has both acidic and basic functional groups that, upon introduction into a solution, can affect the pH, which will influence the strength of Ag^+ binding to NOM. For a meaningful evaluation of the extent of Ag^+ binding to NOM it is, therefore, important to choose pH-buffered test solutions that are representative of environmental samples. There have been several reports of silver speciation in silver nanoparticle solutions as well as of Ag^+ binding to NOM that described the use of pH buffer components such as *N*-morpholino-3-propanesulfonic acid (MOPS) or 4-(2-hydroxyethyl)piperazine-1-ethanesulfonic acid (HEPES).^{259,321,322,339–343}

HEPES and MOPS were recommended because they were reported not to bind several heavy metal ions such as copper, cadmium, and zinc.^{321,344-346} Because HEPES and MOPS contain amino groups (see structure formulas in Scheme S1 in the SI), and because Ag^+ is well known to form stable complexes with amines, we suspected that HEPES and MOPS form complexes with Ag^+ , considerably complicating any speciation studies. The complexation of HEPES and MOPS with Ag^+ was confirmed by monitoring the emf of fluoruous-phase Ag^+ ISE. Immediately after addition of HEPES and MOPS to a $5.0 \mu\text{M}$ Ag^+ solution, the emf decreased, indicating a decrease in the concentration of free Ag^+ as a result of Ag^+ binding to the buffer species (see Figure 2A). To quantify the extent of HEPES and MOPS complexation with Ag^+ , HEPES, MOPS, and phosphate buffers (the latter has a low tendency to coordinate with Ag^+) with $\text{pH}=7.5$ and an ionic strength of 0.1 M were prepared, and potentiometric responses to Ag^+ in these pH buffers as well as in deionized water were measured (see Figure S1). Because of Ag^+ binding to the pH buffer components, the calibration curves shifted to lower emf values when the emf was plotted versus the total silver concentration in the calibration solutions (see Figure 2B).⁶⁸ Use of the calibration curve obtained in deionized water for comparison (Figure S1) shows that only 10% of the Ag^+ in the MOPS buffer and less than 1% of the Ag^+ in the HEPES buffer is in its free (uncomplexed) form. In contrast, almost 99% of the Ag^+ in the phosphate buffer is in the free and non-complexed form (see Figure 2C). This is of great importance because HEPES and MOPS have been used as pH buffer components in a number of Ag^+

speciation and mechanistic studies without consideration of their high tendency for coordination with Ag^+ .^{321,322,340,343}

Figure 2D illustrates the extent of HEPES interference in Ag^+ binding to NOM, where Pony Lake fulvic acid (PLFA) was added to $5.0 \mu\text{M}$ Ag^+ in either HEPES buffer (which competes with NOM in binding to Ag^+) or phosphate buffer (which does not interfere with binding). Both buffers had the same pH (7.5). Upon addition of PLFA to $5.0 \mu\text{M}$ Ag^+ in the phosphate buffer, the emf is significantly decreased by more than 20 mV (which corresponds to a 50% decrease in the free Ag^+ concentration due to Ag^+ binding to NOM), but a similar addition of PLFA to $5.0 \mu\text{M}$ Ag^+ dissolved in HEPES buffer resulted in no detectable emf change (two-tailed t test, $p < 0.05$). This can be explained by considering that 99% of the silver is bound to the HEPES buffer, making it impossible for the PLFA to compete with HEPES to form Ag^+ -NOM complexes in a significant amount.

Coordinating ligands such as HEPES and MOPS are not present in authentic environmental samples. To prevent errors in the evaluation of Ag^+ binding to NOM, such buffers should be avoided. Herein, we will utilize a potassium phosphate buffer with an ionic strength of 0.1 M to minimize buffer artifacts. Use of a fixed ionic strength ensures that the activity coefficients are approximately constant and that the interaction of Ag^+ and the NOM is not simply electrostatically driven but is the result of specific metal ligation to functional groups of the NOM.²⁸⁶ Note that the phosphate buffer is representative of real-life conditions since most high concentration components of real-life samples (i.e., specifically, Na^+ , K^+ , HCO_3^- , SO_4^{2-} , NO_3^- , F^- , Mg^{2+} , and Ca^{2+}) will not directly interfere with Ag^+

speciation.^{68,347} However, chloride, which occurs in natural water supplies in high concentrations, will compete with NOM to bind to Ag^+ and will affect the extent of Ag^+ binding to NOM binding. Therefore, we excluded Cl^- from our test matrix, facilitating the investigation of the extent of Ag^+ binding to NOM and its correlation to protective effects of NOM against Ag^+ toxicity.

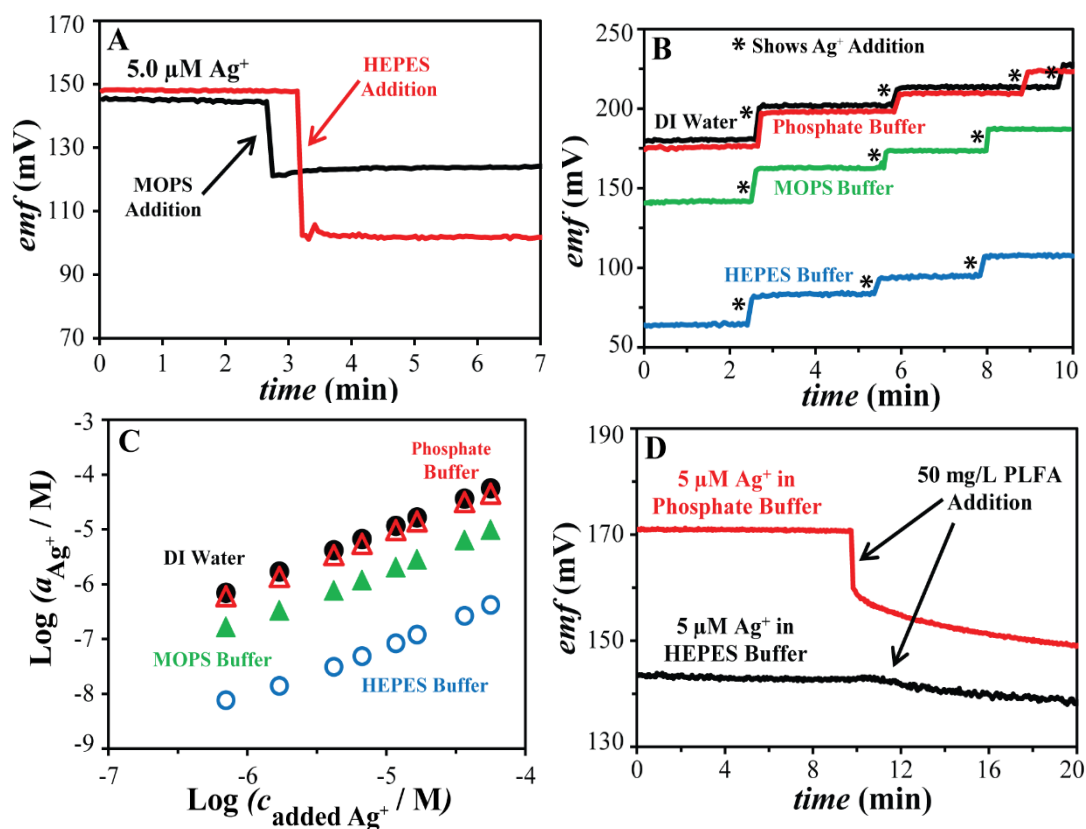


Figure 2. Interference of buffer components on Ag^+ binding to NOM at pH 7.5, as studied by fluorine-phase Ag^+ ISEs. Concentrated HEPES (shown in red) and MOPS (shown in black) were added to $5.0 \mu\text{M Ag}^+$ solutions to reach a final concentration of the buffer of 0.05 M (A). Aliquots of AgNO_3 were added (shown by asterisks) to deionized water (black), phosphate buffer (pH = 7.5, red), MOPS buffer (pH = 7.5, green), and HEPES

buffer (pH = 7.5, blue), while monitoring the emf (B and C). The quickness of the emf response is illustrated by the emf time trace shown in Panel A. Panel C shows the concentration of free Ag^+ in the buffer solutions as a function of the total silver concentration in solution, as determined from the calibration curve in buffer free solution. Panel D illustrates the interference of HEPES when studying Ag^+ binding to NOM.

3.3.3 Binding of Ag^+ to NOM. The concentration of NOM in natural environments ranges from 0.1 to 100 mg/L, with a mean value of 45 mg/L.^{315,318,348–350} Thus, to cover the most environmentally relevant NOM concentration range, we looked at 50 mg/L NOM in this study. We considered five different NOM isolates: Suwannee River humic acid II (SRHA), Suwannee River fulvic acid II (SRFA), Pony Lake fulvic acid (PLFA), Pahokee Peat humic acid standard, PPHA, and Suwannee River Aquatic NOM (SRNOM). To quantify Ag^+ binding to NOM, fluoros-phase Ag^+ ISEs were placed in a solution of 5.0 μM AgCH_3COO with a pH buffered to 7.5 and a fixed ionic strength. Aliquots of concentrated solutions of NOM were added to this solution, and the emf of the ISE was monitored continuously. The Ag^+ concentration of 5 μM was chosen to mimic the concentration of Ag^+ released from 1-5 mg/L Ag NPs (12-nm-diameter).⁶⁸ Results are depicted in Figure 3A. When Ag^+ binds to NOM, the concentration of free Ag^+ is reduced. Consequently, a decrease in the emf is observed. Stronger binding of Ag^+ to NOM results in a larger decrease in the concentration of free Ag^+ ions and, therefore, a greater decrease in the emf values. Addition of SRFA, SRNOM, SRHA, PPHA, and PLFA resulted in $8.5 \pm 0.2\%$, $11.1 \pm 2.1\%$, $15.4 \pm 2.0\%$, $40.4 \pm 1.8\%$, and $57.7 \pm 0.2\%$ decreases in the free Ag^+ concentration,

respectively (all changes were statistically significant, as assessed by the two-tailed t test, $p < 0.05$). It follows that the ability of different NOM types to bind Ag^+ falls in the sequence:



Based on our findings, we conclude that fulvic acid does not bind Ag^+ more or less strongly than humic acid, but it is noticeable that NOM types that are rich in nitrogen show higher binding of Ag^+ . Specifically, the nitrogen contents of PLFA and PPHA of 6.5% and 3.7%, respectively, are much higher than for SRHA, SRFA, and SRNOM, which contain 0.7%, 1.2%, and 1.1% nitrogen, respectively (International Humic Substances Society, 2014). Most of the nitrogen in these NOM samples was shown to be in the form of amides, aminoquinones, amino sugars, and heterocyclic nitrogen structures, which can all bind Ag^+ .²⁹¹ Moreover, NOM also contains sulfur-containing functionalities in the form of exocyclic and heterocyclic sulfur and sulfoxide, sulfone, sulfonate, and sulfate groups.²⁸⁹ It has been shown that the majority of sulfur in SRHA, SRFA, and PLFA is in low oxidation states as exocyclic and heterocyclic sulfur,²⁸⁹ which binds strongly with Ag^+ . Therefore, the high Ag^+ binding ability of PLFA is also the result of its sulfur content (3.0%), which is much higher than in the case of SRFA and SRHA (0.5%).

Our observations are consistent with findings of Sikora and Stevenson, who concluded that amine and thiol functional groups are mainly responsible for Ag^+ complexation while oxygen-containing functional groups have only minor effects on Ag^+ binding to NOM.^{286,318,351} This conclusion is also consistent with representative stability constants for oxygen, nitrogen, and sulfur containing functional groups. For example, the stability

constants K_{11} , for the 1:1 Ag^+ complexes²⁸⁶ are 4.4 with the oxygen ligand acetate, 2.1×10^3 for ammonia, 2.5×10^2 for NEt_3 , 1.2×10^2 for pyridine, and 6.6×10^8 for the sulfur ligand thiosulfate.^{352,353} Further research with techniques such as X-ray photoelectron spectroscopy (XPS) or X-ray absorption near edge structure (XANES) spectroscopy could be used to study the identity of the functional groups involved in the binding process.^{289,354}

Observing a relatively low Ag^+ binding extent for Suwannee River humic and fulvic acids can explain the discrepancies among published reports on the extent of Ag^+ binding to Suwannee River NOM isolates.^{311,321–323,326,329} Differences in the experimental conditions used in those studies, such as different pH values, affect the extent of binding and cause contradicting conclusions. To understand the extent of the pH effect, we quantified Ag^+ binding to SRFA and SRHA at pH = 6.0, 7.5, and 9.0 (see Figure S5). Interestingly, at pH = 6.0, no significant change in the free $[\text{Ag}^+]$ can be detected upon SRFA and SRHA addition to Ag^+ solutions (two-tailed t test, $p < 0.05$), which confirms that Ag^+ does not bind to SRFA or SRHA at acidic pH. Increasing the pH to 7.5 and 9.0 results in $9 \pm 2\%$ and $40 \pm 1\%$ Ag^+ binding to SRFA, and $16 \pm 1\%$ and $55 \pm 1\%$ binding to SRHA, respectively (Figure S5). (Increases in extent of Ag^+ -NOM binding are significant as assessed by the two-tailed t test, $p < 0.05$.) Clearly, the pH at which binding occurs plays a critical role in the extent of Ag^+ and NOM binding when the NOM binds Ag^+ weakly.

Figure 3 also illustrates the kinetics of Ag^+ binding to NOM. Even though binding of Ag^+ to NOM has been studied for more than a decade, and several hypotheses about its kinetics have been proposed, the kinetics of this reaction has not been investigated directly, possibly due to the lack of proper methodology.^{310,324,327} The fast response time of fluoros-phase

Ag⁺ ISEs (< 1.0 s) allows real-time detection of Ag⁺ and makes it possible to directly observe the kinetics of Ag⁺ binding to NOM. On one hand, after additions of SRHA, SRFA, SRNOM, or PPHA to a Ag⁺ solution, the emf decreased in less than 1 s, indicating a fast decrease in the free Ag⁺ concentration as the result of fast Ag⁺ binding to NOM. No further changes were observed over the following 24 hours, showing that equilibrium was reached very quickly.

On the other hand, after addition of PLFA to 5.0 μM AgCH₃COO, the emf did not stabilize after the initial very quick decrease, but continued to drift even after 24 h, albeit at a decreasing rate (see Figure S2). Stepwise addition of PLFA and alteration of the pH of the solution did not eliminate this drift (see Figure S3). To confirm that this behavior was indeed caused by Ag⁺ binding to PLFA and not by an artifact of the ISE measurement, the fluoros-phase Ag⁺ ISEs were recalibrated after exposure to PLFA, confirming that the fluoros-phase Ag⁺ ISEs were still fully functional and that the calibration curve was valid throughout the experiment. Moreover, when fluoros-phase Ag⁺ ISEs were inserted into a solution of Ag⁺ and PLFA that had been preequilibrated for 24 h, the measured emf did not show any drift, confirming that the observed emf drifts after PLFA addition to the Ag⁺ solution were indeed caused by a chemical transformation in the solution (see Figure S4) and not by some unexplained effect of PFLA on the response of the ISE.

An explanation for the slow decrease in the free silver ion activity after the addition of PLFA to 5.0 μM AgCH₃COO is given by the reduction of Ag⁺ to Ag by PLFA as the reducing agent. Indeed, the formation of Ag NPs as the result of Ag⁺ reduction by NOM in environmentally relevant conditions at ambient laboratory temperature and lighting was

shown by Akaighe and co-workers.³⁵⁵ Under their experimental conditions, Ag⁺ reduction by NOM took, depending on the NOM source and concentration, up to several days before the formation of Ag NPs was visually noticed.³⁵⁵ Slow Ag⁺ reduction by NOM under environmentally relevant conditions was also reported by F. Maurer and co-workers.³²⁴ In this study, formation of Ag NPs through reduction of Ag⁺ by PLFA was also confirmed using transmission electron microscopy and dark-field microscopy with hyperspectral imaging (see Figures S7 and S8).

Reduction of Ag⁺ by NOM also appears to be consistent with findings by Glover et al., who observed that longer incubation of Ag⁺ and NOM before addition to *Daphnia magna* (a freshwater flea) resulted in lower Ag⁺ toxicity.³²⁷ Glover et al. explained the time-dependent toxicity of Ag⁺ in the presence of NOM by the hypothesis of slow kinetics of Ag⁺ binding to NOM. However, these authors provided no evidence to exclude alternative explanations, such as the reduction of Ag⁺ by NOM. Based on the findings from our study and evidence from other studies employing a variety of experimental techniques, we believe that binding of Ag⁺ and NOM is fast and that the reduction of Ag⁺ by certain types of NOM in environmentally relevant conditions has slow kinetics and contributes to gradual changes in [Ag⁺] in NOM-containing media.

An alternative explanation for the slow changes in the free Ag⁺ activity could be gradual changes in the macromolecular structure of NOM and, concomitantly, changes in the NOM's ability to bind Ag⁺. The conformation of humic substances depends on physicochemical parameters such as pH, ionic strength, and the composition of the samples,³⁵⁶ which were all kept constant throughout our experiments with a phosphate pH

buffer. Whereas conformational changes of NOM induced by iron complexation have been reported recently,^{356,357} evidence that those conformational changes have a major effect on the activity of free iron does not exist. The slow conformational changes induced by the presence of iron may be preceded by comparatively fast binding of iron to NOM. In the case of Ag^+ , no reports of such conformational changes of NOM have been made to date.

3.3.4 Effect of NOM on Ag^+ Toxicity. NOM has been reported to reduce Ag^+ toxicity to large and micro-organisms by binding to Ag^+ and reducing the concentration of free Ag^+ .^{267,306,325,328,329} After quantifying the extent of Ag^+ binding to different NOM isolates, we were able to assess the validity of the commonly held belief that NOM reduces Ag^+ toxicity to organisms by binding to Ag^+ . We employed a bacterial model (*Shewanella oneidensis* MR-1) to study the effect of NOM on silver toxicity. *Shewanella oneidensis* MR-1 is a facultative anaerobe and also a metal reducing bacterium. This respiratory diversity allows it to survive in a variety of locations, e.g., in freshwater, saltwater, and sediments, making it a relevant model to assess the environmental impact of silver-containing products that may leach silver into a variety of natural environments.³⁵⁸ We assessed changes in membrane integrity of *Shewanella oneidensis* MR-1 (using the LIVE/DEAD BacLight Viability Kit, see Supporting Information) after exposure to Ag^+ with and without NOM, using similar experimental conditions as those used for studying the extent of Ag^+ binding to NOM (pH 7.5, potassium phosphate buffer, $5.0 \mu\text{M}$ Ag^+ , and 51 mg/L NOM). It should be noted that, under nutrient-poor conditions like those employed in these experiments, NOM can serve as a source of nutrition for bacteria and thereby

increase their viability. We observed significantly higher cell viability (two-tailed t test, $p < 0.05$), presented as the ratio of cells identified to be live vs. dead, in the presence of 51 mg/L PLFA, SRFA, SRHA, PPHA, and SRNOM (with no silver present) than in the absence of NOM (see Figure 3C). Exposing the bacteria to 5.0 μM Ag^+ reduced the live to dead cell ratio from 3.2 (0.0 μM Ag^+ control) to less than 1.0 (see Figure 3C), confirming that Ag^+ is toxic to the bacteria at this concentration. Addition of 51 mg/L NOM induced no significant changes in the toxicity of 5.0 μM Ag^+ to the bacteria in the case of SRFA, SRHA, and SRNOM (shown in purple in Figure 3C). Our finding is consistent with precedent studies that observed no significant effect of SRHA on the toxicity of Ag^+ to *Pseudomonas fluorescen*,²⁶⁹ *Chlamydomonas reinhardtii*,³²² and *Pseudokirchneriella subcapitata*.³²² As discussed in the previous section, SRNOM, SRFA, and SRHA have a low affinity for Ag^+ , and less than 20% of the Ag^+ is bound to NOM present in a concentration of 51 mg/L. Given that these NOM types only decrease the free [Ag^+] slightly (see Figure 3A), we attribute their insignificant effects on the Ag^+ toxicity to *Shewanella oneidensis* MR-1 to their low affinity for Ag^+ . Even PPHA with its slightly higher Ag^+ binding affinity (upon binding to Ag^+ reduces its concentration by 50%) did not improve viability of *Shewanella oneidensis* MR-1. This confirms that due to overall weak Ag^+ -NOM binding, the NOM-induced changes in Ag^+ concentration do not necessarily result in significant effects on the Ag^+ toxicity to the *Shewanella oneidensis* MR-1.

Even though PPHA and PLFA showed similar affinities for Ag^+ , i.e., 50% binding for PPHA and 60% binding for PLFA, only the addition of PLFA improved the viability of

cells exposed to 5.0 μM Ag^+ (the live to dead ratio increased from less than 1.0 to 2.0, two-tailed t test, $p < 0.05$), while PPHA had no significant protective effect against Ag^+ toxicity. The latter can be explained based on the gradual decrease in $[\text{Ag}^+]$ in presence of PLFA. Immediately following NOM addition to Ag^+ , the $[\text{Ag}^+]$ was observed to be similar for both PLFA and PPHA (2–3 μM Ag^+). However, during the time that the bacteria were incubated with the Ag^+ - and NOM-containing solution, $[\text{Ag}^+]$ gradually decreased to less than 1.0 μM , likely due to Ag^+ reduction by PLFA, as explained in the previous section, whereas $[\text{Ag}^+]$ remained approximately constant in PPHA-containing solutions. Even though PLFA and PPHA showed similar initial extents of Ag^+ binding, PLFA reduced the total effective exposure of the cells to Ag^+ , resulting in higher cell viability. (Note that 1.0 μM Ag^+ cannot be confirmed to be toxic to the bacteria, while 2.5 μM Ag^+ reduces the viability of *Shewanella oneidensis* MR-1, as shown in Figure S8). Given that PPHA, SRFA, SRHA, and SRNOM all have different binding abilities but exhibit similar effects on Ag^+ toxicity to *Shewanella oneidensis* MR-1, our results demonstrate that the effect of NOM on bacterial cell viability does not necessarily correlate with the extent of Ag^+ binding to NOM, but strongly depends on free Ag^+ concentration. To confirm this, after addition of PLFA or PPHA to 5.0 μM Ag^+ , which significantly reduced the free Ag^+ concentration due to binding to NOM, we adjusted the free Ag^+ concentration to 5.0 μM by adding aliquots of AgNO_3 to the solution while monitoring the emf using fluoruous-phase ISEs (see Figure 3B). AgNO_3 was added until the ISE indicated that the concentration of free Ag^+ had again reached 5.0 μM , as was the case before NOM addition. As shown in Figure 3C, a similar toxicity was found for solutions that contained 5.0 μM free Ag^+ and

no added NOM as for solutions that contained 5.0 μM free Ag^+ and 51.0 mg/L PPHA or PLFA, despite the fact that the latter solutions contained 3.5 and 5.3 μM complexed silver, respectively.

These findings are important since the protective ability of NOM against Ag^+ toxicity is usually attributed to direct binding of Ag^+ to NOM whereas other forms of speciation, such as NOM-induced Ag^+ reduction and nanoparticle formation, are often ignored. This study provides evidence that the protective ability of NOM against Ag^+ toxicity results both from Ag^+ binding to NOM and NOM-induced Ag^+ reduction, and also shows that lack of NOM effect on Ag^+ toxicity does not exclude the possibility of Ag^+ binding to NOM.

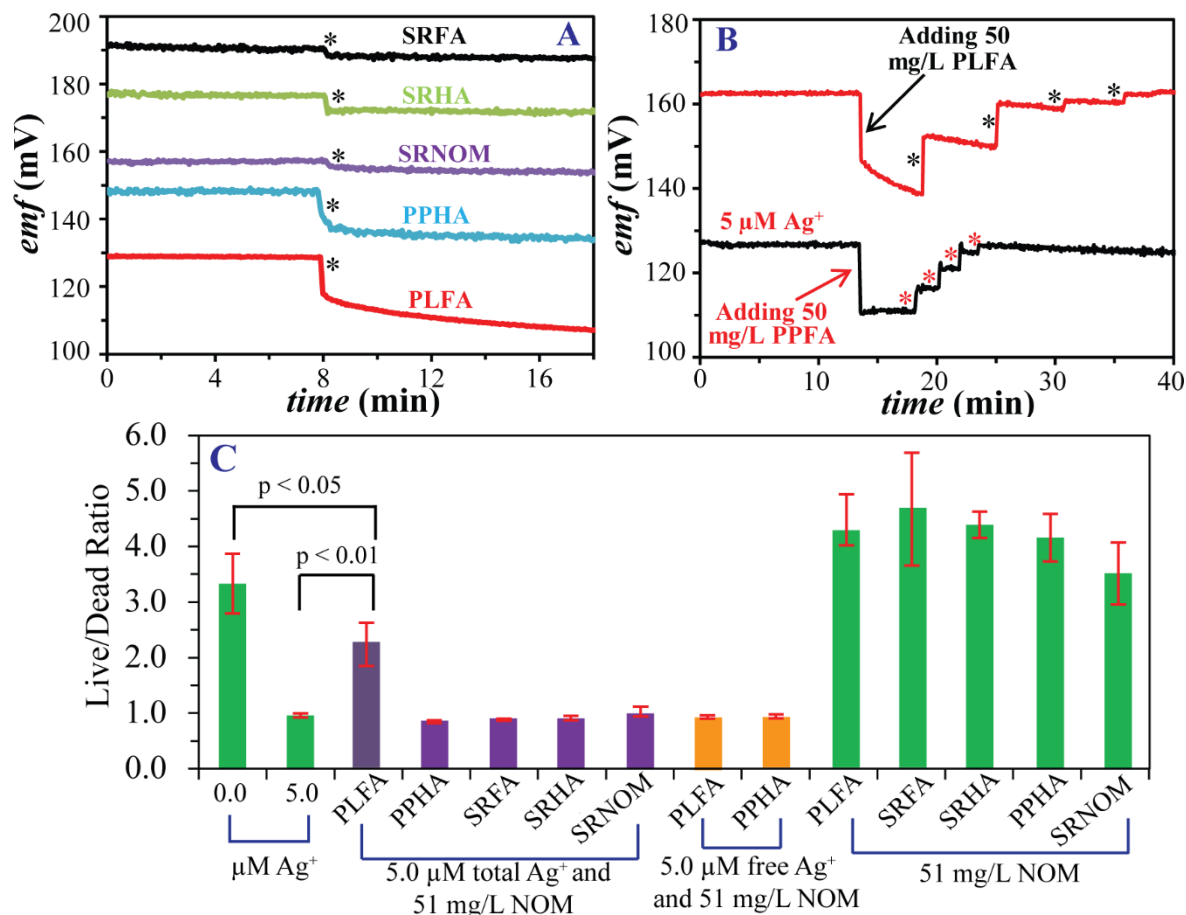


Figure 3. Ag⁺ and NOM binding and its effect on Ag⁺ toxicity: (A) Shown are the emf values measured with fluoros-phase Ag⁺ ISEs in 5.0 μM AgNO₃ followed by 51.0 mg/L addition of (indicated by asterisks) of SRFA (black), SRHA (green), SRNOM (purple), PPHA (blue), or PLFA (red). For better visualization, the emf traces are shifted vertically relative to one another. (B) Aliquots of AgNO₃ were added (indicated by asterisks) to the Ag⁺ and NOM solution to readjust [Ag⁺] to 5.0 μM. (C) Viability of *S. oneidensis* after 30 minute exposure to Ag⁺ and NOM solutions with specified identities and concentrations.

Error bars represent the standard deviation of three biological replicates. Statistical significance was determined using the paired t-test.

3.4 Conclusions

This work has demonstrated that fluoruous-phase Ag^+ ISEs are effective tools for the dynamic investigation of Ag^+ binding to NOM as they can be used to monitor the in situ activity of Ag^+ in a time-resolved manner with high selectivity and without the need for substantial sample preparation. The extent of Ag^+ binding to NOM was quantified using these sensors, showing the following trend for Ag^+ binding capacities of different NOM types: Pony Lake fulvic acid > Pahokee Peat humic acid standard > Suwannee Humic fulvic acid II > Suwannee River Aquatic NOM, SRNOM > Suwannee River fulvic acid II, SRFA.

We showed fast kinetics for Ag^+ binding to NOM and slow kinetics for the reduction of Ag^+ by certain types of NOM in environmentally relevant conditions. This is the first report on the kinetics of Ag^+ binding to NOM with time resolution of less than a second. Moreover, we showed that pH affects the extent of Ag^+ binding to NOM binding, where higher pH results in stronger binding. Studies of Ag^+ speciation should ensure that buffer components are selected to avoid unwanted complexation with Ag^+ . We showed that buffer compounds such as HEPES and MOPS should be excluded from Ag^+ speciation studies since they form stable complexes with Ag^+ and interfere with NOM binding to Ag^+ . Lastly, we showed that the ability of NOM to protect against Ag^+ toxicity does not directly correlate with the extent of Ag^+ binding to NOM. Other aspects of silver speciation, such

as NOM-induced Ag⁺ reduction and nanoparticle formation, also affect the observed toxicity.

3.5 Acknowledgements

This work was supported by a Graham N. Gleysteen Excellence Fellowship and a UMN Doctoral Dissertation Fellowship for M. P. S. Mousavi, a National Science Foundation MRSEC REU award for C. E. Pérez De Jesús, a University of Minnesota Biotechnology Institute Training Grant and Minneapolis Torske Klubben Graduate Fellowship to I. L. Gunsolus, a University of Minnesota Heisig/Gleysteen fellowship to K. Hussein, and National Science Foundation (CHE-1152931) funding to C.L. Haynes.

3.6 Supporting Information

3.6.1 Effect of NOM on Toxicity of Ag⁺ and Ag NPs. There are several reports that NOM extracted from different sources mitigates the toxicity of Ag NPs to various organisms. The decrease in toxicity is usually attributed to complexation of Ag⁺ with NOM. Complexation of Ag⁺ with NOM reduces the concentration and bioavailability of the toxic free metal and reduces its ability to interact with the site of toxic action in the organism, resulting in reduced overall toxicity.^{304,311} Examples include reduced toxicity of Ag⁺ and Ag NPs to *Pseudomonas fluorescens* in the presence of NOM (Pahokee peat humic acid purchased from the International Humic Substances Society, IHSS),⁷⁹ decreased toxicity of Ag NPs to *Daphnia* and *Daphnia magna* with increased concentration of NOM (Suwannee River humic acid II purchased from IHSS and humic acid purchased from Aldrich, St. Louis,

MO),^{311,326} and mitigated toxicity of Ag NPs to *Daphnia magna* in a dose-dependent manner in the presence of NOM (humic acid purchased from Aldrich).³²⁷ Moreover, protective effects of NOM (humic acid from Aldrich) against toxicity of Ag⁺ to *Oncorhynchus mykiss*,^{306,325} Japanese medaka embryos,³²⁸ and *Pimephales Promelas*³²⁹ have been reported. On the contrary, in similar toxicity studies, NOM (Suwannee River humic acid II purchased from IHSS) had no significant effect on the toxicity of Ag⁺ to *Pseudomonas fluorescens*,²⁶⁹ *Chlamydomonas reinhardtii*,³²² and *Pseudokirchneriella subcapitata*.³²² Clearly, these discrepancies in the literature make it difficult to assess toxicity trends and point to the need for time-resolved measurements of Ag species in controlled environments.

3.6.2 Measurements with Ion-selective Electrodes with Fluorous Sensing Membranes.

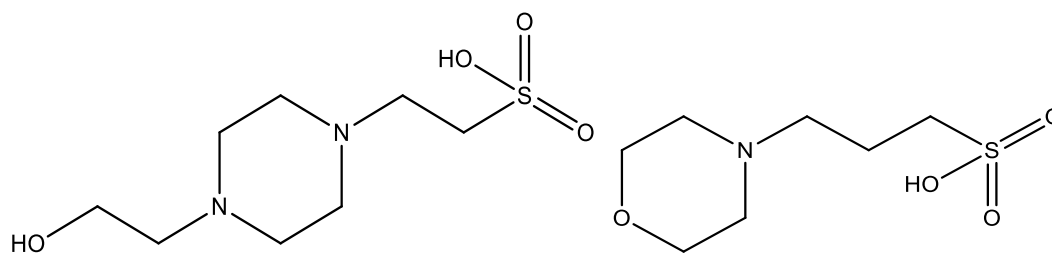
Ag⁺ ion-selective electrodes (ISEs) with fluorous sensing membranes were prepared as reported previously.⁶⁰ For preparation of the sensing phase, 0.5 mM ionic sites (sodium tetrakis[3,5-bis(perfluorohexyl)phenyl]borate) and 1.5 mM ionophore (1,3-bis(perfluorooctyl-ethylthiomethyl)benzene)⁶¹ were added to perfluoroperhydrophenanthrene (Alfa Aesar, Ward Hill, MA), and the resulting mixture was stirred for at least 24 h to ensure that all the membrane components had completely dissolved. Fluoropore filters (porous poly(tetrafluoroethylene), 47 mm diameter, 0.45 μm pore size, 50 μm thick, 85% porosity, EMD Millipore, Bedford, MA) were sandwiched between two small pieces of printing paper, and cut with a 13 mm diameter hole punch, giving porous filter disks to mechanically support the sensing phase. Approximately 25 μL

of fluoruous sensing phase was then applied with a micropipet to a stack of 2 porous filter disks. Full penetration of the fluoruous phase sensing membrane into the porous supports was confirmed by a translucent appearance of the filter disks.

The filter disks that contained the fluoruous sensing phase were then mounted into custom-machined electrode bodies made of poly(chlorotrifluoroethylene), as described previously.⁶¹ In brief, a screw cap with a hole (8.3 mm diameter) in the center was screwed onto the electrode body, mechanically securing the sensing membrane in between the electrode body and the cap but leaving the center of the membrane exposed. The electrode bodies were then filled with 1 μM AgCH_3CO_2 (Sigma Aldrich), and an AgCl/Ag inner reference electrode was inserted into this inner solution. Prior to measurements, all electrodes were soaked first for 24 h in 100 mL 0.1 mM AgCH_3CO_2 solution and then for another 24 h in 100 mL 1.0 μM AgCH_3CO_2 . The same silver salt was used for the inner filling and conditioning solutions.

Potentials were monitored with an EMF 16 potentiometer (Lawson Labs, Malvern, PA) controlled with EMF Suite 1.02 software (Lawson Labs) at room temperature in stirred solutions. The external reference electrode consisted of a double-junction AgCl/Ag electrode with a 1.0 M LiOAc bridge electrolyte and a 3.0 M KCl reference electrolyte. All measurements were performed with at least 3 replicate electrodes. The detection limit was determined by emf measurements of the prepared electrodes in solutions resulting from successive dilutions of 100 μM AgCH_3CO_2 (Fig. S1). Calibration curves were obtained by successive additions of aliquots of a 10 mM AgCH_3CO_2 solution to deionized water or the pH buffers.

3.6.3 Solution Preparation and Binding Measurements. All the solutions were prepared with deionized water (18 M Ω cm specific resistance, EMD Millipore, Burlington, MA). For preparation of the pH = 6.0 buffer, 0.100 M NaCH₃CO₂ and 0.006 M CH₃CO₂H were mixed at room temperature, followed by adjustment of the pH by addition of aliquots of NaOH or CH₃CO₂H. The components of the pH = 7.5 buffer were 0.028 M K₂HPO₄ and 0.015 M KH₂PO₄. The pH of the solution was adjusted to 7.5 by addition of aliquots of KOH. The pH = 9.0 buffer contained 0.087 M NaHCO₃ and 0.044 M Na₂CO₃, and the pH was adjusted by addition of aliquots of NaOH. The HEPES buffer with pH = 7.5 was prepared by dissolving 0.20 M HEPES, 4-(2-hydroxyethyl)piperazine-1-ethanesulfonic acid, in deionized water, and the pH of the solution was adjusted to 7.5 by addition of aliquots of KOH. The MOPS buffer with pH = 7.5 was prepared by dissolving 0.30 M MOPS, *N*-morpholino-3-propanesulfonic acid, in deionized water, and the pH of the solution was adjusted to 7.5 by addition of aliquots of KOH. (Structures of HEPES and MOPS are provided in Scheme S1.)



Scheme S1. The structure of HEPES (on the left) and MOPS (on the right).

The components of the phosphate (pH=7.5), carbonate (pH=9.0), and acetate (pH=6.0) pH buffers were chosen to interact minimally with Ag^+ and thus minimize the interference with respect to Ag^+ binding to NOM. The latter was assessed by measurements of the potentiometric response to Ag^+ by fluoros-phase Ag^+ ISEs in deionized water and in pH buffers. The response for deionized water and all the pH buffer solutions were very similar, which confirmed that Ag^+ did not bind significantly to the pH buffer components (less than 15 mV and 2 mV change in the intercept and slope of the calibration equation, respectively). In the case of Ag^+ binding to the pH buffer components, the calibration equation would have shifted to lower emf values because of the lowering of the concentration of free Ag^+ ions as a result of complexation,⁶⁸ which must be prevented to avoid errors and an unrealistic evaluation of Ag^+ binding to NOM. Binding of buffer components to Ag^+ occurs in the case of the commonly used HEPES and MOPS buffers, as shown in Figure S1. The calibration equations in Figure S1B are shifted to lower emf values because of Ag^+ complexation with HEPES and MOPS. Using the calibration curve obtained in water, the emf values measured with the HEPES and MOPS buffers were converted to Ag^+ concentrations. This showed that in the MOPS and HEPES buffers 90% and 99% of the added Ag^+ is in the complexed form, respectively (Figure S1C).

Concentrated solutions of Suwannee River humic acid II (SRHA), Suwannee River fulvic acid II (SRFA), and Suwannee River Aquatic NOM were prepared by dissolving 30.0 mg of each in 3.0 ml of deionized water, followed by stirring for at least two hours. Concentrated solutions of Pony Lake fulvic acid (PLFA) and Pahokee Peat humic acid

(PPHA) were prepared in an identical manner and were sonicated for two minutes immediately prior to use (to suspend undissolved material).

For NOM titration experiments, Ag^+ ISEs were placed in a pH-buffered solution of $1.0 \mu\text{M}$ AgCH_3COO (pH = 6.0, 7.5, or 9.0), and aliquots of 10.0 g/L NOM were added to this solution while monitoring the emf of the Ag^+ ISEs continuously. In the NOM addition experiments, Ag^+ ISEs were placed in a solution of $5.0 \mu\text{M}$ AgCH_3COO buffered to pH 7.5, and aliquots of 10.0 g/L NOM were added to this solution to achieve the final concentration of 51 mg/L for the NOM.

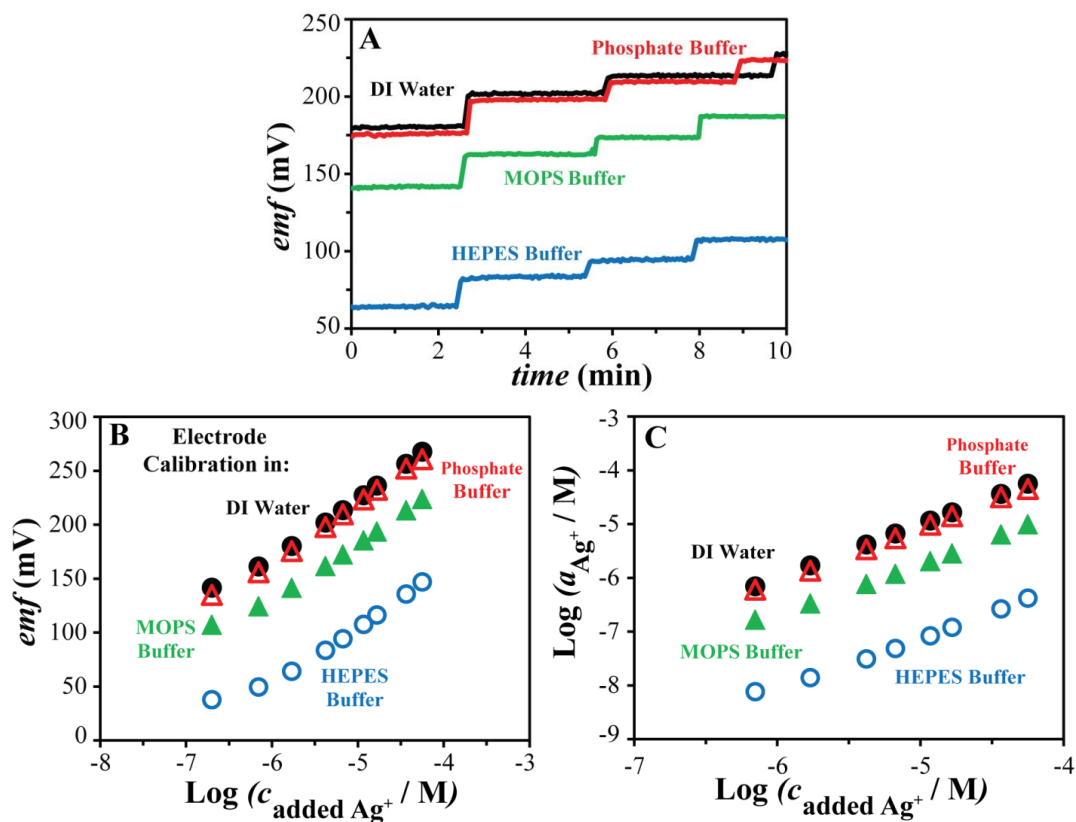


Figure S1. Ag^+ complexation with buffer components studied by fluoros-phase Ag^+ ISEs. Aliquots of AgNO_3 were added to deionized water (shown in black), phosphate buffer with $\text{pH} = 7.5$ (shown in red), MOPS buffer with $\text{pH} = 7.5$ (shown in green), or HEPES buffer with $\text{pH} = 7.5$ (shown in blue), while monitoring the emf. A snapshot of the calibration experiments, i.e., emf values over time, is shown in panel A. AgNO_3 is added to the solution after approximately 2, 6, and 8 min. Panel B shows the response curve in each pH buffer, and panel C shows the corresponding amounts of free Ag^+ after each AgNO_3 addition.

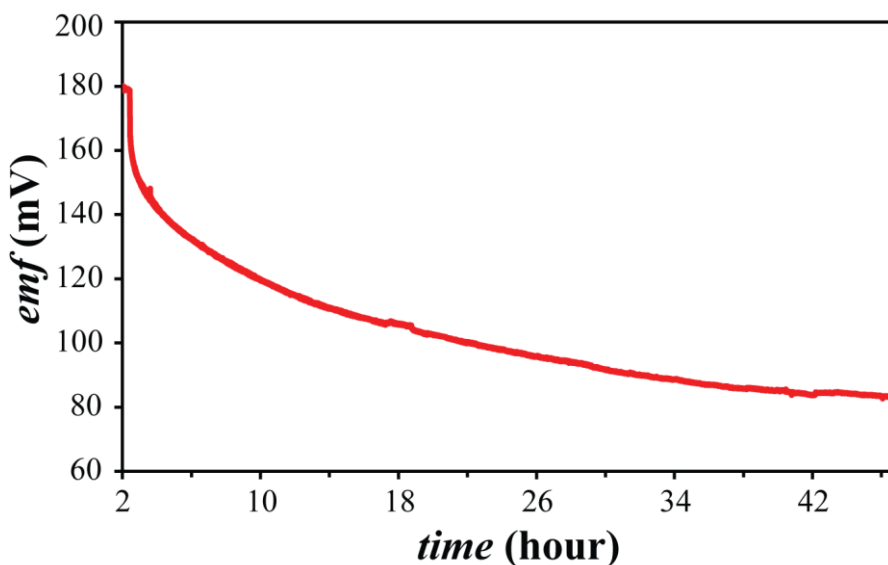


Figure S2. Emf response of a fluoros-phase Ag^+ ISE in a solution containing $5.0 \mu\text{M}$ Ag^+ and 51 mg/L PLFA over 48 h. The concentration of free Ag^+ decreases by one order of magnitude over 48 h.

3.6.4 Kinetics of Ag^+ and NOM binding. For Ag^+ speciation studies, the ability to detect Ag^+ in real time with high time resolution gives ion-selective potentiometry a distinct

advantage over conventional techniques. The response time of fluoruous-phase Ag^+ ISEs is very fast (< 1.0 s), which allows the investigation of the kinetics of Ag^+ binding to NOM. Electrode response is stable over a period of days, allowing measurements of Ag^+ binding to NOM to be performed over ~ 48 h (see Figure S2). In this work, fluoruous-phase Ag^+ ISEs were immersed in a solution of $1 \mu\text{M}$ AgCH_3COO buffered to $\text{pH} = 6.0, 7.5,$ or 9.0 (ionic strength, 0.1 M), and aliquots of concentrated NOM were added to these solutions while the response of the ISEs was monitored continuously. After additions of SRHA and SRFA, a decrease in the emf was observed in less than 1 s, which is indicative of fast complexation of Ag^+ and NOM and a concomitant decrease in the free silver concentration, $[\text{Ag}^+]$. No further changes were observed thereafter, showing that equilibrium was reached very quickly (see Figures S3A and S3B). While Figure S3 shows representative results for $\text{pH} = 9.0$ only, similar results were obtained for $\text{pH} = 6.0$ and 7.5 .

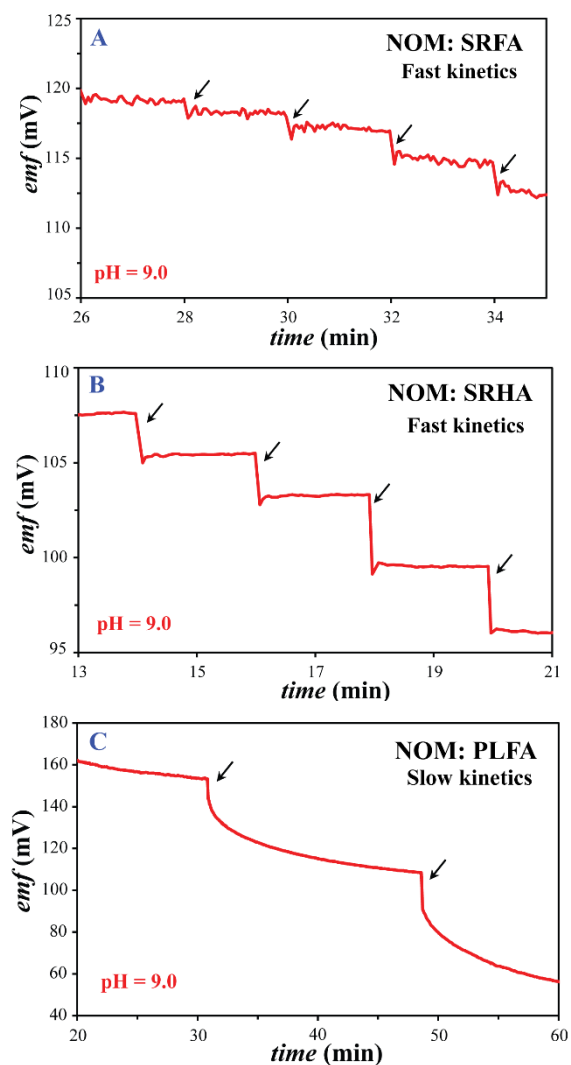


Figure S3. Kinetics of Ag^+ binding to NOM at pH 9: Addition of NOM to $1.0 \mu\text{M}$ AgCH_3COO . Fast binding kinetics is observed for SRFA (A) and SRHA (B), whereas Ag^+ binding to PLFA is slow (C). Similar results were obtained for pH 6.0 and 7.5.

In contrast, after addition of PLFA to $1.0 \mu\text{M}$ AgCH_3COO , the initial decrease in the emf was not followed by a constant emf value, but rather the emf continued to decrease slowly. At low concentrations of PLFA (less than 11.0 mg/L), each addition caused the emf to drift

to lower values over 10 to 20 min before the emf became stable (see Figure S3C). At higher PLFA concentrations (11.0 to 51.0 mg/L), up to 10 h were required for the emf to exhibit a drift smaller than 0.1 mV/min. To confirm that the observed emf drift was indeed caused by Ag^+ binding to PLFA and was not caused by an experimental artifact, two experiments were performed. First, after the PLFA was added to the pH (6.0, 7.5, or 9.0) buffer solution and a stable emf was reached, the fluoruous-phase Ag^+ ISEs were recalibrated. Similar calibration curves were obtained before and after the PLFA addition experiment, confirming that the fluoruous-phase Ag^+ ISEs were not affected by biofouling and were still fully functional after exposure to PLFA. Moreover, the fluoruous-phase Ag^+ ISEs were immersed in a preequilibrated solution of 1.0 μM AgCH_3COO and 51 mg/L PLFA. The result of this latter experiment is shown in Figure S4. The emf values measured in the preequilibrated solutions prepared with 1 μM AgCH_3COO and 51 mg/L PLFA solution were stable and were much lower than for a 1.0 μM AgCH_3COO solution. This confirms that the observed drifts in the emf after addition of PLFA to the 1.0 μM AgCH_3COO are indicative of a chemical transformation in the solution.

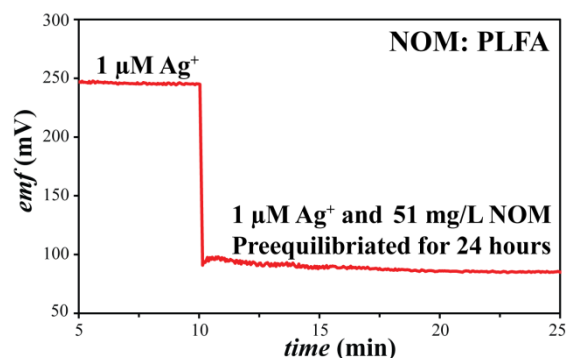


Figure S4. Emf response of a fluoros-phase Ag^+ ISE, first in $1.0 \mu\text{M}$ AgCH_3COO solution, and then in a preequilibrated solution of $1.0 \mu\text{M}$ AgCH_3COO and 51 mg/L PLFA.

3.6.5 Effect of pH on Ag^+ binding to SRHA, SRFA, and PLFA. To investigate the effect of pH on Ag^+ binding to SRHA, SRFA, and PLFA, we studied Ag^+ complexation in three different pH buffers with pH = 6.0, 7.5, or 9.0 as representatives for acidic, neutral, and basic solutions. To keep the ionic strength constant, all pH buffers used in this study had an ionic strength of 0.1 M. To quantify the complexation of Ag^+ and NOM, fluoros-phase Ag^+ ISEs were placed in a solution of $1.0 \mu\text{M}$ AgCH_3COO with a buffered pH (pH = 6.0, 7.5, and 9.0) and fixed ionic strength, aliquots of concentrated solutions of NOM were added to this solution, and the emf of the fluoros-phase Ag^+ ISE was monitored continuously. The results are depicted in Figure S5. When Ag^+ binds to NOM, the concentration of free Ag^+ is reduced. Consequently, a decrease in the emf is observed. Additions of aliquots of all the NOM types resulted in larger emf changes at higher pH than at lower pH (Figures S5A, B, and C). Stronger binding of Ag^+ to NOM resulted in a bigger change in $[\text{Ag}^+]$ (Figure S5D, E, and F) and, therefore, a greater decrease in the emf values. The effect of pH on Ag^+ and NOM complexation can be explained by the

competition between Ag^+ and H^+ for binding to NOM;^{286,318} increasing the pH lowers the H^+ concentration, and thus favors complexation with Ag^+ . As expected from Le Châtelier's principle, increasing the concentration of NOM results in decreasing $[\text{Ag}^+]$ and an increasing concentration of Ag^+ -NOM complexes;³¹⁸ the latter is observed for all NOM types in all three pH buffers (see Figure S5).

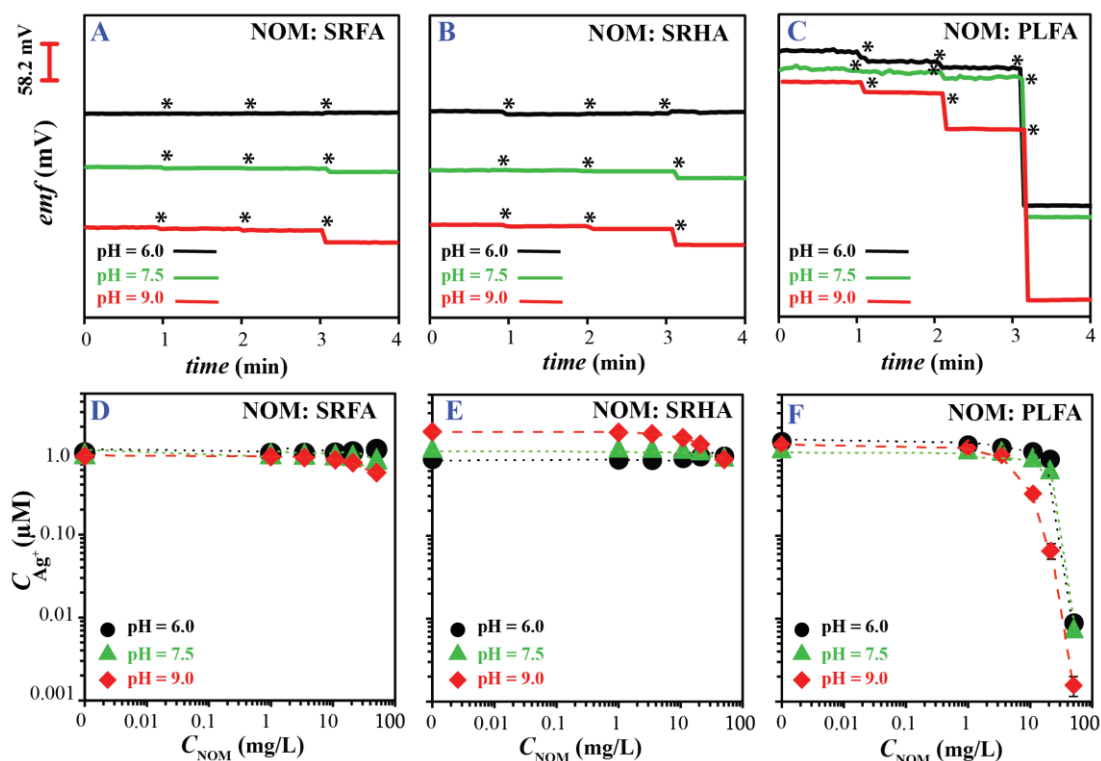


Figure S5. Effect of pH and NOM source on Ag^+ and NOM complexation: Shown are the emf values (at equilibrium) measured with fluoros-phase Ag^+ ISEs in $1.0 \mu\text{M}$ AgCH_3COO with 0.0, 3.5, 11.0, and 51.0 mg/L (indicated by asterisks) SRFA (A), SRHA (B), and PLFA (C) for three pH buffers (pH = 6.0, black; pH = 7.5, green; pH = 9.0, red). The corresponding Ag^+ concentrations are shown in D, E, and F. For better visualization, the emf traces are

shifted vertically relative to one another. Error bars are shown for three replicate measurements (in some cases the data label conceals the error bars.)

Interestingly, SRHA and SRFA bind Ag^+ only weakly. At pH = 6.0, no significant change in the free $[\text{Ag}^+]$ can be detected (Figures S5 A, B, D, and E). At neutral pH, weak complexation can be observed for SRHA and SRFA. For example, at 51 mg/L SRHA, 20% of the silver ions in the 1.0 μM AgCH_3COO solution is in the complexed form whereas at the same concentration of SRFA, only 11% of the silver ions are in the complexed form. The difference in Ag^+ binding ability of SRHA and SRFA is also noticeable at higher pH. SRHA shows slightly stronger binding of Ag^+ than SRFA, i.e., a 55% decrease in concentration of Ag^+ at 51 mg/L SRHA at pH = 9.0 was observed, while a 38% decrease in concentration of Ag^+ was found for 51 mg/L SRFA at pH = 9.0.

Our data show limited Ag^+ binding to SRHA at pH 6.0, which is in agreement with findings by Z. Chen and co-workers, who used the ion exchange equilibrium and equilibrium dialysis techniques and found no significant binding of Ag^+ to SRHA at pH 5.5.³²² Weak binding of Ag^+ to SRHA also explains why SRHA had no significant effect on the toxicity of Ag^+ to *Pseudomonas fluorescens*,²⁶⁹ *Chlamydomonas reinhardtii*,³²² and *Pseudokirchneriella subcapitata*.³²²

3.6.6 Confirmation of Ag NP Formation as a Result of Ag^+ Reduction by PLFA using Dark-field Microscopy with Hyperspectral Imaging and Transmission Electron Microscopy, TEM.

To confirm that Ag^+ is reduced by PLFA, forming Ag NPs and changing the emf response over time, we used dark-field microscopy with hyperspectral imaging and also TEM.

Dark-field micrographs of solutions containing either only Ag^+ or Ag^+ and PLFA were acquired using a modified Olympus microscope (vide infra). Then a visible-near infrared (VNIR) spectral map of the imaged area (consisting of spectra from each pixel within the imaged area and referred to here as a hyperspectral image) was acquired in each case. This was accomplished by recording the scattered light intensity across the VNIR using an in-line spectrophotometer and CCD camera as the sample was incrementally moved into the spectrograph's field of view on an automated sample stage. Assessment of Ag NP formation in solutions of Ag^+ or Ag^+ and PLFA was accomplished by comparing these hyperspectral images to those acquired from a reference solution of Ag NPs (see Figure S6). Areas of high spectral similarity between the solutions in question and the reference solution of Ag NPs were identified using the Spectral Angle Mapping feature of ENVI 4.8 software (Exelis Visual Information Solutions, Boulder, CO), and were taken as evidence of Ag NP formation. A 3 μL aliquot was removed from each solution (1 μM Ag^+ or 1 μM Ag^+ with 51 mg/L PLFA in pH 7.5 buffer after 24 h incubation in the dark at room temperature), placed onto a glass slide, and covered with a glass coverslip. Dark-field micrographs were acquired on an Olympus BX43 microscope (Olympus America, Center Valley, PA) modified with a high signal-to-noise darkfield condenser unit from CytoViva (Auburn, AL), 150 W quartz-halogen lamp (Fiber-Lite DC-950, Dolan-Jenner Industries, Boxborough, MA), 100x 1.3 NA oil-immersion objective, and 12 bit CCD camera (pco.pixelfly, PCO, Kelheim, Germany). Hyperspectral images were acquired in the same field of view using the CytoViva hyperspectral imaging system consisting of a spectrophotometer (Specim, Oulu, Finland) with an integrated CCD (pco.pixelfly, PCO,

Kelheim, Germany). Data were analyzed using the Spectral Angle Mapping feature of ENVI 4.8 software.

The dark-field images of $1.0 \mu\text{M Ag}^+$ and 51 mg/L PLFA incubated for 24 h are shown in Figures S6A and S6B. Regions of these dark-field images identified to have significant spectral similarity to a reference solution of silver nanoparticles are indicated by bright pixels in Figure S6C and S6D. These images indicate that whereas a small number of Ag NPs were formed in a $1.0 \mu\text{M Ag}^+$ lacking PLFA, the abundance of Ag NPs increased with PLFA addition.

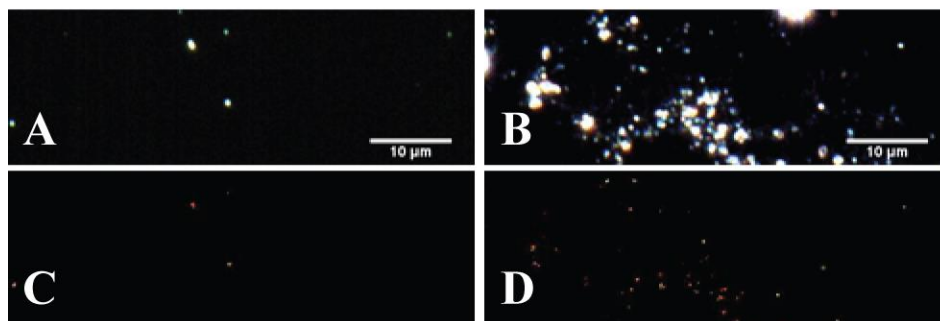


Figure S6. Dark-field microscopy and hyperspectral imaging show that silver nanoparticle formation in a $1.0 \mu\text{M Ag}^+$ solution is greater in the presence of 51 mg/L PLFA (right) than in its absence (left). The top panels show dark-field micrographs of silver nanoparticles formed from a $1.0 \mu\text{M Ag}^+$ solution in the absence (A) and presence (B) of 51 mg/L PLFA after 24 h incubation. The bright features in the bottom panels, C and D, indicate regions in the dark-field micrographs above that have high spectral similarity to a silver nanoparticle reference solution (not shown). This confirms the identity of the silver nanoparticles.

Further confirmation of Ag NP formation in solutions of Ag⁺ with PLFA was obtained using transmission electron microscopy (TEM). Solutions of Ag⁺ and PLFA incubated for 24 h, as well as controls consisting of pure buffer, Ag⁺ alone, and PLFA alone, were loaded onto 200 mesh copper grids with Formvar and carbon supports (Ted Pella). Micrographs were then acquired using a JEOL 1200 EXII microscope operating at 120 kV. The higher electron density of Ag NPs relative to the background carbon grid results in lower electron transmission intensities and high contrast, facilitating detection of Ag NP formation in these solutions. As shown in Figure S7, Ag NP cluster formation was observed in a solution of Ag⁺ with PLFA, but no Ag NPs were observed in the control solutions. Areas of high contrast observed in the pure buffer (Figure S7D) and a solution of Ag⁺ (Figure S7E) that lacked the spherical form characteristic of Ag NPs were attributed to salt crystals.

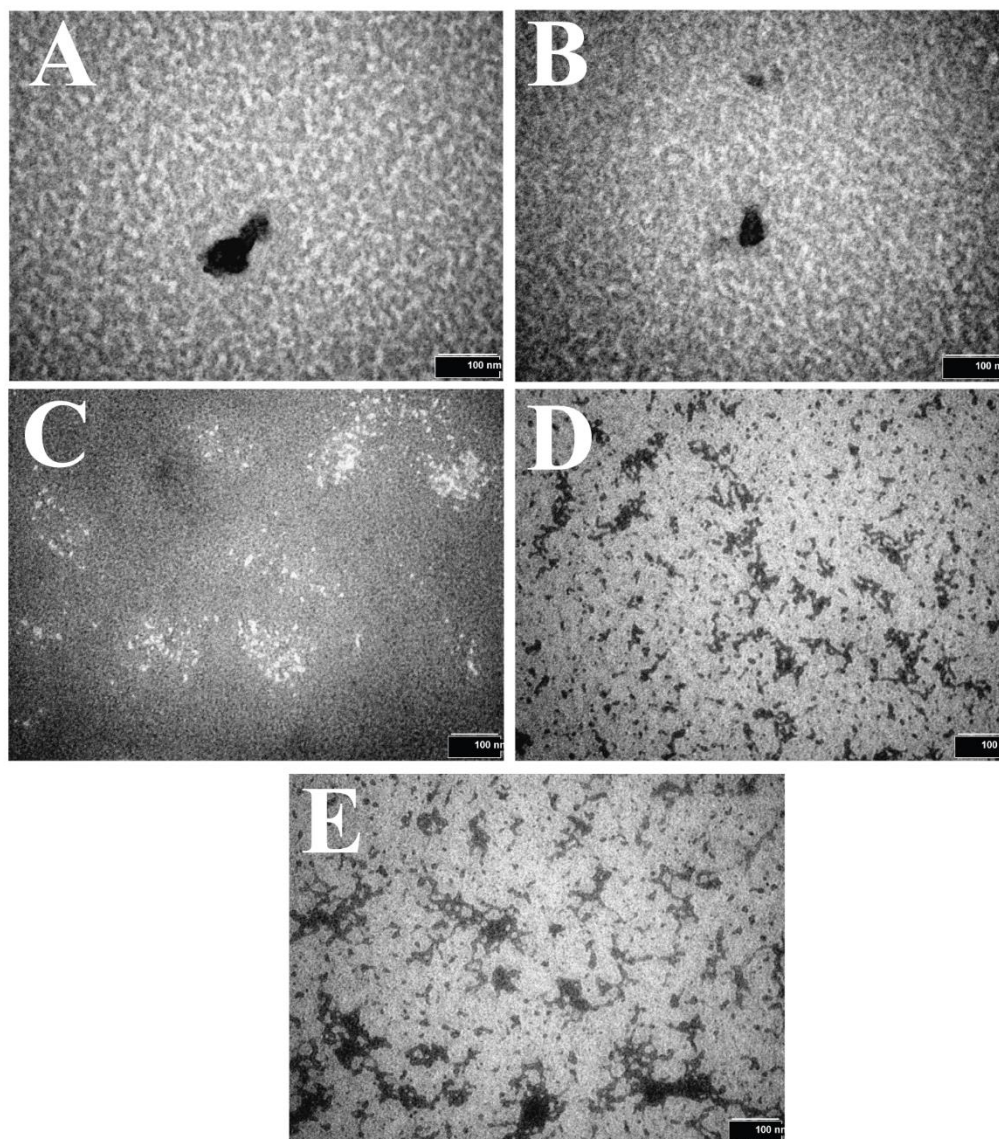


Figure S7. Confirmation of nanoparticle formation through Ag^+ reduction by PLFA. TEM images of $5 \mu\text{M}$ Ag^+ with 51 mg/L PLFA incubated for 24 h in A and B, only 51 mg/L PLFA in C, pure buffer in D, and $5.0 \mu\text{M}$ Ag^+ in E are shown. The distinctive dark spots in A and B represent the nanoparticles. In all images, the scale bar represents a length of 100 nanometers.

3.6.7 Silver Toxicity to *Shewanella oneidensis*. We evaluated bacterial membrane integrity after exposure to Ag⁺ (using AgNO₃ as the source of Ag⁺) using the LIVE/DEAD BacLight Viability Kit (Product L-7012, Life Technologies). *Shewanella oneidensis* MR-1 was cultured on LB agar plates over 24 h and was then inoculated into LB broth. After 1 h, cells were harvested by centrifugation at 2000 RCF (10 min) and resuspended in pH 7.5 phosphate buffer (cell concentration = 2 x 10⁸ cells/mL). Then 1 mL aliquots of the cell suspension were mixed with AgNO₃ to achieve the desired Ag⁺ exposure concentration. For experiments involving NOM, stock AgNO₃ solutions were incubated with NOM for 2 h in the dark prior to bacterial exposure. Cells were incubated with the AgNO₃ solutions for 30 min at room temperature and were then harvested by centrifugation at 2000 RCF (10 min). The cells were resuspended in pH 7.5 phosphate buffer after removing the supernatant. Then 100 μL of each cell suspension was mixed with 100 μL of a mixture of 3.34 mM Syto-9 and 20 mM propidium iodide in a 96 well plate. These reagents were provided in the BacLight Viability Kit described above. Samples were incubated for 15 min at room temperature, and then the fluorescence emission intensities at 528/20 nm (Syto-9 emission) and 635/32 nm (propidium iodide emission) were measured on a Synergy 2 Multi-Mode Reader (BioTek, Winooski, VT) using an excitation wavelength of 485/20 nm. The ratio of the Syto-9 to propidium iodide emission intensities, representing

the ratio of cells with intact membranes to those with damaged membranes, was then calculated.

Exposing the bacteria to 2.5 μM Ag^+ reduced the live to dead cell ratio from 3.2 (0.0 μM Ag^+ control) to less than 2.5 (see Figure S8), confirming that Ag^+ is toxic to the bacteria at this dose.

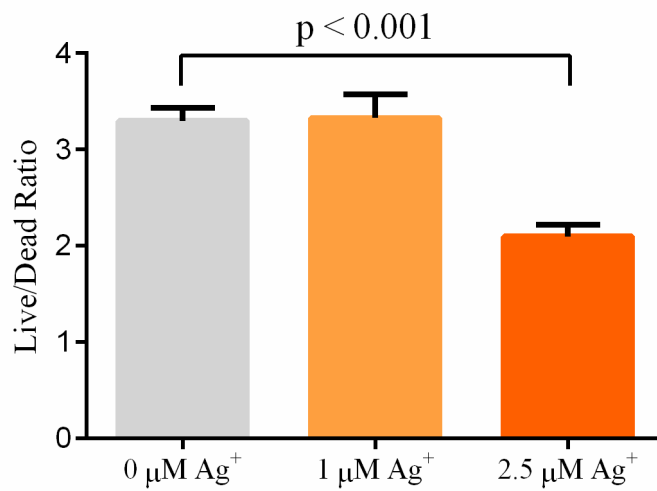


Figure S8. Toxicity of 1.0 μM and 2.5 μM Ag^+ to *Shewanella oneidensis*.

Chapter 4

Facile Method to Stain the Bacterial Cell Surface for Super-Resolution Fluorescence Microscopy

Adapted from:

Gunsolus, I. L.; Hu, D., Mihai, C., Lohse, S. E., Lee, C., Torelli, M. D., Hamers, R. J.,
Murphy, C. J., Orr, G., Haynes, C. L. *Analyst*. **2014**, *139*, 3174-3178

Copyright ©2014 Royal Society of Chemistry. All rights reserved.

This work was a joint effort of this author and Dr. Dehong Hu, who performed stochastic optical reconstruction microscopy, Dr. Cosmin Mihai, who assisted with structured illumination microscopy, and Drs. Samuel Lohse and Chang-soo Lee and Marco Torelli, who synthesized and characterized fluorescent nanoparticles.

A method to fluorescently stain the surfaces of both gram-negative and gram-positive bacterial cells compatible with super-resolution fluorescence microscopy is presented. This method utilizes a commercially-available fluorescent probe to label primary amines at the surface of the cell. We demonstrate efficient staining of two bacterial strains, the gram-negative *Shewanella oneidensis* MR-1 and the gram-positive *Bacillus subtilis* 168. Using structured illumination microscopy and stochastic optical reconstruction microscopy, which require high quantum yield or specialized dyes, we show that this staining method may be used to resolve the bacterial cell surface with sub-diffraction-limited resolution. We further use this method to identify localization patterns of nanomaterials, specifically cadmium selenide quantum dots, following interaction with bacterial cells.

4.1 Introduction

Super-resolution fluorescence microscopy is becoming a popular method for addressing biological questions that require sub-diffraction-limited spatial resolution. Super-resolution fluorescence microscopy techniques include stochastic optical reconstruction microscopy (STORM), a type of localization microscopy³⁵⁹ which requires photo-switching fluorescent dyes to achieve images with 10-30 nm spatial resolution, and structured illumination microscopy (SIM),³⁶⁰ which requires dyes with high quantum yield and photo-stability to achieve images with 120-130 nm spatial resolution. An extension of traditional fluorescence microscopy, super-resolution fluorescence microscopy provides opportunities for imaging intact live and hydrated cells using direct labeling of molecules and cellular structures with resolution that could previously be achieved only by electron microscopy, which requires sectioning of frozen or chemically fixed cells. Fluorescence labeling schemes are a central challenge in super-resolution fluorescence microscopy, requiring probes that have high quantum yield, excellent photostability, and in the case of STORM, dynamic fluorescence behavior (e.g. photoswitching or photoactivation). To date, two primary fluorescence labeling strategies have been utilized: genetically-encoded fluorescent proteins and small molecule fluorescent probes.³⁶¹ Small molecule probes provide several advantages over fluorescent proteins, including higher average quantum yields and increased labeling flexibility.³⁶² Continued development of suitable small molecule fluorescent probes, as well as methods for tagging cellular structures with these probes, are necessary to expand the scope of biological questions that can be addressed via super-resolution fluorescence microscopy.

A ripe area for the application of super-resolution fluorescence microscopy is microbiology, given that many features of microorganisms typically cannot be resolved by traditional fluorescence microscopy. Already, super-resolution microscopy has provided insight into fundamental bacterial cell biology, e.g. the mechanism of cell division and protein distribution and activity.³⁶³ Here, we propose a new application of these techniques to probe the interface of bacterial cells with their extracellular environment. Our specific focus is the nanomaterial-cell interface, an area which has recently received growing attention, motivated by the potential applications of nanomaterials as antimicrobial agents and a desire to assess the potential for unintentional ecological consequences of nanomaterial release into the environment.³¹⁷ To date, researchers have relied heavily on electron microscopy to characterize both nanomaterial localization at the microbial cell membrane³⁶⁴ and cellular penetration,³⁶⁵ while electron microscopy provides unparalleled spatial resolution, it struggles to observe cells in their natural hydrated state. The ability of super-resolution microscopy to observe hydrated cells with nanometer resolution will provide insightful in situ characterization of cell-nanomaterial interactions.

Fluorescent labeling of the microorganism cell wall or surface is a necessary first step in this direction, and labeling methods have been presented in a handful of studies. Foster and coworkers monitored cell wall assembly in gram-positive bacteria by conjugating a fluorescent vanomycin to the peptidoglycan layer at the cell surface,³⁶⁶ while Moerner and coworkers labeled the gram-negative *Caulobacter crescentus* using Cy3-Cy5 covalent heterodimers to target lysine residues at the cell surface.³⁶⁷ Though these two examples are

important, there is no precedent for a simple, fast, and generalizable method to label the bacterial cell wall or surface for super-resolution fluorescence microscopy.

Here, we present a labeling method for both gram-negative and gram-positive bacteria using a commercially available Alexa Fluor dye conjugate used commonly to label free proteins. A subset of the Alexa Fluor dyes are capable of photo-switching between dark, non-fluorescent, and bright, highly fluorescent states, and are among the limited number of fluorophores compatible with STORM or photoactivated localization microscopy (PALM).³⁶⁸ The photo-switching phenomenon can be exploited to achieve images with nanometer resolution using STORM and PALM. Using this labeling strategy, which has been employed in previous studies to label the bacterial cell surface for traditional fluorescence microscopy,^{369–371} we achieve sub-diffraction limited spatial resolution of the cell wall of gram-negative and gram-positive bacteria using both SIM and STORM. We further use SIM to characterize the interface of the gram-negative bacterium *S. oneidensis* with cadmium selenide quantum dots. This focus on the nanomaterial-prokaryote interface runs in parallel to studies of the engineered nanomaterial-eukaryotic cell interface, a topic which has received growing attention as the consumer product and biomedical applications of nanoparticles grow,³⁷² necessitating a greater understanding of cellular response to nanomaterial exposure and the material properties governing this interaction.³⁷³

4.2 Experimental

4.2.1 Bacterial culture preparation. *Shewanella oneidensis* MR-1 was a gift from the lab of Jeff Gralnick at the University of Minnesota, and *Bacillus subtilis* 168 was purchased

from the Bacillus Genetic Stock Center. Both were cultured on LB agar plates (BD Biosciences) from frozen stocks stored at -80 °C. These were incubated at 30 °C to achieve colony formation, and individual colonies were used to inoculate LB broth. Liquid cultures were incubated at 30 °C with 300 RPM shaking until stationary growth phase was reached as determined by optical density measurements.

4.2.2 Cell staining. Cells were harvested at the stationary phase by centrifugation of 1 mL suspensions at 2000 RCF for 10 minutes. The resulting cell pellet was rinsed twice with calcium- and magnesium-free phosphate buffered saline (PBS), (Gibco, Life Technologies) without resuspending the cells. Cells were resuspended in PBS at a cell density of 10⁸ cells/mL. (Note: staining was also successfully performed in 0.1 M bicarbonate buffer though all images presented herein were acquired from suspensions stained in PBS.) A 250 µL aliquot was removed, and then 9.4 µL of 0.5 mg/mL Alexa Fluor 488 carboxylic acid succinimidyl ester (Life Technologies) in DMSO (Sigma Aldrich) was added. The resulting suspension was incubated in the dark for one hour at room temperature with frequent mixing. The suspension was then centrifuged at 2000 RCF for 10 minutes, the supernatant was discarded, and the cell pellet was resuspended in 500 µL of PBS.

4.2.3 Preparation for imaging. To facilitate cell adherence to the glass surface, glass coverslip-bottom dishes were coated with poly-L-lysine by incubating the dishes with 500 µL of 0.1 mg/mL poly-L-lysine (Sigma Aldrich) for four hours at room temperature, then aspirating the solution and drying overnight. The stained cell suspension was loaded onto

the poly-L-lysine-coated dish and incubated for 30 minutes at room temperature to allow cell adherence. The suspension was then aspirated and replaced with 500 μ L of 4% formaldehyde (Ted Pella, Redding CA) in PBS and incubated for 15 minutes at room temperature; then the solution was aspirated and replaced with PBS. SIM imaging was done in PBS. For STORM imaging, the suspension was aspirated and replaced with 100 mM 2-mercaptoethyl amine (Sigma Aldrich) in water.

4.2.4 Preparation of nanomaterials. Cadmium selenide/zinc sulfide core-shell quantum dots were purchased from Life Technologies. According to the manufacturer's specifications, the principal nanoparticle size is approximately 10 nm (see Supporting Information) and the nanoparticle surface is functionalized with amino-poly(ethylene glycol) (Qdot 605: Life Technologies Q21501MP). The stock solution of quantum dots had a concentration of 8 μ M.

4.2.5 Cell exposure to nanomaterials. Cells were cultured in LB broth, harvested, and diluted to 10^8 cells/mL in PBS as described above. Quantum dots, at a concentration of 250 nM, were added to the cells and incubated for 1.5 hours at 30 °C with 300 RPM shaking. Cell staining, as described above, was performed after nanoparticle exposure.

4.2.6 Microscopy parameters. SIM imaging was performed on a Zeiss Elyra S1 microscope using a 100x magnification (NA=1.46) oil-immersion objective. Excitation of Alexa Fluor 488 and cadmium selenide quantum dots was achieved using 488 nm and 561

nm laser excitation, respectively. Emission bandpass filters were 495-550 nm and 570-620 nm, respectively. The two excitation/emission color channels were recorded consecutively. Within each color channel, the raw data contained 5 rotations, 5 phases and 0.1 μm spacing Z stack images. The super-resolution images were then reconstructed from raw images using ZEISS Efficient Navigation (ZEN) 2012 software to provide 2D and 3D projections.

STORM imaging was performed on a Zeiss Axio Observer inverted microscope using a 100x magnification (NA=1.45) oil-immersion objective and additional 1.6x magnification in the emission pathway of the microscope. Excitation of Alexa Fluor 488 was achieved using 473 nm laser excitation at 500 W/cm² and an exposure time of 0.5 seconds. The emission was acquired using a 500-550 nm bandpass filter and an electron multiplying CCD camera (iXon 897, Andor). Thousands of raw single molecule fluorescence images were acquired and processed, and STORM images were reconstructed using in-house software written in MATLAB.

Confocal fluorescence imaging was performed on a Zeiss LSM 710 laser scanning confocal microscope using a 100x magnification (NA=1.46) oil objective. Excitation of Alexa Fluor 488 was achieved using 488 nm excitation, and the emission was acquired in the 499-592 nm spectral window. Optical sections were taken at 1 μm thickness and images were processed in ZEN 2012 software.

4.3 Results and Discussion

The cell surfaces of both gram-positive *Bacillus subtilis* 168 and gram-negative *Shewanella oneidensis* MR-1 were labeled using an amine-reactive fluorescent probe (Alexa Fluor 488 carboxylic acid, succinimidyl ester) that binds to primary amines found in outer-membrane proteins, peptide residues in the surface peptidoglycan layer of gram-positive bacteria, and lipopolysaccharides on the surface of gram-negative bacteria (present in e.g. o-phosphorylethanolamine).³⁷⁴ By utilizing an unmodified, commercially available fluorescent probe and requiring minimal sample preparation, this method offers a simple alternative to existing super-resolution fluorescence microscopy-compatible fluorescence labeling methods and is compatible with both SIM and STORM. This method of live-cell labeling is non-trivial: labeling efficiency depends greatly on the reaction conditions, especially protein concentration, as specified by the manufacturer.

Successful labeling of gram-positive cells is demonstrated in Figure 1, which compares the resolution obtained using laser-scanning confocal microscopy (left) and SIM (right). While confocal microscopy resolves individual cells, it is less capable than SIM of resolving the cell surface from the cell interior.

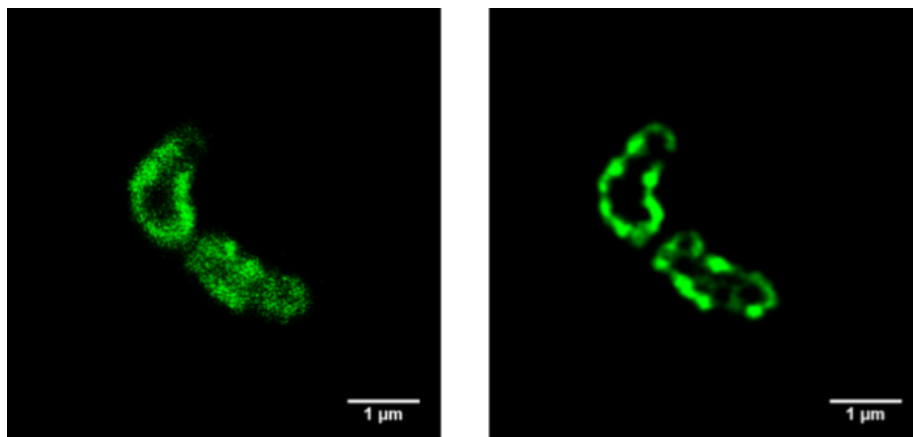


Figure 1. Confocal (left) and SIM (right) images of stained *Bacillus subtilis* 168 adhered to a poly-L-lysine-coated glass surface and immersed in PBS. A single optical section from a z-stack is shown in both images.

Gram-negative bacteria were also successfully labeled and imaged with SIM using identical sample preparation and imaging conditions (Figure 2 left). One major difference between using this method to perform SIM and STORM is that a thiol-containing buffer, 2-mercaptoethyl amine in this case, must be used to achieve STORM because this allows photoswitching of the Alexa Fluor 488.³⁷⁵ Without a thiol group present, Alexa Fluor 488 fluoresces continuously upon irradiation as it cycles primarily between the singlet ground and excited states. In the presence of a thiol, the triplet state of the excited fluorophore can react to form a radical anion, resulting in a dark state that is stable on the millisecond to second time-scale. The fluorescent state is recovered through oxidation by molecular oxygen. Unlike SIM, which is, in principle, compatible with any fluorophore, STORM requires fluorophores capable of cycling repeatedly between dark and bright states.¹⁷¹ This requirement places a strict limitation on the fluorophores available for STORM and makes this facile approach especially powerful. Using the approaches described in Thompson et al. and Mortenson et al.,^{376,377} we estimate the localization precision achieved in STORM images to be 30-40 nm (see Supporting Information), compared with the resolution in SIM images, which is 120-130 nm in the lateral dimension, according to the manufacturer's specifications.

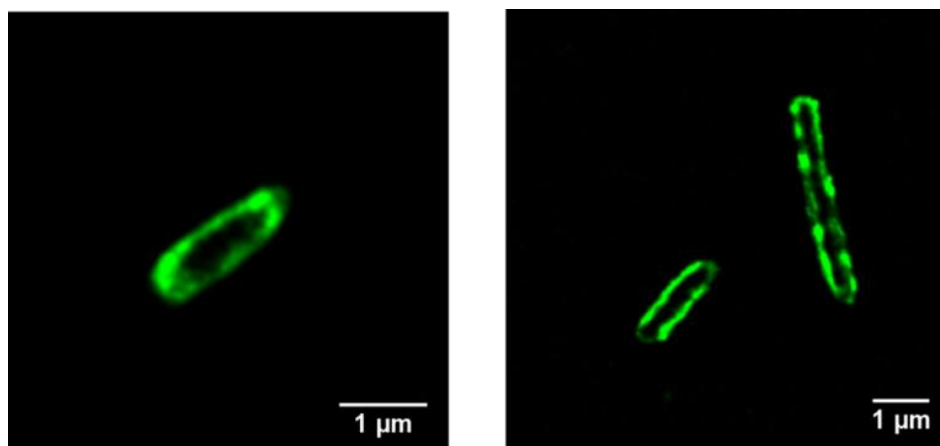


Figure 2. SIM (left) and STORM (right) images of stained *Shewanella oneidensis* MR-1 adhered to a poly-L-lysine-coated glass surface and immersed in PBS for SIM or 2-mercaptoethyl amine for STORM.

The imaging scheme presented here expands the range of biological systems that may be imaged by super-resolution fluorescence microscopy by providing a simple method to fluorescently label either gram-positive or gram-negative bacteria. This approach has the potential to facilitate a wide range of biological fluorescence imaging studies because it targets primary amines, a ubiquitous biological functional group, using a bright, stable, and commercially-available fluorophore.

To demonstrate the potential utility of this imaging scheme, we characterized the localization pattern of an engineered nanomaterial (cadmium selenide quantum dots) with bacterial cells. Such characterization is of great importance to understanding and exerting control over the engineered nanomaterial-biological interaction, and is motivated by the increasing production of nanomaterials and the corresponding increase in the likelihood of

their entry into natural environments;³⁷⁸ given the fundamental role of bacteria in the ecosystem, the consequences of their interactions with engineered nanomaterials (e.g. to cell viability and function) may be significant to ecosystem health.³¹⁷ Electron microscopy (EM) is the current standard for qualitative analysis of bacterial cell-engineered nanomaterial interactions, but requires significant sample preparation that often precludes imaging in the natural hydrated state, has limited options for cell labeling, and is not compatible with low atomic mass nanoparticles (e.g. carbon-based materials). Super-resolution fluorescence microscopy can be used to observe live, intact, and hydrated cells with greater resolving power than traditional fluorescence microscopy and greater flexibility in terms of sample preparation and labeling than EM. As a result, super-resolution fluorescence microscopy will give significant insight into nanomaterial-cell interactions.

Herein, the utility of super-resolution fluorescence microscopy for characterizing nanomaterial-cell interactions was demonstrated by imaging *Shewanella oneidensis* MR-1 after 1.5 hour interaction with fluorescent cadmium selenide/zinc sulfide core-shell quantum dots. A representative image from this analysis is shown in Figure 3. Clusters of quantum dots of approximately 10-15 nm diameter (resolved by transmission electron microscopy, see SI) with amino-poly(ethylene glycol) surface functionalization associate with the cell surface with, at best, partial penetration into the cell membrane. Lack of nanoparticle internalization may be attributed to the rigid cell structure of gram negative bacteria and lack of endocytosis pathways for species that cannot diffuse through outer-

membrane porins. The role of outer-membrane components in preventing nanomaterial permeation of the cell membrane is addressed directly in Chapter 5.

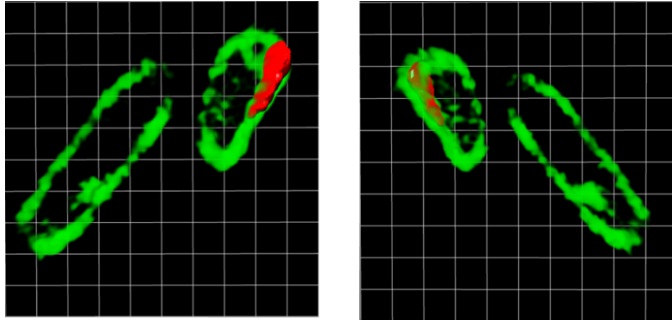


Figure 3. Left: SIM image of *Shewanella oneidensis* MR-1 with associated amino-PEG quantum dots (quantum dots in red and bacterial cell wall in green). Colocalization of the quantum dots and the bacterial cell wall is evident, and quantum dot internalization is not observed. Right: view upon 180° rotation along the vertical axis in the image plane. Each square has side length 0.42 μm .

Traditional laser-scanning confocal microscopy provides insufficient resolution to definitively identify the location of cell-bound quantum dots (inside the cell vs. on the cell surface vs. embedded in the extracellular polymeric matrix). A representative image is shown in Figure 4. Comparison of Figures 3 and 4 demonstrates the power of super-resolution fluorescence microscopy for characterizing the nanomaterial-biological interface in the natural hydrated state.

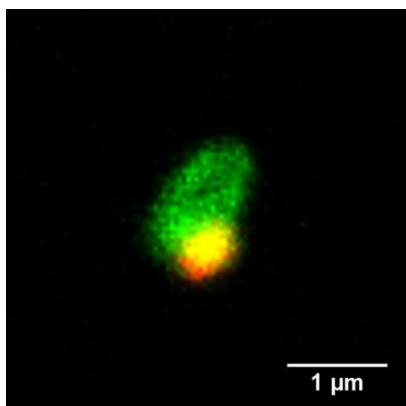


Figure 4. Laser-scanning confocal microscopy image of *Shewanella oneidensis* MR-1 with associated amino-PEG quantum dots (quantum dots in red and bacterial cell wall in green).

4.4 Conclusions

By targeting primary amines on the cell surface, the method presented here provides a facile means to label the surface of both gram-positive and gram-negative bacteria and is compatible with dyes required for super-resolution fluorescence microscopy. Requiring less than two hours of sample preparation time and using only commercially-available materials, this method will make super-resolution fluorescence microscopy more available to researchers lacking experience in designing and preparing novel fluorophores and tagging approaches. Using this method, we have observed quantum dot localization at the membrane of hydrated, gram-negative bacterial cells without membrane penetration. This method will facilitate the application of super-resolution fluorescence microscopy to address new questions in microbiology, for example, assessment of structural changes under environmental stress or interactions with nanomaterials at the cell membrane of hydrated cells.

4.5 Acknowledgements

This work was funded by a grant from the National Science Foundation to the Center for Sustainable Nanotechnology, CHE-1240151. Galya Orr acknowledges partial support from NIEHS grant 1RC2ES018786-01. I.L.G. acknowledges partial support from a training grant from the University of Minnesota Biotechnology Institute. We wish to thank the Jeff Gralnick lab at the University of Minnesota for their donation of *Shewanella oneidensis* MR-1. A portion of the research was performed at EMSL, a national scientific user facility sponsored by the Department of Energy's Office of Biological and Environmental Research and located at PNNL. CSL acknowledges the Bionanotechnology Research Center, Korea Research Institute of Bioscience and Biotechnology (KRIBB), 125 Gwahangno, Yuseong-gu, Daejeon 305-806, Korea.

4.6 Supporting Information

To provide broader context for this work, we include here additional image analysis and images of bacterial cells stained with amine-reactive Alexa Fluor 488 either alone or in combination with quantum dots. Quantum dot material characterization data is also provided.

4.6.1 Estimating the localization precision achieved by STORM. The equation below, taken from Thompson et al. 2002, was used to estimate the localization precision achieved by STORM.³⁷⁶

$$\langle(\Delta x)^2\rangle = \frac{s^2 + a^2/12}{N} + \frac{8\pi s^4 b^2}{a^2 N^2}$$

By estimating $N=500$ photons, $b=10$ photons, $a=100$ nm, and $s=\text{FWHM}/2.35=270/2.35=115$ nm, the value of Δx was found to be 14.3 nm. According to this method, the FWHM resolution of STORM imaging performed herein is $14.3*2.35 = 34$ nm.

A more conservative estimate was also calculated using the equation below, taken from Mortensen et al. 2010.³⁷⁷

$$\text{Variance} = \frac{\sigma_a^2}{N} \left(\frac{16}{9} + \frac{8\pi\sigma_a^2 b^2}{Na^2} \right)$$

where $\sigma_a^2 = \sigma^2 + a^2/12$.

Estimating $N=500$ photons, $b=10$ photons, $a=100$ nm, and $\sigma=\text{FWHM}/2.35=270/2.35=115$ nm, the resulting Δx value was found to be 15.8 nm. Accordingly, the FWHM resolution of STORM is $14.3*2.35 = 37$ nm.

4.6.2 Images of Cells and Nanomaterial-Cell Interactions. Figure S1 demonstrates the resolving power of STORM by comparing wide-field (top) and STORM (bottom) images of *Shewanella oneidensis* MR-1 stained and imaged as described in the methods section.

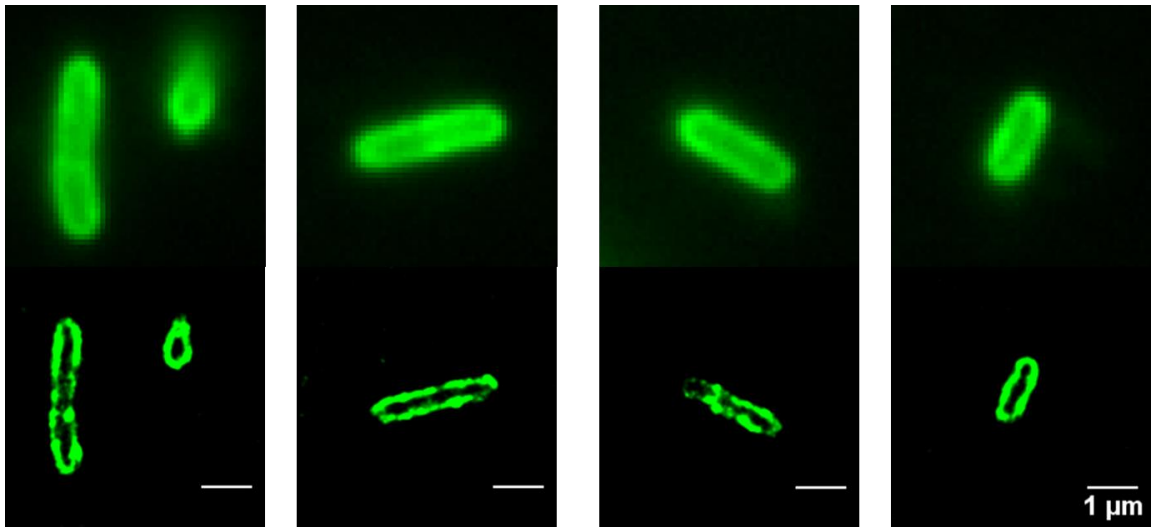


Figure S1: Wide-field (top) and STORM (bottom) images of *Shewanella oneidensis* MR-1 stained with amine-reactive AF-488.

Figure S2 presents an additional SIM image of *Shewanella oneidensis* MR-1 exposed to 250 nM amino-poly(ethylene glycol)-functionalized CdSe/ZnS core-shell quantum dots. Quantum dots, shown in orange, are observed to associate with the cell wall, again showing no penetration into the intracellular space.

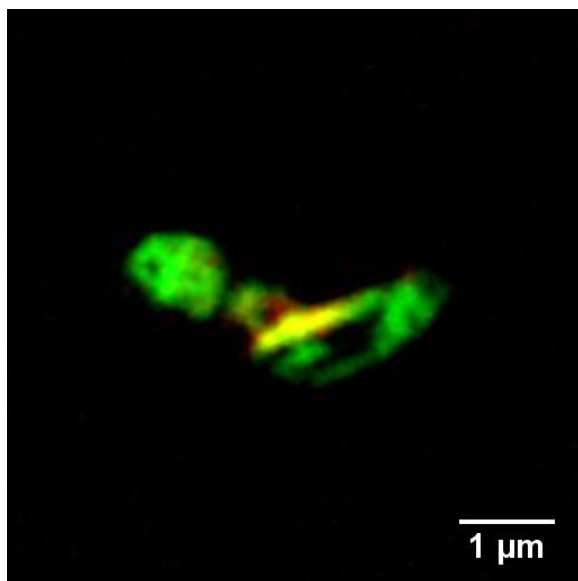


Figure S2: SIM image of *Shewanella oneidensis* MR-1 stained with amine-reactive AF-488 (green), exposed to 250 nM amino-poly(ethylene glycol)-functionalized CdSe/ZnS core-shell quantum dots (orange).

4.6.3 Commercial CdSe/ZnS Quantum Dot Size Characterization. Amino-poly(ethylene glycol) functionalized CdSe(core)/ZnS (shell) nanoparticles were analyzed by transmission electron microscopy (TEM, see Figure S3). Particles were diluted 10-fold in ethanol, dried onto a 300 mesh pure carbon grid (Ted Pella), and viewed with a Philips FEG CM200 Ultra Twin TEM at 200 kV accelerating voltage. Particle size in longest dimension is $9.3 \text{ nm} \pm 1 \text{ nm}$ (n=83).

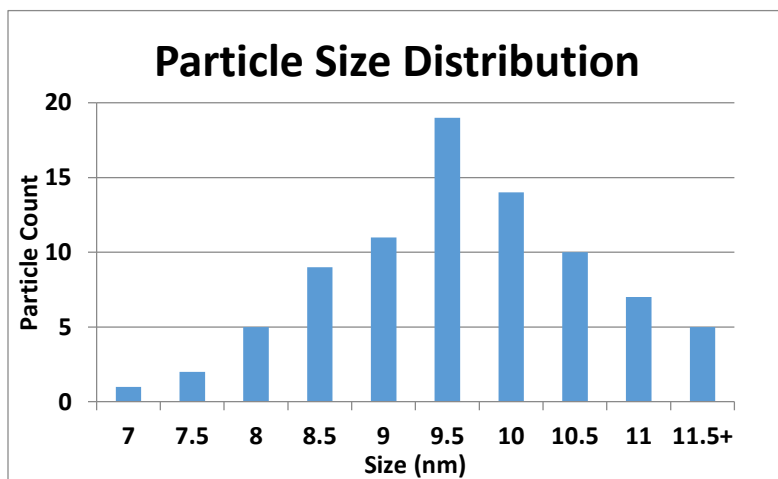
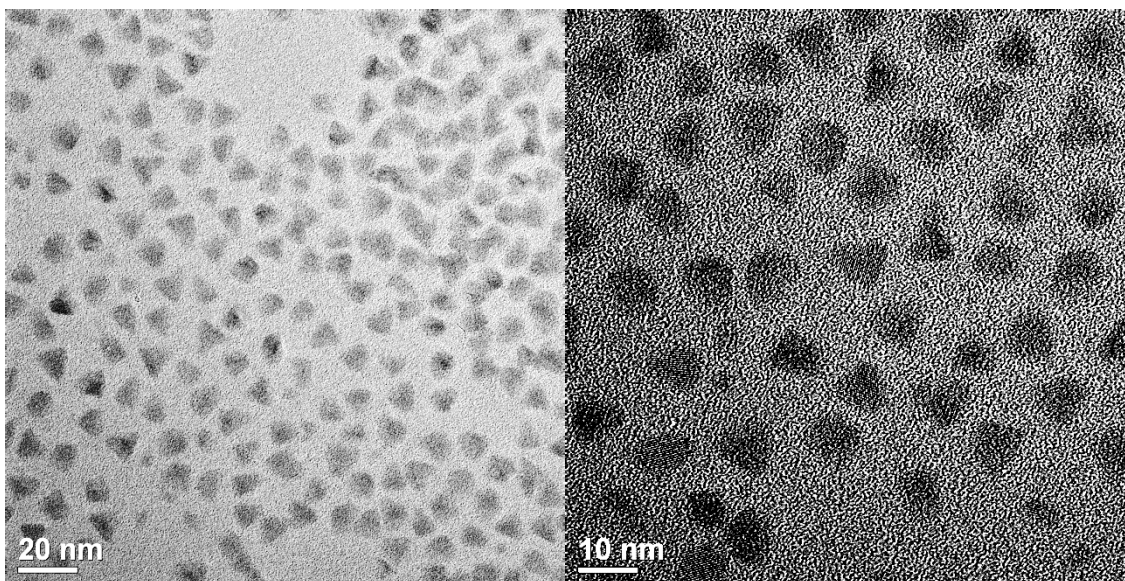


Fig. S3 Representative images of amino-poly(ethylene glycol) functionalized CdSe(core)/ZnS (shell) nanoparticles at 250,000x and 460,000x magnification with size distribution (n=83).

Chapter 5

Lipopolysaccharide Density and Structure Govern the Extent and Distance of Nanoparticle Interaction with Actual and Model Bacterial Outer Membranes

Adapted from:

Gunsolus, I. L.; Jacobson, K. H., Kuech, T. R., Troiano, J. M., Melby, E. S., Lohse, S. E., Hu, D., Chrisler, W. B., Murphy, C. J., Orr, G., Pedersen, J. A., Haynes, C. L. *Environ. Sci. Technol.* **2015**, *49*, 10642-10650

Copyright ©2015 American Chemical Society. All rights reserved.

This work was a joint effort of this author and Drs. Kurt Jacobson and Thomas Kuech, who characterized gold nanoparticle adsorption to supported lipid bilayers using quartz crystal microbalance with dissipation monitoring, Julianne Troiano, who characterized gold nanoparticle association to supported lipid bilayers using second harmonic generation, Eric Melby, who acquired fluorescence micrographs of supported lipid bilayers exposed to gold nanoparticles, and Dr. Dehong Hu and William Chrisler who assisted with fluorescence-activated cell sorting of bacterial cells exposed to nanoparticles.

Design of nanomedicines and nanoparticle-based antimicrobial and antifouling formulations and assessment of the potential implications of nanoparticle release into the environment requires understanding nanoparticle interaction with bacterial surfaces. Here we demonstrate the electrostatically driven association of functionalized nanoparticles with lipopolysaccharides of gram-negative bacterial outer membranes and find that lipopolysaccharide structure influences the extent and location of binding relative to the outer leaflet-solution interface. By manipulating the lipopolysaccharide content in *Shewanella oneidensis* outer membranes, we observed the electrostatically driven interaction of cationic gold nanoparticles with the lipopolysaccharide-containing leaflet. We probed this interaction by quartz crystal microbalance with dissipation monitoring (QCM-D) and second harmonic generation (SHG) using solid-supported lipopolysaccharide-containing bilayers. The association of cationic nanoparticles increased with lipopolysaccharide content, while no association of anionic nanoparticles was observed. The harmonic-dependence of QCM-D measurements suggested that a population of the cationic nanoparticles was held at a distance from the outer leaflet-solution interface of bilayers containing smooth lipopolysaccharides (those bearing a long O-polysaccharide). Additionally, smooth lipopolysaccharides held the bulk of the associated cationic particles outside of the interfacial zone probed by SHG. Our results demonstrate that positively charged nanoparticles are more likely to interact with gram-negative bacteria than are negatively charged particles, and this interaction occurs primarily through lipopolysaccharides.

5.1 Introduction

In the early 2000s, products containing engineered nanomaterials (materials with at least one dimension < 100 nm) began to enter commerce on a large scale.^{379,380} Production and use of these materials has increased dramatically over the intervening years, leading to concerns about their potential environmental health and safety implications. Assessment of the potential risks associated with unintended release of engineered nanoparticles into the environment^{255,381,382} is necessary to ensure the sustainable use of these materials, given their increasing integration into consumer products and the expectation that their contact with living organisms will induce biological responses.^{383–385} Reliable risk assessment is currently hampered by the limited mechanistic insight into how nanoparticles interact with ecologically important organisms including bacteria, which represent entry points into food chains. Current approaches for understanding interactions between nanoparticles and bacteria are typically indirect; many rely on monitoring changes in bacterial activity or survival in response to nanoparticle exposure, for example using quantitative structure-activity or high-throughput screening strategies.^{248,299,386} Such approaches are favored mainly because the small size and biological complexity of bacteria remain barriers to direct characterization of nanomaterial-bacterial cell interactions. While insights have been derived from such indirect, correlative approaches, such as recent suggestions that cell-surface lipopolysaccharides (LPS) may be important in protecting Proteobacteria (a major group of gram-negative bacteria) from the effects of cationic polystyrene and silver nanoparticles,^{299,386} direct characterization of nanoparticle-bacterial cell interactions is needed to validate hypothesized mechanisms of interaction.

Here, we characterize nanoparticle interactions with bacteria directly at a level of molecular detail that is not currently attainable by monitoring microbial activity or survival. Moreover, we provide concrete evidence that LPS molecules protect gram-negative bacteria from nanoparticles by forming a barrier to contact with and penetration of the outer membrane. The direct views of nanoparticle interactions with LPS achieved in this work show that a unique nanobiophysical interface controls nanomaterial interactions with gram-negative bacteria, in which strain and growth condition-specific traits (i.e., LPS structure) influence the extent and nature (i.e., length-scale) of this interaction. A large variety of nanoparticle types may be explored. We focus here on electrostatics as a main driving force for nanoparticle-LPS interactions. Our experimental strategy was to evaluate the role of LPS and its structure in mediating interactions of cationic and anionic gold nanoparticles (AuNPs) with bacterial cell surfaces. We hypothesized that electrostatic interactions contribute strongly to nanoparticle interaction with LPS. To test our hypothesis, we used 4-nm-diameter AuNPs functionalized with mercaptopropyl ligands terminated with either cationic or anionic moieties to probe the influence of nanoparticle charge on interactions with LPS in both live bacterial cells and solid-supported lipid bilayers.

5.2 Experimental Methods

5.2.1 Gold Nanoparticle Preparation and Characterization. Gold nanoparticles (primary particle diameter = 4.0 ± 0.5 nm) were prepared³⁸⁷ by a modified Brust procedure and functionalized with either 3-mercaptopropionic acid (MPA) or 3-mercaptopropyl amine (MPNH₂). These were chosen as model nanomaterials to investigate nanoparticle-

LPS interactions due to their high chemical stability and well-controlled size, shape, and surface functionalization. Except where noted otherwise, experiments with AuNPs were conducted at a 12.8 nM number concentration in 0.002 M HEPES (pH 7.4) and 0.025 M NaCl.

Nanoparticle hydrodynamic diameter (Figure 1a) and electrophoretic mobility (Figure 1b) were measured by dynamic light scattering (DLS) and laser Doppler micro-electrophoresis, respectively, as a function of solution ionic strength, I , using a Malvern ZetaSizer Nano ZS (Worcestershire, UK). Dynamic light scattering and electrophoretic mobility measurements were made 10 min after dilution of particle suspensions into solutions of the desired I . Both types of functionalized AuNPs formed larger aggregates as I increased. The hydrodynamic diameters for the MPA- and MPNH₂-AuNPs increased from ~50 nm at $I = 0.025$ M (Debye length, κ^{-1} , = 1.93 nm) to ~450 nm at $I = 0.100$ M ($\kappa^{-1} = 0.96$ nm) and were statistically indistinguishable from one another at each ionic strength ($p > 0.05$). The electrophoretic mobilities of the MPA- and MPNH₂-AuNPs were negative and positive, respectively, and did not vary with ionic strength over the range studied ($p < 0.05$).

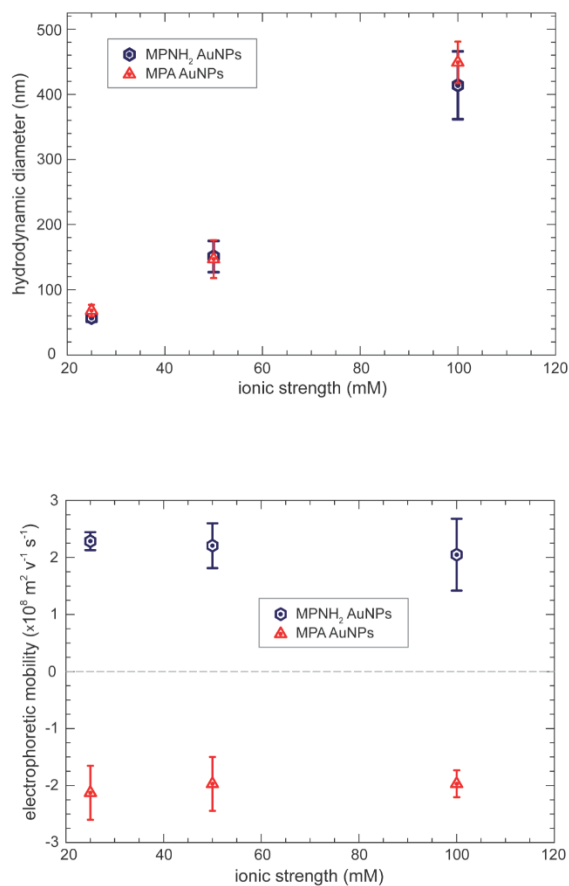


Figure 1. Number-average hydrodynamic diameters (**a**) and electrophoretic mobilities (**b**) of MPA- and MPNH₂-functionalized gold nanoparticles (AuNPs) as a function of solution ionic strength. All values were measured at a (particle number) concentration of 12.8 nM in 2 mM HEPES solution (pH 7.4). The desired ionic strength was achieved by addition of NaCl. Error bars represent one standard deviation ($n = 10$).

5.2.2 Bacterial Culture. *Shewanella oneidensis* MR-1 (courtesy of Jeff Gralnick, University of Minnesota) was cultured in LB broth, achieving cell densities of $\sim 1 \times 10^9$ cells·mL⁻¹ at the stationary growth phase (24 h incubation at 30 °C with continuous shaking at 300 RPM).

5.2.3 Removal of LPS from Cells. Cells in LB broth were sedimented (10 min, 2000g), the supernatant was removed, and the cells were suspended in D-PBS to achieve a final cell density of 2×10^8 cells·mL⁻¹. Cell suspensions were split into two batches, and EDTA was added to one at a concentration of 0.005 M to remove a fraction of cell-surface LPS.³⁸⁸ Both batches were then incubated with continuous shaking (10 min, 30 °C). Cells were sedimented by centrifugation (10 min, 2000g), the supernatant was removed and replaced with buffer (0.002 M HEPES, pH 7.4, $I = 0.025$ M), and the cells were resuspended. Three aliquots from each cell sample were removed and lyophilized, and their dry masses were recorded. The lyophilized cells were dissolved in 0.2 N H₂SO₄, and their LPS content was determined using the method described by Karkhanis et al.³⁸⁹ (see the Supporting Information for details).

5.2.4 Nanoparticle-Cell Attachment Experiments. Following EDTA treatment and redispersal in buffer (*vide supra*), cells were mixed with AuNPs (12.8 nM number density) and incubated with continuous mixing (10 min, room temperature). Cells were then mixed 1:1 with 3.34 mM SYTO 9 (Life Technologies Kit L7012) and incubated 15 min prior to analysis by flow cytometry. Cells associated with AuNPs were identified via a combination of nucleic acid staining with SYTO 9 (to identify cells) and orthogonal (side) light scattering intensity detection (to identify nanoparticles) using a flow cytometer (Becton Dickinson LSRII SORP equipped with a 20 mW, 488 nm laser). Cells were then sorted

into populations with and without associated AuNPs using a FACSARIAIIU cell sorter. Gating parameters for cell sorting are described in the Supporting Information.

After sorting, we acquired dark-field images of cell populations that were positive or negative for AuNPs with an Olympus BX43 microscope modified with a high signal-to-noise dark-field condenser unit (CytoViva, Auburn, AL). Hyperspectral images were acquired in the same field of view using the CytoViva hyperspectral imaging system consisting of a spectrophotometer (Specim) and spectrophotometer-integrated CCD (pco.pixelfly). Data were analyzed using the Spectral Angle Mapping feature of ENVI 4.8 software (Exelis Visual Information Solutions).

5.2.5 Nanoparticle-Bilayer Attachment Experiments. Unilamellar vesicles composed of 1-palmitoyl-2-oleoyl-*sn*-glycero-3-phosphocholine (POPC) or POPC with varying amounts of smooth or rough LPS were prepared and their hydrodynamic sizes, electrophoretic mobilities, and LPS contents³⁸⁹ were determined as described in the Supporting Information. Solid-supported lipid bilayers were formed on SiO₂-coated QCM-D sensors via surface-mediated fusion of POPC or LPS-containing POPC vesicles³⁹⁰ (Figure S4; see Supporting Information for details). The QCM-D instrument used was a Q-Sense E4 instrument (Biolin Scientific, Göteborg, Sweden) containing four sensors mounted in temperature-controlled, liquid flow cells. The fundamental frequency (f_1) of the sensors was 4.96 MHz. Except where noted otherwise, data are reported for the 5th harmonic (~25 MHz.).

Nanoparticle attachment experiments were commenced by pumping AuNP suspensions (12.8 nM number concentration; 0.002 M HEPES, pH 7.4, ionic strength adjusted with NaCl) over the supported lipid bilayers until the Δf and ΔD signals stabilized.³⁹¹ Nanoparticle-free buffer was then pumped through the flow cells to measure the detachment of nanoparticles from the POPC or POPC/LPS bilayers. Final areal mass density of lipid bilayers with and without associated AuNPs were estimated using the Sauerbrey equation^{392,393} or Kelvin-Voight viscoelastic modeling³⁹⁴ (Tables S1 and S3). For details, see the Supporting Information.

5.2.6 Second Harmonic Generation. Second harmonic generation (SHG) experiments were performed using a regeneratively amplified Ti:Sapphire laser system (Hurricane, Spectra-Physics, 1 kHz repetition rate, 120 fs pulses) pumping an optical parametric amplifier (OPA-CF, Spectra-Physics) tuned to a fundamental wavelength between 610 and 615 nm as previously described^{395–398} and further detailed in the Supporting Information. The *p*-polarized beam was focused onto the silica/buffer interface at which the bilayer was formed. The SHG signal was detected following our published procedures.^{395–397} All SHG experiments were performed under static conditions.

Vesicles containing varying amounts of LPS (*vide supra*) were introduced into the cell and allowed to self-assemble into an LPS-containing lipid bilayer on the silica substrate. Various concentrations of AuNPs (10^{-14} to 10^{-8} M number concentration) in buffer were then introduced into the cell, and the SHG signal was monitored until it stabilized for at

least 15 min. Nanoparticle-free buffer was introduced to the cell to assess the reversibility of the interaction of the particles with the bilayer.

5.3 Results and Discussion

5.3.1 Nanoparticle-Cell Attachment. The bacterial cell envelope represents the critical contact point governing access of nanomaterials and their secondary products (e.g., reactive oxygen species, dissolved ions) to the cell interior. The structure of the gram-negative bacterial cell envelope is complex: the inner phospholipid cell membrane is encompassed by a thin peptidoglycan cell wall, which itself is bounded by an outer membrane.³⁹⁹ The outer membrane is an asymmetric structure. The inner leaflet is composed of phospholipids, while a major portion of the outer leaflet consists of complex lipopolysaccharides (LPS), a class of glycolipids.³⁹⁹ LPS covers approximately 75% of the outer membrane surface of some bacteria⁴⁰⁰ and serves as an important hydrophilic barrier (with significantly higher hydration levels than phospholipid bilayers),⁴⁰¹ protecting gram-negative bacteria from antimicrobial peptides, hydrophobic antibiotics, and surfactants such as bile salts.^{399,402} A typical full-length, or “smooth” LPS molecule is composed of three distinct domains: Lipid A (four to seven acyl chains attached to two phosphorylated glucosamines)⁴⁰³ anchoring the LPS molecule in the outer membrane bilayer; a core oligosaccharide composed of hexoses, heptoses, and 3-deoxy-D-mannooctulosonic acids;⁴⁰⁴ and the O-polysaccharide, a variable-length repeating oligosaccharide chain containing up to 50 repeat units⁴⁰⁵ (Figure S1). At pH values typical of the environment, all three domains carry a net negative charge from phosphate groups ($pK_a < 3$), and

glucuronic acid ($pK_a < 3$), galacturonic acid ($pK_a < 4$) and *N*-acetylneuraminic acid ($pK_a 2.6$) residues. Some bacteria exhibit shorter types of LPS, referred to as “rough” LPS, which contains Lipid A and at least part of the core oligosaccharide, but lacks the O-polysaccharide. Due to the abundance of LPS at the interface of the cell envelope of gram-negative bacteria with the extracellular environment, understanding the molecular nature of its interactions with engineered nanoparticles is critical for assessing the potential for disruption or penetration of the gram-negative bacterial cellular envelope.

We examined the association of AuNPs with live gram-negative bacterial cells (*Shewanella oneidensis* MR-1, hereafter denoted *Shewanella*) as a function of cell LPS content and nanoparticle surface charge using a combination of flow cytometry, dark-field microscopy, and hyperspectral imaging. *Shewanella* was selected in part because the cells of this species have only a sparse distribution of extracellular polymeric substances at their membrane,^{406–408} meaning that LPS (and not polysaccharide components that form a capsule around some bacterial cells) form the interface between these cells and their extracellular environment. To test the hypothesis that LPS mediates nanoparticle interaction with gram-negative bacteria, as suggested by recent high-throughput screening studies of *Escherichia coli* interactions with polystyrene and silver nanoparticles^{299,386} and cytotoxicity studies,^{300,409} we prepared LPS-depleted *Shewanella* cells. Brief treatment with EDTA^{388,410} removed ~50% of cell LPS from the outer membrane (Figure S2), as determined by colorimetric measurement of 8-amino-3,8-dideoxy-D-manno-octulosonic acid (8-amino-2-keto-3-deoxy-D-manno-octonate, 8-aminoKdo),³⁸⁹ a *Shewanella* species-specific aminated form of 3-deoxy-D-manno-octulosonic acid,^{411,412} an essential component of LPS. Prior work on

E. coli has demonstrated that this method removes LPS from the outer membrane without concomitant removal of proteins or leakage of cell contents.³⁸⁸ The mechanism is suggested to involve chelation of divalent cations that cross-link LPS molecules through interaction with anionic sites such as phosphates,^{401,410,413} releasing LPS into the solution.³⁸⁸ Quantification of cell LPS content required that cells be sacrificed. Experiments with nanoparticles were performed on live cell populations with either native or depleted LPS content.

We exposed $\sim 2 \times 10^8$ native and LPS-depleted *Shewanella* cells to cationic MPNH₂- or anionic MPA-functionalized AuNPs (10 min, 12.8 nM AuNP, $I = 0.025$ M, pH = 7.4; see Figure 1 for nanoparticle properties) and quantified the number of cells in each treatment associated with AuNPs by flow cytometry. Association of AuNPs with cells increases the light scattering cross-section. High-throughput analysis of the orthogonal light scattering intensity of individual cells was used to identify the presence of cell-associated AuNPs. Cells exhibiting light scattering above an intensity threshold, determined by control experiments with unexposed cells, were identified as positive for AuNPs. In this way, tens of thousands of cells were classified *in situ* as either negative or positive for cell-associated AuNPs. Cell analysis required no preparative steps after cell-nanoparticle exposure and did not disrupt cell-nanoparticle interaction because the measurement was made in solution. Putative AuNP-positive cells were isolated by fluorescence-activated cell sorting (FACS) and imaged by hyperspectral and dark-field microscopy to verify the presence of associated AuNPs⁴¹⁴ and to establish FACS as an approach to discriminate between bacterial cells with and without associated AuNPs (Figures 2, S3, and S5).

Removing ~50% of the cell LPS content decreased the number of cells with associated MPNH₂-AuNPs by ~70% (Figure 2). At the growth temperature used (30 °C), *Shewanella oneidensis* MR-1 produces only rough LPS (see Figure S3b); lower growth temperatures induce synthesis of smooth LPS.⁴⁰⁷ Our results suggest that cationic nanoparticles bind preferentially to LPS, such that its removal decreases nanoparticle binding to the outer membrane. In contrast, anionic MPA-AuNPs did not appreciably associate with the cells, regardless of LPS content. Given the net negative charge of the gram-negative bacterial cell surface at pH values typical of the environment,^{415,416} this result suggests that electrostatic interactions control the association of nanoparticles with bacterial cells, as has been suggested in previous reports.^{299,386,417,418}

We visually confirmed nanoparticle association with cells by dark-field microscopy and hyperspectral imaging. We separated bacterial cells with associated MPNH₂-AuNPs from the total cell population by FACS and acquired dark-field micrographs of them. The micrographs show single bacterial cells with cell-associated material producing high-intensity light scattering, indicative of AuNPs (Figure 2a). We confirmed the presence of AuNPs by comparing hyperspectral images of nanoparticle-associated bacterial cells with a spectral library of bacteria-free colloidal MPNH₂-AuNPs (Figure S3). Regions of the cell hyperspectral image matching the AuNP library are highlighted in the micrographs. This analysis confirmed that the observed cell-associated material was MPNH₂-AuNPs. In addition, dark-field micrographs of bacterial cells exposed to MPNH₂-AuNPs were acquired prior to cell sorting. These micrographs also show cell-associated material producing high-intensity light scattering, consistent with the previous analysis (Figure 2b).

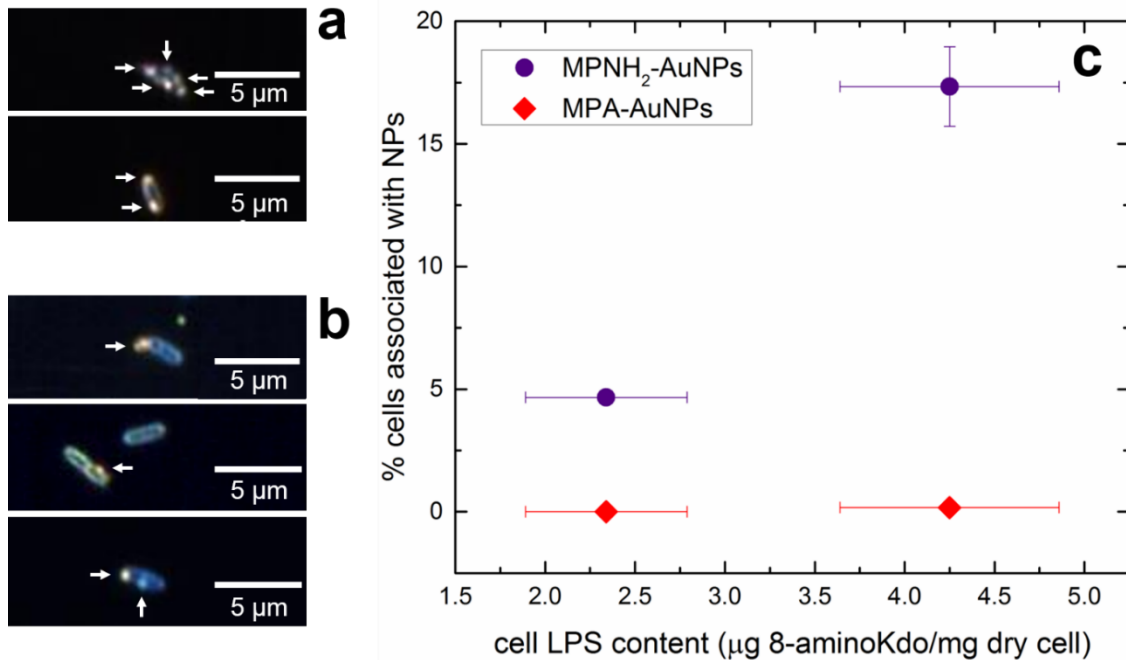


Figure 2. Gold nanoparticle association with bacterial cells is directly observable and depends on cell LPS content. Cells isolated (sorted) from the total cell population after exposure to MPNH₂-AuNPs (**a**). Unsorted cells after exposure to MPNH₂-AuNPs (**b**). In panels (a) and (b) the arrows point to AuNPs associated with the cells as confirmed by hyperspectral imaging. Association of MPA- or MPNH₂-AuNPs with *Shewanella* cells with varying LPS content (indicated by 8-amino-2-keto-3-deoxy-D-manno-octonate (8-aminoKdo) content of lyophilized cells) quantified by flow cytometry (**c**). Error bars (representing one standard deviation, $n = 3$) are smaller than the symbol in some cases.

5.3.2 Attachment of Cationic and Anionic Gold Nanoparticles to LPS-Containing

Bilayers. To gain further molecular insight into the interaction of nanoparticles with lipopolysaccharides identified in the studies with live bacterial cells described above, we investigated the amount, reversibility, and length scale of MPNH₂- and MPA-AuNP association with LPS containing or lacking the O-polysaccharide using quartz crystal microbalance with dissipation monitoring and second harmonic generation. The first step

in these studies was to form LPS-containing lipid bilayers on QCM-D sensor surfaces. We prepared vesicles composed of POPC with variable amounts of rough or smooth LPS (see Figure 3 and the Supporting Information).³⁸⁹ We then formed solid-supported LPS-containing bilayers on SiO₂-coated QCM-D sensors via fusion of LPS-containing POPC vesicles (Figure S4).³⁹⁰

We tested the hypothesis that electrostatics contributed strongly to nanoparticle interaction with LPS-containing bilayers by investigating the amount of cationic MPNH₂- and anionic MPA-AuNPs attaching to bilayers as a function of LPS content. These experiments were performed with 12.8 nM AuNPs in 0.002 M HEPES solution (pH 7.4) at $I = 0.025$ M or 0.100 M. Figure 4a shows maximum frequency shifts measured by QCM-D following association of MPNH₂-AuNPs with lipid bilayers composed of pure POPC or POPC containing different amounts of smooth or rough LPS. The negative frequency shifts observed after introduction of positively charged MPNH₂-AuNPs to all types of bilayers indicate nanoparticle association with the bilayers. The maximal frequency shifts and estimated areal mass densities for these systems are presented in Tables S2 and S3. Small amounts of MPNH₂-AuNP detachment were observed for most systems when they were rinsed with NP-free buffer (Figure S4). We did not detect interaction of the negatively charged MPA-AuNPs with any of the bilayers surveyed (mass detection limit for these systems was ~ 2 ng·cm⁻²).

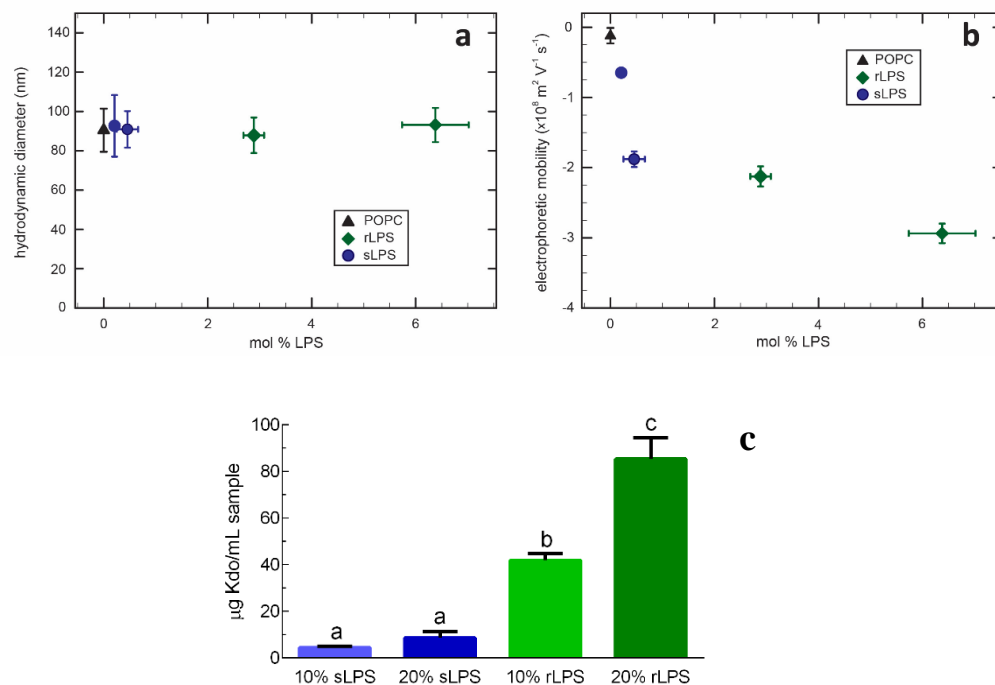


Figure 3. Hydrodynamic diameters (a) and electrophoretic mobilities (b) of unilamellar vesicles composed of POPC or POPC and the indicated mole percent of either smooth LPS (sLPS) or rough LPS (rLPS). Apparent ζ potentials derived from these electrophoretic mobility measurements are presented in Figure S7. All values were measured at a vesicle concentration of $10 \mu\text{g}\cdot\text{mL}^{-1}$ in a 0.002 M HEPES (pH 7.4), 0.001 M NaCl solution. Error bars represent one standard deviation ($n = 5$). Content of 2-keto-3-deoxy-D-mannooctonate (Kdo) in the POPC/LPS vesicles as a function of mass percent LPS addition (used to estimate mol% LPS in vesicles) (c). Each smooth LPS molecule contains three Kdo residues while each rough LPS molecule contains two Kdo residues.^{419,420} Error bars represent one standard deviation ($n = 3$). Values labeled with different letters differ significantly from each other ($p < 0.05$).

In the experiments conducted at 0.025 M NaCl, association of cationic MPNH₂-AuNPs with lipid bilayers increased with the amount of rough or smooth LPS incorporated, and

AuNP association was higher for smooth LPS-containing bilayers on a *per LPS molecule* basis (Figure 4a,b).

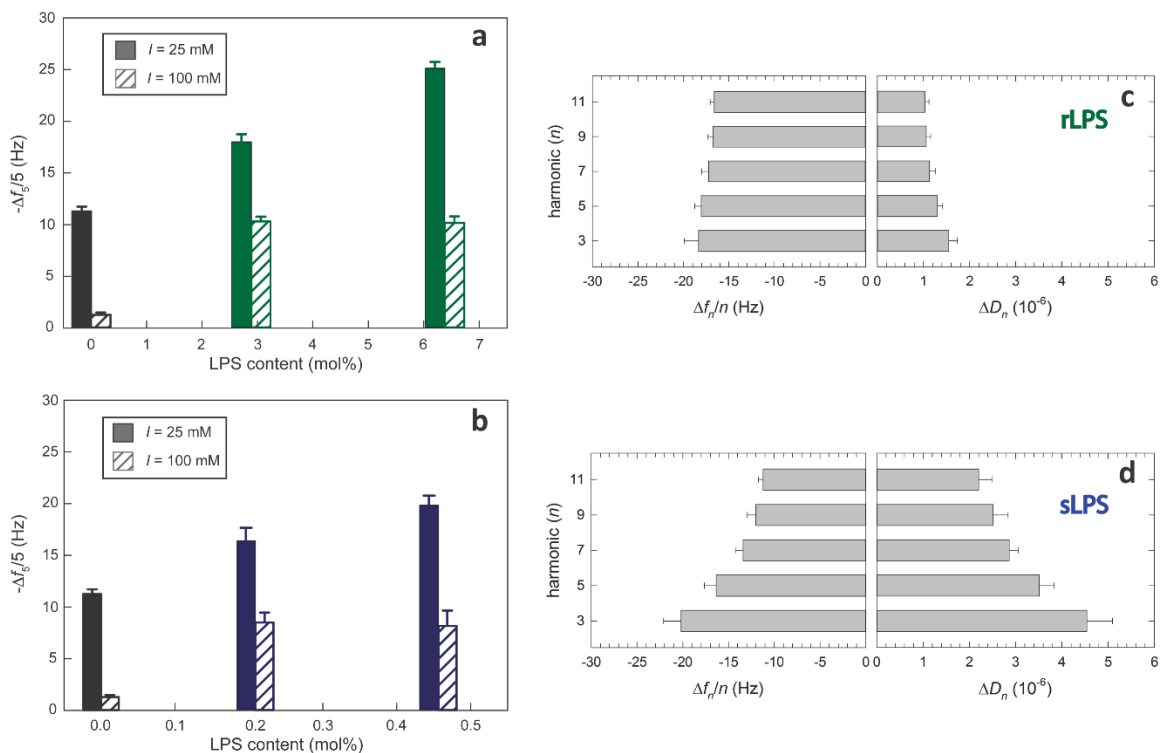


Figure 4. Association of MPNH₂-AuNPs with bilayers containing rough (a) or smooth (b) LPS. Normalized maximum frequency shifts for the 5th harmonic ($\Delta f_5/5$) during nanoparticle-bilayer exposure are displayed. Calculation of mole percent LPS content assumed three Kdo molecules per smooth LPS molecule and two Kdo molecules per smooth LPS molecule.^{419,420} Error bars represent one standard deviation ($n = 3$). (c) and (d) The harmonic-dependence of Δf_n and the energy dissipation factor (ΔD_n), where n is the harmonic number, is more pronounced for MPNH₂-AuNPs interacting with bilayers containing rough LPS (panel c) than smooth LPS (panel d).³⁹⁴ Experiments were performed in 0.002 M HEPES (pH 7.4) and 0.025 M NaCl.

Acoustic masses increased from $200 \pm 10 \text{ ng}\cdot\text{cm}^{-2}$ for POPC bilayers to $320 \pm 10 \text{ ng}\cdot\text{cm}^{-2}$ and $450 \pm 10 \text{ ng}\cdot\text{cm}^{-2}$ for those containing 2.9 and 6.4 mole % rLPS (Table S3). For bilayers

containing smooth LPS, acoustic masses were $280 \pm 20 \text{ ng}\cdot\text{cm}^{-2}$ for bilayers containing 0.21 mol % sLPS and $330 \pm 20 \text{ ng}\cdot\text{cm}^{-2}$ for those containing 0.46 mol % sLPS. These results point to the O-polysaccharide domain of smooth LPS molecules presenting many more potential binding sites for cationic nanoparticles in solution than the solvent-exposed portion of rough LPS molecules. Each rough LPS molecule used in our experiments contains two negative charges (phosphates associated with glucosamine residues in Lipid A).⁴²¹ In contrast, the smooth LPS molecules typically contain additional negatively charged moieties including additional phosphate groups and acidic sugars (e.g., glucuronic and galacturonic acids) in the outer core and O-polysaccharide domains,⁴²² which extend farther into solution than negatively charged moieties in rough LPS molecules. The higher abundance of negatively charged moieties in smooth LPS molecules relative to rough LPS molecules is evidenced in the electrophoretic mobility measurements of LPS-containing vesicles (Fig. 3b). We note that the acyl chains of the ligands on the nanoparticles are three carbons long and terminate in a charged functional group. For bilayers composed solely of POPC, we expect the charged ligands bound to the nanoparticles would interact primarily with the phosphatidylcholine head group of these lipids.

Changes in QCM-D energy dissipation (ΔD) during MPNH₂-AuNP association differed between smooth and rough LPS-containing bilayers. The smooth LPS-containing bilayers exhibited larger increases in ΔD_5 (3.0 to 4.0×10^{-6}) than did POPC or rough LPS-containing bilayers (0.8 to 1.5×10^{-6}). This result indicates that MPNH₂-AuNPs interacting with smooth LPS-containing bilayers were less rigidly coupled to the vibrating resonator than those associated with POPC or rough LPS-containing bilayers.

At higher ionic strength ($I = 0.100$ M), the MPNH₂-AuNPs agglomerated (Figure 1a), and association with all bilayers decreased significantly relative to the experiments conducted at lower ionic strength (Figure 4a,b; Table S3). Association of MPNH₂-AuNPs with bilayers containing LPS (140 to 190 ng·cm⁻²) was higher than those composed of pure POPC (23 ± 4 ng·cm⁻²); however, the amounts associated with LPS-containing bilayers did not differ from each other ($p > 0.05$). These results indicate that smooth LPS induced higher nanoparticle association on a per molecule basis than did rough LPS. This result is consistent with the notion that smooth LPS, due to the presence of the O-polysaccharide, presents a larger number of anionic sites for interaction with cationic AuNPs than does rough LPS on a per molecule basis.

5.3.3 Proximity of MPNH₂-AuNPs to the Phospholipid-Solution Interface. The harmonic-dependence of the QCM-D frequency and dissipation responses allows inference of the relative distance that AuNPs are held from the sensor-solution interface for the bilayers containing rough and smooth LPS. The penetration depth of the shear wave (δ) depends on the harmonic (n): $\delta = \left(\eta_l / \pi \eta f_1 \rho_l \right)^{0.5}$, where η_l is liquid dynamic viscosity, f_1 is the fundamental frequency (4.96 MHz), and ρ_l is the liquid density.³⁹⁴ Lower harmonics penetrate further into the medium overlying the sensor than do higher harmonics. We compared the dependence of changes in frequency ($\Delta f_n/n$) and dissipation (ΔD_n) on the harmonics monitored in experiments probing MPNH₂-AuNP association with smooth and rough LPS-containing bilayers (Figure 4c,d). Both $\Delta f_n/n$ and ΔD_n displayed pronounced harmonic-dependence for MPNH₂-AuNPs association with smooth LPS-containing

bilayers; for the rough LPS-containing bilayer, $\Delta f_n/n$ and ΔD_n did not depend on the harmonic. While the penetration depth for all harmonics monitored (e.g., 145 and 76 nm for the 3rd and 11th harmonics, respectively) exceeded the length of the LPS molecules (7-46 nm for smooth LPS),⁴²³ signals for lower harmonics contain larger contributions from mass farther from the sensor surface than do higher harmonics. The more pronounced harmonic-dependence observed for MPNH₂-AuNP association with smooth compared to rough LPS-containing bilayers suggests that, in the former, at least some of the nanoparticle mass is held at a distance from the sensor surface (i.e., not directly in contact with the outer leaflet-solution interface). This is consistent with the notion that cationic particles interact with the O-polysaccharide domain of smooth LPS, because the O-polysaccharide presents anionic sites available for interaction with cationic nanoparticles that extend away from the bilayer surface.^{424,425}

To gain further insight into the molecular origins of nanoparticle-bilayer interactions observed by QCM-D, we employed second harmonic generation (SHG). When exciting with wavelengths near 600 nm, the SHG intensity near 300 nm increases when supported lipid bilayers are exposed to 4 nm AuNPs.¹⁴⁶ This nanoparticle-induced increase in intensity suggests resonance enhancement to the SHG signal upon AuNP adsorption to the bilayer-solution interface. Since the second-order nonlinear optical response is distance-dependent,^{426,427} SHG can be used to probe the length scale of AuNP-bilayer interactions. This principle allowed us to evaluate the location of AuNPs associated with the bilayers relative to the outer leaflet-solution interface, which is the least symmetric, and thus most SHG-active, region in our system.

Figure 5 shows the summary of our findings, while the Supporting Information contains the detailed results from our concentration-dependent SHG studies. Briefly, we find that exposing pure POPC bilayers to the MPNH₂-AuNPs under otherwise identical buffer and salt conditions increases the SHG signal intensity by more than 30%. Somewhat smaller SHG signal intensity gains were observed when the POPC bilayer contained 10% or 20% rough LPS. In contrast, no significant changes in SHG signal intensity were observed upon addition of nanoparticles to the bilayers containing 10% and 20% smooth LPS. Exposure of LPS-containing bilayers to anionic MPA-AuNPs did not produce an increase in SHG signal intensity either (data not shown), consistent with the lack of interaction between the AuNPs and these bilayers demonstrated in the QCM-D experiments (*vide supra*).

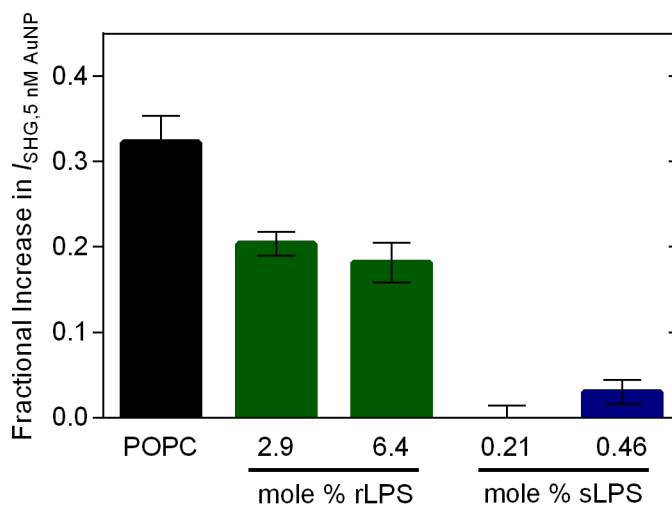


Figure 5. Observed changes in SHG signal intensity following introduction of MPNH₂-AuNPs (5×10^{-9} M number density) to POPC bilayers lacking LPS (black), or containing rough LPS (rLPS, green) or smooth LPS (sLPS, blue). The observed SHG signal arises from nanoparticle-induced resonance enhancement near the bilayer-solution interface. All experiments were performed in 0.002 M HEPES (pH 7.4) and 0.025 M NaCl.

Given that the QCM-D experiments described in the previous section show clear mass gains upon introduction of MPNH₂-AuNPs to bilayers containing both rough LPS and smooth LPS, we hypothesize that the lack of SHG signal intensity gains for the bilayers containing smooth LPS are due to the distance-dependence of the SHG process, as elaborated by Walker and co-workers.^{426,427} Under this hypothesis, nanoparticles associated with LPS are held at a larger distance from the bilayer-solution interface than those bound to POPC. The resulting reduction in SHG resonance enhancement would then lead to smaller increases in SHG intensity induced by nanoparticle association with bilayers, which is indeed observed. This interpretation of the correlated SHG and QCM-D results is supported by reports from Walker and coworkers who used molecular tethers, or rulers, to place SHG-active chromophores at various distances from liquid/liquid interfaces and found longer distances to coincide with diminishing and finally vanishing SHG signal.^{426,427} Quantitative distance measurements would, in principle, be possible by X-ray standing wave measurements⁴²⁸ or by anchoring AuNPs to the LPS-containing bilayers using tethers of varying lengths, but such demanding experiments have their own caveats and exceed the scope of the current study. LPS structure also influenced changes in SHG intensity, evidenced by the smaller increase in SHG intensity upon nanoparticle binding to smooth LPS than rough LPS. Smooth LPS contains the O-polysaccharide absent in rough LPS and thus presents negatively charged binding sites for AuNPs at a larger distance from the bilayer-solution interface (outside the interfacial zone probed by SHG), resulting in lower intensity enhancement.

5.3.4 Effect of Nanoparticle-Bilayer Association on Lipid Structure. To investigate the potential effects of nanoparticle association with bilayers on the underlying lipid structure, super-resolution fluorescence micrographs of POPC bilayers with variable LPS content were acquired before and after addition of MPNH₂-AuNPs (Figure S9). TopFluor PC was used to construct fluorescent bilayers within glass-bottom dishes. Then MPNH₂-AuNPs were introduced under identical conditions to those used in QCM-D experiments ($I = 0.025$ M). The images show that nanoparticle addition to pure POPC bilayers and POPC bilayers containing smooth LPS alters lipid packing, evidenced by the formation of lipid clusters (bright regions due to locally increased fluorophore concentration). In contrast, MPNH₂-AuNP introduction to POPC bilayers with rough LPS had no observable effect on lipid packing. This suggests that nanoparticle association with lipid bilayers, either through direct interaction with lipids or through interaction with LPS, may alter lipid packing. Evaluation of this hypothesis is the subject of ongoing work. We note, however, that the smooth LPS densities achieved in the supported lipid bilayers (0.21 to 0.46 mole %) are considerably lower than those occurring in bacteria that incorporate these molecules into their outer membranes. Our results suggest that bacterial outer membranes with higher smooth LPS densities would prevent contact of cationic nanoparticles with the bilayer.

5.4 Conclusions

The results of this study provide direct evidence for electrostatically driven association of cationic nanoparticles with the negatively charged polysaccharide portions of LPS molecules in the cell envelope of gram-negative bacteria, supporting the hypothesis that

LPS plays a critical role in mediating such nanoparticle-cellular interactions.^{299,300,386,409} Acoustic and spectroscopic data from QCM-D and SHG measurements, respectively, on analogous supported lipid bilayers indicate that these interactions occur farther into solution (farther from the outer leaflet-solution interface) in bacteria that elaborate LPS including the long O-polysaccharide chain (“smooth” LPS) compared to those bearing short, “rough” LPS. Correlated super-resolution fluorescence imaging studies of these lipid bilayers demonstrate that interaction of cationic nanoparticles with the smooth LPS-containing bilayer impacts lipid packing. Electrostatic repulsion is expected to prevent most associations of anionic particles with membrane-bound LPS molecules both in whole bacterial cells and the model lipid bilayers.

The propensity of smooth LPS to hold bound nanoparticles at a distance from the bilayer-solution interface suggests a barrier function for the O-antigen that may protect bacteria from the effects of nanoparticles that require contact with the outer membrane bilayer to induce adverse effects. This insight leads to the expectation that bacteria bearing rough LPS may be more susceptible to the effects of intact nanoparticles than are those that produce smooth LPS, despite lower association of nanoparticles with the former. The efficacy of nanoparticles that exert their antimicrobial effect via dissolution (e.g., silver nanoparticles)⁴²⁹ or production of reactive oxygen species (e.g., zinc oxide nanoparticles)^{48,418} is expected to depend on the balance between higher association with smooth LPS (for cationic NPs) and the greater availability of sites for interaction or reaction on these molecules vis-à-vis rough LPS, to the extent that damage to LPS is not deleterious. The detailed characterization of nanoparticle interactions with bacterial cells

and solid-supported lipid bilayers presented in this study demonstrates that LPS molecules mediate nanoparticle interactions with gram-negative bacteria and provides the molecular-level insight necessary to design engineered nanoparticles with reduced biological impact. Intriguingly, the LPS molecules that confer a barrier function to the outer membrane may also facilitate the entry of bacterial surface-bound nanoparticle into food chains.

5.5 Acknowledgements.

This study was supported by the National Science Foundation (NSF) under the Center for Sustainable Nanotechnology (CHE-1240151). Part of the research was performed at EMSL, a Scientific User Facility sponsored by DOE-BER and located at PNNL. We thank the University of Minnesota's University Flow Cytometry Resource for flow cytometric analysis and FACS. ILG gratefully acknowledges support through a National Institutes of Health Training for Future Biotechnology Development Grant (T32 GM008347) and a Minneapolis Torske Klubben Graduate Fellowship. JMT gratefully acknowledges support through an NSF Graduate Research Fellowship. Partial funding for the QCM-D instrument was from NSF grants DMR-0832760 and CBET-0826204. We thank Robert Hamers and Bill Hickey for helpful comments on the manuscript.

5.6 Supporting Information

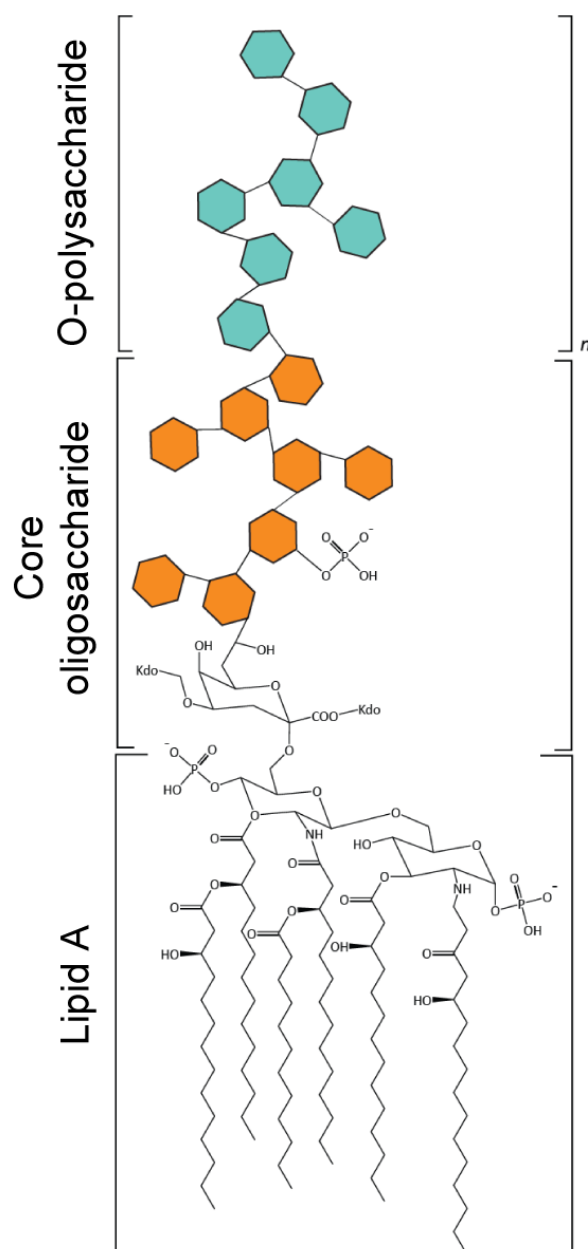


Figure S1. Representation of the general structure of lipopolysaccharide (LPS) from gram-negative bacteria such as *Salmonella enterica*.⁴³⁰ The LPS molecule can be divided into three domains: Lipid A, the core oligosaccharide, and the O-polysaccharide (or O-antigen). The fatty acid chains of Lipid A vary in number and length depending on the bacterial species and anchor the LPS molecule in the outer leaflet of the outer membrane. These are bound to a phosphorylated glucosamine disaccharide. The core oligosaccharide is

covalently bound to Lipid A and contains two or three 2-keto-3-deoxy-D-*manno*-octonate (Kdo) repeat units^{419,420} and commonly L-glycero-D-*manno*-heptose, in addition to other saccharides such as galactose, glucose and glucuronic acid.⁴⁰⁴ Some of these saccharides might also be phosphorylated. The outermost domain of LPS is the O-polysaccharide, a repeating oligosaccharide composed primarily of hexoses such as galactose, abequose, mannose, and rhamnose. The presence or absence (or reduction to a non-repeating oligosaccharide)⁴³¹ of the O-polysaccharide is used to classify LPS as smooth or rough, respectively. The length and degree of branching of polysaccharide chains varies across bacterial strains and species, but the overall three-component LPS structure depicted is conserved.

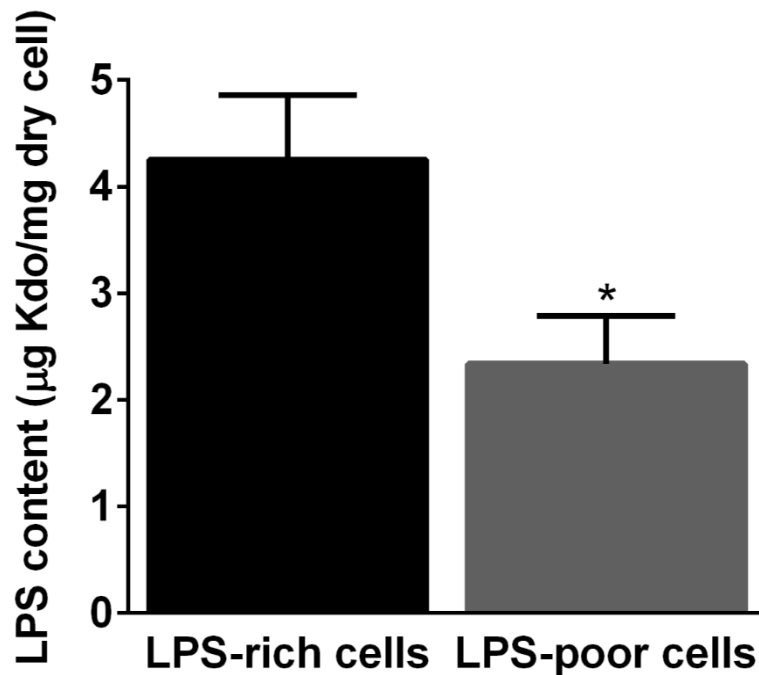


Figure S2. Lipopolysaccharide content of native (no EDTA treatment) and LPS-poor (EDTA-treated) *Shewanella oneidensis* MR-1 quantified by colorimetric detection 8-amino-3,8-dideoxy-D-*manno*-octulosonic acid (8-amino-Kdo).³⁸⁹ Error bars represent the standard deviation of three replicate measurements. The 8-amino-Kdo content of LPS-

depleted cells is significantly lower than that of native cells ($p < 0.05$), indicated by a single asterisk.

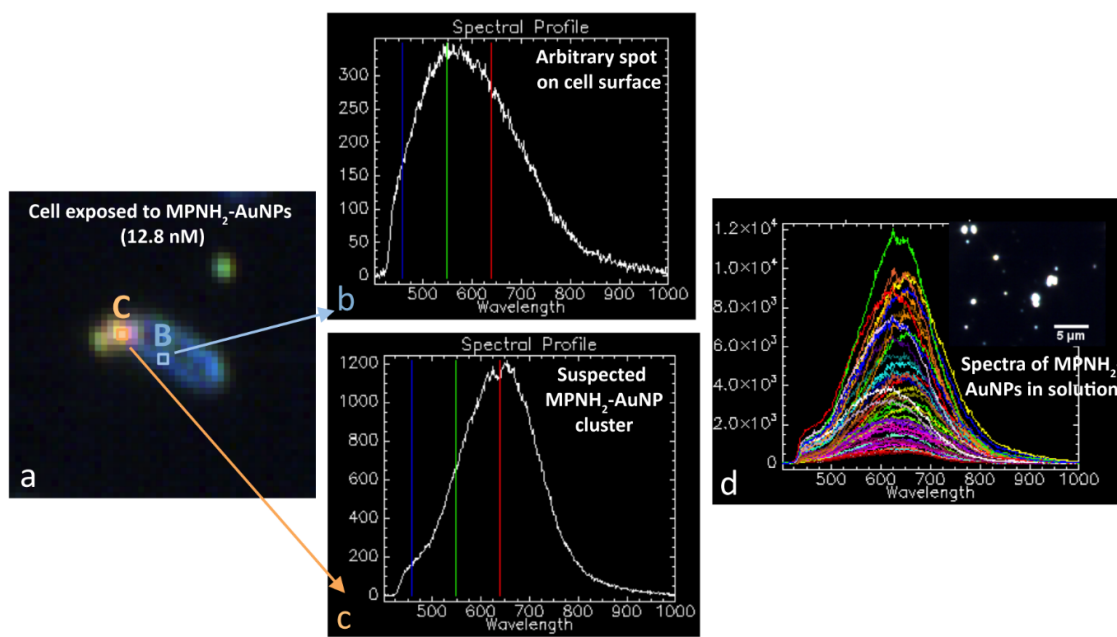


Figure S3. (a) The dark-field micrograph of a single *Shewanella* cell after 10-min exposure to 12.8 nM MPNH₂-functionalized gold nanoparticles (MPNH₂-AuNPs) (top panel, Figure 3b). A dark-field micrograph was acquired using an Olympus BX43 microscope (Olympus America, Inc., Center Valley, PA) modified with a high signal-to-noise condenser (CytoViva, Auburn, AL). A visible-near infrared (VNIR) spectral map of the cell with approximately 2.8 nm vertical and lateral resolution was acquired using the push-broom technique. An in-line spectrophotometer (Specim, Oulu, Finland) and CCD camera (pco.pixelfly, PCO, Kelheim, Germany) recorded scattered light intensity as the sample stage automatically and incrementally moved the sample into the spectrograph's field of view. Using this technique, a unique VNIR spectrum was acquired for each pixel within the dark-field image. Two pixels are highlighted, and their corresponding spectra are presented in panels (b) and (c). Panel B shows the spectrum obtained from an arbitrary spot on the cell surface. This spectrum is representative of the spectra obtained over the entire surface of the cell, excluding the suspected nanoparticle cluster shown in Panel C. At this

location (and neighboring locations within the yellow cluster in the dark-field image), the scattered light intensity is approximately four times higher and red-shifted relative to elsewhere on the cell surface. The spectrum obtained from Point C overlaps with spectra acquired from MPNH₂-functionalized gold nanoparticles in solution (**d**). Similarity analysis performed using the Spectral Angle Mapping feature of ENVI 4.8 software (Exelis Visual Information Solutions, Boulder, CO) indicates higher than 90% similarity between spectra obtained from the yellow cluster in the dark-field image and the library of spectra obtained from MPNH₂-functionalized gold nanoparticles in solution. This suggests that the yellow cluster associated with the cell surface is composed of MPNH₂-functionalized AuNPs.

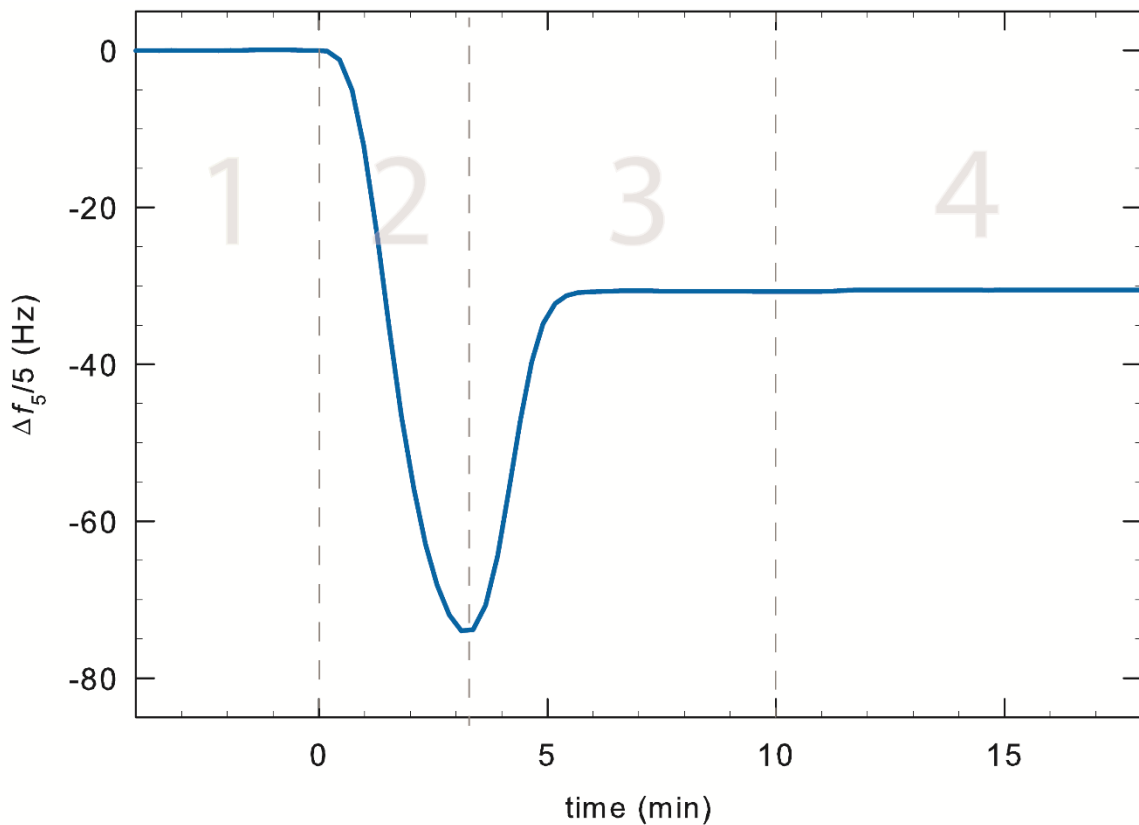


Figure S4. Formation of a representative POPC bilayer containing 0.21 mol% smooth LPS from *Salmonella enterica* serotype minnesota (sLPS) monitored by quartz crystal microbalance with dissipation monitoring (QCM-D). The plot show normalized changes

in the frequency of the 5th harmonic ($\Delta f_5/5$). Stable bilayer masses calculated using the Sauerbrey equation^{392,393} are presented in Table S1. After the SiO₂-coated QCM-D sensors attained a stable frequency signal under lipid free buffer (Zone 1), a solution containing vesicles (0.125 mg·mL⁻¹) was introduced to the flow cell (Zone 2). Intact vesicles associate with the SiO₂ surface until a critical vesicle coverage is attained and the vesicles rupture and fuse to form a bilayer (Zone 3). The water previously trapped in the vesicles is released, causing a decrease in the measured frequency. Any loosely bound lipid molecules or un-ruptured vesicles are then rinsed away with a lipid free buffer (Zone 4).

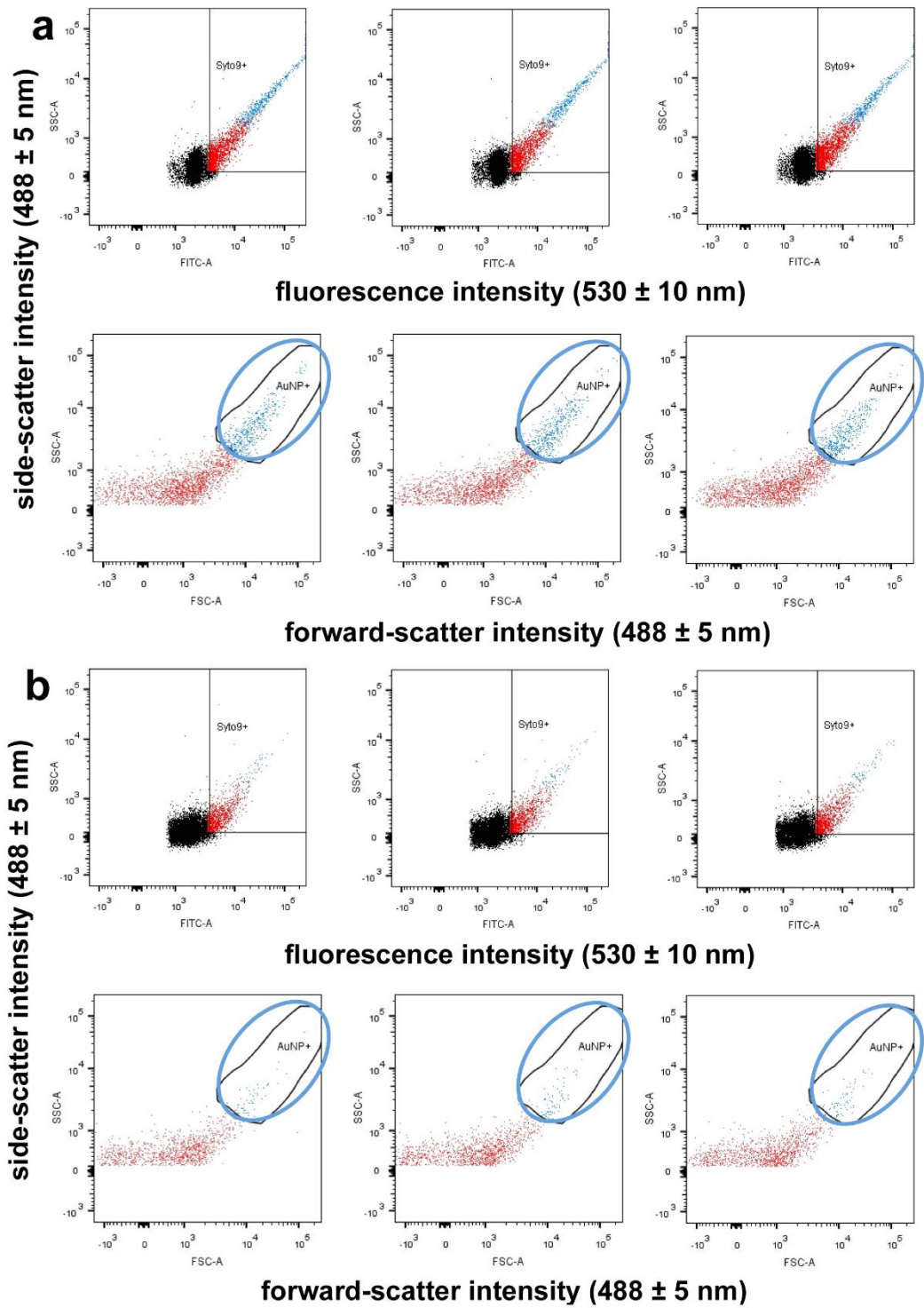


Figure S5. MPNH₂-functionalized gold nanoparticles (MPNH₂-AuNPs) associate more with native *Shewanella* cells than those depleted in LPS. Triplicate measurements of

MPNH₂-AuNP association with cells with native LPS content ($4.25 \pm 0.61 \mu\text{g Kdo/mg dry cell}$) (**a**) and cells depleted in LPS by brief treatment with EDTA³⁸⁸ ($2.34 \pm 0.45 \mu\text{g Kdo/mg dry cell}$) (**b**). The following abbreviations are used as axes labels: SSC-A (orthogonal or side-scattered light intensity); FITC-A (fluorescence emission intensity in the range $530 \pm 10 \text{ nm}$); FSC-A (forward-scattered light intensity). Black points indicate electronic noise and cell debris excluded from analysis; red points indicate cells stained with the nucleic acid stain SYTO-9; blue points indicate cells stained with SYTO-9 with cell-associated gold nanoparticles. In both panels, the top set of bivariate plots display events recorded by the flow cytometer as a function of fluorescence intensity (in the emission window of SYTO-9) and side-scattered light intensity. The boxed region in the top bivariate plots was gated using the minimum SYTO-9 fluorescence intensity of cells stained with SYTO-9, based on controls not exposed to AuNPs. This region, which contains all cells above the threshold staining intensity, acts as the reference population to calculate percent association of gold nanoparticles to cells. The bottom set of bivariate plots display only the events contained within the boxed region of the plots above, plotted using side-scattered vs. forward-scattered light intensity. The region highlighted by a blue circle was gated using the maximum side-scattered light intensity corresponding to cells not exposed to gold nanoparticles. Side-scattered light intensity above this threshold was contributed by the presence of gold nanoparticles, based on controls of gold nanoparticles without cells. The size of this region, corresponding to cells with association gold nanoparticles, decreases significantly with removal of LPS, as seen by comparing the size of this population from the plots in panels (**a**) and (**b**).

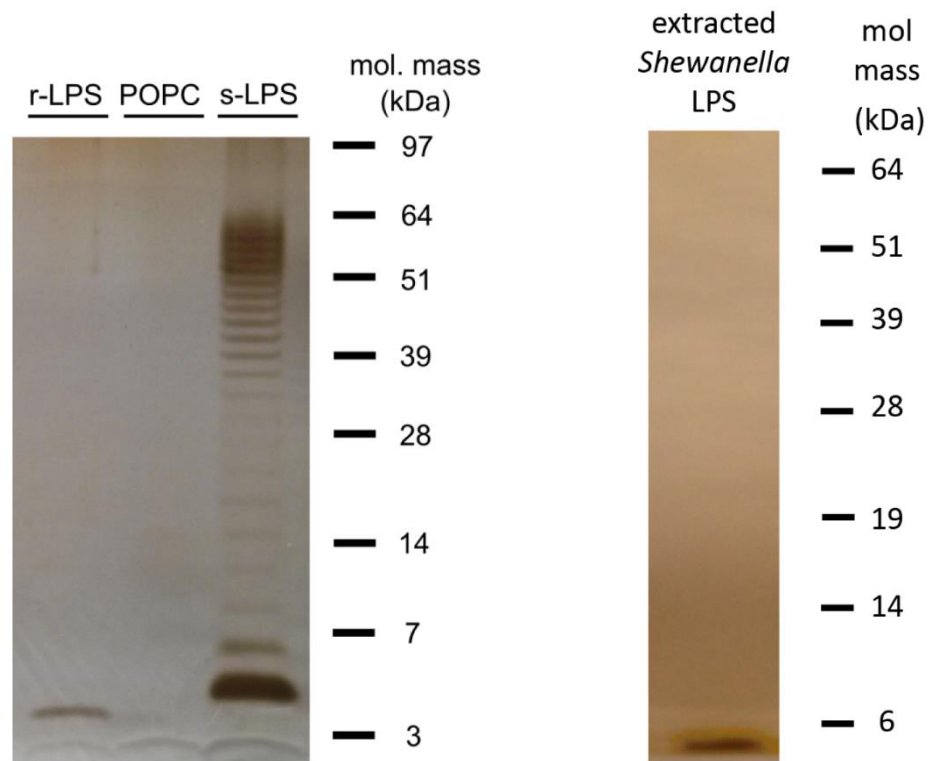


Figure S6. (a) SDS-PAGE/silver staining reveals the much larger average molecular mass of smooth LPS (sLPS, left) than rough LPS (rLPS, right) from *Salmonella enterica* serotype minnesota. POPC shown for comparison (does not stain). **(b)** LPS extracted from *Shewanella oneidensis* MR-1 shows similar molecular mass as rough LPS from *Salmonella*.

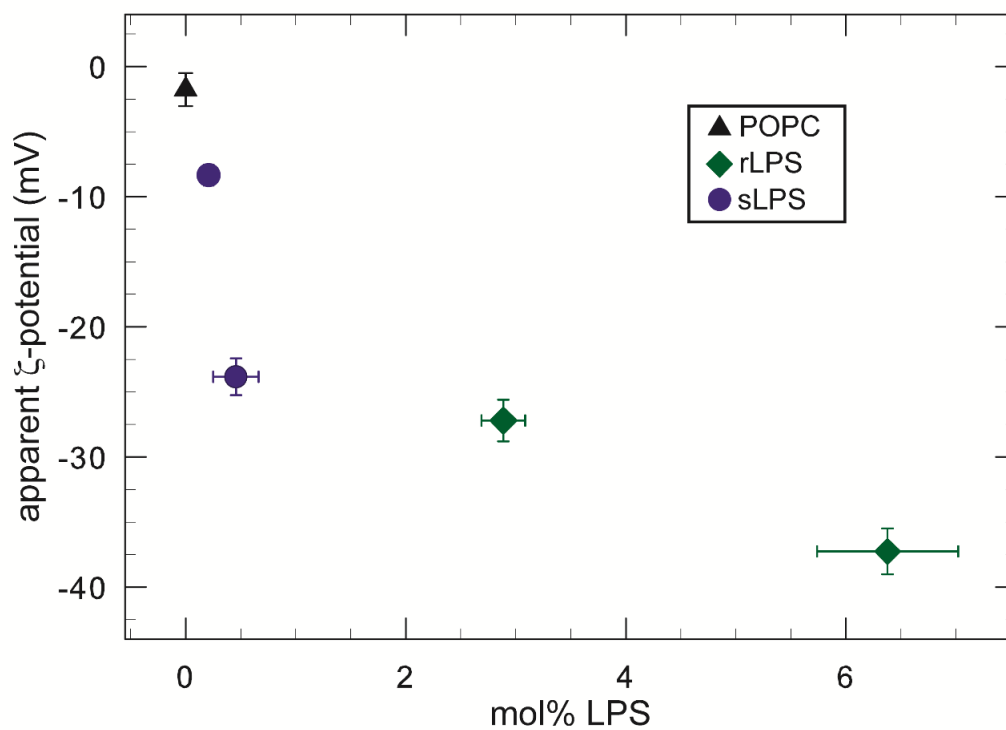


Figure S7. Apparent ζ potentials of unilamellar vesicles composed of POPC or POPC and the indicated mole percent of either smooth LPS (sLPS) or rough LPS (rLPS). Apparent ζ potentials were calculated from the electrophoretic mobility measurements using the Smoluchowski equation.

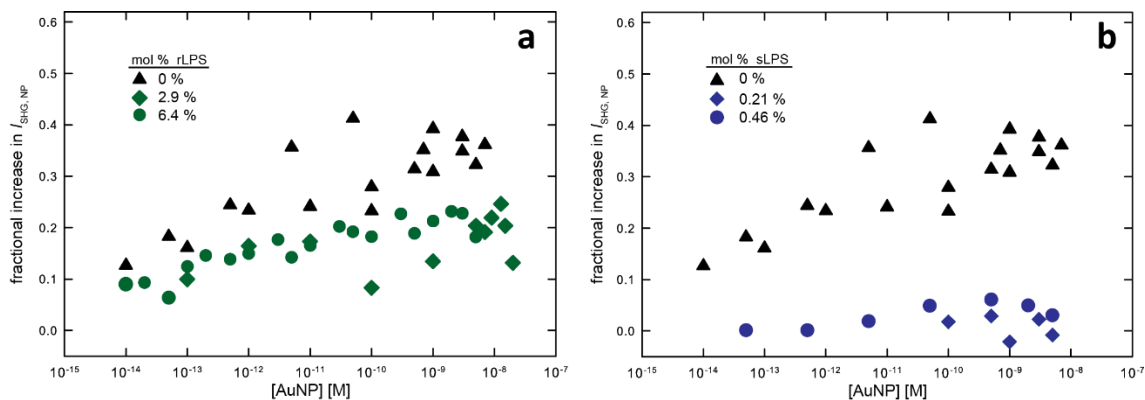


Figure S8. Observed changes in SHG signal intensity following introduction of MPNH₂-AuNPs to (a) smooth LPS (sLPS)-containing POPC bilayers and (b) rough LPS (rLPS)-containing bilayers due to nanoparticle-induced resonance enhancement near the bilayer-solution interface. All experiments were performed in 0.002 M HEPES (pH 7.4) and 0.025 M NaCl. Uncertainties on each SHG E -field are $< 1\%$ as given by the Poisson statistics of photon counting.

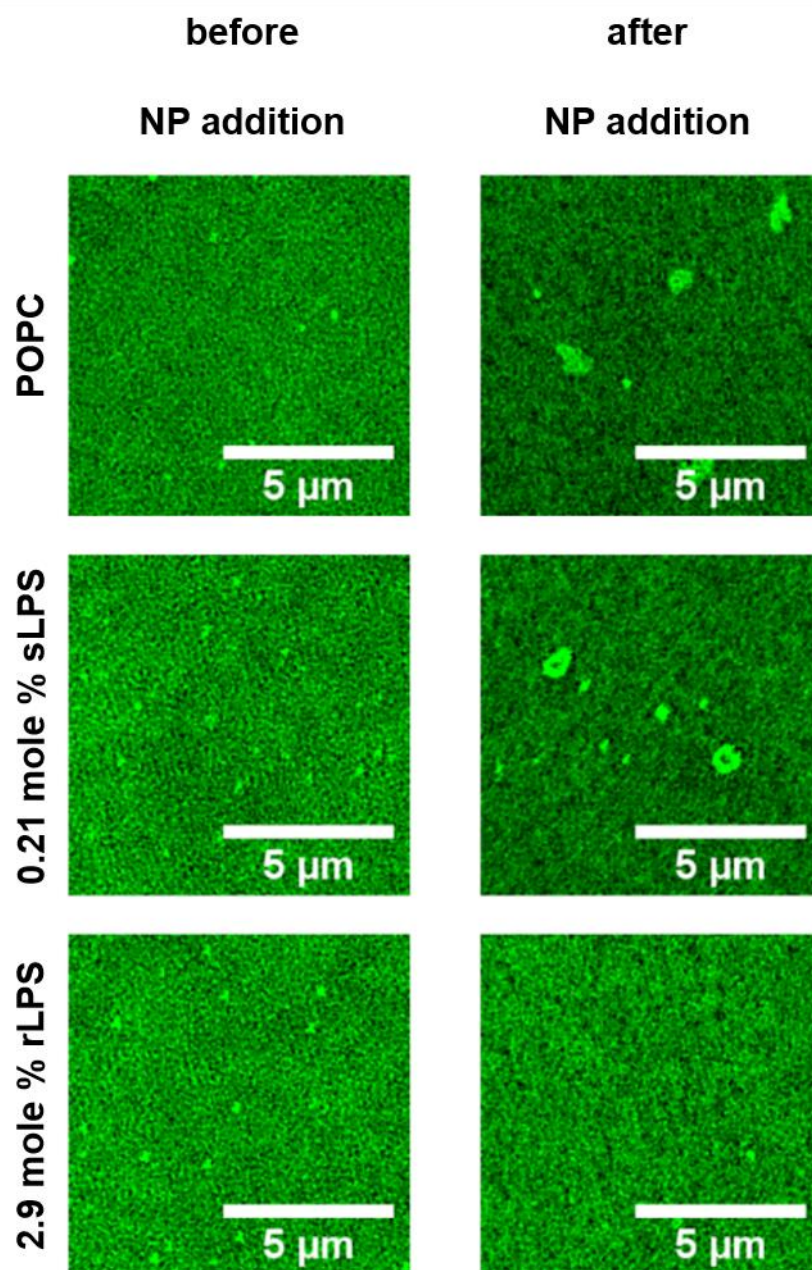


Figure S9. Fluorescence micrographs of LPS-containing POPC bilayers incorporating 0.1 mass percent POPC tagged with the fluorophore dipyrrometheneboron difluoride before and after introduction of 12.8 nM (number density) MPNH₂-functionalized gold nanoparticles. Changes in lipid ordering following nanoparticle introduction are observed by the formation of bright clusters, regions with enriched fluorescent lipid concentration.

Table S1. Areal acoustic mass densities ($\Delta m_{\text{QCM-D}}$) of SiO₂-supported bilayers composed of POPC and lipopolysaccharide

bilayer composition	mol% LPS		frequency, $\Delta f_5/5$ (Hz)*		dissipation, $\Delta D_5/5$ ($\times 10^6$)*		$\Delta m_{\text{QCM-D}}$ (ng·cm ⁻²) [†]	
	mean	std. dev.	mean	std. dev.	mean	std. dev.	mean	std. dev.
100% POPC	–	–	–25.42	0.26	0.375	0.078	458 [‡]	4.6
9:1 POPC:rLPS	2.89	0.20	–26.15	0.38	0.133	0.016	471 [§]	6.8
8:2 POPC:rLPS	6.38	0.64	–26.36	0.22	0.288	0.136	474 [§]	3.9
9:1 POPC:sLPS	0.21	0.05	–30.05	0.24	1.577	0.030	541 [¶]	4.3
8:2 POPC:sLPS	0.46	0.21	–32.17	0.45	1.920	0.101	579 [#]	8.0

* Means and standard deviations from at least 12 bilayers of each composition

[†] Calculated using the Sauerbrey equation

[‡], [§], [¶], [#] Statistically distinct areal mass densities

Table S2. Final frequency shifts ($\Delta f_5/5$) following AuNP association with LPS-amended POPC bilayers*

ionic strength (M)	mass % sLPS	MPNH ₂ -AuNPs	
		– $\Delta f_5/5$ (Hz)	mass % rLPS
0.025	0	11.3 ± 0.4	0
	10	16.4 ± 1.3	10
	20	19.8 ± 0.9	20
0.1	0	1.3 ± 0.2	0
	10	8.5 ± 0.9	10
	20	8.2 ± 1.5	20

* No detectable attachment of MPA-AuNPs.

Table S3. Estimated final acoustic areal mass densities ($\Delta m_{\text{QCM-D}}$) following AuNP association with LPS-amended POPC bilayers*

ionic strength (M)	mass % sLPS	MPNH ₂ -AuNPs $\Delta m_{\text{QCM-D}}$ (ng·cm ⁻²)	mass % rLPS	MPNH ₂ -AuNPs $\Delta m_{\text{QCM-D}}$ (ng·cm ⁻²)
0.025	0	200 ± 10 [†]	0	200 ± 10 [†]
	10	280 ± 20 [‡]	10	320 ± 10 [†]
	20	330 ± 20 [‡]	20	450 ± 10 [†]
0.1	0	23 ± 4 [†]	0	23 ± 4 [†]
	10	170 ± 20 [‡]	10	190 ± 10 [†]
	20	140 ± 30 [‡]	20	190 ± 10 [†]

* No detectable attachment of MPA-AuNPs.

[†] Acoustic areal mass densities calculated using the Sauerbrey equation.

[‡] Acoustic areal mass densities calculated using Kelvin-Voight continuum viscoelastic modeling.

5.6.1 Chemicals. We purchased 3-mercaptopropionic acid and 3-mercaptopropyl amine from Sigma-Aldrich (St. Louis, MO). EDTA was procured from Ambion Life Technologies. Chloroform solutions of 1-palmitoyl-2-oleoyl-*sn*-glycero-3-phosphocholine (POPC) and TopFluor®-labeled phosphatidylcholine (1-palmitoyl-2-(dipyrometheneboron difluoride) undecanoyl-*sn*-glycero-3-phosphocholine) were purchased from Avanti Polar Lipids (Alabaster AL). Lipopolysaccharide (LPS) purified from *Salmonella enterica* serotype minnesota (smooth type) and *Salmonella enterica* serotype minnesota Re595 mutant (rough type) were purchased from Sigma-Aldrich (St. Louis, MO). The Re595 LPS is of the deep rough type and is composed of Lipid A and two Kdo residues.⁴²¹ Smooth LPS from *Salmonella enterica* labeled with the fluorophore Alexa488 was purchased from Life Technologies (Carlsbad, CA). LPS from *Shewanella oneidensis* MR-1 (cultured as described in the main text) was extracted using the method of Galanos and co-authors⁴³² and then treated with Benzonase nuclease to remove co-

purified nucleic acids. Smooth LPS (from *Salmonella*) was dissolved in 8:2 (v/v) ultrapure H₂O:methanol, while rough LPS (from both *Salmonella* and *Shewanella*) was dissolved in neat CHCl₃. The distribution of molecular masses of each type of LPS was assessed by silver-staining LPS samples that had been separated by sodium dodecyl sulfate-polyacrylamide gel electrophoresis (SDS-PAGE; see Figure S3).

All aqueous solutions were buffered to pH 7.4 (\pm 0.05) with 0.002 M 4-(2-hydroxyethyl)-1-piperazineethanesulfonic acid (HEPES; Fisher Scientific). The ionic strength (*I*) was set to the desired level through addition of NaCl. Prior to use, all solutions were passed through a 0.22 μ m syringe filter (Millipore, Billerica, MA).

5.6.2 Bacterial culture media. *Shewanella oneidensis* MR-1 was cultured in LB broth purchased from Becton, Dickinson and Company (Franklin Lakes, NJ), and cell EDTA treatment was performed in Dulbecco's phosphate-buffered saline (D-PBS) purchased from Mediatech, Inc. (Manassa, VA).

5.6.3 Cell Sorting by Flow Cytometry. Cells with and without associated AuNPs were sorted on a FACSAria IIU cell sorter equipped with a 488 nm 50 mW laser into 1.5 mL polypropylene microcentrifuge tubes using a 100 μ m nozzle at 138 kPa. Gating for cell sorting was performed as follows: following staining with SYTO 9 to discriminate bacterial cells from other particles of similar sizes (i.e., cell debris), cells were analyzed via forward- vs. side-scattering light collected with a 488/10 bandpass filter. Gold nanoparticles formed a distinctive pattern on orthogonal scatter (Figure S5). Cell populations with and without

associated AuNPs were distinguished using as controls SYTO 9-stained cells not exposed to AuNPs (to determine the SYTO 9 fluorescence intensity threshold positively identifying stained cells) and unstained cells exposed to AuNPs (to determine the orthogonal light scattering intensity threshold identifying cells with associated AuNPs).

5.6.4 Preparation of Lipid Vesicles. Lipid vesicles were prepared by mixing solutions of POPC with and without lipopolysaccharides in the desired mass ratios (viz. 100% POPC and 9:1, 8:2 and 7:3 POPC:LPS mass ratios) in glass vials, evaporating off the majority of the solvent under flowing N₂ gas, before evaporating any remaining solvent in a vacuum chamber for 12 h. The lipid/lipopolysaccharide formulations were then hydrated and suspended in a buffered solution (0.002 M HEPES, pH 7.4, *I* = 0.150 M) and subjected to four cycles of sonication (5 min, Branson 2510 sonic bath, Branson Ultrasonics, Danbury, CT) and flash freezing in liquid N₂. Unilamellar vesicles were then formed by extruding the lipid suspension through a 50 nm polycarbonate membrane filter (Whatman) 15 times using an Avanti 610000 extruder kit. The electrophoretic mobility and number-average hydrodynamic diameter of the extruded vesicles in buffered solutions (0.002 M HEPES, pH 7.4, *I* = 0.001 M) at 25.0 ± 0.1 °C were determined from laser Doppler microelectrophoresis and dynamic light scattering (DLS) measurements using a Malvern ZetaSizer Nano ZS (Worcestershire, UK). The mean values and standard deviations reported represent the average of five measurements performed on each of five solutions (25 total measurements). These data are reported in Figure 4 in the main text.

Lipopolysaccharide incorporation was quantified on an absolute basis using the method described by Karkhanis et al.³⁸⁹ This method selectively converts 3-deoxy-D-*manno*-oct-2-ulosonic acid (also denoted 2-keto-3-deoxy-D-*manno*-octonate, Kdo), an acidic residue present in all LPS molecules, to a chromophore that can be used to quantify total LPS content. Briefly, a calibration curve was created using 0-10 μg of synthetic Kdo (Sigma Aldrich, St. Louis, MO) dissolved in 0.2 N sulfuric acid. Solutions of LPS-containing lipid vesicles ($2.5 \text{ mg}\cdot\text{mL}^{-1}$) were also dissolved in 0.2 N sulfuric acid. Then all solutions were treated as described by Karkhanis et al.³⁸⁹ and loaded into acrylic cuvettes. Light absorption at 552 nm from the resultant chromophore was recorded using an OceanOptics USB2000 spectrometer coupled to a MicroPack DH-2000 UV-vis-NIR light source. The LPS content of bacterial cells was determined in an identical manner after dissolving the lyophilized cells in 0.2 N sulfuric acid.

Vesicles containing between 0 and 20% smooth or rough LPS by mass had hydrodynamic diameters within experimental error (Figure 3a; determined by DLS in 0.002 M HEPES, pH 7.4, $I = 0.001 \text{ M}$), consistent with a prior report.³⁹⁰ Incorporation of increasing amounts of either rough or smooth LPS molecules into the vesicles shifted their electrophoretic mobilities (determined by laser Doppler microelectrophoresis) to more negative values (Figure 3b) as expected given the net negative charge of these molecules. Average electrophoretic mobility (μ_e) declined from small values typical of neutral bilayers ($-0.12 \times 10^8 \text{ m}^2\cdot\text{V}^{-1}\cdot\text{s}^{-1}$) for pure POPC vesicles to more strongly negative values (near $-3.5 \times 10^8 \text{ m}^2\cdot\text{V}^{-1}\cdot\text{s}^{-1}$) for vesicles incorporating 30% rough LPS by mass (Figure 3b). Values for μ_e of vesicles formed with rough LPS were more negative than those formed with equal mass

percent of smooth LPS; for example, vesicles containing 20% smooth and rough LPS by mass had μ_e of $-1.9 (\pm 0.11) \times 10^8$ and $-2.2 (\pm 0.14) \times 10^8 \text{ m}^2 \cdot \text{V}^{-1} \cdot \text{s}^{-1}$, respectively. This result is attributable to the higher molecular mass of smooth than rough LPS molecules (Figure S6) leading to the presence of a lower number of smooth than rough LPS molecules for a given mass of LPS incorporated. We determined the amount of LPS in vesicles from their Kdo content.³⁸⁹ For an equivalent mass of LPS incorporated into vesicles, the number of rough LPS molecules was approximately five times higher than smooth LPS molecules ($M_r = 20$ to 70 kDa, see Figure 3c).

5.6.5 Quartz Crystal Microbalance with Dissipation (QCM-D) Monitoring. Quartz crystal microbalance with dissipation monitoring measurements were conducted on a Q-Sense E4 instrument (Biolin Scientific, Göteborg, Sweden) containing four sensors mounted in liquid flow cells (QFM 401) that achieve laminar flow across the sensor surface. The temperature was controlled to 25.0 ± 0.5 °C. In QCM-D measurements, changes in the measured resonance frequency (Δf) of an AT-cut piezoelectric quartz crystal can be attributed to changes of mass ($\Delta m_{\text{QCM-D}}$) coupling to the coated surface of the sensor.⁴³³ All experiments reported here used SiO₂-coated sensors (QSX303, Biolin Scientific). To assess the viscoelastic properties of the adlayer on the sensor surface, the driving voltage to the crystal is switched off at a frequency of $\sim 5 \text{ s}^{-1}$, and the energy dissipation (ΔD) is calculated from the decay in amplitude of the resonator.⁴³³ Here, normalized Δf and ΔD values are reported for the 5th harmonic (~ 25 MHz.).

All QCM-D experiments were conducted under constant flow conditions ($100 \mu\text{L}\cdot\text{min}^{-1}$) using a peristaltic pump (Isamatec IPC, IDEX, Oak Harbor, Washington). Under these conditions, the sensitivity limit was determined to be $\sim 5 \text{ ng}\cdot\text{cm}^{-2}$. POPC or POPC/LPS bilayers were formed on QCM-D sensors *in situ* by flowing a vesicle-containing solution ($0.125 \text{ mg}\cdot\text{mL}^{-1}$ vesicles in 0.002 M HEPES, $\text{pH } 7.4$, $I = 0.150 \text{ M}$) over a SiO_2 -coated sensor. The association and rupturing of the vesicles to form a lipid bilayer was monitored by QCM-D. Following rinsing with vesicle-free solution of otherwise identical composition, solution ionic strength was adjusted to that desired for nanoparticle attachment experiments ($I = 0.025, 0.050$ or 0.100 M), and the QCM-D signal was allowed to stabilize ($df_5\cdot dt^{-1} < 0.05 \text{ Hz}\cdot\text{min}^{-1}$).³⁹¹ Gold nanoparticles (12.8 nM number concentration) suspended in buffer were then pumped through the flow cells until both the Δf and ΔD signals stabilized. Nanoparticle-free buffer was then pumped through the flow cells to measure the detachment of nanoparticles from the POPC or POPC/LPS bilayers.

5.6.6 Estimation of Masses Measured by QCM-D. The frequency shifts recorded by the QCM-D were used to estimate areal acoustic mass densities in one of two ways depending on the energy dissipation of the adlayer. In both cases, the estimated mass includes the mass of the analyte and any hydrodynamically coupled water. For more rigid adlayers, defined as having a ΔD -to- Δf ratio $< 0.4 \times 10^{-6}$,³⁹³ the Sauerbrey equation³⁹² was used to directly convert measured Δf to adlayer areal mass density ($\Delta m_{\text{QCM-D}}$):

$$\Delta m_{\text{QCM-D}} = -C \frac{\Delta f_n}{n}$$

where C is the mass sensitivity constant (for the sensor crystals used here, $18 \text{ ng}\cdot\text{cm}^{-2}\cdot\text{Hz}^{-1}$) and Δf_n is the change in frequency of the n^{th} harmonic.

For adlayers that were less rigid, Kelvin-Voigt continuum viscoelastic modeling of the collected Δf and ΔD data was performed using the QTools software package (version 3.1.25.604).^{393,394}

5.6.7 Preparation of Solid-supported LPS-containing Lipid Bilayers. We formed solid-supported LPS-containing bilayers on SiO_2 -coated QCM-D sensors via fusion of LPS-containing POPC vesicles.³⁹⁰ Figure S4 shows a representative trace of the normalized frequency of the fifth harmonic ($\Delta f_5/5$) vs. time measured during the formation of a smooth LPS-containing lipid bilayer on SiO_2 surfaces. Lipid-free buffer is pumped over the SiO_2 surface until a stable frequency baseline is obtained (Zone 1). Upon introduction of vesicle-containing solutions (Zone 2), $\Delta f_5/5$ decreases as intact vesicles attach to the SiO_2 surface (decreases in frequency correspond to increases in mass associated with the sensor).⁴³⁴ Vesicle attachment continues until the critical vesicle coverage is attained (maximum change in frequency), at which point the vesicles begin to rupture on the surface and fuse, releasing the water trapped inside them and causing the frequency to increase (Zone 3).⁴³⁴ After vesicle rupture and fusion, a stable frequency is reached corresponding to the formation of a bilayer on the sensor surface.^{434,435} Any poorly bound lipids or vesicles are rinsed away with lipid-free buffer (Zone 4). Bilayer formation kinetics decreased as the amount of LPS in the vesicles increased. The slower rate of bilayer formation was likely due to stronger electrostatic repulsion between the negatively charged SiO_2 sensor surface

(point of zero charge = 3.5)⁴³⁵ and the net negatively charged LPS-containing vesicles. The steady-state frequency shift of the POPC bilayer was consistent with expectations for a well-formed bilayer⁴³⁴ and corresponded to 60 Å² per headgroup. Steady-state frequency shifts of rough and smooth LPS-containing bilayers were larger than those composed of pure POPC, indicating retention of LPS in the bilayers. The magnitude of these shifts were larger for smooth LPS- than rough LPS-containing bilayers, likely attributable to the larger mass contribution from the long polysaccharide chains of smooth LPS than the short polysaccharide chains of rough LPS. Furthermore, the smooth LPS was likely more hydrated than the rough LPS. Areal acoustic mass densities ($\Delta m_{\text{QCM-D}}$) of the rough LPS-containing bilayers, calculated using the Sauerbrey equation^{392,393} ($\Delta m_{\text{QCM-D}} = -C\Delta f_n/n$, where C is the mass sensitivity factor and Δf_n is the change in frequency of the n^{th} harmonic; see SI), were consistent with the measured LPS content of the vesicles used to form the bilayers (based on the measured vesicle Kdo content and the rough LPS molecular mass; Figure S6a). Stable bilayers were formed containing up to 20% by mass of smooth LPS without the use of divalent cations, in contrast to the one previous report of LPS-containing lipid bilayer formation on SiO₂ by Kaufmann et al.³⁹⁰ We attribute this difference to origins of the LPS molecules used in this and the previous study (different species of *Salmonella* with different O-polysaccharide structures). Attempts to form bilayers from vesicles containing 30% smooth LPS proved unsuccessful.

5.6.8 Second Harmonic Generation. As described previously,^{395–398} second harmonic generation (SHG) experiments were performed using a regeneratively amplified

Ti:Sapphire laser system (Hurricane, Spectra-Physics, 1 kHz repetition rate, 120 fs pulses) pumping an optical parametric amplifier (OPA-CF, Spectra-Physics) tuned to a fundamental wavelength between 610 and 615 nm. Using a variable density filter, the beam was attenuated to 0.4 $\mu\text{J}/\text{pulse}$ for all experiments, which is below the sample damage threshold. The *p*-polarized beam was focused onto the silica/buffer interface at which the bilayer was formed. The beam exiting the sample was passed through a UV-grade Schott filter to remove any radiation other than the signal. The SHG signal was directed into a monochromator set to the SHG wavelength and then into a photomultiplier tube, where it was amplified and collected using a gated single-photon detection system. The SHG signal was detected following our published procedures.^{395–398}

All SHG experiments were performed under static conditions. A fused silica hemisphere was placed on top of a custom-built Teflon flow cell and held leak-tight using a Viton O-ring and a clamp. First, HEPES buffer solution (0.002 M, pH 7.4) adjusted to an ionic strength of 0.150 M was introduced into the cell and the SHG response was recorded until a steady signal was attained for at least 15 min. Next, vesicles containing varying amounts of LPS were introduced into the cell and allowed to self-assemble into an LPS-containing lipid bilayer on the silica substrate for 30 min. The bilayer was rinsed with the formation buffer, a steady SHG signal was collected, and then buffer adjusted to an ionic strength of 0.025 M was introduced and used for the remainder of the experiment. Various concentrations of gold nanoparticles (between 10^{-14} and 10^{-8} M number concentration) in buffer were then introduced into the cell, and the SHG signal was monitored until it stabilized for at least 15 min. After five to six nanoparticle solutions were exposed to the

bilayer, nanoparticle-free buffer was introduced to the cell to assess the reversibility of the interaction of the particles with the bilayer.

5.6.9 Super-resolution Fluorescence Microscopy. Solid-supported lipid bilayers were formed within 35/22 mm #1.5 glass bottom dishes (PELCO, Willco Wells). Dishes were rinsed with ultrapure water (18 M Ω ·cm; MilliQ Advantage A10, Millipore), dried with N₂, and cleaned in a UV/Ozone chamber (PSD Pro Series, Novascan) for 20 min. Cleaned dishes were equilibrated with 0.002 M HEPES, pH 7.4, *I* = 0.150 M solution for at least 1 h. Vesicles with 0.1 mass% TopFluor PC (Avanti Polar Lipids) were introduced to the dish in the same buffered solution used to equilibrate the dishes (0.0625 mg mL⁻¹ vesicle concentration), and bilayer formation was monitored by structured illumination microscopy (ALYRA, Zeiss), using a 63 \times magnification objective lens. Determining bilayer formation by fluorescence was possible utilizing fluorescence recovery after photobleaching (FRAP) experiments, as non-ruptured vesicles do not recover after photobleaching, whereas solid-supported lipid bilayers do recover upon photobleaching. Upon bilayer formation, the solution contained within the dish was exchanged 5 times with 2 mL aliquots of the buffer solution. Following rinsing, *I* was adjusted to 0.025 M.

Chapter 6

Impact of Nanoscale Lithium Nickel Manganese Cobalt Oxide (NMC) on the Bacterium *Shewanella oneidensis* MR-1

Adapted from:

Gunsolus, I. L.; Hang, M. N., Wayland, H., Melby, E. S., Mensch, A. C., Hurley, K. R.,
Pedersen, J. A., Hamers, R. J., Haynes, C. L. *Chem. Mater.*, **2016**, 28, 1092-1100

Copyright ©2016 American Chemical Society. All rights reserved.

This work was a joint effort of this author and Mimi Hang, who synthesized and characterized lithium nickel manganese cobalt oxide nanoparticles, Hunter Wayland who assisted Mimi Hang with nanoparticle synthesis, Eric Melby, who performed speciation modeling of soluble metal ions in bacterial growth medium, Arielle Mensch, who acquired atomic force micrographs of nanoparticles, and Katie Hurley, who acquired transmission electron micrographs of nanoparticles.

Nickel manganese cobalt oxide (NMC) comprises a class of lithium intercalation compounds with the composition $\text{Li}_x\text{Ni}_y\text{Mn}_z\text{Co}_{1-y-z}\text{O}_2$ ($0 < x,y,z < 1$). These compounds are of emerging importance in nanoparticle form as cathode materials for lithium-ion batteries used in transportation and consumer electronics. To evaluate the potential environmental impact of release of this material in the environment, we synthesized NMC nanosheets and investigated their interaction with *Shewanella oneidensis*, a soil and sediment bacterium. Exposure to 5 mg/L NMC significantly impaired bacterial population growth and respiration. Measurements of NMC surface composition by X-ray photoelectron spectroscopy and of the composition of the suspending solution via inductively coupled plasma-optical emission spectroscopy (ICP-OES) demonstrated incongruent material dissolution and measurable release of all four metal constituents (Li, Mn, Co, and Ni) into solution. Speciation modeling and assessment of bacterial response to metal ion exposure (via cell growth and respiration measurements) established that the observed bacterial inhibition arose from the metal ions released from the NMC, with the largest effects arising from Ni(II) and Co(II) species.

6.1 Introduction

Lithium intercalation compounds based on transition metal oxides such as LiCoO_2 are widely employed as cathode materials in lithium-ion batteries.⁴³⁶⁻⁴³⁸ The rapid expansion of mobile electronics and use of rechargeable batteries in transportation has heightened interest in replacing Co with other transition metals such as nickel and manganese to improve stability and rate performance while mitigating the high cost of cobalt.⁴³⁹⁻⁴⁴² Lithium nickel manganese cobalt oxide ($\text{Li}_x\text{Ni}_y\text{Mn}_z\text{Co}_{1-y-z}\text{O}_2$, $0 < x, y, z < 1$, abbreviated NMC) has emerged as a class of battery materials providing high performance at reduced cost,⁴⁴³⁻⁴⁴⁵ widely considered for large-scale implementation in electric vehicles.⁴⁴³ NMC and other cathode materials are increasingly used in nanoparticle form because nanoparticles yield enhanced lithium transport, better electrical conduction, and reduced fragmentation from mechanical stresses during lithium intercalation and de-intercalation.⁴⁴⁶⁻⁴⁴⁸ Fig. S1 in Supporting Information shows an example of stress-induced fracturing of a current-generation commercial NMC material, producing even smaller nanoparticles.

Rapid, large-scale commercialization of NMC and related lithium intercalation materials in nanoparticle form increases the potential for environmental release and exposure during manufacture, use, and disposal. A single, modest electric vehicle with a typical ~24 kWh battery pack using NMC (specific capacity = 165 mAh/g at 3.8 V potential)⁴⁴⁹ contains >38 kg of nanoscale cathode material. With estimates of 20 million electric vehicles on the road by the year 2020,⁴⁵⁰ nanoscale metal oxides represent an emerging potential environmental contaminant. In contrast to lead-acid batteries, little

infrastructure exists for recycling lithium-ion batteries, due in part to a lower economic incentive for recycling.⁴⁵¹ Understanding the environmental behavior of the materials that comprise batteries can provide important insights into a comprehensive assessment of how to optimally use new materials to reduce energy usage and make more effective use of renewable sources.^{440,452,453}

Here, we report investigations of the interaction of NMC with a representative soil- and sediment-dwelling bacterium, *Shewanella oneidensis* MR-1. We choose the specific composition $\text{Li}_x\text{Ni}_{1/3}\text{Mn}_{1/3}\text{Co}_{1/3}\text{O}_2$ (with $x=1$ corresponding to fully lithiated materials) for our studies due to its widespread use.^{454,455} The genus *Shewanella* comprises gram-negative bacteria that are distributed globally; *Shewanella oneidensis* MR-1 plays an important role in the cycling of metals in the environment and is a model system for environmental studies.⁴⁵⁶ We characterize the influence of NMC nanoparticles on *S. oneidensis* population growth and respiration and link these with corresponding changes in solution composition by inductively coupled plasma optical emission spectroscopy and NMC surface composition via X-ray photoelectron spectroscopy. Our results show that NMC nanoparticles in aqueous medium undergo partial incongruent dissolution, preferentially releasing Li^+ and the transition metals Ni^{2+} and Co^{2+} into solution and leaving behind chemically transformed nanoparticles that are depleted in Ni and enriched in Mn. Bacterial growth and respiration measurements show that intentional introduction of Ni^{2+} and Co^{2+} at the experimentally measured concentrations can fully reproduce the observed toxicity to *S. oneidensis*, demonstrating that the toxicity of NMC arises from the transition metal ions released in solution rather than the remaining transformed

nanoparticles. This work provides new insights into the fundamental chemical processes that control the impact of NMC and related cathode materials in the environment.

Ultimately this work may contribute to an understanding of how to design environmentally benign materials for energy storage and related applications.

6.2 Experimental

6.2.1 NMC synthesis. We synthesized sheet-like nanoparticles (“nanosheets”) of $\text{LiNi}_{1/3}\text{Mn}_{1/3}\text{Co}_{1/3}\text{O}_2$ by adapting a molten-salt method reported previously for synthesis of LiCoO_2 nanosheets.⁴⁵⁷ All reagents were purchased from Sigma-Aldrich, and ultrapure water ($>18 \text{ M}\Omega\cdot\text{cm}$ resistivity; Barnstead Nano-pure) was used. A $\text{Ni}_{1/3}\text{Mn}_{1/3}\text{Co}_{1/3}(\text{OH})_2$ precursor was synthesized by dropwise addition of an aqueous solution containing 0.2 M cobalt (II) acetate, 0.2 M nickel (II) acetate, and 0.2 M manganese (II) acetate to 0.1 M aqueous LiOH under stirring. The dark brown $\text{Ni}_{1/3}\text{Mn}_{1/3}\text{Co}_{1/3}(\text{OH})_2$ precipitate was collected and purified via repeated (5x) cycles of centrifugation and resuspension in ultrapure water to eliminate excess acetate salts. The $\text{Ni}_{1/3}\text{Mn}_{1/3}\text{Co}_{1/3}(\text{OH})_2$ precipitate was then dried in a vacuum oven for 2 days at 40 °C. The mixed metal hydroxide (0.250 g) was then added to a 10 g mixture of molten lithium salt flux (6:4 molar ratio of $\text{LiNO}_3:\text{LiOH}$) at 205 °C in a poly(tetrafluorethylene) container with magnetic stirring for 30 minutes to intercalate lithium into the nanosheets and drive off water. The reaction was quenched with water, and the NMC precipitate was collected, purified via centrifugation (5x) in ultrapure water, and dried again in a vacuum oven for 2 days at 40 °C. All centrifugation was done using the Thermo Scientific Sorvall Legend X1R

Centrifuge with a Thermo TX-400 rotor at 4696g.

6.2.2 Inductively coupled plasma optical emission spectroscopy (ICP-OES)

characterization of NMC stoichiometry and of metal release into growth medium. A

Perkin Elmer Optima 2000 ICP-OES was used to determine metal concentrations in aqueous solutions. To determine the stoichiometry of NMC, samples were digested in freshly prepared aqua regia (3:1 v/v mixture of 37% v/v HCl and 70% v/v HNO₃; Caution – highly corrosive!) and diluted in ultrapure water. Three replicate measurements were made of the ion concentrations, yielding Li/Ni = (1.042 ± 0.012), Mn/Ni = (1.076 ± 0.015), and Co/Ni = (1.021 ± 0.014); these ratios indicate that the NMC material is stoichiometric in metal concentration and lithiated to an extent of ~35%, with full lithiation corresponding to Li/Ni = 3.0.

All experiments employing *S. oneidensis* used a bacterial growth medium containing 11.6 mM NaCl, 4.0 mM KCl, 1.4 mM MgCl₂, 2.8 mM Na₂SO₄, 2.8 mM NH₄Cl, 88.1 μM Na₂HPO₄, 50.5 μM CaCl₂, 10 mM HEPES, and 100 mM sodium lactate. To characterize metal release into this bacterial growth medium, a suspension of NMC was constantly stirred in the medium at concentrations of 5 mg/L or 50 mg/L, and samples were collected periodically over 72 h. The measurements were collected with three sample replicates and three analytical replicates per sample. Samples were centrifuged at 4696g for 10 min to remove the majority of NMC nanoparticles in solution. The supernatant was then ultracentrifuged for 2 h at 288,000g using a Beckman Coulter Optima Ultracentrifuge with a SW-41 Ti Rotor to further ensure removal of any remaining NMC

nanoparticles. Dynamic light scattering (Malvern Zetasizer Nano ZS) was used to verify effective sedimentation of nanoparticles under these centrifugation conditions.

Concentrations of dissolved metal species in the resulting supernatants were measured by ICP-OES, with experiments conducted in triplicate.

6.2.3 X-ray photoelectron spectroscopy (XPS). Samples for XPS analysis were prepared via spin-coating a methanolic solution of NMC onto Au foil. We acquired XPS data using a custom-built, ultrahigh-vacuum Phi system incorporating a monochromatized Al K α source (1486.6 eV photon energy) and a hemispherical electron energy analyzer. All spectra were collected at 45° photoelectron take-off angles, and XPS spectra were fit using CasaXPS software.⁴⁵⁸ Inelastic mean free paths of 2.4 nm (Co), 2.2 nm (Ni), and 2.8 nm (Mn) were estimated using the NIST Effective Attenuation Length Database⁴⁵⁹ via the TPP-2M equation.⁴⁶⁰

6.2.4 Scanning electron microscopy (SEM). Samples for SEM images were prepared by drop-casting a dilute methanolic solution of NMC onto boron-doped SiO₂. A Leo Supra55 VP scanning electron microscope (SEM) was used to obtain detailed images of NMC nanosheets. We obtained SEM images using 1 kV incident electron energy with a standard in-lens detector.

6.2.5 Transmission electron microscopy (TEM). Samples for TEM analysis were prepared by dispersing NMC into ultrapure water via 10-minute sonication (at a

maximum power of 70 W) and vortexing. A large droplet (~10 μ L) of the suspension was deposited onto a copper TEM grid (200 mesh with carbon and formvar supports, Ted Pella Inc.) held with reverse-grip tweezers. The tweezers were slowly turned 180° so that the droplet was suspended upside down to allow for a higher probability of edge-on NMC nanosheets on the grid, and the grid was air-dried for 2 h. TEM images were acquired on a Tecnai T12 transmission electron microscope with an operating voltage of 120 kV. Samples of bacterial cells exposed to NMC were prepared for TEM imaging through a typical process of fixation, dehydration, and embedding in epoxy. Slices of ~70 nm thickness were cut with a Leica EM UC6 Ultramicrotome and placed on 200 mesh copper grids with carbon and formvar supports for imaging on a FEI Tecnai Spirit Bio-Twin microscope at 120 kV.

6.2.6 Bacterial response to NMC exposure. Bacterial growth was monitored by measuring the turbidity (via optical absorbance measurements) of cell suspensions maintained in a 96-well plate. *Shewanella oneidensis* MR-1 stored in 30% glycerol at –80 °C was inoculated onto lysogeny broth (LB) agar plates and incubated at 30 °C for 24 h. The resulting bacterial colonies were suspended in growth medium to create a suspension with absorbance ~0.2 at 600 nm (Spectronic 20D, Milton Roy Co.). Cell suspensions were diluted 1:1 v/v into fresh media in each well of a 96-well plate, to a total volume of 250 μ L. NMC nanoparticles (2000 mg/L) were dispersed in growth medium through 10 minutes of sonication (at a maximum power of 70 W) and added to wells to achieve NMC concentrations of 5, 15, 25, 35, and 50 mg/L. Similarly, stock solutions of NiCl₂,

CoCl₂, MnSO₄, and LiOH prepared in growth medium were added to wells to achieve metal ion concentrations expected to occur in exposures to NMC between 5 and 50 mg/L based on ICP-OES measurements.

The 96-well plate was then loaded into a Synergy 2 Multi-Mode Reader (BioTek, Winooski, VT) at 30 °C. At one-hour intervals, the plate was slowly shaken for 20 seconds to ensure a homogenous distribution of cells, and the absorbance at 630 nm through each well (due to light scattering by cells) was recorded to determine the suspension turbidity.

Bacterial respiration was monitored during exposure to NMC or metal ions by measuring O₂(g) consumption using a 16-vessel respirometer system (Respirometry Systems and Applications, Inc., Springdale, AR). Bacterial cell suspensions prepared from colonies formed on LB agar plates were diluted 1:10 v/v into fresh medium, and 100 mL aliquots of this suspension were placed in 125 mL glass vessels fitted with removable rubber septa. NMC nanoparticles, dispersed in bacterial growth medium at 2000 mg/L, were added to three vessels to achieve a concentration of 5 mg/L NMC. Similarly, stock solutions of NiCl₂ and CoCl₂ prepared in bacterial growth medium were added to triplicate vessels to achieve Ni²⁺ and Co²⁺ concentrations of 6.2 and 3.4 μM, respectively (corresponding to the dissolved metal content of a solution of 5 mg/L NMC nanoparticles as determined by ICP-OES). The samples were placed in a 30 °C water bath for 60 h under a constant O₂(g) pressure. The CO₂ produced by cellular respiration was removed from the gas phase by reaction with concentrated KOH (aq) present in the headspace above the liquid culture. Consumption of O₂(g) through cellular respiration decreased the

total pressure in the sealed vessel. $O_2(g)$ was supplied to the vessel as needed at 10-minute intervals to maintain a constant pressure, and total $O_2(g)$ delivery to each vessel was tracked as a function of time to measure bacterial respiration. Constant stirring of the bacterial cell suspension (500 rpm) ensured rapid equilibration of $O_2(g)$ between the headspace and the liquid. Since $O_2(g)$ delivery to the vessel was proportional to cellular respiratory activity, the total mass of $O_2(g)$ delivered served as our metric for assessing cellular response to NMC or metal ion exposure, where decreased respiration indicates inhibited cell activity.

6.3 Results and Discussion

6.3.1 Preparation and characterization of nanoscale NMC. Figure 1a shows an SEM image of the synthesized $Li_{1/3}Ni_{1/3}Mn_{1/3}Co_{1/3}O_2$ nanoparticles, displaying hexagonal sheet-like structures. Atomic force microscopy (AFM) and transmission electron microscopy were used to analyze sheet thickness. AFM analysis (Supporting Information, Fig. S2) of 125 individual NMC nanosheets from 12 line profiles yielded average thickness of 0.88 ± 0.61 nm. Edge-on TEM images (Figure S3) show stacked NMC nanosheets and corroborate the nanosheet thickness measured by AFM. Figure 1b shows an NMC nanosheet <5 nm in thickness, consistent with the thicknesses observed in AFM. Synthesized NMC nanosheets were indexed to a R-3m space group using powder X-ray diffraction (Supporting Information, Fig. S11). Suspended in growth medium, the measured electrophoretic mobility of the NMC nanosheets is $-1.18 \pm 0.10 \mu\text{m}\cdot\text{cm}/\text{Vs}$ (Malvern Nanosizer ZS).

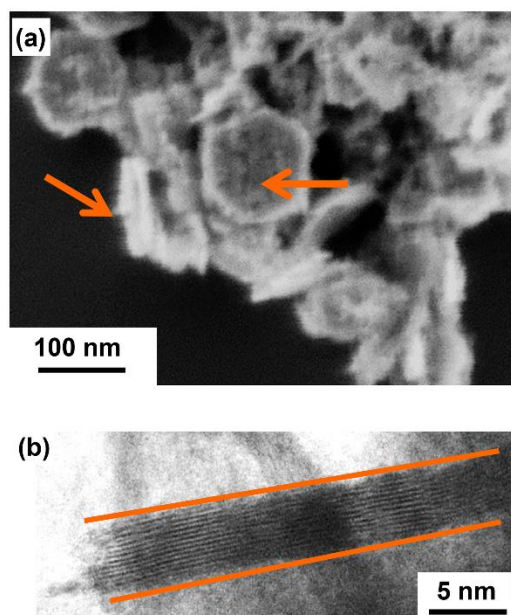


Figure. 1. Size analysis of NMC nano-sheets. Scanning electron microscope image of NMC (a). Orange arrows point to different orientations of the nanosheets. Representative TEM thickness profile of NMC nano-sheets (b).

6.3.2 Impact of NMC on *Shewanella oneidensis* MR-1. The impact of NMC on *Shewanella oneidensis* MR-1 was assessed by monitoring bacterial aerobic respiration and growth. Cellular respiration was monitored over 60 h during continual exposure to 5 mg/L NMC (Figure 2a). NMC nanoparticles aggregated under these conditions but remained available for interaction with cells due to rapid stirring (500 rpm). No effort was made to control the NMC aggregation state since nanoparticle aggregation and sedimentation are expected to occur under many environmental exposure scenarios (though these processes depend strongly on environmental variables including pH, ionic strength, and dissolved organic matter concentration).^{461,462} Consumption of oxygen increased with the number of actively respiring cells (Figure 2a, 0 mg/L NMC), resulting

in oxygen consumption curves that mirrored growth curves collected by absorbance measurements (Figure 2b). As shown in Figure 2a, cells exposed to 5 mg/L NMC showed a delay in exponential growth by more than 30 h relative to 0 mg/L NMC. Replicate experiments indicated that the delay of exponential growth was variable (from 30 to 80 h, see Figure S4), suggesting that exposure to 5 mg/L NMC significantly disturbs bacterial respiratory activity and the rate of recovery of bacterial activity from this disruption varies. Additional experiments performed in the absence of cells indicated that NMC nanoparticles had negligible impact on oxygen consumption independent of cellular respiration (see Fig. S5).

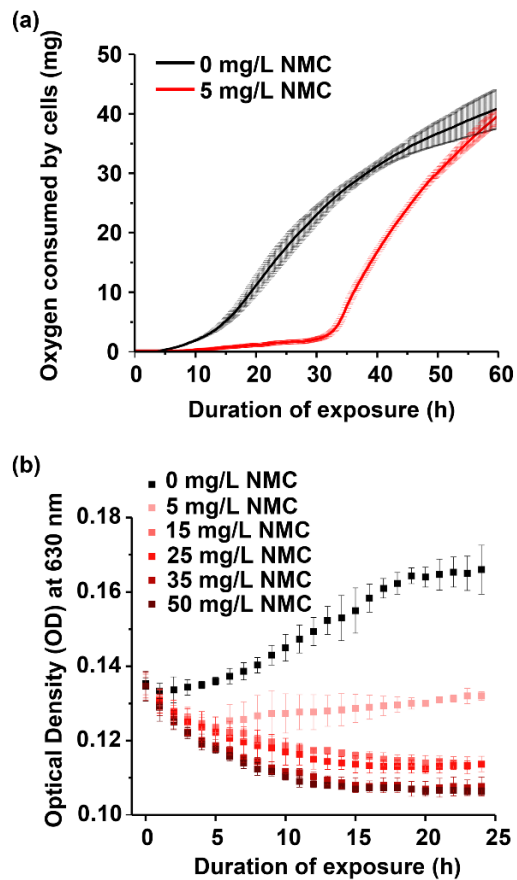


Figure 2. Response of *S. oneidensis* to NMC exposure. Oxygen consumption due to
258

cellular respiration increases with cell population size and was monitored over 60 h for cells grown in medium without NMC (black trace) or cells grown in medium containing 5 mg/L NMC (red trace) **(a)**. The dark trace represents the mean of three biological replicates; lighter bars indicate standard deviations. The corresponding oxygen uptake rate profiles (obtained by differentiating the oxygen consumption profiles) are shown in Figure S12. Suspension turbidity, which increases with cell population growth, was monitored over 24 h for cells grown in medium without NMC (black symbols) or cells grown in medium with 5 to 50 mg/L NMC (light to dark red symbols) **(b)**. The mean and standard deviation of three biological replicates is plotted for each condition as a function of time, corrected to remove the light scattering contribution from NMC (as described in the text).

Previous work on heavy metal toxicity to bacteria (e.g. Sengor et al.⁴⁶³) has shown that exposure of bacterial cultures to heavy metals can delay onset of exponential growth (increased lag time). Mechanisms proposed to explain this effect include decreased cell viability following heavy metal exposure, a slow metal detoxification process, and physiological adaptations by the cells. Any of these mechanisms may contribute to our observation that the respiratory activity of *S. oneidensis* recovers after long exposure times to NMC, although it is beyond the scope of the current work to address these mechanisms explicitly. To understand the variation in the time required to recover respiratory activity, we considered the possibility that NMC decreases cell viability and is detoxified over time. The onset of the exponential growth phase is highly sensitive to the

initial viable cell population size (Supporting Information, Figure S6). If exposure to NMC inactivated a significant fraction of the first generation of bacterial cells but had less impact on subsequent generations due to detoxification, the logarithmic growth model⁴⁶⁴ predicts recovery of cell activity after long exposure times, as we observed. Similarly, if the fraction of first-generation cells inactivated by NMC varied slightly between experiments (due to, for example, small variations in NMC exposure concentration), the model predicts significant changes in recovery time.

To supplement our assessment of the impact of NMC on bacterial respiration, bacterial growth was monitored over 24 h during continual exposure to NMC at mass concentrations between 5 and 50 mg/L. The time scale of these experiments was limited to 24 h due to cell settling. Cell suspensions were loaded into a 96-well plate and illuminated with visible light (630 nm) at 1 h intervals. Suspension turbidity was monitored by measuring optical density (OD), defined as

$$OD = -\log_{10} \frac{I}{I_0},$$

where I is the intensity of the transmitted beam and I_0 is the intensity of the incident beam. The optical density is attributed to scattering of light by cells rather than optical absorption, and was assumed to be proportional to the number of light-scattering species (cells).⁴⁶⁵ A plot of the optical density over time (Figure 2b) showed three distinct phases: a lag phase wherein the cell density remains approximately constant, a phase where the cell density increases rapidly, and a third phase where the cell density increases at a lower rate. This growth curve mirrors the well-known growth dynamics of bacteria, where the

lag phase is followed by exponential growth of the bacterial population until a stationary phase (steady-state) is attained.⁴⁶⁶ Cells exposed to 5 through 50 mg/L NMC (Figure 2b) showed lower absorbance values than the negative control, indicating lower cell densities and inhibition of cell growth. Cells suspensions exposed to 15 through 50 mg/L NMC showed decreasing absorbance over 24 h, suggesting that cell density was continuously decreasing. This is likely caused by cell death and lysis, resulting in reduced light scattering relative to whole live cells.⁴⁶⁵

The above analysis of Figure 2b assumes that cells are the only light-scattering species present in suspension, in which case the absorbance is expected to be directly proportional to the cell density. However, we observed that addition of NMC to cell suspensions increases the absorbance due to scattering from both cells and NMC. To remove the contribution from NMC, we subtracted a fixed value, dependent on the NMC concentration, from each absorbance reading (i.e., the difference in absorbance at time zero between a cell suspension with and without NMC at a given concentration). However, because the light scattering from NMC is continuously variable (see Figure S7) we cannot rigorously exclude it from our OD measurements. Consequently, our OD measurements cannot be directly correlated with cell counts; doing so would assume that the OD intensity is the product of light interaction with cells alone, which is not the case in our samples. Additional details regarding light-scattering analysis are provided in the Supporting Information (see Figure S7).

NMC mass conc. (mg/L)	Dissolved metal conc. after 24 h (μM)				Dissolved metal conc. after 72 h (μM)				Expected total conc. of ions if full dissolution (μM)			
	Ni	Co	Mn	Li	Ni	Co	Mn	Li	Ni	Co	Mn	Li
5	7 \pm 1	3 \pm 1	3 \pm 1	23 \pm 3	9 \pm 1	5 \pm 2	5 \pm 2	23 \pm 3	18.1	18.1	18.1	19
25	32 \pm 1	13 \pm 1	9 \pm 2	84 \pm 2	37 \pm 1	21 \pm 2	17 \pm 2	84 \pm 1	90.5	90.5	90.5	95
50	59 \pm 6	20 \pm 5	9 \pm 4	189 \pm 55	68 \pm 8	28 \pm 10	25 \pm 13	216 \pm 74	181	181	181	190

Table 1: Measured concentrations of ions produced in solution by dissolution of NMC, and expected concentration if NMC dissolved completely. The mean and standard deviation of three replicate samples are listed for measured values.

To explore the cause of inhibited bacterial growth and activity following exposure to NMC, we used ICP-OES and XPS to investigate the chemical stability of NMC in the bacterial growth medium in the absence of bacteria. We hypothesized that dissolution of NMC in the growth medium contributed to the observed toxicity of NMC to bacterial cells. To test this, we analyzed the composition of the aqueous phase and of the nanoparticles.

Table 1 shows the concentrations of dissolved Ni, Co, Mn, and Li species after NMC at concentrations of 5 mg/L, 25 mg/L or 50 mg/L was introduced into cell-free growth medium for 24 h and 72 h. Figures 3a and 3b show the dissolution behavior of 5 mg/L NMC upon exposure to bacterial media for 72 h. Dissolution behavior of 50 mg/L NMC (see Figure S8) upon exposure to bacterial media showed very similar trends.

These data show that dissolved Ni is present at higher concentrations than dissolved Mn or Co, indicating incongruent dissolution of the MO_2 framework with preferential release of Ni species. For all metals, the concentration in solution is proportional to the starting

NMC concentration; this indicates that none of the metals are reaching a solubility limit that would constrain further dissolution.

To complement measurements of metal ion concentration in the bulk, we used XPS to characterize the concentration of metal species in the near-surface region of the nanoparticle sheets before and after 72 h exposure to the same bacterial growth medium utilized in the bacterial growth and respirometry studies. NMC nanoparticles exposed to the growth medium were purified via centrifugation in ultrapure water (5x) prior to XPS analysis. We quantify the surface composition using the fractional atomic composition, f_x , defined as

$$f_x = \frac{\frac{A_x}{S_x \lambda_x}}{\sum \frac{A_i}{S_i \lambda_i}} \quad (1)$$

where $x = \text{Mn, Co, or Ni}$ as appropriate, A_i is the measured XPS area for the element i , S_i is the atomic sensitivity factor for that element, and λ_i is the inelastic mean free path (IMFP) for element i in the NMC. We excluded Li from this analysis because the Li concentration is continuously variable in lithium intercalation compounds and can vary even in the absence of incongruent dissolution.

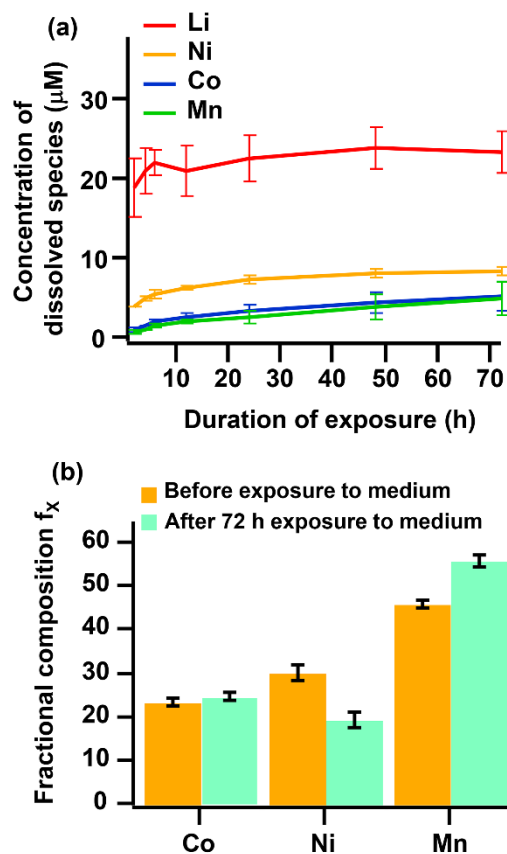


Figure 3. Time-dependent changes in chemical composition of aqueous and solid phase. Concentration of dissolved species produced from 5 mg/L NMC nanoparticles over time in growth medium (a). Fractional composition f_x for $x = \text{Co}$, Ni, and Mn at NMC surface measured by XPS before and after exposure of 50 mg/L NMC to growth medium for 72 h (b).

Figure 3b shows the fractional composition of the transition metals from NMC samples (50 mg/L) before and after exposure to growth medium for 72 h. These XPS data show that the relative abundances of Ni, Mn, and Co in the near-surface region of NMC were altered relative to those measured at 0 h, with the Ni content in the surface region

decreasing from $f_{\text{Ni}} = 0.30 \pm 0.02$ to $f_{\text{Ni}} = 0.19 \pm 0.02$ and Mn increasing from $f_{\text{Mn}} 0.46 \pm 0.01$ to $f_{\text{Mn}} 0.56 \pm 0.01$ (estimated errors represent uncertainty in peak area measurement). The changes in composition are readily apparent upon visual inspection of the XPS spectra (Figure S9). These XPS data further support the observed non-stoichiometric dissolution of the transition metal components and particularly, the preferential release of Ni ions into solution, yielding NMC particles with surfaces deficient in Ni and enriched in Mn. Together, these results demonstrate that NMC is chemically unstable in the growth medium, and that NMC serves as a source of dissolved metals to aqueous environments.

To identify whether the metals dissolved in solution could be responsible for the observed impact on cell growth, we used the absorbance measurement methods described above to monitor bacterial growth during continual exposure to Li^+ (as LiOH), Ni^{2+} (as NiCl_2), Co^{2+} (as CoCl_2), and Mn^{2+} (MnSO_4). The metal ion concentrations used encompassed the range of expected dissolved metal content based on ICP-OES measurements from 5 through 50 mg/L NMC nanoparticle exposures after 24 h. As shown in Figures S10a and b, Li^+ and Mn^{2+} had little or no effect on bacterial growth relative to a negative control. In contrast, Figures 4a and b shows that Ni^{2+} and Co^{2+} significantly decreased growth ($p < 0.05$, with the exception of 3.4 and 10.2 μM Co^{2+}).

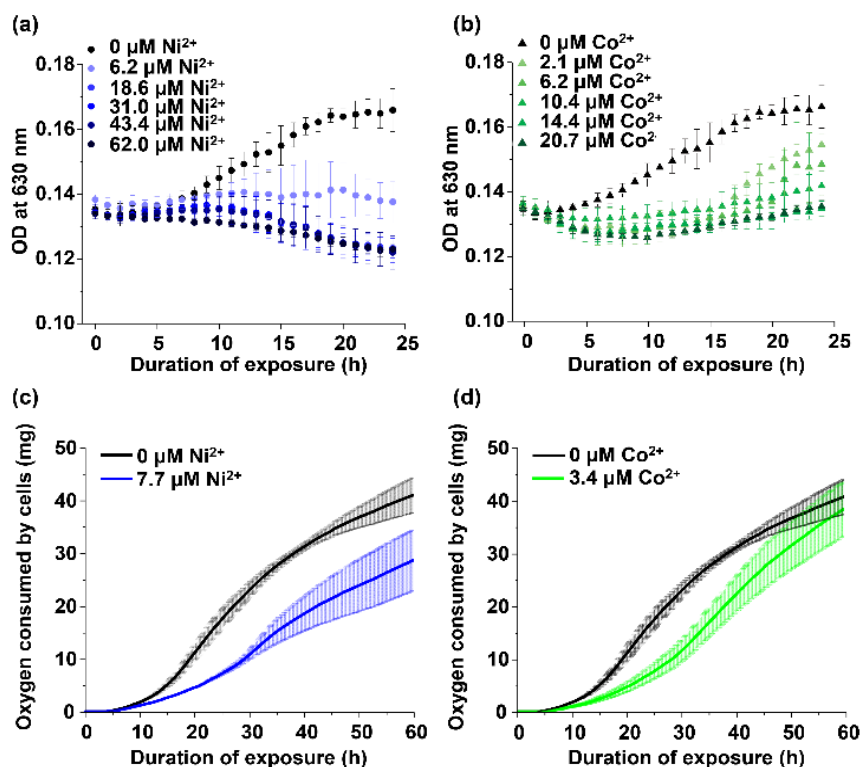


Figure 4. Growth (a, b) and respiration (c, d) profiles of *S. oneidensis* exposed to Ni²⁺ and Co²⁺ ions. In (a, b) the range of metal ion concentrations represents the range of expected metal release into growth medium over 24 h from 0 through 50 mg/L NMC, based on ICP-OES measurements. As in Figure 2, optical density (OD) is proportional to the cell population and was monitored over 24 h to assess the effect of metal ions on cell growth. Cells were grown in metal-free growth medium (black symbols in a-d) or in medium containing 6.2 to 62 μM NiCl₂ (a), 3.4 to 34 μM CoCl₂ (b). The mean and standard deviation of three biological replicates is plotted for each condition as a function of time, corrected to remove the light-scattering contribution from NMC (as described in the text). In (c, d), metal ion exposure concentrations represent metal release into bacterial growth medium over 60 h from 5 mg/L NMC, based on ICP-OES measurements. Oxygen

consumption due to cellular respiration increases with cell population size and was monitored over 60 h for cells grown in growth medium (black traces) and cells grown in growth medium containing 7.7 μM Ni^{2+} (**c**), 3.4 μM Co^{2+} (**d**). The mean of three biological replicates is indicated by the dark trace, while standard deviations are indicated by lighter bars. The corresponding oxygen uptake rate profiles (obtained by differentiating the oxygen consumption profiles) are shown in Supporting Information, Figure S12.

In addition to bacterial growth, we measured bacterial respiration during continual exposure to metal ions, using the metal concentrations measured by ICP-OES from 5 mg/L NMC after 60 h (Figures S10c, d and 4c, d). Figures S10c and d shows that exposure to Li^+ and Mn^{2+} had no significant effect on bacterial respiration compared to controls lacking added metal ions. Conversely, Figure 4c and d show that exposure to Ni^{2+} and Co^{2+} delayed the onset of exponential growth and, in the case of Ni^{2+} , reduced total oxygen consumption. In replicate experiments, the relative toxicities of Co^{2+} and Ni^{2+} varied, such that in some experiments Co^{2+} appeared more toxic and in others Ni^{2+} appeared more toxic. However, in all experiments, neither Ni^{2+} nor Co^{2+} inhibited cellular respiration to the extent that resulted from exposure to NMC (Figure 2a). These results suggest that metal ions released from NMC, particularly Ni^{2+} and Co^{2+} , inhibit bacterial growth, but cannot individually account for the full magnitude of inhibition induced by exposure to NMC.

We hypothesized that cells exposed to multiple metals may experience complex

inhibitory effects that cannot be predicted from the outcomes of exposures to individual metals, as has been previously demonstrated for Ni and Co species.⁴⁶⁷ To assess this hypothesis, we exposed cells jointly to Ni²⁺ and Co²⁺ and monitored cell growth and respiration. Simultaneous exposure of cells to concentrations of Ni²⁺ and Co²⁺ equivalent to those released from 5 mg/L NMC inhibited growth (Figure 5a) and respiration (Figure 5b). The magnitudes of these effects were very similar to those induced by NMC. Remarkably, cells exposed to both Ni²⁺ and Co²⁺ showed a delayed onset of exponential growth that overlapped completely with that of cells exposed to NMC (Figure 5b).

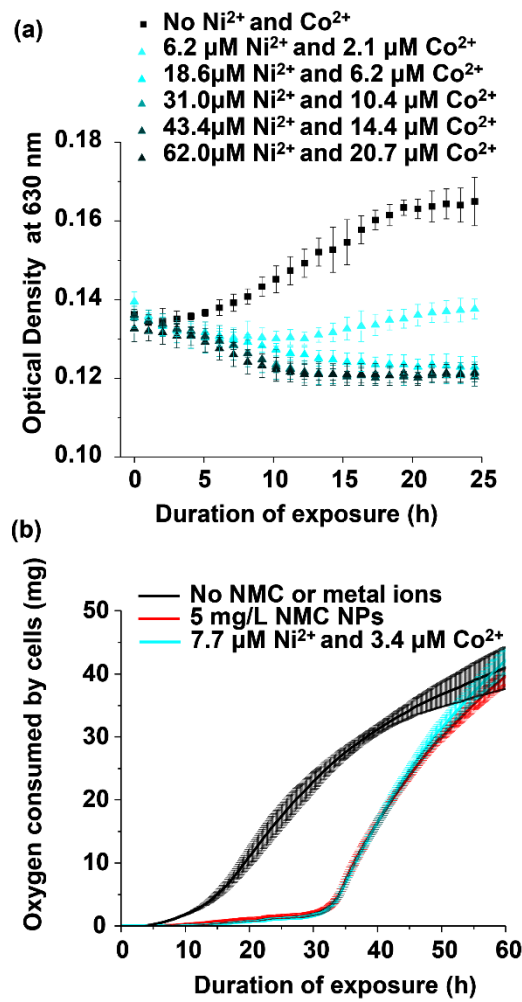


Figure 5. Response of *S. oneidensis* to simultaneous Ni²⁺ and Co²⁺ exposure. Suspension turbidity, which increases with cell population growth in growth medium (black), was monitored over 24 h as a function of metal ion exposure concentration (a). The range of metal ion concentrations (light to dark cyan) represent the range of metal ions release into growth medium over 24 h from 0, 5, 15, 25, 35, and 50 mg/L NMC (refer to Figure 2b). The mean and standard deviation of three biological replicates is plotted for each condition. Oxygen consumption due to cellular respiration increases with cell population size and was monitored over 60 h for cells grown in medium (black trace), medium containing 5 mg/L NMC (red trace), and medium containing 7.7 μM Ni²⁺ with 3.4 μM Co²⁺ (cyan trace) (b). The metal ion concentrations represent metal release into growth medium over 60 h from 5 mg/L NMC. The mean of three biological replicates is indicated by the dark trace, while standard deviations are indicated by lighter bars. The corresponding oxygen uptake rate profiles (obtained by differentiating the oxygen consumption profiles) are shown in Figure S12.

6.3.3 Mechanism of Toxicity. The above studies show that the presence of NMC in solution dramatically changes the growth dynamics of *S. oneidensis*, leading to lowered growth rates and decreased respiration. Measurements of dissolved metal ions by ICP-OES and of the NMC surface composition by XPS both show that NMC undergoes incongruent dissolution with preferential release of Ni. Cellular exposure to solutions containing Ni²⁺ and Co²⁺ at the concentrations released from the NMC nanoparticles yielded decreases in growth and respiration that almost exactly mimicked the response of

cells to NMC nanoparticles. These results clearly show that the biological impact of NMC on *S. oneidensis* is dominated by the release into solution of Ni and Co species, which have known toxicity to microorganisms.⁴⁶⁷⁻⁴⁷⁰ This mechanism suggests that close proximity of NMC nanoparticles to bacterial cells is not required for cells to experience toxic effects, since metal ions released from NMC diffuse freely in solution.

Transmission electron micrographs of cells exposed to NMC nanoparticles for 30 minutes showed no significant attachment of NMC to the cell surface (Figure 6), corroborating this point. While exposure to low concentrations of metals, like Co, that serve as enzyme cofactors may stimulate bacterial growth, our results suggest that both Ni and Co species, at concentrations released from 5 mg/L NMC, are toxic to *S. oneidensis*.⁴⁶³

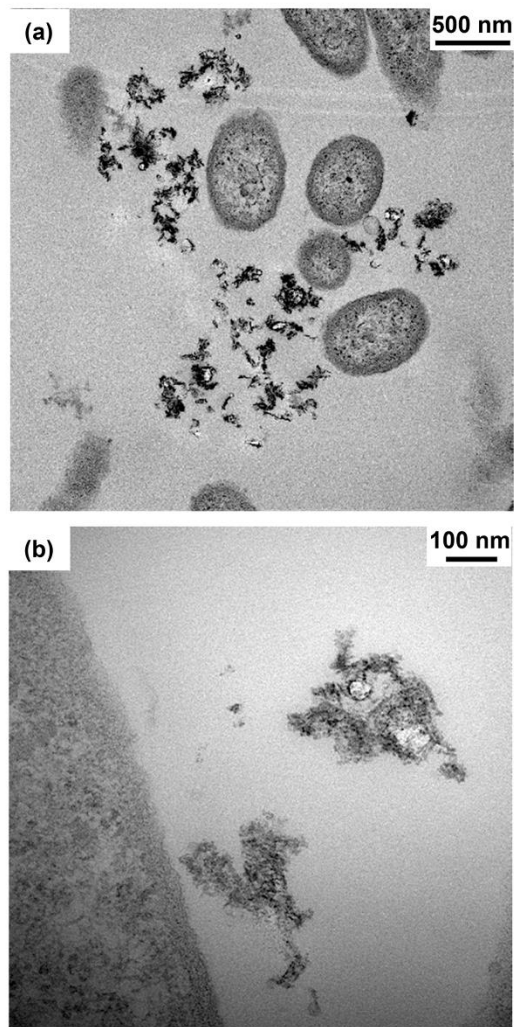


Figure 6. Transmission electron micrographs of *S. oneidensis* exposed to 5 mg/L NMC nanoparticles for 30 minutes in growth medium. Analysis of these and additional micrographs (not shown) indicated no adsorption of nanoparticles to the cell membrane for over 100 cells co-localized with nanoparticles in the field of view.

Both cobalt and nickel are essential trace nutrients for microbes, and microbes have specific uptake pathways designed to bring them inside the cell.⁴⁷¹ Under stress (i.e., exposure to micro- or millimolar metal concentrations) these metals can move into the

cell in larger concentrations by less-specific transport pathways, inducing toxicity by, e.g., binding to proteins, competing with other metal cation cofactors in enzymes, and damaging DNA structures.^{471,472} As discussed in two reviews, a combination of in vitro and in vivo studies have shown that nickel can disrupt the activity of metalloenzymes and non-metal enzymes.^{471,472} For example, nickel has been shown to inhibit ferrous ion-dependent dioxygenases by replacing the redox-active iron ion with the stable nickel (II) ion and to inhibit a number of proteins containing catalytic cysteine residues. At least three in vivo studies using *B. vietnamiensis*, *P. putida*, and *E. coli* have shown either increased superoxide dismutase (SOD) concentrations or decreased growth in SOD-depleted mutants following nickel exposure; these results suggest that nickel can induce oxidative stress in microorganisms.

To understand the species present in solution, we note that the transition metals in NMC are formally in the +III or +IV oxidation states depending on the state of lithiation. Ni³⁺ and Ni⁴⁺, in particular, lie outside the stability limits of water^{473,474} and would therefore be expected to undergo spontaneous dissolution, oxidizing water via reactions such as $4 \text{LiMO}_2 + 6 \text{H}_2\text{O} \rightarrow 4 \text{Li}^+ + 12 \text{OH}^- + \text{O}_2 + 4 \text{M}^{2+}$ where M = Ni, Co, or Mn. In addition, protons can exchange for Li⁺ in the layered oxides,^{475,476} via $\text{LiMO}_2 + x\text{H}^+ \rightarrow \text{Li}_{(1-x)}\text{H}_x\text{MO}_2 + x\text{Li}^+$, allowing Li⁺ to be readily leached in aqueous media. The detailed mechanism of water oxidation by high-valent metal oxides is complex⁴⁷⁷ and is not discussed here. To model the solution composition and identify whether any solid precipitates would be expected to form under the conditions of our experiments, we used Visual Minteq (see Table S1) to calculate the complete distribution of species in the

growth medium with added 0.270 mM LiOH, 0.062 mM NiCl₂, 0.021 mM CoCl₂, and 0.008 mM MnSO₄ (corresponding to metal content released from 50 mg/L NMC). For Ni, Mn, and Co, the metal-lactate complexes are the primary form of metal ions in solution, with a smaller amount (7.5% for Ni²⁺, 43% for Mn²⁺, and 16% for Co²⁺) as the free divalent cations. The expected percentages of free metal ions were similar for the metal ion concentrations resulting from dissolution of 5 mg/L NMC. Notably, under the conditions of our experiments, no substantial precipitates of metal hydroxides or metal phosphates are expected. For Mn, a very small amount (corresponding to 9.6×10^{-7} M) of solid MnHPO₄ is predicted to be formed. The resulting detailed speciation of Ni, Mn, Co, and Li is provided in Table S1 in Supporting Information.

Our findings implicate incongruent dissolution of NMC to yield dissolved Ni, Co, and Mn as the explanation for the impact of this material on the respiration of *S. oneidensis*. In particular, Ni and Co had the strongest impact in altering the bacterial growth profile. Numerous studies have examined biological effects of nanoparticles composed of simple metal oxides.^{48,248,478–480} Nanoparticles composed of simple oxides of the metals composing NMC, such as NiO, CoO, Co₃O₄, and Mn₂O₃, promote oxidative stress in cells through interaction with cellular redox couples.⁴⁷⁹ Direct association of some nanoparticles with cell membranes may promote adverse effects.⁴⁷⁸ The biological effects of complex metal oxides such as NMC have not been previously considered. Our data indicate that direct contact with the material would not be necessary for NMC to exert toxicity on bacteria. The high oxidation state of the Ni in NMC places it outside the stability limit of water, leading to dissolution of the material.

6.4 Conclusions

Our results suggest that NMC entering aqueous environments (e.g., resulting from battery disposal into landfills) may act as a source of dissolved nickel and cobalt, potential bacterial toxicants, as well as other ions such as Mn and Li. This work provides additional motivation for efforts to develop and implement effective recycling strategies for lithium-ion batteries. We suggest that by reducing dissolution of metals from NMC, its toxicity to bacteria and other organisms in natural environments can be reduced. Ultra-thin (~1 nm thickness) surface coatings of Al₂O₃ and other stable oxides have been shown to reduce the reactivity of NMC cathodes and thereby improve the performance of NMC-containing lithium-ion batteries.^{481–484} Data for Al₂O₃ dissolution⁴⁸⁵ suggests that at pH ~6, a 1 nm thick coating would require on the order of one year to dissolve. This suggests that surface coatings may also have an important role in the environmental impact of NMC and other complex oxides.

6.5 Acknowledgements

This work was supported by the National Science Foundation Center for Chemical Innovation Program grant CHE-1503408 for the Center for Sustainable Nanotechnology. I.L.G. acknowledges the Minneapolis Torske Klubben Graduate Fellowship. K.R.H. was supported by a University of Minnesota Doctoral Dissertation Fellowship. M.N.H. acknowledges the National Science Foundation Graduate Fellowship Program. The authors acknowledge Shuyu Fang for assistance with cycling commercial NMC for figure

S1.

6.6 Supporting Information

6.6.1 Cycling-Induced Fracture of Commercial NMC. Cycling of batteries causes stress-induced fracture of the cathode material, resulting in formation of nanoparticles and nano-sheets. The SEM images of the commercial NMC material (Toda) in Figure S1 show that while current generation NMC cathode materials use nano-sized particles sintered into larger aggregates, upon cycling in a battery the NMC particles break into nanoscale fragments that have a sheet-like morphology due to the inherent anisotropy of the NMC crystal structure.

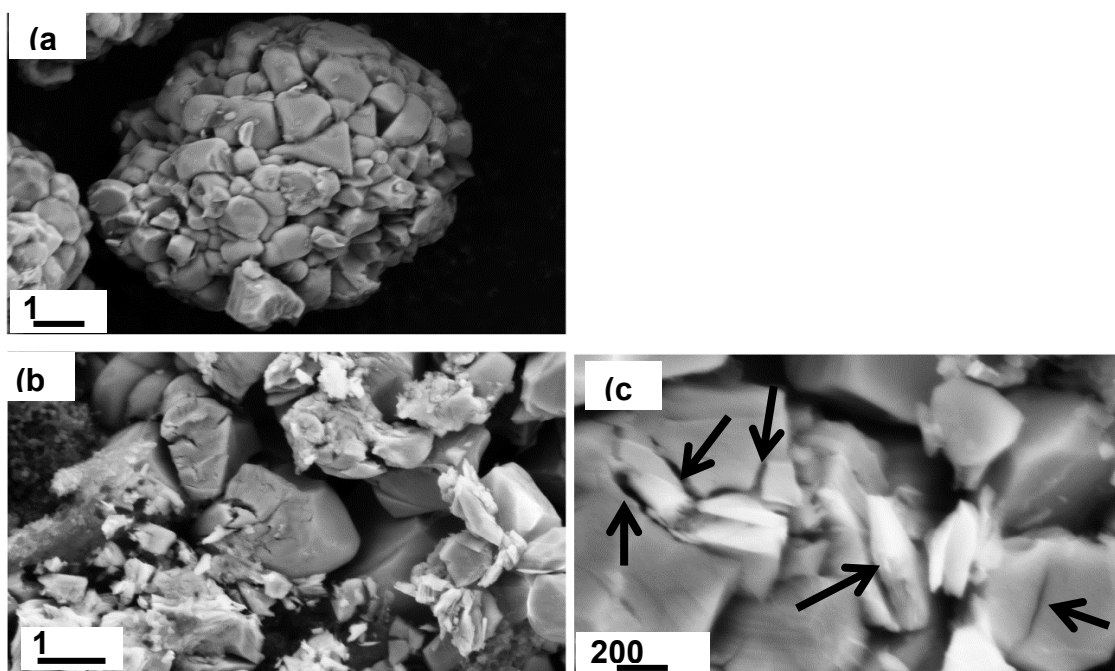


Figure S1. SEM image of commercial NMC material showing stress-induced fracturing and formation of nano-sheets. Commercial NMC (Toda) before cycling (a). Cathodes after

200 charge-discharge cycles in a standard battery-grade electrolyte (1:1 v/v ethylene carbonate / dimethyl carbonate + 1 M LiPF₆) cycled 200 times between 2.5 V and 4.3 V (b) and (c). (b) and (c) show clear fracturing and formation of nanoparticles. In (c), several fracture points are indicated by the arrows. Since the NMC material has an anisotropic, layer crystal structure, many of the fractured particles are in the form of nanosheets.

6.6.2. Atomic Force Microscopy of NMC. Samples for AFM analysis were prepared by spin-coating a dilute methanolic solution of NMC onto a mica disc (V1 grade, Ted Pella). Imaging was carried out on a Multimode™ AFM with a Nanoscope IV controller (Digital Instruments) in tapping mode using diamond-like-carbon coated tips (Tap300DLC, Budget Sensors). Image processing was performed using Gwyddion. For analysis, three different spots on a single sample were measured. For each of the three spots, four line profiles were obtained resulting in 12 total line profiles, which measured 125 total nanosheets. Figure S2a shows one of the three spots used for analysis and confirms that whole hexagonal sheets break up into smaller sheets < 100 nm in diameter upon sample preparation for biological assays. Figure S2b shows the height profile along a line passing over several NMC nanosheets as referenced to the dotted white line profile from Figure S2a. The average height was 0.88 ± 0.61 nm.

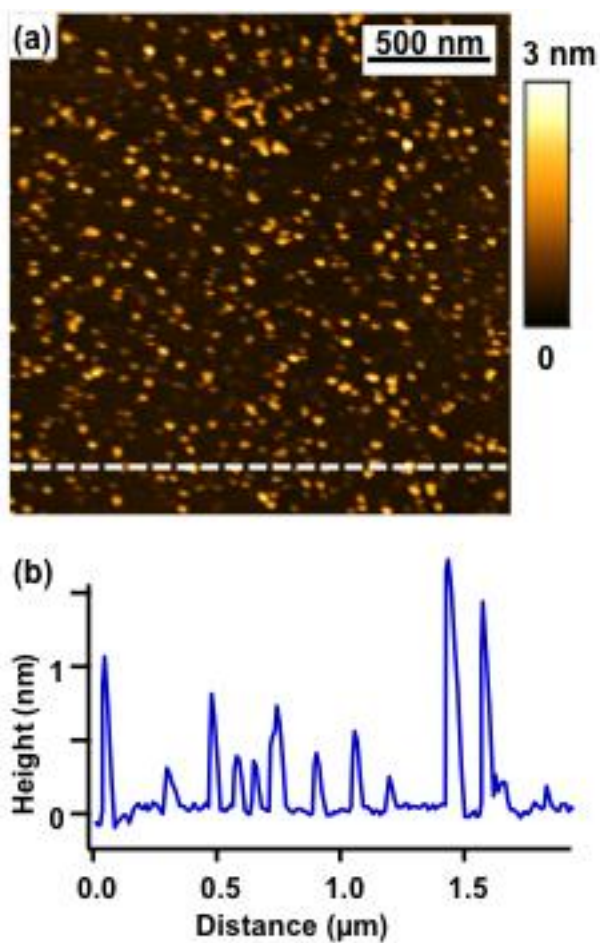


Figure S2. Representative AFM image of NMC nanoparticles deposited on freshly cleaved mica (a). Representative AFM height profiles measured across individual NMC nanosheets (b).

6.6.3. Transmission Electron Micrographs of NMC

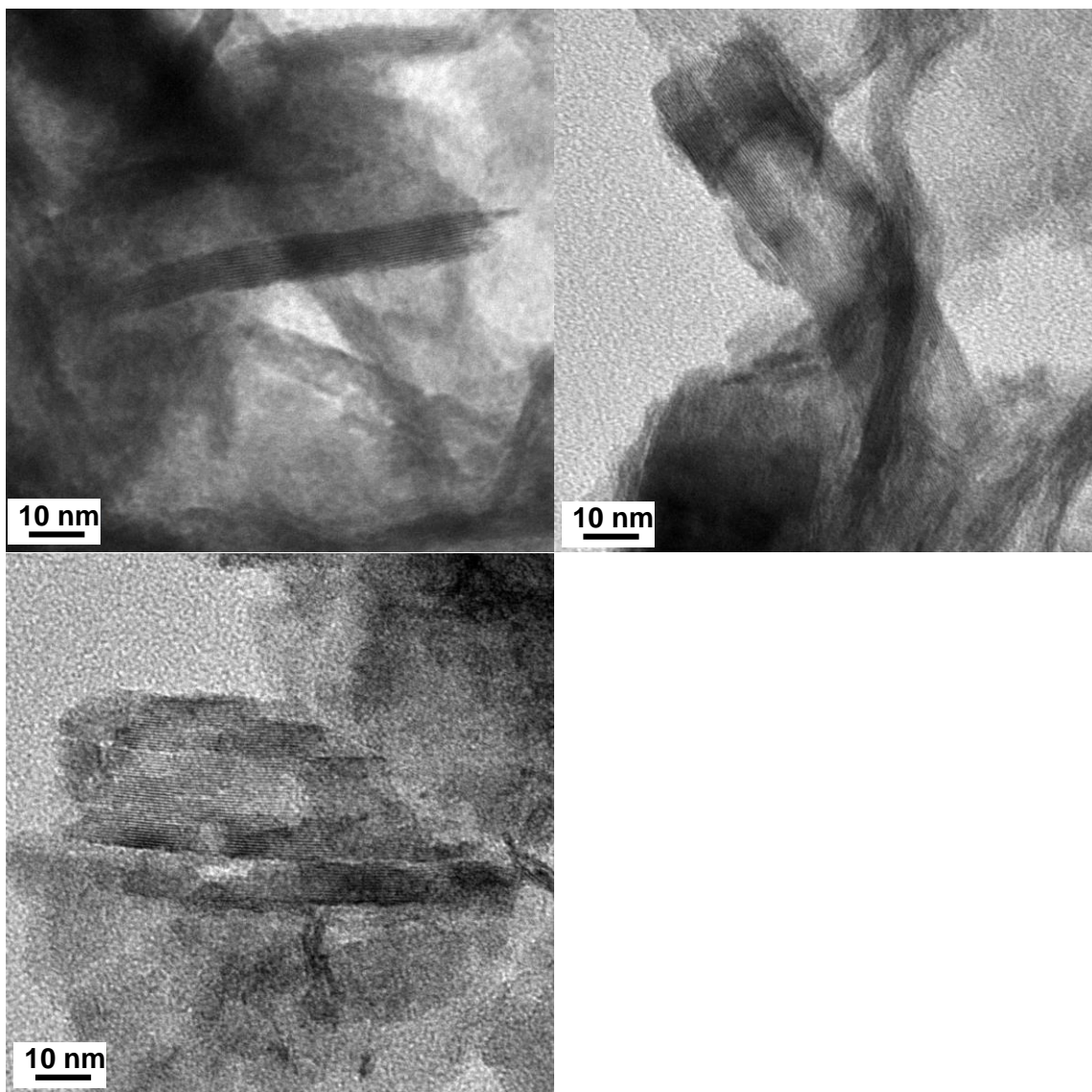


Figure S3. Selected edge-on transmission electron micrographs of stacks of NMC nanosheets.

6.6.4 Variable Recovery of Exponential Growth for *S. oneidensis* Exposed to 5 mg/L NMC. The reproducibility of cellular recovery after long exposure times to NMC (recovery of exponential growth) was evaluated by monitoring cellular respiration in

media or in media containing 5 mg/L NMC using the procedure described in the main text. Cell suspensions prepared from colonies formed on LB agar plates as described in the main text were diluted 1:10 v/v into fresh media, and 100 mL aliquots of this suspension were placed in 125 mL glass vessels fitted with removable rubber septa. NMC nanoparticles, dispersed in bacterial growth media at 200 mg/L through 10-minute sonication, were added to three vessels to achieve a concentration of 5 mg/L NMC, while additional three vessels received no NMC. The six samples were then placed in a water bath at 30 °C, and the cells were allowed to grow under a constant pressure of O₂ (g) with continuous stirring at 500 rpm. The CO₂ (g) produced through cellular respiration was removed from the gas phase by reaction with concentrated KOH (aq) present in the headspace above the liquid culture. O₂ (g) was supplied to the vessel as needed at 10-minute intervals to maintain a constant pressure, and total O₂ (g) delivery to each vessel was tracked as a function of time to measure bacterial respiration.

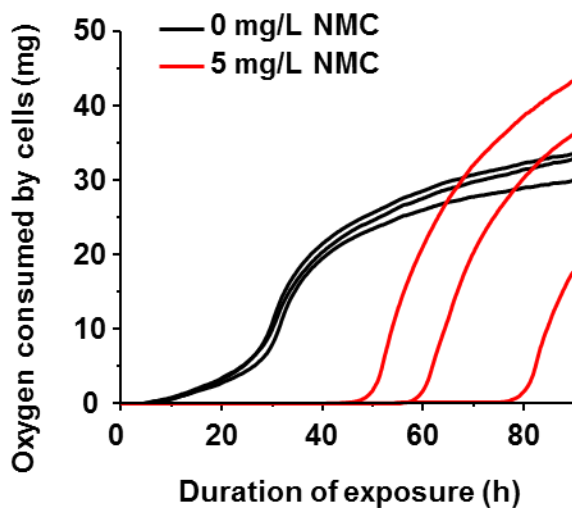


Figure S4. Respiration profiles of *S. oneidensis* grown in bacterial growth medium lacking (black traces) or containing (red traces) 5 mg/L NMC. Data from three independent replicates are shown separately for clarity. In this experiment, exposure to NMC delayed the onset of exponential growth by approximately 40 to 80 h.

6.6.5 Negligible impact of NMC on oxygen consumption independent of cellular respiration. Oxygen consumption was monitored in samples containing bacterial growth media and 0 or 5 mg/L NMC in the absence of cells using methods described in the Experimental section. Data were collected in triplicate and negligible oxygen consumption was observed in either condition. These results indicate that oxygen consumption due to processes other than cellular respiration was negligible.

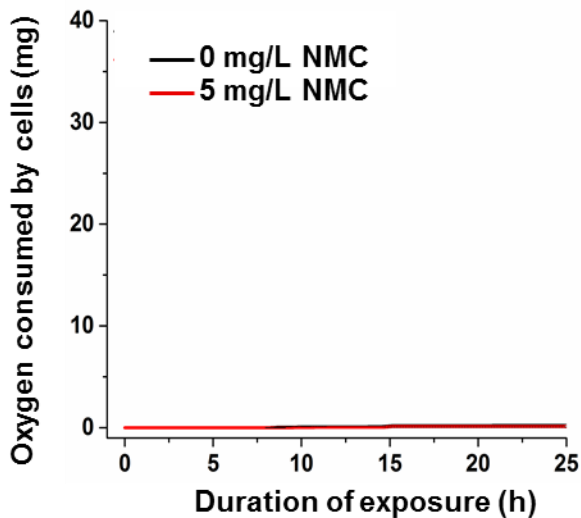


Figure S5. Oxygen consumption in cell-free bacterial growth medium in the absence (black traces) or presence (red traces) of 5 mg/L NMC. The mean and standard deviation

of three replicates is presented for each condition. Negligible oxygen consumption is observed for each condition.

6.6.6 Modeling the Effect of Initial Cell Population Size on Population Growth

Bacterial cell population growth was modeled for various initial population sizes using a logistic growth model. According to this model, population size (cell count) is a function of the initial population size, the carrying capacity of the environment, the growth rate, and the number of elapsed generations. Mathematically, this is expressed as

$$Y = Y_0 \cdot \frac{K}{Y_0 + (K - Y_0) \cdot e^{-r \cdot n}}$$

where Y is the cell count, Y_0 is the initial cell count, K is the carrying capacity, r is the growth rate, and n is the number of elapsed generations. Arbitrary values were chosen for the carrying capacity and growth rate, because our analysis focused on determining only the effect of initial cell count on population growth.

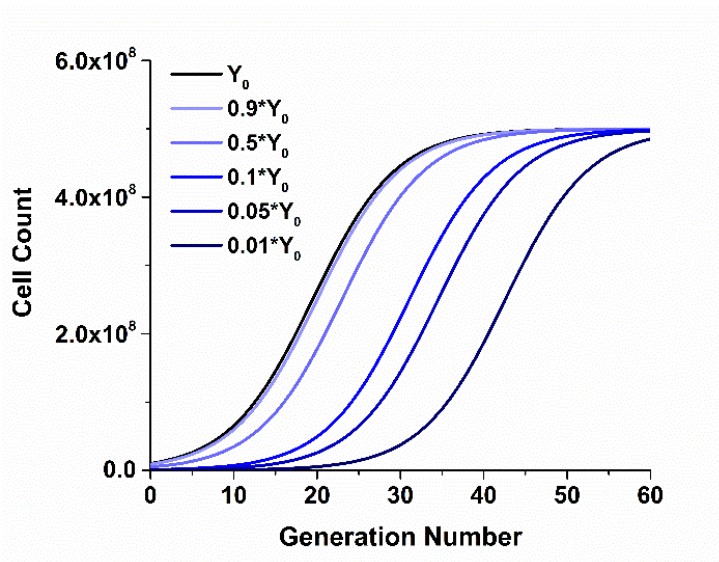


Figure S6. Modeled population growth over 60 generations for a bacterial cell culture with an initial cell density of 1×10^7 cells (black trace), or this initial cell density depleted by 10%, 50%, 90%, 95%, or 99% (light to dark blue traces).

6.6.7 Suspension Turbidity Due to NMC in Cell-free Media

NMC nanoparticles, dispersed in bacterial growth media at a concentration of 2000 mg/L through 10-minutes of sonication, were added to triplicate wells in a 96-well plate to achieve NMC concentrations of 5, 15, 25, 35, and 50 mg/L in the absence of cells (250 μ L sample volume). The 96-well plate was loaded into a Synergy 2 Multi-Mode Reader (BioTek, Winooski, VT) held at 30 °C. At one-hour intervals, the plate was slowly shaken for 20 seconds and light absorbance at 630 nm (due to light scattering by NMC) was recorded as a measure of suspension turbidity.

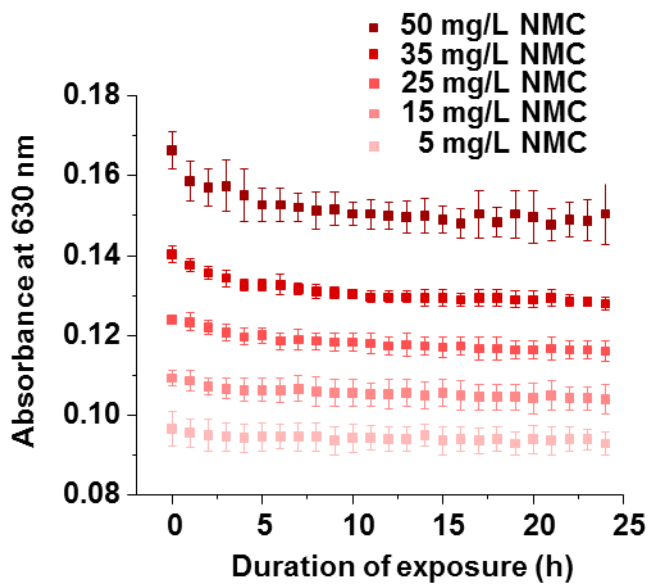


Figure S7. Turbidity profiles at 630 nm for 5 to 50 mg/L NMC over 24 h in bacterial growth media.

6.6.8 Time-dependent Changes in Chemical Composition of Aqueous Phase.

Dissolution behavior of 50 mg/L NMC upon exposure to bacterial growth medium show similar trends to those observed with 5 mg/L NMC exposure.

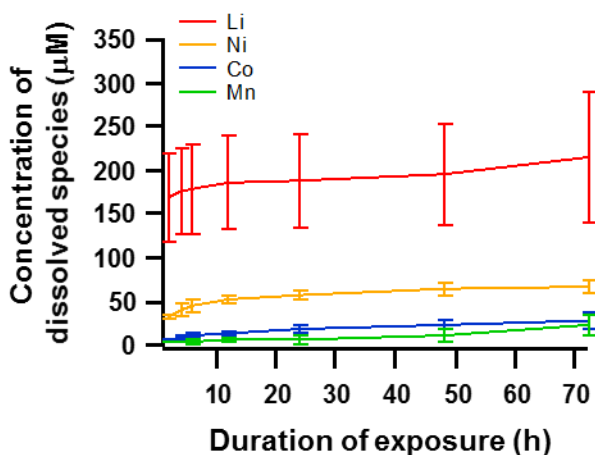


Figure S8. Concentration of dissolved species produced from 50 mg/L NMC nanoparticles over time in bacterial growth medium.

6.6.9 X-ray Photoelectron Spectroscopy of Co, Ni, and Mn in NMC. XPS was used to measure changes in the surface composition of NMC (Co, Ni, and Mn species) upon exposure to bacterial growth media for 72 h. Fig. S9 shows representative XPS spectra of the Co(2p), Ni(2p), and Mn(2p) regions. Spectra of each element are expected to show two peaks in a 2:1 area ratio corresponding to the $2p_{3/2}$ and $2p_{1/2}$ spin-orbit components, respectively.

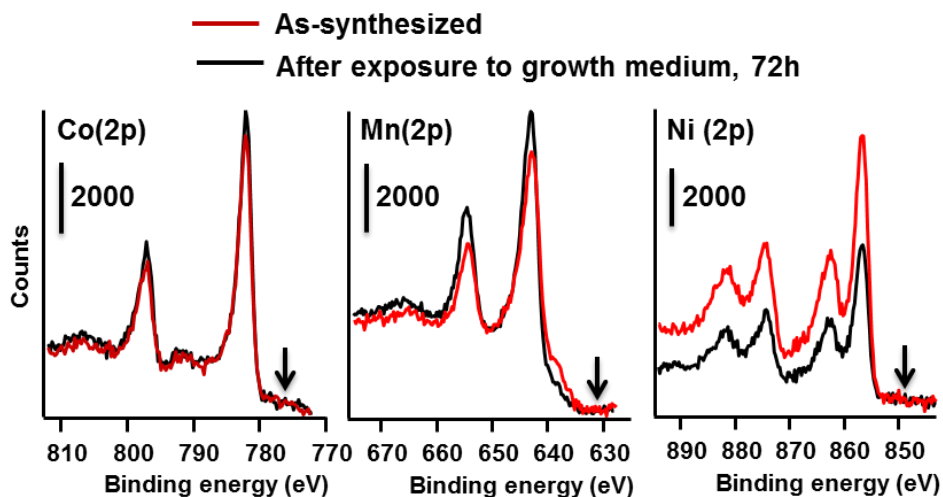


Figure S9. XPS spectra of NMC before (“as-synthesized”) and after exposure to bacteria growth medium for 72 hours. The arrow in each figure indicates the energy at which the before and after were aligned, to facilitate visual comparison of the changes in intensity

6.6.10 Growth and Respiration Profiles for Li^+ and Mn^{2+} Exposures.

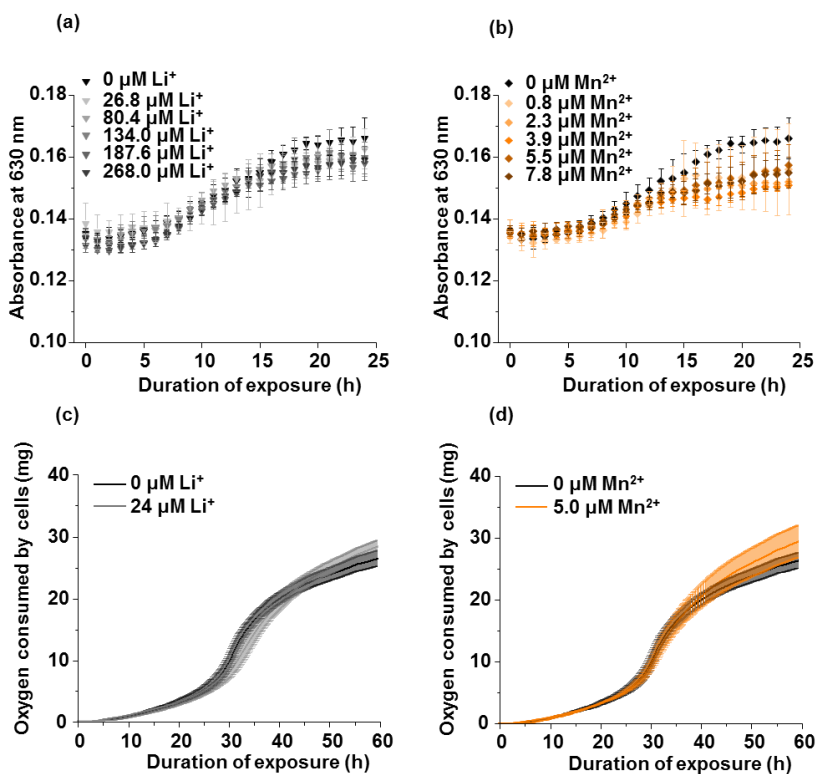


Figure S10. Growth (a, b) and respiration (c, d) profiles of *S. oneidensis* exposed to Li^+ and Mn^{2+} ions. In (a, b), the range of metal ion concentrations represents the range of expected metal release into bacterial growth medium over 24 h from 0 through 50 mg/L NMC, based on ICP-OES measurements. As in Figure 2, turbidity is proportional to the cell population size and was monitored over 24 h by measuring light absorbance to assess the effect of metal ions on cell growth. Cells were grown in metal-free medium (black symbols in a-d) or in medium containing (a) 26.8 to 268 μM LiOH , (b) 0.78 to 7.8 μM MnSO_4 . The mean and standard deviation of three biological replicates is plotted for each condition as a function of time, corrected to remove the light scattering contribution from NMC (as described in the text). In (c, d), metal ion exposure concentrations represent metal release into bacterial growth medium over 72 h from 5 mg/L NMC, based on ICP-OES measurements. Oxygen consumption due to cellular respiration increases with cell population size and was monitored over 60 h for cells grown in medium (black traces) and cells grown in medium containing (a) 24.0 μM Li^+ , (b) 5.0 μM MnSO_4 . The mean of three biological replicates is indicated by the dark trace, while standard deviations are indicated by lighter bars.

6.6.11 Powder X-ray Diffraction. The spectrum shows primary reflections that can be indexed to a R-3m space group previously reported for NMC, as indicated by the vertical bars.^{442,486} Smaller peaks, marked by asterisks, are associated with a presence of small amounts of hydroxide phases.^{442,486} The broad reflections arise from the small thickness (~1 nm) of the nanosheets and because of residual disorder in the material. Synthesized

NMC powder was deposited onto a zero diffraction plate (SiO₂ from MTI corp) for XRD analysis.

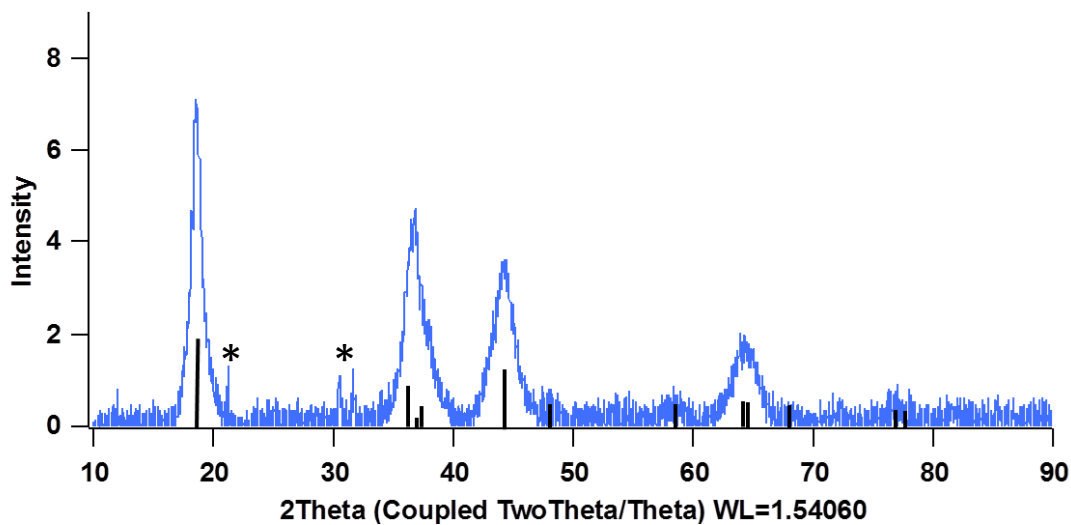


Figure S11. Powder X-ray diffraction obtained using a Cu K α shows that Li_{1/3}Ni_{1/3}Mn_{1/3}Co_{1/3}O₂ nanoparticles can be indexed to a R-3m space group. The remaining peaks can be indexed to metal (Co, Ni, Mn) hydroxides.

6.6.12 Oxygen Uptake Rate Profiles for NMC and Metal Ion Exposures.

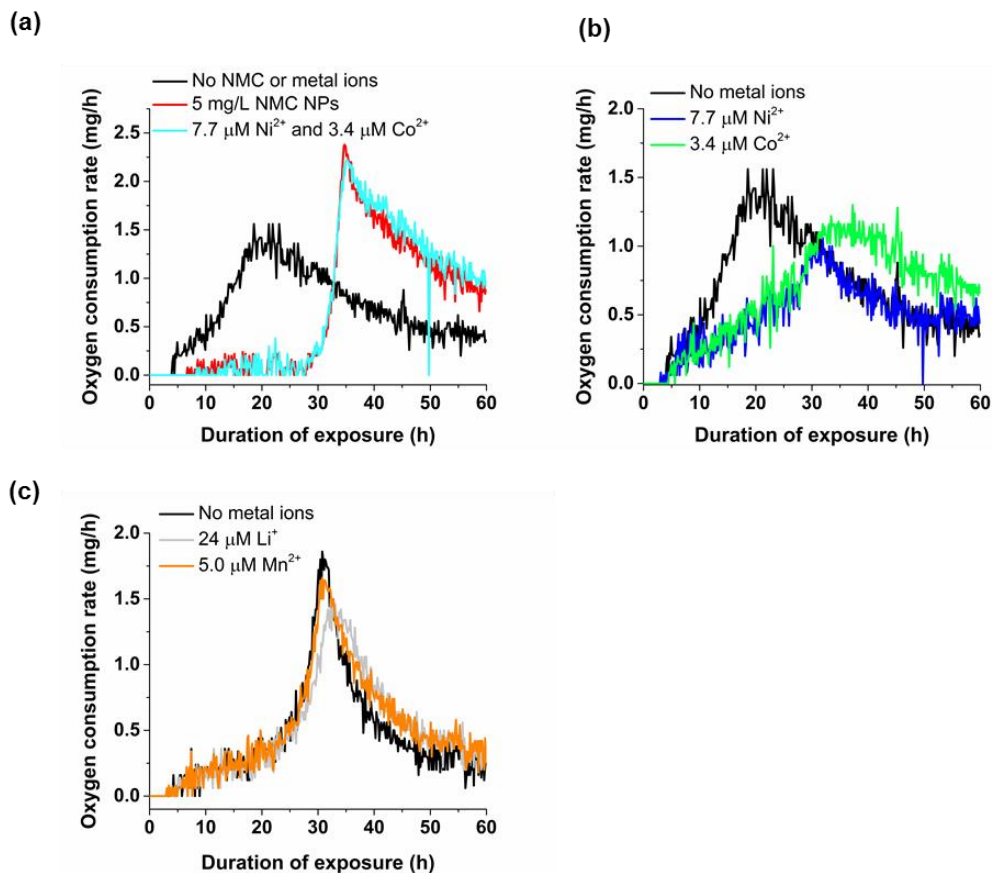


Figure S12. Oxygen uptake rates (OUR) profiles were obtained by differentiating oxygen consumption curves. Panels **a**, **b**, and **c** show OUR profiles corresponding to oxygen consumption profiles presented in Figures 2a and 5b; 4c and 4d; and S10c and S10d, respectively.

6.6.13 Visual Minteq Modeling of Solution Speciation.

Table S1. Speciation of soluble metals in bacterial growth medium with added 0.270 mM LiCl, 0.062 mM NiCl₂, 0.021 mM for CoCl₂, and 0.0078 mM MnCl₂. Mn(HPO₄) is predicted to form as a solid.

Metal	% of total concentration	Species name
Ni ⁺²	7.524	Ni ⁺²
	0.02	NiCl ⁺
	0.391	NiSO ₄ (aq)
	0.076	NiNH ₃ ⁺²
	0.034	NiHPO ₄ (aq)
	7.675	Ni-(Lactate) ³⁻
	43.272	Ni-(Lactate) ₂ (aq)
	41	Ni-Lactate ⁺
Li ⁺¹	90.779	Li ⁺¹
	8.155	Li-Lactate (aq)
	0.74	LiCl (aq)
	0.306	LiSO ₄ ⁻
	0.019	LiHPO ₄ ⁻
Co ⁺²	15.639	Co ⁺²
	0.022	CoOH ⁺
	0.05	CoCl ⁺
	0.813	CoSO ₄ (aq)
	0.032	Co(NH ₃) ⁺²
	0.089	CoHPO ₄ (aq)
	4.007	Co-(Lactate) ₃ ⁻

	36.639	Co-(Lactate) ₂ (aq)
	42.709	Co-Lactate ⁺
Mn ⁺²	43.231	Mn ⁺²
	0.309	MnCl ⁺
	2.002	MnSO ₄ (aq)
	0.578	MnHPO ₄ (aq)
	1.395	Mn-(Lactate) ₃ ⁻
	12.461	Mn-(Lactate) ₂ (aq)
	40.005	Mn-Lactate ⁺
	9.58×10 ⁻⁷ M	MnHPO ₄ (s)

Chapter 7

Ongoing and Future Research

7.1 Lipopolysaccharide-Mediated Interactions between Nanoparticles and Gram-negative Bacteria

Chapter 5 demonstrates that LPS plays a critical role in mediating nanoparticle interactions with gram-negative bacteria. Results show that LPS density controls the extent of nanoparticle association with the cell surface while LPS length controls the distance at which nanoparticles bind from the underlying lipid membrane. These insights form a basic model for understanding and predicting nanoparticle interactions with gram-negative bacteria. This model predicts that (i) nanoparticle association to bacteria bearing smooth (long) LPS will be greater than to bacteria bearing rough (short) LPS due to the greater number of binding sites present in the former, and (ii) that nanoparticles will bind closer to the underlying lipid membrane of bacteria bearing rough LPS than smooth LPS.

Nanoparticle toxicity may be influenced by both the number of nanoparticles adsorbed to the cell and their proximity to the cell membrane: toxicity is expected to increase with increasing nanoparticle adsorption (likely to be greater for smooth LPS- vs. rough LPS-expressing cells) and increasing nanoparticle proximity to the cell membrane (likely to be greater for rough LPS- vs. smooth LPS-expressing cells). We do not yet know which of these factors dominates; consequently, our current model of nanoparticle interactions with gram-negative bacteria cannot predict the impact of LPS length on nanoparticle toxicity. Ongoing work seeks to build a link between our current model of nanoparticle-cell association and its implications for cellular toxicity by characterizing the effects of LPS length on nanoparticle toxicity to *S. oneidensis*.

Initial studies have focused on controlling the length of LPS expressed by live *S. oneidensis* cells. Precedent work suggests that cell growth temperature influences LPS length and can be used to enrich cells in either smooth or rough LPS.⁴⁰⁷ In particular, low growth temperatures (between 5 and 20 °C) were shown to produce *S. oneidensis* cells enriched in smooth LPS versus cells grown at 30 °C.⁴⁰⁷ Results from our lab suggest, in contrast, that a lower growth temperature (20 °C) produces cells enriched in rough LPS versus cells growth at 30 °C. The reason for this discrepancy with literature precedent is unknown at this time.

To assess the impact of growth temperature on LPS production by *S. oneidensis*, cells were cultured at 20 °C or 30 °C, and their LPS contents were subsequently extracted and characterized using gel electrophoresis. Cells were cultured in LB broth over 24 h with continuous mixing at 300 RPM at a temperature of either 20 °C or 30 °C. Each culture was then diluted in LB broth to achieve a cell density of 5×10^8 cells/mL and subsequently centrifuged at a speed of 10800 RCF for 10 min. The supernatant was discarded and the cell pellet stored at -20 °C. LPS was subsequently extracted from the cells using a published protocol.⁴⁸⁷ Frozen cell pellets were resuspended using pipetting action (not vortexing) in 200 μ L of 2% sodium dodecyl sulfate (SDS), 2% β -mercaptoethanol, 10% glycerol in 0.1 M Tris-HCl at pH 6.8 containing a pinch of bromophenol blue (for coloring). The suspensions were boiled in a water bath for 15 minutes and allowed to cool to room temperature. Then 10 μ L of 10 mg/mL Proteinase K was added to each sample and these were incubated at 59 °C overnight. Then 200 μ L of ice-cold Tris-saturated phenol was added and to each sample and these were incubated at

65 °C for 15 minutes. The samples were cooled to room-temperature and 1 mL of diethyl ether was added to each. The samples were centrifuged at 17000 RCF for 10 minutes and the bottom blue-colored layer (containing LPS) was extracted.

Upon extraction from cells, LPS length was characterized using polyacrylamide gel electrophoresis (PAGE). Sample aliquots (10 µL) were loaded into wells of a 4-15% precast polyacrylamide gel (Bio-Rad, Mini-PROTEAN TGX) and separated using a running buffer composed of 4% sodium dodecyl sulfate (SDS), 4% β-mercaptoethanol, and 20% glycerol in 0.1 M Tris-HCl at pH 6.8 using an applied voltage of 120 mV. The gel was subsequently immersed in 200 mL of an aqueous solution of 50% methanol and 5% acetic acid, rinsed twice with 1 L of 3% acetic acid, and immersed in 250 mL of 3% glacial acetic acid containing periodic acid (supplied by the fluorescent staining kit manufacturer, *vide infra*). The gel was washed twice with 100 mL of 3% acetic acid and then incubated with Pro-Q Emerald 300 Staining Solution (ThermoFisher Scientific) for 2 h. The gel was washed three times with 100 mL of 3% acetic acid and then imaged using a Gel Doc EZ System (Bio-Rad) fitted with the ultraviolet sample tray.

Extracted LPS molecules were separated into discrete bands on the gel based on their average molecular mass; lower molecular mass LPS molecules (i.e., those containing shorter polysaccharide chains, characteristic of rough LPS) moved farther down the gel than higher molecular mass LPS molecules (i.e., those containing longer polysaccharide chains, characteristic of smooth LPS) due to their higher mobility through the gel's pores.

As shown in Figure 1, LPS extracted from cells cultured at 20 and 30 °C produced bands

at identical locations on the gel (confirmed using both biological and technical replicates, as indicated), but with different intensities. The intensity of each band in the gel is indicative of the concentration of LPS molecules present. Cells cultures at 30 °C showed a greater abundance of higher molecular mass (less mobile) LPS than those grown at 20 °C, as indicated by the higher intensity of the band closer to the top of the gel. LPS extracted from *E. coli* (which was provided by the fluorescent staining kit manufacturer) served as a control to ensure that fluorescent staining of LPS was successful.

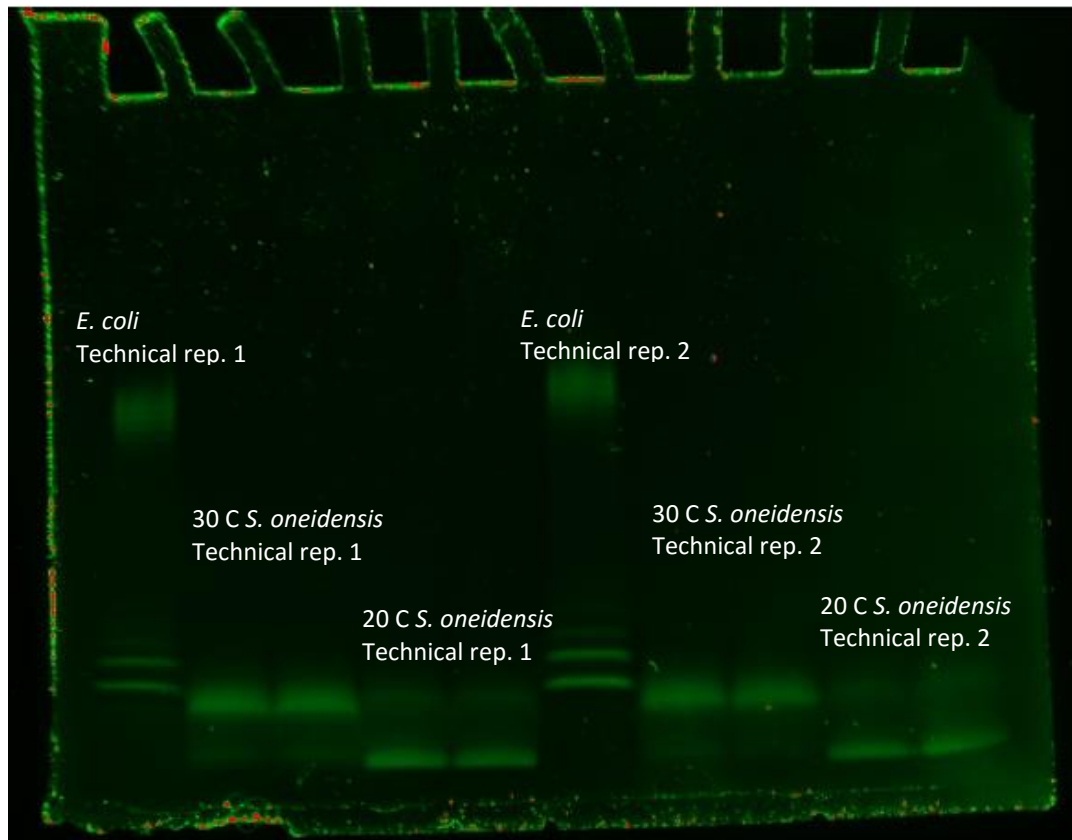


Figure 1. SDS-PAGE characterization of LPS extracted from *S. oneidensis* cultured at 20 or 30 °C. Adjacent bands under a particular label LPS were prepared from independent biological replicates while technical replicates are indicated in the labels. LPS extracted

from *E. coli* served as an indicator of successful LPS labeling with the fluorescent probe.

These results demonstrate that cell culturing temperature can be used to control the length of LPS expressed by *S. oneidensis*, and may provide a means to assess the effect of LPS length on nanoparticle toxicity to gram-negative bacteria in future work. However, additional studies need to assess the potential effects of cell culturing temperature on other features of the cell membrane architecture (e.g., lipid membrane fluidity). These studies will determine whether LPS length can be independently controlled from other membrane characteristics. Future work in collaboration with Prof. Erin Carlson will assess the impact of growth temperature on the composition of lipids extracted from *S. oneidensis* membranes using mass spectrometry. A negative result (i.e., no significant difference between the membrane lipid compositions of cells grown at 20 vs 30 °C) is required to pursue growth temperature as a means to control LPS length in isolation and assess the impact of LPS length on nanoparticle toxicity to *S. oneidensis*. Nanomaterials known to induce toxicity through diffusion-mediated mechanisms (e.g., release of toxic ions or production of reactive oxygen species) will be used to assess the impact of LPS length on nanomaterial toxicity; such diffusion-mediated processes are expected to depend on nanomaterial proximity to the cell membrane, which varies with LPS length. Candidate materials include copper nanoparticles and NMC.

7.2 Nanoscale Battery Cathode Material Toxicity to Bacteria

Chapter 6 demonstrates that incongruent dissolution of NMC is responsible for its toxicity towards *S. oneidensis*. Ongoing work has sought to reduce the toxicity of NMC

to *S. oneidensis* by enriching the material in Mn (which showed minimal toxicity in ionic form) at the expense of Ni and Co (which showed significant toxicity in the ionic form).

Mn-enriched NMC has been prepared by Mimi Hang in Dr. Robert Hamers' laboratory using a modified version of the procedure described in section 6.2.1. While the original synthesis used equimolar concentrations of each metal acetate salt to prepare the mixed metal hydroxide precursor (ultimately achieving NMC with stoichiometry $\text{Ni}_1\text{Mn}_1\text{Co}_1$), subsequent syntheses varied the molar ratios of these salts. Three new NMC formulations have been prepared using this modified procedure, with stoichiometry $\text{Ni}_1\text{Mn}_{4.7}\text{Co}_1$, $\text{Ni}_1\text{Mn}_{2.5}\text{Co}_1$, and $\text{Ni}_1\text{Mn}_{1.3}\text{Co}_1$ (as measured by ICP-OES, described in section 6.2.2).

medium has been

results shown in Figure

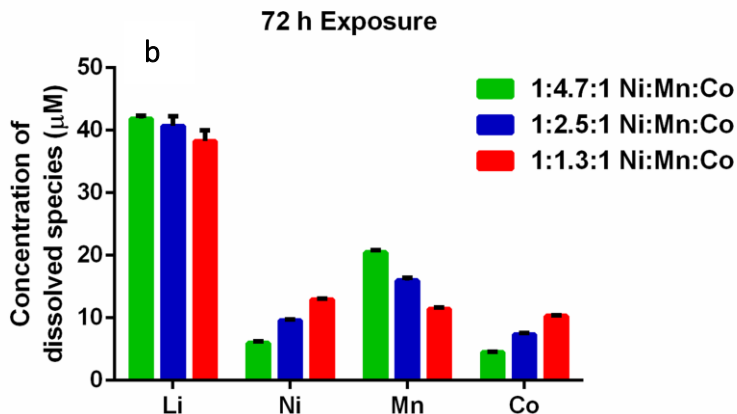
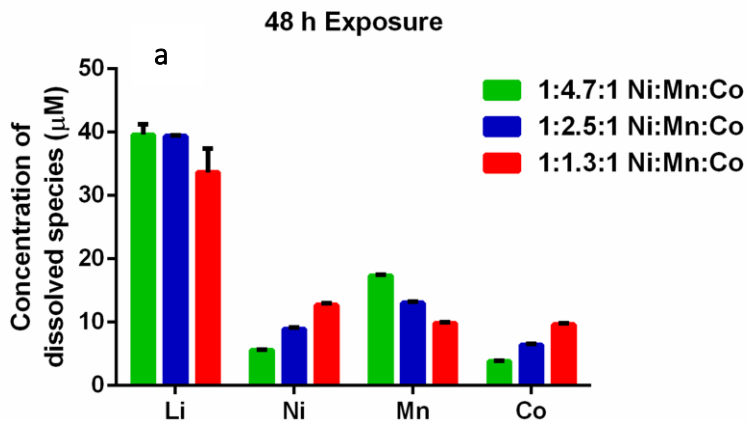


Figure 2. Concentration of dissolved species produced from 5 mg/L NMC nanoparticles in growth medium after 48 h (a) and 72 h (b). Shown are the average and standard deviation of two independent replicates and three technical replicates for each sample.

With increasing Mn enrichment, the dissolved Mn concentration in solution increased while the dissolved Ni and Co concentrations decreased; the concentrations of these dissolved metal species varied approximately linearly with the concentrations of metals in the NMC starting material. Dissolved concentrations of Li species remained approximately constant, indicating that the amount of Li intercalation between nanosheets is largely independent of the metal oxide framework composition for the NMC formulations considered here.

Based on the results shown in Figure 2 and our previous work presented in Chapter 6, we expected that Mn-enrichment would reduce NMC's toxicity to *S. oneidensis*. This hypothesis was evaluated by measuring changes in cellular respiration in response to NMC exposure (Figure 3) using the methods described in section 6.2.6.

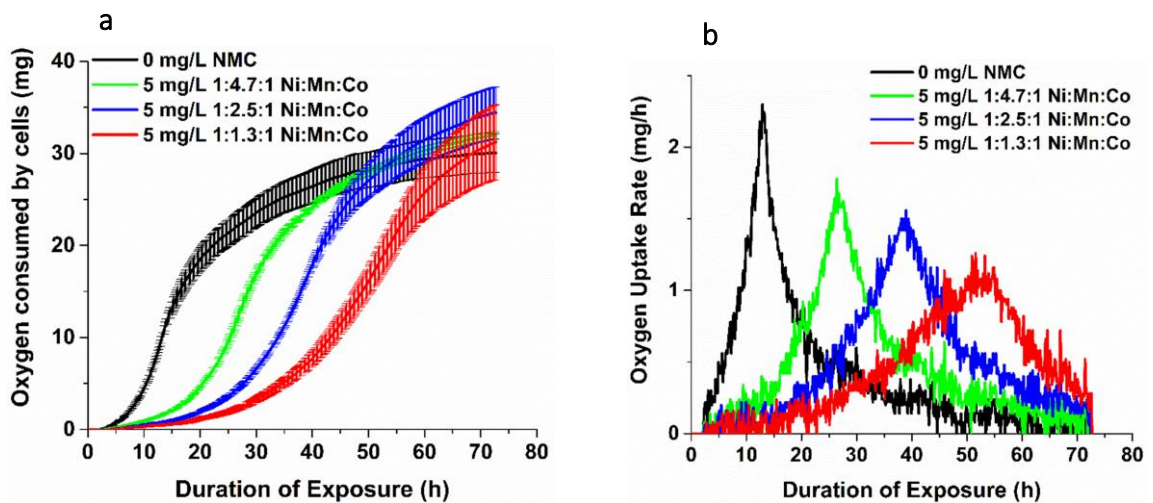


Figure 3. Response of *S. oneidensis* to NMC exposure as a function of Mn-enrichment. Oxygen consumption due to cellular respiration increased with cell population size (**a**) and was monitored over 72 h for cells grown in medium without NMC (black trace) or cells grown in medium containing 5 mg/L NMC (green, blue, and red traces). Molar ratios of Ni, Mn, and Co in the NMC material (as measured by ICP-OES) are indicated in the legend; Mn-enrichment increases from red to blue to green. The dark trace represents the mean of three biological replicates; lighter bars indicate standard deviations. Oxygen uptake rate profiles (**b**) were obtained by differentiating the oxygen consumption curves shown in (**a**).

Our results indicate that NMC's toxicity to *S. oneidensis* decreases with increasing Mn-enrichment. Consumption of oxygen increased with the number of actively respiring cells (Figure 3a, 0 mg/L NMC). Cells exposed to 5 mg/L NMC of any formulation showed a delay in growth relative to cells exposed to 0 mg/L NMC (Figure 3a, 5 mg/L NMC). The maximal growth rate of cells exposed to NMC was delayed relative to unexposed cells and varied with Mn-enrichment (Figure 3b); cells exposed to NMC with the least Mn-enrichment ($\text{Ni}_1\text{Mn}_{1.3}\text{Co}_1$) showed the greatest delay (42 h, red trace), while cells exposed to NMC with the greatest Mn-enrichment ($\text{Ni}_1\text{Mn}_{4.7}\text{Co}_1$) showed the least delay (13 h, green trace). The delay induced by the least Mn-enriched NMC ($\text{Ni}_1\text{Mn}_{1.3}\text{Co}_1$) was comparable to that induced by the original NMC formulation considered in Chapter 6 (i.e., $\text{Ni}_1\text{Mn}_1\text{Co}_1$); compare Chapter 7 Figure 3 and Chapter 6 Figure 2.

Results presented in Chapter 6 showed that simultaneous exposure of cells to concentrations of Ni²⁺ and Co²⁺ equivalent to those released from 5 mg/L NMC inhibited growth (Chapter 6, Figure 5a) and respiration (Chapter 6, Figure 5b) to a very similar extent as that induced by NMC itself. To identify whether dissolved metal ions were also responsible for the observed impact of NMC on cell respiration when NMC was enriched in Mn, we monitored respiration during continual exposure to both Ni²⁺ (as NiCl₂) and Co²⁺ (as CoCl₂) and to Ni²⁺ and Co²⁺ together with Mn²⁺ (as MnSO₄) and Li⁺ (as LiOH). The metal ion concentrations used encompassed the range of expected dissolved metal content based on ICP-OES measurements from 5 mg/L NMC nanoparticle exposures of each formulation after 72 h incubation in growth medium (Figure 2b).

Consistent with the results presented in Figure 3, the maximal growth rate of cells exposed to NMC of any composition was generally lower than that of unexposed cells and the onset of exponential growth was delayed (Figure 4, dark traces); these effects decreased in magnitude with increasing Mn-enrichment. Simultaneous exposure of cells to Ni²⁺ and Co²⁺ at concentrations equivalent to those released from 5 mg/L NMC inhibited respiration to a similar extent as the corresponding NMC exposure (Figure 4a); the highest degree of overlap was observed between the most Mn-enriched NMC and equivalent Ni²⁺ and Co²⁺ exposures (green traces), while the lowest degree of overlap was observed between the least Mn-enriched NMC and equivalent Ni²⁺ and Co²⁺ exposures (red traces). These results suggest that enrichment of NMC with Mn reduces its toxicity to *S. oneidensis* by reducing the release and corresponding toxicity of Ni and Co species.

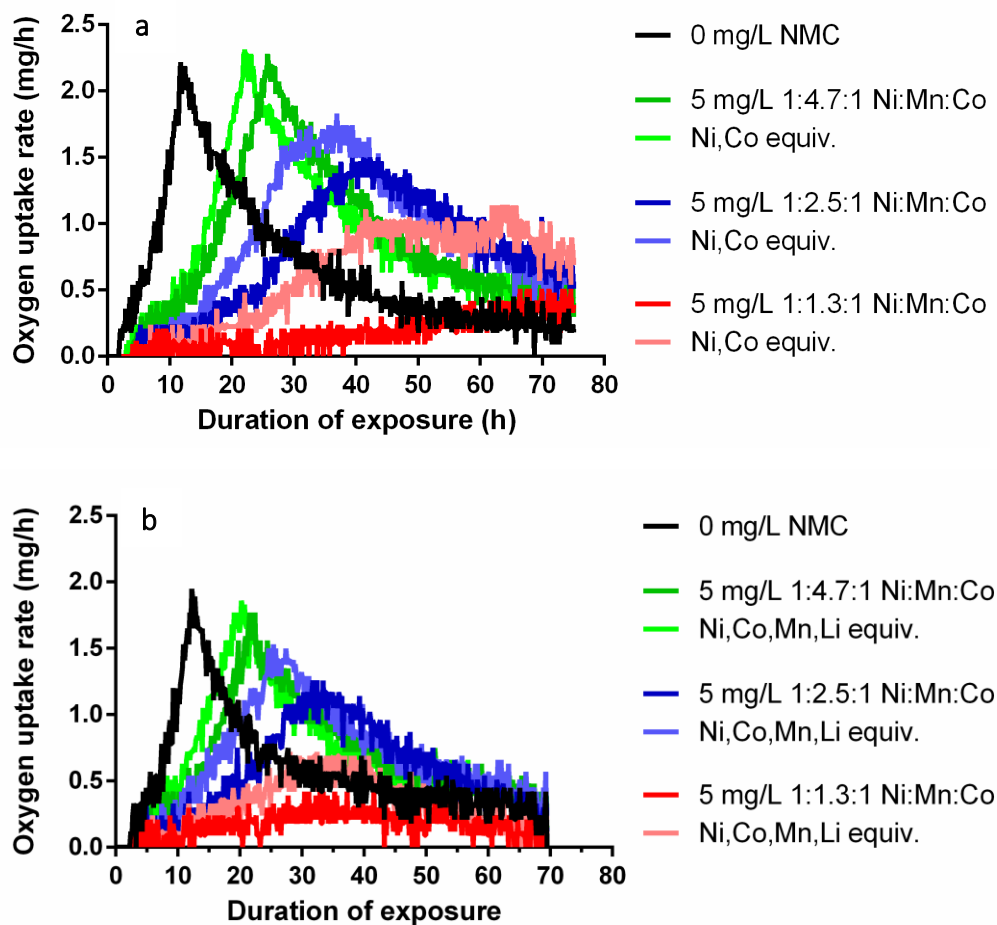


Figure 4. Response of *S. oneidensis* to Ni²⁺ and Co²⁺ or NMC exposure as a function of Mn-enrichment (a), and response of *S. oneidensis* to Ni²⁺, Co²⁺, Mn²⁺, and Li⁺ or NMC exposure as a function of Mn-enrichment (b). The data plotted in (a) and (b) were collected in two independent experiments and each trace represents the mean of two

biological replicates. In (a), oxygen consumption was monitored over 72 h for cells grown in medium without NMC (black trace), cells grown in medium containing 5 mg/L NMC (dark green, blue, and red traces), and cells grown in medium containing Ni^{2+} and Co^{2+} at equivalent concentrations to that released by NMC (light green, blue, and red traces). Oxygen consumption profiles were differentiated to produce the oxygen uptake rate profiles shown. Molar ratios of Ni, Mn, and Co in the NMC material (as measured by ICP-OES) are indicated in the legend; Mn-enrichment increases from red to blue to green. The same is true in (b), with the exception that medium was supplemented with Mn^{2+} and Li^+ in addition to Ni^{2+} and Co^{2+} (light green, blue, and red traces).

We sought to determine why soluble Ni and Co species did not fully account for the toxicity of the three Mn-enriched NMC compositions studied here, in contrast to the NMC composition considered in Chapter 6. We hypothesized that Mn^{2+} and Li^+ ions, which are released from Mn-enriched NMC at two- to four-times the concentration released from non-Mn-enriched NMC (compare Figure 2 to Chapter 6 Figure 3a), contributed to Mn-enriched NMC's impact on cellular respiration. This hypothesis was assessed by simultaneously exposing cells to Ni^{2+} , Co^{2+} , Mn^{2+} and Li^+ (present as NiCl_2 , CoCl_2 , MnSO_4 , and LiOH) at concentrations released from each of the three Mn-enriched NMC compositions and comparing cellular respiration to that of cells exposed to each composition of NMC. Results, presented in Figure 4b, show that overlap between oxygen uptake rate profiles of cells exposed to NMC and cells exposed to metal ion-equivalents is greater in the presence of Mn and Li species (Figure 4b) than in their absence (Figure 4). These results suggest that Mn and Li species contribute to the inhibition of cellular

respiration induced by Mn-enriched NMC (along with Ni and Co species) but that metal ion release cannot completely account for the toxicity of Mn-enriched NMC. Reducing or eliminating metal ion release (e.g., by coating NMC nanoparticles with an ultrathin layer of Al₂O₃, as discussed in Section 6.4) remains a viable strategy for reducing the toxicity of Mn-enriched NMC due to the strong contribution of soluble metal ions to its toxicity.

Future work must assess lithium-ion battery performance as a function of NMC Mn-enrichment or surface passivation (vide infra) to determine the commercial relevance of these toxicity-mitigation strategies. New experiments may not be necessary if such work has already been performed by the battery production industry. Collaboration with industrial partners in the battery production community, a strength of our collaborator Dr. Robert Hamers, will play an important role in determining the extent of Mn-enrichment that is commercially feasible. Alternative toxicity-mitigation strategies should also be pursued given the inability of Mn-enrichment to eliminate NMC's toxicity to *S.*

oneidensis. One proposed approach would be to incorporate an insoluble shell around the nickel manganese cobalt oxide framework. The insoluble shell may restrict access of the interior metal oxide framework to water, preventing the high-oxidation state Ni and Co species (present in the III and IV oxidation states) from oxidizing water and being released into solution. The composition of this shell may be informed by research in the battery industry, which has identified LiMPO₄ (where M is a transition metal, e.g., Co) as an effective barrier to exothermic reactions between the battery cathode and electrolyte.⁴⁸⁸ Such coatings, on the order of 7 nm in thickness, have been shown to increase the battery working voltage and reduce volume expansion and thermal runaway

relative to batteries employing uncoated cathodes.⁴⁸⁸ We hypothesize that the positive impacts of cathode material coatings on battery performance may extend to positive impacts on environmental toxicity by reducing cathode material dissolution in aqueous environments.

References

- (1) Skandan, G.; Singhal, A. *Dekker Encyclopedia of Nanoscience and Nanotechnology*; Taylor & Francis.
- (2) Nanotechnology Inventories <http://www.nanotechproject.org/inventories/> (accessed Apr 29, 2015).
- (3) Detailed information on nanomaterials from A to Z | Knowledge Base Nanomaterials <http://nanopartikel.info/en/nanoinfo/materials> (accessed Apr 29, 2015).
- (4) Sun, T. Y.; Gottschalk, F.; Hungerbühler, K.; Nowack, B. *Environ. Pollut.* **2014**, *185*, 69–76.
- (5) Stark, W. J.; Stoessel, P. R.; Wohlleben, W.; Hafner, A. *Chem. Soc. Rev.* **2015**, *44*, 5793–5805.
- (6) Malam, Y.; Loizidou, M.; Seifalian, A. M. *Trends Pharmacol. Sci.* **2009**, *30* (11), 592–599.
- (7) Kamat, P. V. *J. Phys. Chem. C* **2007**, *111* (7), 2834–2860.
- (8) Wu, Z.-S.; Ren, W.; Wen, L.; Gao, L.; Zhao, J.; Chen, Z.; Zhou, G.; Li, F.; Cheng, H.-M. *ACS Nano* **2010**, *4* (6), 3187–3194.
- (9) Schultz, A. G.; Boyle, D.; Chamot, D.; Ong, K. J.; Wilkinson, K. J.; McGeer, J. C.; Sunahara, G.; Goss, G. G. *Environ. Chem.* **2014**, *11* (3), 207–226.
- (10) Doak, S. H.; Griffiths, S. M.; Manshian, B.; Singh, N.; Williams, P. M.; Brown, A. P.; Jenkins, G. J. S. *Mutagenesis* **2009**, *24* (4), 285–293.
- (11) Wörle-Knirsch, J. M.; Pulskamp, K.; Krug, H. F. *Nano Lett.* **2006**, *6* (6), 1261–1268.
- (12) Monteiro-Riviere, N. A.; Inman, A. O.; Zhang, L. W. *Toxicol. Appl. Pharmacol.* **2009**, *234* (2), 222–235.
- (13) Kroll, A.; Pillukat, M. H.; Hahn, D.; Schneidenburger, J. *Arch. Toxicol.* **2012**, *86* (7), 1123–1136.
- (14) Karlsson, H. L.; Cronholm, P.; Hedberg, Y.; Tornberg, M.; De Battice, L.; Svedhem, S.; Wallinder, I. O. *Toxicology* **2013**, *313* (1), 59–69.
- (15) Murphy, C. J.; Vartanian, A. M.; Geiger, F. M.; Hamers, R. J.; Pedersen, J.; Cui, Q.; Haynes, C. L.; Carlson, E. E.; Hernandez, R.; Klaper, R. D.; Orr, G.; Rosenzweig, Z. *ACS Cent. Sci.* **2015**, *1* (3), 117–123.
- (16) Koshkina, O.; Lang, T.; Thiermann, R.; Docter, D.; Stauber, R. H.; Secker, C.; Schlaad, H.; Weidner, S.; Mohr, B.; Maskos, M.; Bertin, A. *Langmuir* **2015**, *31* (32), 8873–8881.
- (17) Tsarfati, Y.; Strauss, V.; Kuhri, S.; Krieg, E.; Weissman, H.; Shimoni, E.; Baram, J.; Guldi, D. M.; Rybtchinski, B. *J. Am. Chem. Soc.* **2015**, *137* (23), 7429–7440.
- (18) Liao, H.-G.; Niu, K.; Zheng, H. *Chem. Commun.* **2013**, *49* (100), 11720–11727.
- (19) Zobel, M.; Neder, R. B.; Kimber, S. A. J. *Science* **2015**, *347* (6219), 292–294.
- (20) Firlar, E.; Çınar, S.; Kashyap, S.; Akinc, M.; Prozorov, T. *Sci. Rep.* **2015**, *5*.
- (21) Chen, Q.; Smith, J. M.; Park, J.; Kim, K.; Ho, D.; Rasool, H. I.; Zettl, A.; Alivisatos, A. P. *Nano Lett.* **2013**, *13* (9), 4556–4561.
- (22) Roth, G. A.; Tahiliani, S.; Neu-Baker, N. M.; Brenner, S. A. *Wiley Interdiscip. Rev. Nanomed. Nanobiotechnol.* **2015**, *7* (4), 565–579.
- (23) Badireddy, A. R.; Wiesner, M. R.; Liu, J. *Environ. Sci. Technol.* **2012**, *46* (18), 10081–10088.
- (24) Badireddy, A. R.; Budarz, J. F.; Marinakos, S. M.; Chellam, S.; Wiesner, M. R. *Environ. Eng. Sci.* **2014**, *31*, 338–349.
- (25) Cho, T. J.; Hackley, V. A. *Anal. Bioanal. Chem.* **2010**, *398* (5), 2003–2018.

- (26) Demeester, J.; De Smedt, S.; Sanders, N.; Haestraete, J. In *Methods for structural analysis of protein pharmaceuticals*; 2005.
- (27) Tsai, D.-H.; DelRio, F. W.; Keene, A. M.; Tyner, K. M.; MacCusprie, R. I.; Cho, T. J.; Zachariah, M. R.; Hackley, V. A. *Langmuir* **2011**, *27* (6), 2464–2477.
- (28) Filipe, V.; Hawe, A.; Jiskoot, W. *Pharm. Res.* **2010**, *27* (5), 796–810.
- (29) Anderson, W.; Kozak, D.; Coleman, V. A.; Jämting, Å. K.; Trau, M. *J. Colloid Interface Sci.* **2013**, *405*, 322–330.
- (30) Coulter, W. H. Means for counting particles suspended in a fluid. US2656508 (A), October 20, 1953.
- (31) DeBlois, R. W.; Bean, C. P. *Rev. Sci. Instrum.* **1970**, *41* (7), 909–916.
- (32) Roberts, G. S.; Kozak, D.; Anderson, W.; Broom, M. F.; Vogel, R.; Trau, M. *Small* **2010**, *6* (23), 2653–2658.
- (33) Pal, A. K.; Aalaei, I.; Gadde, S.; Gaines, P.; Schmidt, D.; Demokritou, P.; Bello, D. *ACS Nano* **2014**, *8* (9), 9003–9015.
- (34) Kozak, D.; Anderson, W.; Vogel, R.; Chen, S.; Antaw, F.; Trau, M. *ACS Nano* **2012**, *6* (8), 6990–6997.
- (35) Tai, J.-T.; Lai, C.-S.; Ho, H.-C.; Yeh, Y.-S.; Wang, H.-F.; Ho, R.-M.; Tsai, D.-H. *Langmuir* **2014**, *30* (43), 12755–12764.
- (36) Elzey, S.; Tsai, D.-H.; Yu, L. L.; Winchester, M. R.; Kelley, M. E.; Hackley, V. A. *Anal. Bioanal. Chem.* **2013**, *405* (7), 2279–2288.
- (37) Cavicchi, R. E.; Meier, D. C.; Presser, C.; Prabhu, V. M.; Guha, S. *J. Phys. Chem. C* **2013**, *117* (20), 10866–10875.
- (38) Tsai, D.-H.; Cho, T. J.; DelRio, F. W.; Gorham, J. M.; Zheng, J.; Tan, J.; Zachariah, M. R.; Hackley, V. A. *Langmuir* **2014**, *30* (12), 3397–3405.
- (39) Li, M.; You, R.; Mulholland, G. W.; Zachariah, M. R. *Aerosol Sci. Technol.* **2014**, *48* (1), 22–30.
- (40) Tai, J.-T.; Lai, Y.-C.; Yang, J.-H.; Ho, H.-C.; Wang, H.-F.; Ho, R.-M.; Tsai, D.-H. *Anal. Chem.* **2015**, *87* (7), 3884–3889.
- (41) Pease, L. F.; Tsai, D.-H.; Fagan, J. A.; Bauer, B. J.; Zangmeister, R. A.; Tarlov, M. J.; Zachariah, M. R. *Small* **2009**, *5* (24), 2894–2901.
- (42) Degueldre, C.; Favarger, P.-Y. *Colloids Surf. Physicochem. Eng. Asp.* **2003**, *217* (1–3), 137–142.
- (43) Degueldre, C.; Favarger, P.-Y. *Talanta* **2004**, *62* (5), 1051–1054.
- (44) Degueldre, C.; Favarger, P.-Y.; Bitea, C. *Anal. Chim. Acta* **2004**, *518* (1–2), 137–142.
- (45) Degueldre, C.; Favarger, P.-Y.; Wold, S. *Anal. Chim. Acta* **2006**, *555* (2), 263–268.
- (46) Xiu, Z.-M.; Ma, J.; Alvarez, P. J. J. *Environ. Sci. Technol.* **2011**, *45* (20), 9003–9008.
- (47) Xiu, Z.; Zhang, Q.; Puppala, H. L.; Colvin, V. L.; Alvarez, P. J. *Nano Lett.* **2012**.
- (48) Xia, T.; Kovichich, M.; Liong, M.; Mädler, L.; Gilbert, B.; Shi, H.; Yeh, J. I.; Zink, J. I.; Nel, A. E. *ACS Nano* **2008**, *2* (10), 2121–2134.
- (49) Pace, H. E.; Rogers, N. J.; Jarolimek, C.; Coleman, V. A.; Gray, E. P.; Higgins, C. P.; Ranville, J. F. *Environ. Sci. Technol.* **2012**, *46* (22), 12272–12280.
- (50) Peters, R.; Herrera-Rivera, Z.; Undas, A.; Lee, M. van der; Marvin, H.; Bouwmeester, H.; Weigel, S. *J. Anal. At. Spectrom.* **2015**.
- (51) Tuoriniemi, J.; Cornelis, G.; Hassellöv, M. *Anal. Chem.* **2012**, *84* (9), 3965–3972.
- (52) Liu, J.; Murphy, K. E.; MacCusprie, R. I.; Winchester, M. R. *Anal. Chem.* **2014**, *86* (7), 3405–3414.

- (53) Laborda, F.; Jiménez-Lamana, J.; Bolea, E.; Castillo, J. R. *J. Anal. At. Spectrom.* **2011**, *26* (7), 1362–1371.
- (54) Pace, H. E.; Rogers, N. J.; Jarolimek, C.; Coleman, V. A.; Higgins, C. P.; Ranville, J. F. *Anal. Chem.* **2011**, *83* (24), 9361–9369.
- (55) DeLoid, G.; Cohen, J. M.; Darrach, T.; Derk, R.; Rojanasakul, L.; Pyrgiotakis, G.; Wohlleben, W.; Demokritou, P. *Nat. Commun.* **2014**, *5*.
- (56) Cohen, J. M.; Teeguarden, J. G.; Demokritou, P. *Part. Fibre Toxicol.* **2014**, *11* (1), 20.
- (57) Hinderliter, P. M.; Minard, K. R.; Orr, G.; Chrisler, W. B.; Thrall, B. D.; Pounds, J. G.; Teeguarden, J. G. *Part. Fibre Toxicol.* **2010**, *7* (1), 36.
- (58) Harris, A. R.; Zhang, J.; Cattrall, R. W.; Bond, A. M. *Anal. Methods* **2013**, *5* (16), 3840–3852.
- (59) Buhlmann, P.; Chen, L. D. Wiley, 2012; pp 2539–2579.
- (60) Lai, C.-Z.; Fierke, M. A.; Corrêa da Costa, R.; Gladysz, J. A.; Stein, A.; Bühlmann, P. *Anal. Chem.* **2010**, *82* (18), 7634–7640.
- (61) Boswell, P. G.; Bühlmann, P. *J. Am. Chem. Soc.* **2005**, *127* (25), 8958–8959.
- (62) Boswell, P. G.; Lugert, E. C.; Rábai, J.; Amin, E. A.; Bühlmann, P. *J. Am. Chem. Soc.* **2005**, *127* (48), 16976–16984.
- (63) Boswell, P. G.; Szijjártó, C.; Jurisch, M.; Gladysz, J. A.; Rábai, J.; Bühlmann, P. *Anal. Chem.* **2008**, *80* (6), 2084–2090.
- (64) Navarro, E.; Piccapietra, F.; Wagner, B.; Marconi, F.; Kaegi, R.; Odzak, N.; Sigg, L.; Behra, R. *Environ. Sci. Technol.* **2008**, *42* (23), 8959–8964.
- (65) Fabricius, A.-L.; Duester, L.; Meermann, B.; Ternes, T. A. *Anal. Bioanal. Chem.* **2013**, *406* (2), 467–479.
- (66) Farkas, J.; Peter, H.; Christian, P.; Gallego Urrea, J. A.; Hassellöv, M.; Tuoriniemi, J.; Gustafsson, S.; Olsson, E.; Hylland, K.; Thomas, K. V. *Environ. Int.* **2011**, *37* (6), 1057–1062.
- (67) Käkinen, A.; Bondarenko, O.; Ivask, A.; Kahru, A. *Sensors* **2011**, *11* (11), 10502–10521.
- (68) Maurer-Jones, M. A.; Mousavi, M. P. S.; Chen, L. D.; Bühlmann, P.; Haynes, C. L. *Chem. Sci.* **2013**, *4* (6), 2564–2572.
- (69) Koch, M.; Kiefer, S.; Cavellius, C.; Kraegeloh, A. *J. Nanoparticle Res.* **2012**, *14* (2), 1–11.
- (70) Lynch, I.; Dawson, K. A.; Linse, S. *Sci. STKE Signal Transduct. Knowl. Environ.* **2006**, *2006* (327), pe14.
- (71) Monopoli, M. P.; Åberg, C.; Salvati, A.; Dawson, K. A. *Nat. Nanotechnol.* **2012**, *7* (12), 779–786.
- (72) Hellstrand, E.; Lynch, I.; Andersson, A.; Drakenberg, T.; Dahlbäck, B.; Dawson, K. A.; Linse, S.; Cedervall, T. *FEBS J.* **2009**, *276* (12), 3372–3381.
- (73) Ghosh, S.; Mashayekhi, H.; Bhowmik, P.; Xing, B. *Langmuir* **2010**, *26* (2), 873–879.
- (74) Huynh, K. A.; Chen, K. L. *Environ. Sci. Technol.* **2011**, *45* (13), 5564–5571.
- (75) Walkey, C. D.; Chan, W. C. W. *Chem. Soc. Rev.* **2012**, *41* (7), 2780–2799.
- (76) Maiorano, G.; Sabella, S.; Sorce, B.; Brunetti, V.; Malvindi, M. A.; Cingolani, R.; Pompa, P. *ACS Nano* **2010**, *4* (12), 7481–7491.
- (77) Wan, S.; Kelly, P. M.; Mahon, E.; Stöckmann, H.; Rudd, P. M.; Caruso, F.; Dawson, K. A.; Yan, Y.; Monopoli, M. P. *ACS Nano* **2015**, *9* (2), 2157–2166.
- (78) Khang, D.; Lee, Y. K.; Choi, E.-J.; Webster, T. J.; Kim, S.-H. *Int. J. Nanomedicine* **2014**, *97*.
- (79) Wirth, S. M.; Lowry, G. V.; Tilton, R. D. *Environ. Sci. Technol.* **2012**, *46* (22), 12687–12696.

- (80) Yang, X.; Jiang, C.; Hsu-Kim, H.; Badireddy, A. R.; Dykstra, M.; Wiesner, M.; Hinton, D. E.; Meyer, J. N. *Environ. Sci. Technol.* **2014**, *48* (6), 3486–3495.
- (81) Gunsolus, I. L.; Mousavi, M. P. S.; Hussein, K.; Bühlmann, P.; Haynes, C. L. *Environ. Sci. Technol.* **2015**, *49* (13), 8078–8086.
- (82) Torelli, M. D.; Putans, R. A.; Tan, Y.; Lohse, S. E.; Murphy, C. J.; Hamers, R. J. *ACS Appl. Mater. Interfaces* **2015**, *7* (3), 1720–1725.
- (83) Mudunkotuwa, I. A.; Minshid, A. A.; Grassian, V. H. *Analyst* **2014**, *139* (5), 870–881.
- (84) Roncaroli, F.; Blesa, M. A. *Phys. Chem. Chem. Phys.* **2010**, *12* (33), 9938–9944.
- (85) Young, A. G.; McQuillan, A. J. *Langmuir* **2009**, *25* (6), 3538–3548.
- (86) Gulley-Stahl, H.; Hogan, P. A.; Schmidt, W. L.; Wall, S. J.; Buhrlage, A.; Bullen, H. A. *Environ. Sci. Technol.* **2010**, *44* (11), 4116–4121.
- (87) Jedlovsky-Hajdú, A.; Bombelli, F. B.; Monopoli, M. P.; Tombácz, E.; Dawson, K. A. *Langmuir* **2012**, *28* (42), 14983–14991.
- (88) Treuel, L.; Malissek, M.; Grass, S.; Diendorf, J.; Mahl, D.; Meyer-Zaika, W.; Epple, M. *J. Nanoparticle Res.* **2012**, *14* (9), 1–12.
- (89) Weissig, V., Elbayoumi, T., Olsen, M., Eds.; *Methods in Molecular Biology*; Humana Press, 2013.
- (90) Li, R.; Chen, R.; Chen, P.; Wen, Y.; Ke, P. C.; Cho, S. S. *J. Phys. Chem. B* **2013**, *117* (43), 13451–13456.
- (91) Gagner, J. E.; Lopez, M. D.; Dordick, J. S.; Siegel, R. W. *Biomaterials* **2011**, *32* (29), 7241–7252.
- (92) Scaletti, F.; Feis, A.; Centi, S.; Pini, R.; Rotello, V. M.; Messori, L. *J. Inorg. Biochem.*
- (93) Wang, J.; Jensen, U. B.; Jensen, G. V.; Shipovskov, S.; Balakrishnan, V. S.; Otzen, D.; Pedersen, J. S.; Besenbacher, F.; Sutherland, D. S. *Nano Lett.* **2011**, *11* (11), 4985–4991.
- (94) Abraham, A.; Mihaliuk, E.; Kumar, B.; Legleiter, J.; Gullion, T. *J. Phys. Chem. C* **2010**, *114* (42), 18109–18114.
- (95) Abraham, A.; Ilott, A. J.; Miller, J.; Gullion, T. *J. Phys. Chem. B* **2012**, *116* (27), 7771–7775.
- (96) Giri, J.; Diallo, M. S.; Simpson, A. J.; Liu, Y.; Goddard, W. A.; Kumar, R.; Woods, G. C. *ACS Nano* **2011**, *5* (5), 3456–3468.
- (97) Mayer, M.; Meyer, B. *Angew. Chem. Int. Ed.* **1999**, *38* (12), 1784–1788.
- (98) Sisco, P. N.; Wilson, C. G.; Chernak, D.; Clark, J. C.; Grzincic, E. M.; Ako-Asare, K.; Goldsmith, E. C.; Murphy, C. J. *PLoS ONE* **2014**, *9* (2), e86670.
- (99) Monopoli, M. P.; Walczyk, D.; Campbell, A.; Elia, G.; Lynch, I.; Baldelli Bombelli, F.; Dawson, K. A. *J. Am. Chem. Soc.* **2011**, *133* (8), 2525–2534.
- (100) Cedervall, T.; Lynch, I.; Lindman, S.; Berggård, T.; Thulin, E.; Nilsson, H.; Dawson, K. A.; Linse, S. *Proc. Natl. Acad. Sci.* **2007**, *104* (7), 2050–2055.
- (101) Cedervall, T.; Lynch, I.; Foy, M.; Berggård, T.; Donnelly, S. C.; Cagney, G.; Linse, S.; Dawson, K. A. *Angew. Chem. Int. Ed.* **2007**, *46* (30), 5754–5756.
- (102) Albanese, A.; Walkey, C. D.; Olsen, J. B.; Guo, H.; Emili, A.; Chan, W. C. W. *ACS Nano* **2014**, *8* (6), 5515–5526.
- (103) Tenzer, S.; Docter, D.; Kuharev, J.; Musyanovych, A.; Fetz, V.; Hecht, R.; Schlenk, F.; Fischer, D.; Kiouptsi, K.; Reinhardt, C.; Landfester, K.; Schild, H.; Maskos, M.; Knauer, S. K.; Stauber, R. H. *Nat. Nanotechnol.* **2013**, *8* (10), 772–781.
- (104) Walczyk, D.; Bombelli, F. B.; Monopoli, M. P.; Lynch, I.; Dawson, K. A. *J. Am. Chem. Soc.* **2010**, *132* (16), 5761–5768.

- (105) Yan, B.; Jeong, Y.; Mercante, L. A.; Tonga, G. Y.; Kim, C.; Zhu, Z.-J.; Vachet, R. W.; Rotello, V. M. *Nanoscale* **2013**, *5* (11), 5063–5066.
- (106) Szakal, C.; McCarthy, J. A.; Ugelow, M. S.; Konicek, A. R.; Louis, K.; Yezer, B.; Herzing, A. A.; Hamers, R. J.; Holbrook, R. D. *J. Environ. Monit.* **2012**, *14* (7), 1914–1925.
- (107) Szakal, C.; Ugelow, M. S.; Gorham, J. M.; Konicek, A. R.; Holbrook, R. D. *Anal. Chem.* **2014**, *86* (7), 3517–3524.
- (108) Jensen, G. V.; Shi, Q.; Deen, G. R.; Almdal, K.; Pedersen, J. S. *Macromolecules* **2012**, *45* (1), 430–440.
- (109) Pedersen, J. S.; Gerstenberg, M. C. *Macromolecules* **1996**, *29* (4), 1363–1365.
- (110) Henzler, K.; Haupt, B.; Rosenfeldt, S.; Harnau, L.; Narayanan, T.; Ballauff, M. *Phys. Chem. Chem. Phys.* **2011**, *13* (39), 17599–17605.
- (111) Kelly, P. M.; Åberg, C.; Polo, E.; O’Connell, A.; Cookman, J.; Fallon, J.; Krpetić, Ž.; Dawson, K. A. *Nat. Nanotechnol.* **2015**, advance online publication.
- (112) Ge, C.; Du, J.; Zhao, L.; Wang, L.; Liu, Y.; Li, D.; Yang, Y.; Zhou, R.; Zhao, Y.; Chai, Z.; Chen, C. *Proc. Natl. Acad. Sci.* **2011**, *108* (41), 16968–16973.
- (113) Maiti, S.; Haupts, U.; Webb, W. W. *Proc. Natl. Acad. Sci.* **1997**, *94* (22), 11753–11757.
- (114) Milani, S.; Baldelli Bombelli, F.; Pitek, A. S.; Dawson, K. A.; Rädler, J. *ACS Nano* **2012**, *6* (3), 2532–2541.
- (115) Rusu, L.; Gambhir, A.; McLaughlin, S.; Rädler, J. *Biophys. J.* **2004**, *87* (2), 1044–1053.
- (116) Treuel, L.; Brandholt, S.; Maffre, P.; Wiegele, S.; Shang, L.; Nienhaus, G. U. *ACS Nano* **2014**, *8* (1), 503–513.
- (117) Gebauer, J. S.; Malissek, M.; Simon, S.; Knauer, S. K.; Maskos, M.; Stauber, R. H.; Peukert, W.; Treuel, L. *Langmuir* **2012**, *28* (25), 9673–9679.
- (118) Treuel, L.; Malissek, M.; Gebauer, J. S.; Zellner, R. *ChemPhysChem* **2010**, *11* (14), 3093–3099.
- (119) Zeng, Z.; Patel, J.; Lee, S.-H.; McCallum, M.; Tyagi, A.; Yan, M.; Shea, K. J. *J. Am. Chem. Soc.* **2012**, *134* (5), 2681–2690.
- (120) Loosli, F.; Vitorazi, L.; Berret, J.-F.; Stoll, S. *Environ. Sci. Nano* **2015**, *2* (5), 541–550.
- (121) Helfrich, A.; Brüchert, W.; Bettmer, J. *J. Anal. At. Spectrom.* **2006**, *21* (4), 431–434.
- (122) Krueger, K. M.; Al-Somali, A. M.; Falkner, J. C.; Colvin, V. L. *Anal. Chem.* **2005**, *77* (11), 3511–3515.
- (123) Zhou, X.-X.; Liu, R.; Liu, J.-F. *Environ. Sci. Technol.* **2014**, *48* (24), 14516–14524.
- (124) Proulx, K.; Wilkinson, K. J. *Environ. Chem.* **2014**, *11* (4), 392–401.
- (125) Gray, E. P.; Bruton, T. A.; Higgins, C. P.; Halden, R. U.; Westerhoff, P.; Ranville, J. F. *J. Anal. At. Spectrom.* **2012**, *27* (9), 1532–1539.
- (126) Mitrano, D. M.; Barber, A.; Bednar, A.; Westerhoff, P.; Higgins, C. P.; Ranville, J. F. *J. Anal. At. Spectrom.* **2012**, *27* (7), 1131–1142.
- (127) Giddings, J. C. *Science* **1993**, *260* (5113), 1456–1465.
- (128) Ashby, J.; Schachermeyer, S.; Pan, S.; Zhong, W. *Anal. Chem.* **2013**, *85* (15), 7494–7501.
- (129) Koopmans, G. F.; Hiemstra, T.; Regelink, I. C.; Molleman, B.; Comans, R. N. J. *J. Chromatogr. A.*
- (130) Mitrano, D.; Ranville, J.; Neubauer, K.; Thomas, R. *Spectroscopy* **2012**, *27* (9), 36–44.
- (131) Leshner, E. K.; Poda, A. R.; Bednar, A. J.; Ranville, J. F. In *Field Flow Fractionation in Biopolymer Analysis*; Springer-Verlag; pp 277–299.
- (132) Johann, C.; Eisenberg, S.; Schuch, H.; Rösch, U. *Anal. Chem.* **2015**.

- (133) de Yanes, G. S.; Elsaesser, A.; Howard, C. V.; Kim, E.-M.; McKerr, G.; O’Hare, E.; Taylor, A. *Nanomed.* **2010**, *5* (9), 1447+.
- (134) McDonald, K. I. *J. Microsc.* **2009**, *235* (3), 273–281.
- (135) Omajali, J. B.; Mikheenko, I. P.; Merroun, M. L.; Wood, J.; Macaskie, L. E. *J. Nanoparticle Res.* **2015**, *17* (6), 1–17.
- (136) Klein, N. D.; Hurley, K. R.; Feng, Z. V.; Haynes, C. L. *Anal. Chem.* **2015**, *87* (8), 4356–4362.
- (137) Plascencia-Villa, G.; Starr, C. R.; Armstrong, L. S.; Ponce, A.; José-Yacamán, M. *Integr. Biol.* **2012**, *4* (11), 1358–1366.
- (138) Mu, Q.; Hondow, N. S.; Krzemiński, Ł.; Brown, A. P.; Jeuken, L. J.; Routledge, M. N. *Part. Fibre Toxicol.* **2012**, *9* (1), 29.
- (139) Hernandez-Viezcas, J. A.; Castillo-Michel, H.; Andrews, J. C.; Cotte, M.; Rico, C.; Peralta-Videa, J. R.; Ge, Y.; Priester, J. H.; Holden, P. A.; Gardea-Torresdey, J. L. *ACS Nano* **2013**, *7* (2), 1415–1423.
- (140) Gilbert, B.; Fakra, S. C.; Xia, T.; Pokhrel, S.; Mädler, L.; Nel, A. E. *ACS Nano* **2012**, *6* (6), 4921–4930.
- (141) Szymanski, C. J.; Munusamy, P.; Mihai, C.; Xie, Y.; Hu, D.; Gilles, M. K.; Tyliszczak, T.; Thevuthasan, S.; Baer, D. R.; Orr, G. *Biomaterials* **2015**, *62*, 147–154.
- (142) James, S. A.; Feltis, B. N.; de Jonge, M. D.; Sridhar, M.; Kimpton, J. A.; Altissimo, M.; Mayo, S.; Zheng, C.; Hastings, A.; Howard, D. L.; Paterson, D. J.; Wright, P. F. A.; Moorhead, G. F.; Turney, T. W.; Fu, J. *ACS Nano* **2013**, *7* (12), 10621–10635.
- (143) Drescher, D.; Zeise, I.; Traub, H.; Guttman, P.; Seifert, S.; Büchner, T.; Jakubowski, N.; Schneider, G.; Kneipp, J. *Adv. Funct. Mater.* **2014**, *24* (24), 3765–3775.
- (144) Schneider, G.; Guttman, P.; Heim, S.; Rehbein, S.; Mueller, F.; Nagashima, K.; Heymann, J. B.; Müller, W. G.; McNally, J. G. *Nat. Methods* **2010**, *7* (12), 985–987.
- (145) Drescher, D.; Guttman, P.; Büchner, T.; Werner, S.; Laube, G.; Hornemann, A.; Tarek, B.; Schneider, G.; Kneipp, J. *Nanoscale* **2013**, *5* (19), 9193–9198.
- (146) Troiano, J. M.; Olenick, L. L.; Kuech, T. R.; Melby, E. S.; Hu, D.; Lohse, S. E.; Mensch, A. C.; Dogangun, M.; Vartanian, A. M.; Torelli, M. D.; Ehimighe, E.; Walter, S. R.; Fu, L.; Anderton, C. R.; Zhu, Z.; Wang, H.; Orr, G.; Murphy, C. J.; Hamers, R. J.; Pedersen, J. A.; Geiger, F. M. *J. Phys. Chem. C* **2015**, *119* (1), 534–546.
- (147) Bhattacharya, R.; Kanchi, S.; C, R.; Lakshminarayanan, A.; Seeck, O. H.; Maiti, P. K.; Ayappa, K. G.; Jayaraman, N.; Basu, J. K. *Soft Matter* **2014**, *10* (38), 7577–7587.
- (148) Spurlin, T. A.; Gewirth, A. A. *Nano Lett.* **2007**, *7* (2), 531–535.
- (149) Leroueil, P. R.; Berry, S. A.; Duthie, K.; Han, G.; Rotello, V. M.; McNerny, D. Q.; Baker, James R.; Orr, B. G.; Banaszak Holl, M. M. *Nano Lett.* **2008**, *8* (2), 420–424.
- (150) Van Lehn, R. C.; Ricci, M.; Silva, P. H. J.; Andreozzi, P.; Reguera, J.; Voitchovsky, K.; Stellacci, F.; Alexander-Katz, A. *Nat. Commun.* **2014**, *5*.
- (151) Dorobantu, L. S.; Fallone, C.; Noble, A. J.; Veinot, J.; Ma, G.; Goss, G. G.; Burrell, R. E. *J. Nanoparticle Res.* **2015**, *17* (4).
- (152) Hwang, E. T.; Lee, J. H.; Chae, Y. J.; Kim, Y. S.; Kim, B. C.; Sang, B.-I.; Gu, M. B. *Small* **2008**, *4* (6), 746–750.
- (153) Jung, W. K.; Koo, H. C.; Kim, K. W.; Shin, S.; Kim, S. H.; Park, Y. H. *Appl. Environ. Microbiol.* **2008**, *74* (7), 2171–2178.
- (154) Liu, S.; Ng, A. K.; Xu, R.; Wei, J.; Tan, C. M.; Yang, Y.; Chen, Y. *Nanoscale* **2010**, *2* (12), 2744–2750.

- (155) Liu, S.; Wei, L.; Hao, L.; Fang, N.; Chang, M. W.; Xu, R.; Yang, Y.; Chen, Y. *ACS Nano* **2009**, *3* (12), 3891–3902.
- (156) Romero-Vargas Castrillón, S.; Perreault, F.; de Faria, A. F.; Elimelech, M. *Environ. Sci. Technol. Lett.* **2015**, *2* (4), 112–117.
- (157) Gurunathan, S.; Han, J. W.; Dayem, A. A.; Eppakayala, V.; Kim, J.-H. *Int. J. Nanomedicine* **2012**, *7*, 5901–5914.
- (158) Mangadlao, J. D.; Santos, C. M.; Felipe, M. J. L.; Leon, A. C. C. de; Rodrigues, D. F.; Advincula, R. C. *Chem. Commun.* **2015**, *51* (14), 2886–2889.
- (159) Pratsinis, A.; Hervella, P.; Leroux, J.-C.; Pratsinis, S. E.; Sotiriou, G. A. *Small* **2013**, *9* (15), 2576–2584.
- (160) Smith, B. R.; Ghosn, E. E. B.; Rallapalli, H.; Prescher, J. A.; Larson, T.; Herzenberg, L. A.; Gambhir, S. S. *Nat. Nanotechnol.* **2014**, *9* (6), 481–487.
- (161) Schwab, F.; Bucheli, T. D.; Camenzuli, L.; Magrez, A.; Knauer, K.; Sigg, L.; Nowack, B. *Environ. Sci. Technol.* **2013**, *47* (13), 7012–7019.
- (162) Mortimer, M.; Gogos, A.; Bartolomé, N.; Kahru, A.; Bucheli, T. D.; Slaveykova, V. I. *Environ. Sci. Technol.* **2014**, *48* (15), 8760–8767.
- (163) Yang, X.; Liu, Y.; Wang, J.; Zhang, S.; Xie, H.; Chen, X.; Xi, P. 2013; Vol. 8845, p 88450C–88450C–5.
- (164) Leménager, G.; Luca, E. D.; Sun, Y.-P.; Pompa, P. P. *Nanoscale* **2014**, *6* (15), 8617–8623.
- (165) Gunsolus, I. L.; Hu, D.; Mihai, C.; Lohse, S. E.; Lee, C.; Torelli, M. D.; Hamers, R. J.; Murphay, C. J.; Orr, G.; Haynes, C. L. *Analyst* **2014**, *139* (12), 3174–3178.
- (166) Melby, E. S.; Mensch, A. C.; Lohse, S. E.; Hu, D.; Orr, G.; Murphy, C.; Hamers, R.; Pedersen, J. A. *Environ. Sci. Nano* **2015**.
- (167) Shen, Y. R. *J. Phys. Chem. C* **2012**, *116* (29), 15505–15509.
- (168) Candeloro, P.; Tirinato, L.; Malara, N.; Fregola, A.; Casals, E.; Puntès, V.; Perozziello, G.; Gentile, F.; Coluccio, M. L.; Das, G.; Liberale, C.; Angelis, F. D.; Fabrizio, E. D. *Analyst* **2011**, *136* (21), 4402–4408.
- (169) Shah, N. B.; Dong, J.; Bischof, J. C. *Mol. Pharm.* **2011**, *8* (1), 176–184.
- (170) Lamprecht, C.; Gierlinger, N.; Heister, E.; Unterauer, B.; Plochberger, B.; Brameshuber, M.; Hinterdorfer, P.; Hild, S.; A Ebner. *J. Phys. Condens. Matter* **2012**, *24* (16), 164206.
- (171) Rust, M. J.; Bates, M.; Zhuang, X. *Nat. Methods* **2006**, *3* (10), 793–795.
- (172) Ayas, S.; Cinar, G.; Ozkan, A. D.; Soran, Z.; Ekiz, O.; Kocaay, D.; Tomak, A.; Toren, P.; Kaya, Y.; Tunc, I.; Zareie, H.; Tekinay, T.; Tekinay, A. B.; Guler, M. O.; Dana, A. *Sci. Rep.* **2013**, *3*.
- (173) Li, J.; Strong, R.; Trevisan, J.; Fogarty, S. W.; Fullwood, N. J.; Jones, K. C.; Martin, F. L. *Environ. Sci. Technol.* **2013**, *47* (17), 10005–10011.
- (174) Li, J.; Ying, G.-G.; Jones, K. C.; Martin, F. L. *Analyst* **2015**.
- (175) Sancey, L.; Kotb, S.; Truillet, C.; Appaix, F.; Marais, A.; Thomas, E.; van der Sanden, B.; Klein, J.-P.; Laurent, B.; Cottier, M.; Antoine, R.; Dugourd, P.; Panczer, G.; Lux, F.; Perriat, P.; Motto-Ros, V.; Tillement, O. *ACS Nano* **2015**, *9* (3), 2477–2488.
- (176) Carlson, C.; Hussain, S. M.; Schrand, A. M.; K. Braydich-Stolle, L.; Hess, K. L.; Jones, R. L.; Schlager, J. J. *J. Phys. Chem. B* **2008**, *112* (43), 13608–13619.
- (177) AshaRani, P. V.; Low Kah Mun, G.; Hande, M. P.; Valiyaveetil, S. *ACS Nano* **2009**, *3* (2), 279–290.
- (178) Shi, M.; Kwon, H. S.; Peng, Z.; Elder, A.; Yang, H. *ACS Nano* **2012**, *6* (3), 2157–2164.

- (179) Ahmad, J.; Alhadlaq, H. A.; Siddiqui, M. A.; Saquib, Q.; Al-Khedhairi, A. A.; Musarrat, J.; Ahamed, M. *Environ. Toxicol.* **2015**, *30* (2), 137–148.
- (180) Kohno, M. *J. Clin. Biochem. Nutr.* **2010**, *47* (1), 1–11.
- (181) Saito, K.; Takahashi, M.; Kamibayashi, M.; Ozawa, T.; Kohno, M. *Free Radic. Res.* **2009**, *43* (7), 668–676.
- (182) Weiwei He; Yitong Liu; Wamer, W. G.; Jun-Jie Yin. *J. Food Drug Anal.* **2014**, *22* (1), 49–63.
- (183) Perelshtein, I.; Lipovsky, A.; Perkas, N.; Gedanken, A.; Moschini, E.; Mantecca, P. *Nano Res.* **2014**, *8* (2), 695–707.
- (184) Ahlberg, S.; Meinke, M. C.; Werner, L.; Epple, M.; Diendorf, J.; Blume-Peytavi, U.; Lademann, J.; Vogt, A.; Rancan, F. *Eur. J. Pharm. Biopharm.* **2014**, *88* (3), 651–657.
- (185) Nelson, B. C.; Petersen, E. J.; Marquis, B. J.; Atha, D. H.; Elliott, J. T.; Cleveland, D.; Watson, S. S.; Tseng, I.-H.; Dillon, A.; Theodore, M.; Jackman, J. *Nanotoxicology* **2011**, *7* (1), 21–29.
- (186) Dunnick, K. M.; Pillai, R.; Pisane, K. L.; Stefaniak, A. B.; Sabolsky, E. M.; Leonard, S. S. *Biol. Trace Elem. Res.* **2015**, 1–12.
- (187) Celardo, I.; De Nicola, M.; Mandoli, C.; Pedersen, J. Z.; Traversa, E.; Ghibelli, L. *ACS Nano* **2011**, *5* (6), 4537–4549.
- (188) Dan, Y.; Zhang, W.; Xue, R.; Ma, X.; Stephan, C.; Shi, H. *Environ. Sci. Technol.* **2015**, *49* (5), 3007–3014.
- (189) US Department of Commerce, N. NIST Manuscript Publication Search http://www.nist.gov/manuscript-publication-search.cfm?pub_id=915946 (accessed Mar 31, 2015).
- (190) Scanlan, L. D.; Reed, R. B.; Loguinov, A. V.; Antczak, P.; Tagmount, A.; Aloni, S.; Nowinski, D. T.; Luong, P.; Tran, C.; Karunaratne, N.; Pham, D.; Lin, X. X.; Falciani, F.; Higgins, C. P.; Ranville, J. F.; Vulpe, C. D.; Gilbert, B. *ACS Nano* **2013**, *7* (12), 10681–10694.
- (191) Chen, S.; Xiong, C.; Liu, H.; Wan, Q.; Hou, J.; He, Q.; Badu-Tawiah, A.; Nie, Z. *Nat. Nanotechnol.* **2015**, *10* (2), 176–182.
- (192) Zhu, Z.-J.; Ghosh, P. S.; Miranda, O. R.; Vachet, R. W.; Rotello, V. M. *J. Am. Chem. Soc.* **2008**, *130* (43), 14139–14143.
- (193) Yan, B.; Kim, S. T.; Kim, C. S.; Saha, K.; Moyano, D. F.; Xing, Y.; Jiang, Y.; Roberts, A. L.; Alfonso, F. S.; Rotello, V. M.; Vachet, R. W. *J. Am. Chem. Soc.* **2013**, *135* (34), 12564–12567.
- (194) Zhu, Z.-J.; Yeh, Y.-C.; Tang, R.; Yan, B.; Tamayo, J.; Vachet, R. W.; Rotello, V. M. *Nat. Chem.* **2011**, *3* (12), 963–968.
- (195) Drescher, D.; Giesen, C.; Traub, H.; Panne, U.; Kneipp, J.; Jakubowski, N. *Anal. Chem.* **2012**, *84* (22), 9684–9688.
- (196) Arlinghaus, H. F.; Kriegeskotte, C.; Fartmann, M.; Wittig, A.; Sauerwein, W.; Lipinsky, D. *Appl. Surf. Sci.* **2006**, *252* (19), 6941–6948.
- (197) Arlinghaus, H. F. *Appl. Surf. Sci.* **2008**, *255* (4), 1058–1063.
- (198) Haase, A.; Arlinghaus, H. F.; Tentschert, J.; Jungnickel, H.; Graf, P.; Manton, A.; Draude, F.; Galla, S.; Plendl, J.; Goetz, M. E.; Masic, A.; Meier, W.; Thünemann, A. F.; Taubert, A.; Luch, A. *ACS Nano* **2011**, *5* (4), 3059–3068.
- (199) Wang, D.; Ye, J.; Hudson, S. D.; Scott, K. C. K.; Lin-Gibson, S. *J. Colloid Interface Sci.* **2014**, *417*, 244–249.
- (200) Zhang, X.; Yang, S. *Langmuir* **2011**, *27* (6), 2528–2535.

- (201) Jacobson, K. H.; Gunsolus, I. L.; Kuech, T. R.; Troiano, J. M.; Melby, E. S.; Lohse, S. E.; Hu, D.; Chrisler, W. B.; Murphy, C. J.; Orr, G.; Geiger, F. M.; Haynes, C. L.; Pedersen, J. A. *Environ. Sci. Technol.* **2015**, *49* (17), 10642–10650.
- (202) Wang, G.; Dewilde, A. H.; Zhang, J.; Pal, A.; Vashist, M.; Bello, D.; Marx, K. A.; Braunhut, S. J.; Therrien, J. M. *Part. Fibre Toxicol.* **2011**, *8* (1), 4.
- (203) Özel, R. E.; Liu, X.; Alkasir, R. S. J.; Andreescu, S. *TrAC Trends Anal. Chem.* **2014**, *59*, 112–120.
- (204) Cheran, L.-E.; Cheung, S.; Wang, X.; Thompson, M. *Electrochimica Acta* **2008**, *53* (23), 6690–6697.
- (205) Pliquett, U. *Food Eng. Rev.* **2010**, *2* (2), 74–94.
- (206) Hondroulis, E.; Liu, C.; Li, C.-Z. *Nanotechnology* **2010**, *21* (31), 315103.
- (207) Zhu, X.; Hondroulis, E.; Liu, W.; Li, C. *Small* **2013**, *9* (9–10), 1821–1830.
- (208) Cimpan, M. R.; Mordal, T.; Schölermann, J.; Allouni, Z. E.; Pliquett, U.; Cimpan, E. *J. Phys. Conf. Ser.* **2013**, *429* (1), 12026.
- (209) Chuang, S.-M.; Lee, Y.-H.; Liang, R.-Y.; Roam, G.-D.; Zeng, Z.-M.; Tu, H.-F.; Wang, S.-K.; Chueh, P. J. *Biochim. Biophys. Acta BBA - Gen. Subj.* **2013**, *1830* (10), 4960–4973.
- (210) Giaever, I.; Keese, C. R. *Proc. Natl. Acad. Sci.* **1991**, *88* (17), 7896–7900.
- (211) Tarantola, M.; Schneider, D.; Sunnick, E.; Adam, H.; Pierrat, S.; Rosman, C.; Breus, V.; Sönnichsen, C.; Basché, T.; Wegener, J.; Janshoff, A. *ACS Nano* **2009**, *3* (1), 213–222.
- (212) Tarantola, M.; Pietuch, A.; Schneider, D.; Rother, J.; Sunnick, E.; Rosman, C.; Pierrat, S.; Sönnichsen, C.; Wegener, J.; Janshoff, A. *Nanotoxicology* **2010**, *5* (2), 254–268.
- (213) Zhang, S.; Nelson, A.; Beales, P. A. *Langmuir* **2012**, *28* (35), 12831–12837.
- (214) Özel, R. E.; Hayat, A.; Wallace, K. N.; Andreescu, S. *RSC Adv.* **2013**, *3* (35), 15298–15309.
- (215) Özel, R. E.; Alkasir, R. S. J.; Ray, K.; Wallace, K. N.; Andreescu, S. *Small* **2013**, *9* (24), 4250–4261.
- (216) Maurer-Jones, M. A.; Christenson, J. R.; Haynes, C. L. *J. Nanoparticle Res.* **2012**, *14* (12), 1–13.
- (217) Love, S. A.; Liu, Z.; Haynes, C. L. *Analyst* **2012**, *137* (13), 3004–3010.
- (218) Fröhlich, E.; Meindl, C.; Wagner, K.; Leitinger, G.; Roblegg, E. *Toxicol. Appl. Pharmacol.* **2014**, *280* (2), 272–284.
- (219) Tilton, S. C.; Karin, N. J.; Tolic, A.; Xie, Y.; Lai, X.; Hamilton, R. F.; Waters, K. M.; Holian, A.; Witzmann, F. A.; Orr, G. *Nanotoxicology* **2014**, *8* (5), 533–548.
- (220) Sohm, B.; Immel, F.; Bauda, P.; Pagnout, C. *PROTEOMICS* **2015**, *15* (1), 98–113.
- (221) Fisichella, M.; Berenguer, F.; Steinmetz, G.; Auffan, M.; Rose, J.; Prat, O. *BMC Genomics* **2014**, *15* (1).
- (222) Li, X.; He, Q.; Shi, J. *ACS Nano* **2014**, *8* (2), 1309–1320.
- (223) McQuillan, J. S.; Shaw, A. M. *Nanotoxicology* **2014**, *8* (S1), 177–184.
- (224) Huang, Y.; Lü, X.; Ma, J. *J. Biomed. Nanotechnol.* **2014**, *10* (11), 3304–3317.
- (225) Feliu, N.; Kohonen, P.; Ji, J.; Zhang, Y.; Karlsson, H. L.; Palmberg, L.; Nyström, A.; Fadeel, B. *ACS Nano* **2015**, *9* (1), 146–163.
- (226) van Aerle, R.; Lange, A.; Moorhouse, A.; Paszkiewicz, K.; Ball, K.; Johnston, B. D.; de-Bastos, E.; Booth, T.; Tyler, C. R.; Santos, E. M. *Environ. Sci. Technol.* **2013**, *47* (14), 8005–8014.
- (227) Rainville, L.-C.; Carolan, D.; Varela, A. C.; Doyle, H.; Sheehan, D. *Analyst* **2014**, *139* (7), 1678–1686.

- (228) Pan, C.-H.; Liu, W.-T.; Bien, M.-Y.; Lin, I.-C.; Hsiao, T.-C.; Ma, C.-M.; Lai, C.-H.; Chen, M.-C.; Chuang, K.-J.; Chuang, H.-C. *Int. J. Nanomedicine* **2014**, *9*, 3631–3643.
- (229) Ng, C.-T.; Yung, L.-Y. L.; Swa, H. L.-F.; Poh, R. W.-Y.; Gunaratne, J.; Bay, B.-H. *Biomaterials* **2015**, *39*, 31–38.
- (230) Tsai, Y.-Y.; Huang, Y.-H.; Chao, Y.-L.; Hu, K.-Y.; Chin, L.-T.; Chou, S.-H.; Hour, A.-L.; Yao, Y.-D.; Tu, C.-S.; Liang, Y.-J.; Tsai, C.-Y.; Wu, H.-Y.; Tan, S.-W.; Chen, H.-M. *ACS Nano* **2011**, *5* (12), 9354–9369.
- (231) Leung, Y. H.; Ng, A. M. C.; Xu, X.; Shen, Z.; Gethings, L. A.; Wong, M. T.; Chan, C. M. N.; Guo, M. Y.; Ng, Y. H.; Djurišić, A. B.; Lee, P. K. H.; Chan, W. K.; Yu, L. H.; Phillips, D. L.; Ma, A. P. Y.; Leung, F. C. C. *Small* **2014**, *10* (6), 1171–1183.
- (232) Mirzajani, F.; Askari, H.; Hamzelou, S.; Schober, Y.; Römpf, A.; Ghassempour, A.; Spengler, B. *Ecotoxicol. Environ. Saf.* **2014**, *100*, 122–130.
- (233) Hu, W.; Culloty, S.; Darmody, G.; Lynch, S.; Davenport, J.; Ramirez-Garcia, S.; Dawson, K. A.; Lynch, I.; Blasco, J.; Sheehan, D. *Chemosphere* **2014**, *108*, 289–299.
- (234) Rabilloud, T.; Lescuyer, P. *PROTEOMICS* **2015**, *15* (5–6), 1051–1074.
- (235) Abdelhamid, H. N.; Wu, H.-F. *TrAC Trends Anal. Chem.* **2015**, *65*, 30–46.
- (236) Chen, G.; Gharib, T. G.; Huang, C.-C.; Taylor, J. M. G.; Misek, D. E.; Kardia, S. L. R.; Giordano, T. J.; Iannettoni, M. D.; Orringer, M. B.; Hanash, S. M.; Beer, D. G. *Mol. Cell. Proteomics* **2002**, *1* (4), 304–313.
- (237) Ghazalpour, A.; Bennett, B.; Petyuk, V. A.; Orozco, L.; Hagopian, R.; Mungrue, I. N.; Farber, C. R.; Sinsheimer, J.; Kang, H. M.; Furlotte, N.; Park, C. C.; Wen, P.-Z.; Brewer, H.; Weitz, K.; Camp, D. G., II; Pan, C.; Yordanova, R.; Neuhaus, I.; Tilford, C.; Siemers, N.; Gargalovic, P.; Eskin, E.; Kirchgessner, T.; Smith, D. J.; Smith, R. D.; Lusic, A. J. *PLoS Genet* **2011**, *7* (6), e1001393.
- (238) Haider, S.; Pal, R. *Curr. Genomics* **2013**, *14* (2), 91–110.
- (239) Schnackenberg, L. K.; Sun, J.; Begeer, R. D. *Methods Mol. Biol. Clifton NJ* **2012**, *926*, 141–156.
- (240) Whitfield Åslund, M. L.; McShane, H.; Simpson, M. J.; Simpson, A. J.; Whalen, J. K.; Hendershot, W. H.; Sunahara, G. I. *Environ. Sci. Technol.* **2012**, *46* (2), 1111–1118.
- (241) Bu, Q.; Yan, G.; Deng, P.; Peng, F.; Lin, H.; Xu, Y.; Cao, Z.; Zhou, T.; Xue, A.; Wang, Y.; Cen, X.; Zhao, Y.-L. *Nanotechnology* **2010**, *21* (12), 125105.
- (242) Carrola, J.; Bastos, V.; Ferreira de Oliveira, J. M. P.; Oliveira, H.; Santos, C.; Gil, A. M.; Duarte, I. F. *Arch. Biochem. Biophys.*
- (243) Hu, X.; Ouyang, S.; Mu, L.; An, J.; Zhou, Q. *Environ. Sci. Technol.* **2015**, *49* (18), 10825–10833.
- (244) Kaweeteerawat, C.; Ivask, A.; Liu, R.; Zhang, H.; Chang, C. H.; Low-Kam, C.; Fischer, H.; Ji, Z.; Pokhrel, S.; Cohen, Y.; Telesca, D.; Zink, J.; Mädler, L.; Holden, P. A.; Nel, A.; Godwin, H. *Environ. Sci. Technol.* **2015**, *49* (2), 1105–1112.
- (245) Liu, R.; Zhang, H. Y.; Ji, Z. X.; Rallo, R.; Xia, T.; Chang, C. H.; Nel, A.; Cohen, Y. *Nanoscale* **2013**, *5* (12), 5644–5653.
- (246) Puzyn, T.; Leszczynska, D.; Leszczynski, J. *Small* **2009**, *5* (22), 2494–2509.
- (247) Fourches, D.; Pu, D.; Tassa, C.; Weissleder, R.; Shaw, S. Y.; Mumper, R. J.; Tropsha, A. *ACS Nano* **2010**, *4* (10), 5703–5712.
- (248) Puzyn, T.; Rasulev, B.; Gajewicz, A.; Hu, X.; Dasari, T. P.; Michalkova, A.; Hwang, H.-M.; Toropov, A.; Leszczynska, D.; Leszczynski, J. *Nat. Nanotech* **2011**, *6* (3), 175–178.
- (249) Oksel, C.; Ma, C. Y.; Wang, X. Z. *Procedia Eng.* **2015**, *102*, 1500–1510.

- (250) *Archived: The Nanotechnology Consumer Products Inventory*; Archived: The Project on Emerging Nanotechnologies at the Woodrow Wilson International Center for Scholars, 2011.
- (251) Kaegi, R.; Voegelin, A.; Sinnet, B.; Zuleeg, S.; Hagendorfer, H.; Burkhardt, M.; Siegrist, H. *Environ. Sci. Technol.* **2011**, *45* (9), 3902–3908.
- (252) Benn, T. M.; Westerhoff, P. *Environ. Sci. Technol.* **2008**, *42* (11), 4133–4139.
- (253) Li, L.; Hartmann, G.; Do?blinger, M.; Schuster, M. *Environ. Sci. Technol.* **2013**, *47* (13), 7317–7323.
- (254) Marambio-Jones, C.; Hoek, E. M. V. *J. Nanoparticle Res.* **2010**, *12* (5), 1531–1551.
- (255) Mueller, N. C.; Nowack, B. *Environ. Sci. Technol.* **2008**, *42* (12), 4447–4453.
- (256) Rai, M.; Yadav, A.; Gade, A. *Biotechnol. Adv.* **2009**, *27*, 76–83.
- (257) Liu, J.; Hurt, R. H. *Environ. Sci. Technol.* **2010**, *44* (6), 2169–75.
- (258) Yu, S.; Yin, Y.; Chao, J.; Shen, M.; Liu, J. *Environ. Sci. Technol.* **2013**, *48* (1), 403–411.
- (259) Angel, B. M.; Batley, G. E.; Jarolimek, C. V.; Rogers, N. J. *Chemosphere* **2013**, *93* (2), 359–365.
- (260) Chinnapongse, S. L.; MacCusprie, R. I.; Hackley, V. A. *Sci. Total Environ.* **2011**, *409*, 2443–2450.
- (261) Li, X.; Lenhart, J. J.; Walker, H. W. *Langmuir* **2010**, *26* (22), 16690–16698.
- (262) Gondikas, A. P.; Morris, A.; Reinsch, B. C.; Marinakos, S. M.; Lowry, G. V.; Hsu-Kim, H. *Environ. Sci. Technol.* **2012**, *46* (13), 7037–7045.
- (263) Yang, X.; Lin, S.; Wiesner, M. R. *J. Hazard. Mater.* **2014**, *264*, 161–168.
- (264) Liu, J.; Sonshine, D. A.; Shervani, S.; Hurt, R. H. *ACS Nano* **2010**, *4*, 6903–6913.
- (265) Pokhrel, L. R.; Dubey, B.; Scheuerman, P. R. *Environ. Sci. Nano* **2014**, *1*, 45.
- (266) Pokhrel, L. R.; Dubey, B.; Scheuerman, P. R. *Environ. Sci. Technol.* **2013**.
- (267) Zhang, H.; Smith, J. A.; Oyanedel-Craver, V. *Water Res.* **2012**, *46*, 691–699.
- (268) Mousavi, M. P. S.; Gunsolus, I. L.; Pérez De Jesús, C. E.; Lancaster, M.; Hussein, K.; Haynes, C. L.; Bühlmann, P. *Sci. Total Environ.* **2015**, *537*, 453–461.
- (269) Fabrega, J.; Fawcett, S. R.; Renshaw, J. C.; Lead, J. R. *Environ. Sci. Technol.* **2009**, *43* (19), 7285–7290.
- (270) Levard, C.; Reinsch, B. C.; Michel, F. M.; Oumahi, C.; Lowry, G. V.; Brown, G. E. *Environ. Sci. Technol.* **2011**, *45* (12), 5260–5266.
- (271) Kittler, S.; Greulich, C.; Diendorf, J.; Köller, M.; Eppe, M. *Chem Mater* **2010**, *22* (16), 4548–4554.
- (272) Robertson, A. I.; Bunn, S. E.; Boon, P. I.; Walker, K. F. *Mar. Freshw. Res.* **1999**, *50*, 813.
- (273) <http://www.humicsubstances.org/acidity.html>. 2013.
- (274) <http://www.humicsubstances.org/sources.html>. 2013.
- (275) <http://www.humicsubstances.org/elements.html>. 2013.
- (276) Millero, F. J. *Pure Appl. Chem.* **1985**, *57*, 1015–1024.
- (277) Zeman, E. J.; Schatz, G. C. *J Phys Chem* **1987**, *91* (3), 634–643.
- (278) Tejamaya, M.; Römer, I.; Merrifield, R. C.; Lead, J. R. *Environ. Sci. Technol.* **2012**, *46* (13), 7011–7017.
- (279) Li, Y.; Zhang, W.; Niu, J.; Chen, Y. *Environ. Sci. Technol.* **2013**, *47* (18), 10293–10301.
- (280) Badawy, A. M. E.; Luxton, T. P.; Silva, R. G.; Scheckel, K. G.; Suidan, M. T.; Tolaymat, T. M. *Environ. Sci. Technol.* **2010**, *44* (4), 1260–1266.
- (281) Saidi, W. A.; Feng, H.; Fichthorn, K. A. *J. Phys. Chem. C* **2012**, *117* (2), 1163–1171.
- (282) Al-Saidi, W. A.; Feng, H.; Fichthorn, K. A. *Nano Lett.* **2011**, *12* (2), 997–1001.

- (283) Huang, H. H.; Ni, X. P.; Loy, G. L.; Chew, C. H.; Tan, K. L.; Loh, F. C.; Deng, J. F.; Xu, G. Q. *Langmuir* **1996**, *12* (4), 909–912.
- (284) Wang, H.; Qiao, X.; Chen, J.; Wang, X.; Ding, S. *Mater. Chem. Phys.* **2005**, *94*, 449–453.
- (285) Zhang, Z.; Zhao, B.; Hu, L. *J. Solid State Chem.* **1996**, *121*, 105–110.
- (286) Sikora, F. J.; Stevenson, F. J. *Geoderma* **1988**, *42* (3–4), 353–363.
- (287) Deonaraine, A.; Lau, B. L. T.; Aiken, G. R.; Ryan, J. N.; Hsu-Kim, H. *Environ. Sci. Technol.* **2011**, *45* (8), 3217–3223.
- (288) Gordon, O.; Slenters, T. V.; Brunetto, P. S.; Villaruz, A. E.; Sturdevant, D. E.; Otto, M.; Landmann, R.; Fromm, K. M. *Antimicrob. Agents Chemother.* **2010**, *54* (10), 4208–4218.
- (289) Manceau, A.; Nagy, K. L. *Geochim. Cosmochim. Acta* **2012**, *99*, 206–223.
- (290) Vos, J. G.; Forster, R. J.; Keyes, T. E. Wiley, 2003; pp 90–91.
- (291) Thorn, K. A.; Cox, L. G. *Org. Geochem.* **2009**, *40* (4), 484–499.
- (292) Waples, J. S.; Nagy, K. L.; Aiken, G. R.; Ryan, J. N. *Geochim. Cosmochim. Acta* **2005**, *69*, 1575–1588.
- (293) Hyung, H.; Kim, J.-H. *Environ. Sci. Technol.* **2008**, *42* (12), 4416–4421.
- (294) Louie, S. M.; Tilton, R. D.; Lowry, G. V. *Environ. Sci. Technol.* **2013**, *47* (9), 4245–4254.
- (295) Duarte, R. M. B. O.; Barros, A. C.; Duarte, A. C. *J. Chromatogr. A* **2012**, *1249*, 138–146.
- (296) Zhang, W.; Yao, Y.; Sullivan, N.; Chen, Y. *Environ. Sci. Technol.* **2011**, *45* (10), 4422–4428.
- (297) Chen, D.; Qiao, X.; Qiu, X.; Chen, J. *J. Mater. Sci.* **2009**, *44* (4), 1076–1081.
- (298) Grubbs, R. B. *Polym. Rev.* **2007**, *47* (2), 197–215.
- (299) Ivask, A.; ElBadawy, A.; Kaweeteerawat, C.; Boren, D.; Fischer, H.; Ji, Z.; Chang, C. H.; Liu, R.; Tolaymat, T.; Telesca, D.; Zink, J. I.; Cohen, Y.; Holden, P. A.; Godwin, H. A. *ACS Nano* **2013**, *8* (1), 374–386.
- (300) Sonodi, I.; Salopek-Sonodi, B. *J. Colloid Interface Sci.* **2004**, *275* (1), 177–182.
- (301) Schneider, C. A.; Rasband, W. S.; Eliceiri, K. W. *Nat. Methods* **2012**, *9* (7), 671–675.
- (302) Ratte, H. T. *Environ. Toxicol. Chem.* **1999**, *18* (1), 89–108.
- (303) Hogstrand, C.; Galvez, F.; Wood, C. M. *Environ. Toxicol. Chem.* **1996**, *15* (7), 1102–1108.
- (304) Janes, N.; Playle, R. C. *Environ. Toxicol. Chem.* **1995**, *14* (11), 1847–1858.
- (305) Leblanc, G. A.; Mastone, J. D.; Paradise, A. P.; Wilson, B. F.; Jr, H. B. L.; Robillard, K. A. *Environ. Toxicol. Chem.* **1984**, *3* (1), 37–46.
- (306) Rose-Janes, N. G.; Playle, R. C. *Aquat. Toxicol.* **2000**, *51* (1), 1–18.
- (307) Di Toro, D. M.; Allen, H. E.; Bergman, H. L.; Meyer, J. S.; Paquin, P. R.; Santore, R. C. *Environ. Toxicol. Chem. SETAC* **2001**, *20* (10), 2383–2396.
- (308) Hayes, M. *Nature*. June 30, 1983, pp 835–836.
- (309) Hering, J. G.; Morel, F. M. M. *Environ. Sci. Technol.* **1988**, *22* (10), 1234–1237.
- (310) Ma, H.; Kim, S. D.; Cha, D. K.; Allen, H. E. *Environ. Toxicol. Chem.* **1999**, *18* (5), 828–837.
- (311) Glover, C. N.; Wood, C. M. *Aquat. Toxicol.* **2005**, *73* (4), 406–417.
- (312) Pagenkopf, G. K. *Environ. Sci. Technol.* **1983**, *17* (6), 342–347.
- (313) Benoit, R.; Wilkinson, K. J.; Sauv e, S. *Chem. Cent. J.* **2013**, *7* (1), 75.
- (314) Bone, A. J.; Colman, B. P.; Gondikas, A. P.; Newton, K. M.; Harrold, K. H.; Cory, R. M.; Urline, J. M.; Klaine, S. J.; Matson, C. W.; Di Giulio, R. T. *Environ. Sci. Technol.* **2012**, *46* (13), 6925–6933.
- (315) Gatselou, V. A.; Giokas, D. L.; Vlessidis, A. G. *Anal. Chim. Acta* **2014**, *812*, 121–128.
- (316) Urline, J. M.; Colman, B. P.; Bone, A. J.; Gondikas, A. P.; Matson, C. W. *Environ. Sci. Technol.* **2012**, *46* (13), 6915–6924.

- (317) Maurer-Jones, M. A.; Gunsolus, I. L.; Murphy, C. J.; Haynes, C. L. *Anal. Chem.* **2013**, *85* (6), 3036–3049.
- (318) Seitz, M. G.; Livermore, D.; Boggs, S. J. **1985**.
- (319) International, H. S. S. **2013**.
- (320) Cumberland, S. A.; Lead, J. R. *J. Chromatogr. A* **2009**, *1216* (52), 9099–9105.
- (321) Chen, Z.; Campbell, P. G. C.; Fortin, C. *J. Phys. Chem. A* **2012**, *116* (25), 6532–6539.
- (322) Chen, Z.; Porcher, C.; Campbell, P. G. C.; Fortin, C. *Environ. Sci. Technol.* **2013**, *130724121438003*.
- (323) Hou, W.-C.; Stuart, B.; Howes, R.; Zepp, R. G. *Environ. Sci. Technol.* **2013**, *47* (14), 7713–7721.
- (324) Maurer, F.; Christl, I.; Hoffmann, M.; Kretzschmar, R. *Environ. Sci. Technol.* **2012**, *46* (16), 8808–8816.
- (325) Brauner, C. J.; Wood, C. M. *Comp. Biochem. Physiol. Part C Toxicol. Pharmacol.* **2002**, *133* (1–2), 161–173.
- (326) Gao, J.; Powers, K.; Wang, Y.; Zhou, H.; Roberts, S. M.; Moudgil, B. M.; Koopman, B.; Barber, D. S. *Chemosphere* **2012**, *89* (1), 96–101.
- (327) Glover, C. N.; Playle, R. C.; Wood, C. M. *Environ. Toxicol. Chem. SETAC* **2005**, *24* (11), 2934–2940.
- (328) Kim, J. Y.; Kim, K.-T.; Lee, B. G.; Lim, B. J.; Kim, S. D. *Ecotoxicol. Environ. Saf.* **2013**, *92*, 57–63.
- (329) VanGenderen, E. J.; Ryan, A. C.; Tomasso, J. R.; Klaine, S. J. *Environ. Toxicol. Chem. SETAC* **2003**, *22* (11), 2746–2751.
- (330) Peretyazhko, T. S.; Zhang, Q.; Colvin, V. L. *Environ. Sci. Technol.* **2014**, *48* (20), 11954–11961.
- (331) Bühlmann, P.; Pretsch, E.; Bakker, E. *Chem. Rev.* **1998**, *98* (4), 1593–1688.
- (332) Chang, Q.; Park, S. B.; Kliza, D.; Cha, G. S.; Yim, H.; Meyerhoff, M. E. *Am. Biotechnol. Lab.* **1990**, *8* (15), 10, 12–16, 18–21.
- (333) Külpmann, W. R. *J. Clin. Chem. Clin. Biochem. Z. Für Klin. Chem. Klin. Biochem.* **1989**, *27* (10), 815–824.
- (334) Park, S. B.; Matuszewski, W.; Meyerhoff, M. E.; Liu, Y. H.; Kadish, K. M. *Electroanalysis* **1991**, *3* (9), 909–916.
- (335) Frost, M. C.; Meyerhoff, M. E. *Curr. Opin. Chem. Biol.* **2002**, *6* (5), 633–641.
- (336) Ward, W. K.; Casey, H. M.; Quinn, M. J.; Federiuk, I. F.; Wood, M. D. *Diabetes Technol. Ther.* **2003**, *5* (6), 943–952.
- (337) Lindner, E.; Tóth, K.; Pungor, E. *Bunseki Kagaku* **1981**, *30* (11), S67–S92.
- (338) Yajima, S.; Tohda, K.; Bühlmann, P.; Umezawa, Y. *Anal. Chem.* **1997**, *69* (10), 1919–1924.
- (339) Choi, C.; Cui, Y. *Bioresour. Technol.* **2012**, *107*, 522–525.
- (340) Kostigen Mumper, C.; Ostermeyer, A.-K.; Semprini, L.; Radniecki, T. S. *Chemosphere* **2013**, *93* (10), 2493–2498.
- (341) Picciapetra, F.; Sigg, L.; Behra, R. *Environ. Sci. Technol.* **2012**, *46* (2), 818–825.
- (342) Sun, R. W.-Y.; Chen, R.; Chung, N. P.-Y.; Ho, C.-M.; Lin, C.-L. S.; Che, C.-M. *Chem. Commun. Camb. Engl.* **2005**, No. 40, 5059–5061.
- (343) Zhan, D.; Li, X.; Zhan, W.; Fan, F.-R. F.; Bard, A. J. *Anal. Chem.* **2007**, *79* (14), 5225–5231.
- (344) Mash, H. E.; Chin, Y.-P.; Sigg, L.; Hari, R.; Xue, H. *Anal. Chem.* **2003**, *75* (3), 671–677.
- (345) Poulson, S. R.; Drever, J. I. *Talanta* **1996**, *43* (11), 1975–1981.

- (346) Soares, H. M. V. M.; Conde, P. C. F. L.; Almeida, A. A. N.; Vasconcelos, M. T. S. D. *Anal. Chim. Acta* **1999**, *394* (2–3), 325–335.
- (347) Hem, J. D. *Study and Interpretation of the Chemical Characteristics of Natural Water*; Department of the Interior, U.S. Geological Survey, 1985.
- (348) McDonald, S.; Bishop, A. G.; Prenzler, P. D.; Robards, K. *Anal. Chim. Acta* **2004**, *527* (2), 105–124.
- (349) Nagao, S.; Matsunaga, T.; Suzuki, Y.; Ueno, T.; Amano, H. *Water Res.* **2003**, *37* (17), 4159–4170.
- (350) Robards, K.; McKelvie, I. D.; Benson, R. L.; Worsfold, P. J.; Blundell, N. J.; Casey, H. *Anal. Chim. Acta* **1994**, *287* (3), 147–190.
- (351) Glover, C. N.; Sharma, S. K.; Wood, C. M. *Environ. Toxicol. Chem.* **2005**, *24* (11), 2941.
- (352) Harris, D. C. *Quantitative Chemical Analysis*; W. H. Freeman: United States of America, 2003.
- (353) Skoog, D.; West, D.; Holler, F.; Crouch, S. *Fundamentals of Analytical Chemistry*; Cengage Learning, 2013.
- (354) Boudou, J.-P.; Schimmelmann, A.; Ader, M.; Mastalerz, M.; Sebilio, M.; Gengembre, L. *Geochim. Cosmochim. Acta* **2008**, *72* (4), 1199–1221.
- (355) Akaighe, N.; MacCuspie, R. I.; Navarro, D. A.; Aga, D. S.; Banerjee, S.; Sohn, M.; Sharma, V. K. *Environ. Sci. Technol.* **2011**, *45* (9), 3895–3901.
- (356) Baalousha, M.; Motelica-Heino, M.; Coustumer, P. L. *Colloids Surf. Physicochem. Eng. Asp.* **2006**, *272* (1–2), 48–55.
- (357) Nuzzo, A.; Sánchez, A.; Fontaine, B.; Piccolo, A. *J. Geochem. Explor.* **2013**, *129*, 1–5.
- (358) Hau, H. H.; Gralnick, J. A. *Annu Rev Microbiol* **2007**, *61* (1), 237–258.
- (359) Patterson, G.; Davidson, M.; Manley, S.; Lippincott-Schwartz, J. *Annu Rev Phys Chem* **2010**, *61*, 345–368.
- (360) Gustafsson, M. G. L. *J Microsc Oxf.* **2000**, *198* (2), 82–87.
- (361) Fernandez-Suarez, M.; Ting, A. Y. *Nat Rev Mol Cell Biol* **2008**, *9* (12), 929–943.
- (362) Lord, S. J.; Conley, N. R.; Lee, H. D.; Samuel, R.; Liu, N.; Twieg, R. J.; Moerner, W. E. *J. Am. Chem. Soc.* **2008**, *130*, 9204–9205.
- (363) Coltharp, C.; Xiao, J. *Cell. Microbiol.* **2012**, *14* (12), 1808–1818.
- (364) Hayden, S. C.; Zhao, G.; Saha, K.; Phillips, R. L.; Li, X.; Miranda, O. R.; Rotello, V. M.; El-Sayed, M. A.; Schmidt-Krey, I.; Bunz, U. H. F. *J. Am. Chem. Soc.* **2012**, *134* (16), 6920–6923.
- (365) Brayner, R.; Ferrari-Iliou, R.; Brivois, N.; Djediat, S.; Benedetti, M. F.; Fievet, F. *Nano Lett.* **2006**, *6*, 866–870.
- (366) Wheeler, R.; Mesnage, S.; Boneca, I. G.; Hobbs, J. K.; Foster, S. J. *Mol. Microbiol.* **2011**, *82* (5), 1096–1109.
- (367) Conley, N. R.; Biteen, J. S.; Moerner, W. E. *J. Phys. Chem. B* **2008**, *112* (38), 11878–11880.
- (368) Hu, D.; Orr, G. *Nano Rev. Vol 1 2010 Incl Suppl.* **2010**.
- (369) Turner, L.; Ryu, W. S.; Berg, H. C. *J Bacteriol* **2000**, *182* (10), 2793–2801.
- (370) De Pedro, M. A.; Grunfelder, C. G.; Schwarz, H. *J Bacteriol* **2004**, *186* (9), 2594–2602.
- (371) Wirth, R.; Bellack, A.; Bertl, M.; Bilek, Y.; Heimerl, T.; Herzog, B.; Leisner, M.; Probst, A.; Rachel, R.; Sarbu, C.; Schopf, S.; Wanner, G. *Appl Env. Microbiol* **2011**, *77* (5), 1556–1562.

- (372) Etheridge, M. L.; Campbell, S. A.; Erdman, A. G.; Haynes, C. L.; Wolf, S. M.; McCullough, J. *Nanomedicine Nanotechnol. Biol. Med.* **2013**, *9* (1), 1–14.
- (373) Alkilany, A. M.; Lohse, S. E.; Murphy, C. J. *Acc. Chem. Res.* **2013**, *46* (3), 650–661.
- (374) Yeh, H.-Y.; Price, R. M.; Jacobs, D. M. *APMIS* **1992**, *100* (1–6), 503–508.
- (375) van de Linde, S.; Loschberger, A.; Klein, T.; Heidbreder, M.; Wolter, S.; Heilemann, M.; Sauer, M. *Nat Protoc.* **2011**, *6* (7), 991–1009.
- (376) Thompson, R. E.; Larson, D. R.; Webb, W. W. *Biophys. J.* **2002**, *82* (5), 2775–2783.
- (377) Mortensen, K. I.; Churchman, L. S.; Spudich, J. A.; Flyvbjerg, H. *Nat Methods* **2010**, *7* (5), 377–381.
- (378) Wiesner, M. R.; Lowry, G. V.; Alvarez, P.; Dionysiou, D.; Biswas, P. *Environ. Sci. Technol.* **2006**, *40* (14), 4336–4345.
- (379) Sharifi, S.; Behzadi, S.; Laurent, S.; Forrest, M. L.; Stroeve, P.; Mahmoudi, M. *Chem Soc Rev* **2012**, *41* (6), 2323.
- (380) **2014.**
- (381) Nowack, B.; Bucheli, T. D. *Env. Pollut. Amst. Neth* **2007**, *150* (1), 5–22.
- (382) Moore, M. N. *Environ. Int.* **2006**, *32* (8), 967–976.
- (383) Ge, Y.; Priester, J. H.; Van De Werfhorst, L. C.; Schimel, J. P.; Holden, P. A. *Environ. Sci. Technol.* **2013**, *47* (24), 14411–14417.
- (384) Kumar, N.; Shah, V.; Walker, V. K. *J. Hazard. Mater.* **2011**, *190* (1–3), 816–822.
- (385) Collins, D.; Luxton, T.; Kumar, N.; Shah, S.; Walker, V. K.; Shah, V. *PLoS ONE* **2012**, *7* (8), 42663.
- (386) Ivask, A.; Suarez, E.; Patel, T.; Boren, D.; Ji, Z.; Holden, P.; Telesca, D.; Damoiseaux, R.; Bradley, K. A.; Godwin, H. *Environ. Sci. Technol.* **2012**, *46* (4), 2398–2405.
- (387) Lohse, S. E.; Eller, J. R.; Sivapalan, S. T.; Plews, M. R.; Murphy, C. J. *ACS Nano* **2013**, *7* (5), 4135–4150.
- (388) Leive, L. *Biochem. Biophys. Res. Commun.* **1965**, *21*, 290–296.
- (389) Karkhanis, Y. D.; Zeltner, J. Y.; Jackson, J. J.; Carlo, D. J. *Anal. Biochem.* **1978**, *85*, 595–601.
- (390) Kaufmann, S.; Ilg, K.; Mashaghi, A.; Textor, M.; Priem, B.; Aebi, M.; Reimhult, E. *Langmuir* **2012**, *28* (33), 12199–12208.
- (391) Jacobson, K. H.; Kuech, T. R.; Pedersen, J. A. *Environ. Sci. Technol.* **2013**, *47*, 6925–6934.
- (392) Sauerbrey, G. *Z Phys.* **1959**, *155* (2), 206–222.
- (393) Reviakine, I.; Johannsmann, D.; Richter, R. P. *Anal. Chem.* **2011**, *83* (23), 8838–8848.
- (394) Voinova, M. V.; Rodahl, M.; Jonson, M.; Kasemo, B. *Phys. Scr.* **1999**, *59* (5), 391–396.
- (395) Malin, J. N.; Hayes, P. L.; Geiger, F. M. *J Phys Chem C* **2009**, *113* (6), 2041–2052.
- (396) Hayes, P. L.; Chen, E. H.; Achtyl, J. L.; Geiger, F. M. *J Phys Chem A* **2009**, *113* (16), 4269–4280.
- (397) Hayes, P. L.; Gibbs-Davis, J. M.; Musorrafiti, M. J.; Mifflin, A. L.; Scheidt, K. A.; Geiger, F. M. *J Phys Chem C* **2007**, *111* (25), 8796–8804.
- (398) Konek, C. T.; Ilg, K. D.; Al-Abadleh, H. A.; Voges, A. B.; Yin, G.; Musorrafiti, M. J.; Schmidt, C. M.; Geiger, F. M. *J Am Chem Soc* **2005**, *127* (45), 15771–15777.
- (399) Silhavy, T. J.; Kahne, D.; Walker, S. *Cold Spring Harb. Perspect Biol* **2010**, *2* (5), No pp. given.
- (400) Le Brun, A. P.; Clifton, L. A.; Halbert, C. E.; Lin, B.; Meron, M.; Holden, P. J.; Lakey, J. H.; Holt, S. A. American Chemical Society, 2013; Vol. 14, pp 2014–2022.

- (401) Nascimento, A.; Pontes, F. J. S.; Lins, R. D.; Soares, T. A. *Chem Commun* **2014**, 50 (2), 231.
- (402) Papo, N.; Shai, Y. *J. Biol. Chem.* **2005**, 280 (11), 10378–10387.
- (403) Wang, X.; Quinn, P. J. *Prog. Lipid Res.* **2010**, 49, 97–107.
- (404) Kirschner, K. N.; Lins, R. D.; Maass, A.; Soares, T. A. *J. Chem. Theory Comput.* **2012**, 8, 4719–4731.
- (405) Nikaido, H. *Microbiol. Mol. Biol. Rev.* **2003**, 67, 593–656.
- (406) Furukawa, Y.; Dale, J. R. *Geochem. Trans.* **2013**, 14, 3.
- (407) Korenevsky, A. A.; Vinogradov, E.; Gorby, Y.; Beveridge, T. J. *Appl. Environ. Microbiol.* **2002**, 68, 4653–4657.
- (408) Neal, A. L.; Dublin, S. N.; Taylor, J.; Bates, D. J.; Burns, J. L.; Apkarian, R.; DiChristina, T. J. *Biomacromolecules* **2006**, 8 (1), 166–174.
- (409) Thill, A.; Zeyons, O.; Spalla, O.; Chauvat, F.; Rose, J.; Auffan, M.; Flank, A. M. *Environ. Sci. Technol.* **2006**, 40 (19), 6151–6156.
- (410) Amro, N. A.; Kotra, L. P.; Wadu-Mesthrige, K.; Bulychev, A.; Mobashery, S.; Liu, G. *Langmuir* **2000**, 16 (6), 2789–2796.
- (411) Vinogradov, E.; Korenevsky, A.; Beveridge, T. J. *Carbohydr. Res.* **2003**, 338 (19), 1991–1997.
- (412) Gattis, S. G.; Chung, H. S.; Trent, M. S.; Raetz, C. R. H. *J. Biol. Chem.* **2013**, 288 (13), 9216–9225.
- (413) Kotra, L. P.; Golemi, D.; Amro, N. A.; Liu, G.-Y.; Mobashery, S. *J Am Chem Soc* **1999**, 121 (38), 8707–8711.
- (414) Vetten, M. A.; Tlotleng, N.; Rascher, D. T.; Skepu, A.; Keter, F. K.; Boodhia, K.; Koekemoer, L.-A.; Andraos, C.; Tshikhudo, R.; Gulumian, M. *Part Fibre Toxicol* **2013**, 10 (1), 50.
- (415) Hancock, I. C. Mozes, N., Handley, P. S., Busscher, H. J., Rouxhet, P. G., Eds.; VCH, 1991; pp 21–59.
- (416) Brooks, G. F.; Carroll, K. C.; Butel, J. S.; Morse, S. A.; Mietzner, T. A. *Jawetz, Melnick, & Adelberg's Medical Microbiology*, 25th ed.; McGraw-Hill, 2010.
- (417) Radovic-Moreno, A. F.; Lu, T. K.; Puscasu, V. A.; Yoon, C. J.; Langer, R.; Farokhzad, O. C. *ACS Nano* **2012**, 6 (5), 4279–4287.
- (418) Feris, K.; Otto, C.; Tinker, J.; Wingett, D.; Punnoose, A.; Thurber, A.; Kongara, M.; Sabetian, M.; Quinn, B.; Hanna, C.; Pink, D. *Langmuir* **2010**, 26 (6), 4429–4436.
- (419) Strain, S. M.; Armitage, I. M. *J. Biol. Chem.* **1985**, 260, 12974–12977.
- (420) Raetz, C. R. H.; Whitfield, C. *Annu Rev Biochem* **2002**, 71 (1), 635–700.
- (421) Chng, S.-S.; Ruiz, N.; Chimalakonda, G.; Silhavy, T. J.; Kahne, D. *Proc. Natl. Acad. Sci.* **2010**, 107 (12), 5363–5368.
- (422) Dumitriu, S. *Polysaccharides: Structural Diversity and Functional Versatility*; Hoboken: CRC Press, 1998.
- (423) Strauss, J.; Burnham, N. A.; Camesano, T. A. *J. Mol. Recognit.* **2009**, 22 (5), 347–355.
- (424) Beveridge, T. J.; Graham, L. L. *Microbiol. Rev.* **1991**, 55 (4), 684–705.
- (425) Soares, T. A.; Straatsma, T. P.; Lins, R. D. *J Braz Chem Soc* **2008**, 19 (2), 312–320.
- (426) Steel, W. H.; Walker, R. A. *Nat. Lond. U K* **2003**, 424 (6946), 296–299.
- (427) Steel, W. H.; Damkaci, F.; Nolan, R.; Walker, R. A. *J Am Chem Soc* **2002**, 124 (17), 4824–4831.
- (428) Liu, P.; Kendelewicz, T.; Nelson, E. J.; Brown, G. E. *Surf. Sci.* **1998**, 415 (1–2), 156–169.

- (429) Eckhardt, S.; Brunetto, P. S.; Gagnon, J.; Priebe, M.; Giese, B.; Fromm, K. M. *Chem. Rev.* **2013**, *113* (7), 4708–4754.
- (430) Richards, S. M.; Strandberg, K. L.; Gunn, J. S. *Endotoxins Struct. Funct. Recognit.* **2010**, 101–122.
- (431) Rittig, M. G. *J. Leukoc. Biol.* **2003**, *74* (6), 1045–1055.
- (432) Galanos, C.; Luderitz, O.; Westphal, O. *Eur J Biochem* **1969**, *9* (2), 245–249.
- (433) Rodahl, M.; Höök, F.; Krozer, A.; Brzezinski, P.; Kasemo, B. *Rev Sci Instrum* **1995**, *66* (7), 3924.
- (434) Cho, N.-J.; Frank, C. W.; Kasemo, B.; Höök, F. *Nat. Protoc.* **2010**, *5* (6), 1096–1106.
- (435) Stumm, W.; Morgan, J. J. *Aquatic Chemistry: Chemical Equilibria and Rates in Natural Waters; Third Edition*; 1995.
- (436) Whittingham, M. S. *Chem. Rev.* **2004**, *104* (10), 4271–4302.
- (437) Armand, M.; Tarascon, J.-M. *Nature* **2008**, *451* (7179), 652–657.
- (438) Johnson, C. S.; Li, N.; Lefief, C.; Vaughey, J. T.; Thackeray, M. M. *Chem. Mater.* **2008**, *20* (19), 6095–6106.
- (439) Kang, K.; Meng, Y. S.; Bréger, J.; Grey, C. P.; Ceder, G. *Science* **2006**, *311* (5763), 977–980.
- (440) Kang, D. H. P.; Chen, M.; Ogunseitan, O. A. *Environ. Sci. Technol.* **2013**, *47* (10), 5495–5503.
- (441) Poizot, P.; Laruelle, S.; Grugeon, S.; Dupont, L.; Tarascon, J.-M. *Nature* **2000**, *407* (6803), 496–499.
- (442) Lu, Z.; MacNeil, D. D.; Dahn, J. R. *Electrochem. Solid-State Lett.* **2001**, *4* (12), A200–A203.
- (443) Belharouak, I.; Sun, Y.-K.; Liu, J.; Amine, K. *J. Power Sources* **2003**, *123* (2), 247–252.
- (444) Conry, T. E.; Mehta, A.; Cabana, J.; Doeff, M. M. *Chem. Mater.* **2012**, *24* (17), 3307–3317.
- (445) Goodenough, J. B.; Kim, Y. *Chem. Mater.* **2010**, *22* (3), 587–603.
- (446) Tang, M.; Huang, H.-Y.; Meethong, N.; Kao, Y.-H.; Carter, W. C.; Chiang, Y.-M. *Chem. Mater.* **2009**, *21* (8), 1557–1571.
- (447) Song, H.-K.; Lee, K. T.; Kim, M. G.; Nazar, L. F.; Cho, J. *Adv. Funct. Mater.* **2010**, *20* (22), 3818–3834.
- (448) Mukhopadhyay, A.; Sheldon, B. W. *Prog. Mater. Sci.* **2014**, *63*, 58–116.
- (449) Doeff, M. In *Encyclopedia of Sustainability Science and Technology*; Springer, 2013.
- (450) International Energy Agency. April 2013.
- (451) Dunn, J. B.; Gaines, L.; Kelly, J. C.; James, C.; Gallagher, K. G. *Energy Env. Sci* **2015**, *8* (1), 158–168.
- (452) Sadik, O.; Karn, B.; Keller, A. *ACS Sustain. Chem. Eng.* **2014**, *2* (7), 1543–1544.
- (453) Karn, B. *J. Environ. Monit.* **2011**, *13* (5), 1184–1189.
- (454) Martha, S. K.; Sclar, H.; Szmuk Framowitz, Z.; Kovacheva, D.; Saliyski, N.; Gofer, Y.; Sharon, P.; Golik, E.; Markovsky, B.; Aurbach, D. *J. Power Sources* **2009**, *189* (1), 248–255.
- (455) Li, J.; Klöpsch, R.; Stan, M. C.; Nowak, S.; Kunze, M.; Winter, M.; Passerini, S. *J. Power Sources* **2011**, *196* (10), 4821–4825.
- (456) Beliaev, A. S.; Klingeman, D. M.; Klappenbach, J. A.; Wu, L.; Romine, M. F.; Tiedje, J. M.; Nealson, K. H.; Fredrickson, J. K.; Zhou, J. *J. Bacteriol.* **2005**, *187* (20), 7138–7145.
- (457) Qian, D.; Hinuma, Y.; Chen, H.; Du, L.-S.; Carroll, K. J.; Ceder, G.; Grey, C. P.; Meng, Y. S. *J. Am. Chem. Soc.* **2012**, *134* (14), 6096–6099.

- (458) *CasaXPS, software version 2.3.16.*
- (459) Powell, C. J.; Jablonski, A. National Institute of Standards and Technology 2011.
- (460) Tanuma, S.; Powell, C. J.; Penn, D. R. *Surf. Interface Anal.* **2003**, *35* (3), 268–275.
- (461) Lin, D.; Tian, X.; Wu, F.; Xing, B. *J. Environ. Qual.* **2010**, *39* (6), 1896–1908.
- (462) Quik, J. T. K.; Vonk, J. A.; Hansen, S. F.; Baun, A.; Van De Meent, D. *Environ. Int.* **2011**, *37* (6), 1068–1077.
- (463) Sengör, S. S.; Barua, S.; Gikas, P.; Ginn, T. R.; Peyton, B.; Sani, R. K.; Spycher, N. F. *Environ. Toxicol. Chem. SETAC* **2009**, *28* (10), 2020–2029.
- (464) Zwietering, M. H.; Jongenburger, I.; Rombouts, F. M.; van 't Riet, K. *Appl. Environ. Microbiol.* **1990**, *56* (6), 1875–1881.
- (465) Yang, K. C.; Hogg, R. *Anal. Chem.* **1979**, *51* (6), 758–763.
- (466) Young, J. C.; Cowan, R. . *Respirometry for Environmental Science and Engineering*; SJ Enterprises: Springdale, Arkansas, USA, 2004.
- (467) Gikas, P. *J. Hazard. Mater.* **2008**, *159* (2–3), 187–203.
- (468) Macomber, L.; Hausinger, R. P. *Metallomics* **2011**, *3* (11), 1153.
- (469) Kamika, I.; Momba, M. N. B. *Sci. Total Environ.* **2011**, *410–411*, 172–181.
- (470) Babich, H.; Stotzky, G. *Environ. Res.* **1982**, *29* (2), 335–350.
- (471) Nies, D. H. *Plasmid* **1992**, *27* (1), 17–28.
- (472) Bruins, M. R.; Kapil, S.; Oehme, F. W. *Ecotoxicol. Environ. Saf.* **2000**, *45* (3), 198–207.
- (473) Takeno, N. Geological Survey of Japan Open File Report No. 419 May 2005.
- (474) Li, W.; Dahn, J. R. *J. Electrochem. Soc.* **1995**, *142* (6), 1742–1746.
- (475) Choi, J.; Alvarez, E.; Arunkumar, T. A.; Manthiram, A. *Electrochem. Solid-State Lett.* **2006**, *9* (5), A241–A244.
- (476) Luo, J.-Y.; Cui, W.-J.; He, P.; Xia, Y.-Y. *Nat. Chem.* **2010**, *2* (9), 760–765.
- (477) Zhang, M.; de Respinis, M.; Frei, H. *Nat. Chem.* **2014**, *6* (4), 362–367.
- (478) Nel, A. E.; Mädler, L.; Velegol, D.; Xia, T.; Hoek, E. M. V.; Somasundaran, P.; Klaessig, F.; Castranova, V.; Thompson, M. *Nat Mater* **2009**, *8* (7), 543–557.
- (479) Zhang, H.; Ji, Z.; Xia, T.; Meng, H.; Low-Kam, C.; Liu, R.; Pokhrel, S.; Lin, S.; Wang, X.; Liao, Y.-P.; Wang, M.; Li, L.; Rallo, R.; Damoiseaux, R.; Telesca, D.; Mädler, L.; Cohen, Y.; Zink, J. I.; Nel, A. E. *ACS Nano* **2012**, *6* (5), 4349–4368.
- (480) Nel, A.; Xia, T.; Mädler, L.; Li, N. *Science* **2006**, *311* (5761), 622–627.
- (481) Myung, S.-T.; Izumi, K.; Komaba, S.; Sun, Y.-K.; Yashiro, H.; Kumagai, N. *Chem. Mater.* **2005**, *17* (14), 3695–3704.
- (482) Scott, I. D.; Jung, Y. S.; Cavanagh, A. S.; Yan, Y.; Dillon, A. C.; George, S. M.; Lee, S.-H. *Nano Lett.* **2011**, *11* (2), 414–418.
- (483) Li, C.; Zhang, H. P.; Fu, L. J.; Liu, H.; Wu, Y. P.; Rahm, E.; Holze, R.; Wu, H. Q. *Electrochimica Acta* **2006**, *51* (19), 3872–3883.
- (484) Kim, J. W.; Travis, J. J.; Hu, E.; Nam, K.-W.; Kim, S. C.; Kang, C. S.; Woo, J.-H.; Yang, X.-Q.; George, S. M.; Oh, K. H.; Cho, S.-J.; Lee, S.-H. *J. Power Sources* **2014**, *254*, 190–197.
- (485) Furrer, G.; Stumm, W. *Geochim. Cosmochim. Acta* **1986**, *50* (9), 1847–1860.
- (486) Okubo, M.; Hosono, E.; Kim, J.; Enomoto, M.; Kojima, N.; Kudo, T.; Zhou, H.; Honma, I. *J. Am. Chem. Soc.* **2007**, *129* (23), 7444–7452.
- (487) Davis, M. R.; Goldberg, J. B. *J. Vis. Exp. JoVE* **2012**, No. 63.
- (488) Lee, H.; Kim, M. G.; Cho, J. *Electrochem. Commun.* **2007**, *9* (1), 149–154.

Ian L. Gunsolus

University of Minnesota
Department of Chemistry
225 Pleasant Street SE, Minneapolis MN 55455

Email: guns0018@umn.edu
Tel: 612-518-9093

Education

- Current Doctoral Thesis: Engineered Nanomaterial Interactions with Bacterial Cells
 Thesis Advisor: Christy Haynes
 University of Minnesota, Dept. of Chemistry, Minneapolis, MN, GPA 3.8
- 2013 M.S., Chemistry, GPA 3.8, University of Minnesota, Minneapolis, MN.
 Thesis Advisor: Christy Haynes
- 2011 B.A., Chemistry, Mathematics, *cum laude*, St. Olaf College, Northfield, MN

Fellowships and Recognition

- 2015 University of Minnesota Doctoral Dissertation Fellowship Recipient
- 2013, 2014 Minneapolis Torske Klubben Graduate Student Fellowship Recipient
- 2013, 2014 National Institutes of Health Biotechnology Training Grant Recipient
- 2012 Robert L. Ferm Outstanding Graduate Teaching Assistant Award

Professional Experience

Pacific Northwest National Laboratory | May – July 2013

Supervisor: Galya Orr

Guided collaboration among researchers from three institutions to accomplish specific project aims within a time-limited setting, resulting in a publication. Developed and applied novel methods of flow-cytometry and super-resolution microscopy for high-resolution imaging of engineered nanomaterial interactions with bacterial cells.

Minnesota Department of Agriculture | May – Aug. 2009, 2010

Supervisor: Kathryn Reynolds

Prepared samples for water quality and pesticide misuse analysis using LC-MS/MS and GC-MS/MS.

Publications

I. L. Gunsolus, M. N. Hang, H. Wayland, E. S. Melby, A. C. Mensch, K. R. Hurley, J. A. Pedersen, C. L. Haynes, R. J. Hamers, Impact of Nanoscale Lithium Nickel Manganese Cobalt Oxide (NMC) on the Bacterium *Shewanella oneidensis* MR-1, *Chem. Mat.*, **2016**, 28, 1092-1100.

I. L. Gunsolus, C. L. Haynes, Analytical Aspects of Nanotoxicology. *Anal. Chem.*, **2016**, 88, 451-479.

I. L. Gunsolus, K. H. Jacobson, T. R. Kuech, J. M. Troiano, E. S. Melby, S. E. Lohse, D. Hu, W. B. Chrisler, C. J. Murphy, G. Orr, F. M. Geiger, C. L. Haynes, J. A. Pedersen, Lipopolysaccharide density and structure governs the extent and distance of nanoparticle interaction with actual and model bacterial outer membranes, *Environ. Sci. Technol.*, **2015**, 49, 10642-10650.

M. P. S. Mousavi, I. L. Gunsolus, M. Lancaster, K. Hussein, C. Haynes, P. Buhlmann, Dynamic silver speciation as studied with fluorosoluble-phase ion-selective electrodes: Effect of natural organic matter on the toxicity and speciation of silver, *Sci. Tot. Environ.*, **2015**, 537, 453-461.

Z. V. Feng, I. L. Gunsolus, T. A. Qiu, K. R. Hurley, L. H. Nyberg, H. Frew, K. P. Johnson, A. M. Vartanian, L. M. Jacob, S. E. Lohse, M. D. Torelli, R. J. Hamers, C. J. Murphy, C. L. Haynes. Impacts of Gold Nanoparticle Charge and Ligand Type on Surface Binding and Toxicity to Gram-Negative and Gram-Positive Bacteria. *Chem. Sci.*, **2015**, 6, 5186-5196.

I. L. Gunsolus, M. P. S. Mousavi, K. Hussein, P. Buhlmann, C. Haynes, Effects of Humic and Fulvic Acids on Silver Nanoparticle Stability, Dissolution, and Toxicity, *Environ. Sci. Technol.*, **2015**, 49, 8078-8086.

I. L. Gunsolus, D. Hu, C. Mihai, S. E. Lohse, C. Lee, M. D. Torelli, R. J. Hamers, C. J. Murphy, G. Orr, C. L. Haynes, Facile Method to Label Bacteria for Super-resolution Microscopy, *Analyst*, **2014**, 139, 3174-3178.

M. A. Maurer-Jones, I. L. Gunsolus, B. M. Meyer, C. J. Christenson, C. L. Haynes, Impact of TiO₂ Nanoparticles on Growth, Biofilm Formation, and Flavin Secretion in *Shewanella oneidensis*, *Anal. Chem.*, **2013**, 85, 5810-5818.

M. A. Maurer-Jones, I. L. Gunsolus, C. J. Murphy, C. L. Haynes, Toxicity of Engineered Nanoparticles in the Environment, *Anal. Chem.*, **2013**, 85, 3036-3049.

Presentations

- 2015 Contributed Poster, Midwest Universities Analytical Chemistry Conference, Minneapolis, MN, *Lipopolysaccharides Mediate Nanoparticle Interactions with Bacterial Cell Membranes*
- Contributed Poster, Gordon Research Conference, Environmental Nanotechnology, Mount Snow, VT, *Effects of Humic and Fulvic Acids on Silver Nanoparticle Stability, Dissolution, and Toxicity*
- Contributing Speaker, National Science Foundation Review of the *Center for Sustainable Nanotechnology*, Washington, D.C.
- Invited Lecture, University of Minnesota iPrime Mid-year Workshop, Minneapolis, MN, *Engineered Nanoparticle Interaction with Living and Model Cell Membranes*
- 2014 Contributed Lecture, American Chemical Society National Meeting, San Francisco, CA, *Engineered Nanoparticle Interaction with Living and Model Cell Membranes*
- Contributed Lecture, University of Minnesota Chemistry Graduate Student Symposium, Minneapolis, MN, *Engineered Nanoparticle Interaction with Living and Model Cell Membranes*
- Contributed Lecture, University of Minnesota Institute on the Environment, Sustainability Symposium, St. Paul, MN, *Towards Sustainable Nanomaterial Design*
- Contributing Speaker, National Science Foundation Cyber Review of the *Center for Sustainable Nanotechnology*, Madison, WI.
- 2013 Invited Lecture, St. Olaf College, Department of Chemistry, Northfield, MN, *Towards Sustainable Nanotechnology: Understanding the Nano-Bio Interface*
- Poster Session, SciX, Milwaukee, WI, *Material and Biological Properties Controlling the Interaction of Bacterial Cells with Nanomaterials*

Teaching Experience

- 2014 – Present Private Tutor, University of Minnesota, Department of Chemistry, Minneapolis, MN, General Chemistry Program
- 2011 – 2012 Laboratory Teaching Assistant, University of Minnesota, Department of Chemistry, Minneapolis, MN, General Chemistry Program

Select Leadership and Outreach Experience

2013 – Present Contributing author and editor for the *Center for Sustainable Nanotechnology's* blog: *sustainable-nano.com*

2014 – Present Chemistry Department Representative, University of Minnesota Council of Graduate Students

2013 – Present Research Mentor to undergraduate researchers, University of Minnesota, Department of Chemistry and *Center for Sustainable Nanotechnology* REU program

2012 – 2015 Visiting teacher at W. 7th Community Center, St. Paul, MN, guiding kindergarten through middle-school students through science demonstrations and activities